UNIVERSITY OF SOUTHAMPTON

FACULTY OF ENGINEERING, SCIENCE & MATHEMATICS
Southampton Oceanography Centre
School of Ocean & Earth Sciences

Time variability of sea surface parameters in the tropical Atlantic using satellite and in situ data

by

Antonio Caetano Vaz Caltabiano

Thesis for the degree of Doctor of Philosophy

September 2004

---

* This study has been sponsored by Conselho Nacional de Desenvolvimento Científico e Tecnológico (CNPq) – Science and Technology Ministry, Brazilian Government, grant number 201076/97-7

Graduate School of the
Southampton Oceanography Centre

This PhD dissertation by

Antonio Caetano Vaz Caltabiano

has been produced under the supervision of the following persons

Supervisor

Professor Ian S. Robinson

Chair of Advisory Panel

Professor Michael Collins

Member of Advisory Panel

Dr Neil Wells

UNIVERSITY OF SOUTHAMPTON

ABSTRACT

FACULTY OF ENGINEERING, SCIENCE & MATHEMATICS
SCHOOL OF OCEAN & EARTH SCIENCES

Doctor of Philosophy

TIME VARIABILITY OF SEA SURFACE PARAMETERS IN THE TROPICAL ATLANTIC USING SATELLITE AND IN SITU DATA

by Antonio Caetano Vaz Caltabiano

The influence of the tropical Atlantic Ocean over the climate of Europe, Africa and America is well known today. However, several questions about high-frequency processes in this region remain open. This thesis addresses the characterisation of the diurnal and other short timescale variability of the meteo-ocean variables measured in the tropical Atlantic Ocean by the PIRATA array, as well as derived air-sea heat fluxes. By combining the complementarity and mitigating the disadvantages of using the high temporal resolution of in situ data in conjunction with the excellent spatial coverage of satellite based data, this work also aims to investigate the characteristics of the Tropical Instability Waves in the tropical Atlantic. The satellite data validation process used in this study assesses each of the buoys individually, to take into account possible regional biases.

A complete picture of the mean diurnal cycle and the seasonal variability of the diurnal signal is performed for the first time for the whole tropical Atlantic basin. The SST diurnal signal presents strong characteristics during the respective summer in both hemispheres. However, through the wavelet technique used in this analysis, a significant diurnal signal at the equator could be noticed during the second half of each year, indicating a possible modulation of the diurnal signal by processes with different timescales. It is suggested that Tropical Instability Waves could be one of these processes. The results presented here show that the TIW clearly vary their position and time of activity, depending on the degree of development of the equatorial cold tongue. The most active year analysed in this study was 2001, when the spectral characteristics could be observed as far north as 4^{o}N. The imprints of the TIW are well marked in the wind fields, showing that clearly there are coupled mechanisms associated with the TIW. Moreover, this study confirms that a coupling mechanism suggested for the Pacific Ocean is also applicable to the tropical Atlantic basin. The measurements made by the TMI sensor, in conjunction with the Qscat wind data showed that the atmospheric fields are highly correlated with the SST fields at the timescale associated with the TIW.

The analysis of the cross-scale relationship suggests that the passage of instability waves might affect the diurnal amplitude of SST, skin-SST and latent heat flux. The mechanisms that interact on the eastern and western side of the equatorial Atlantic tend to be distinct, especially due to the local oceanographic and meteorological conditions, and due to the different level of TIW activity.

TABLE OF CONTENTS

CHAPTER 1 - INTRODUCTION

CHAPTER 2 – VARIABILITY OF THE TROPICAL ATLANTIC

CHAPTER 3 – DATASET AND METHODS OF ANALYSIS

CHAPTER 4 – VALIDATION OF THE DATASET

CHAPTER 5 – DIURNAL CYCLE IN THE TROPICAL OCEANS

CHAPTER 6 – TROPICAL INSTABILITY WAVES

CHAPTER 7 – INTERACTIONS BETWEEN DIURNAL VARIABILTY AND TIW

CHAPTER 8 – DISCUSSION, CONCLUSIONS AND FUTURE WORK

LIST OF FIGURES

LIST OF TABLES

DECLARATION OF AUTHORSHIP

I, Antonio Caetano Vaz Caltabiano,

declare that the thesis entitled

Time variability of sea surface parameters in the tropical Atlantic using satellite and in situ data

and the work presented in it are my own. I confirm that:

- this work was done wholly or mainly while in candidature for a research degree at this University;
- where any part of this thesis has previously been submitted for a degree or any other qualification at this University or any other institution, this has been clearly stated;
- where I have consulted the published work of others, this is always clearly attributed;
- where I have quoted from the work of others, the source is always given. With the exception of such quotations, this thesis is entirely my own work;
- I have acknowledged all main sources of help;
- where the thesis is based on work done by myself jointly with others, I have made clear exactly what was done by others and what I have contributed myself;
- none of this work has been published before submission.

Signed: …………………………………………………………………………..

Date:……………………………………………………………………………….

ACKNOWLEDGEMENTS

I would not be able to finish this thesis without the help and support of several people. For this I would like to thanks:

- My supervisor, Professor Ian Robinson, and the members of my panel, Professor Michael Collins and Dr Neil Wells;

- Ministério da Ciência e Tecnologia – Brasil, through Conselho Nacional de Desenvolvimentto Científico e Tecnológico (CNPq) for financial support during my candidature;

- The whole LSO group for allowing me to use its facilities and for storing all satellite data used in this thesis. Remote Sensing Systems (http://www.ssmi.com/) for providing TMI and QuikScat datasets. TAO Project Office for providing the PIRATA (http://www.pmel.noaa.gov/pirata/) dataset. Wavelet software was provided by C. Torrence and G. Compo (http://paos.colorado.edu/research/wavelets/);

- A very special thanks to David Cromwell for all his support and friendship during all my time here, in particular at the end by revising the whole document. Also, many thanks to Christine, Cipo, Helen, Lisa, Graham, Peter, Richenda and Andrew for their friendship and help with Matlab, data management, maths, data processing, etc…

- Alice Stuart-Menteth for her friendship and for always being there for discussing things. And for listening.

- My friends in Southampton (and some who moved on): Susanne and Hans, Boris and Tamaris (+ Rozanna and Natalia), Martin, Ollie, James, Isabel and Carlos, Dohyung, Ana Hilário, Xana, Maria, Dave Lambkin, Babete and Alex, Sinhue and Sara, Adriana and Ben, Anita and Alessio, Taro and Alessandra;

- The “Brazilian Gang”: Ronald and Tati (+ Bela and Flora), Rodrigo and Dhesi (+ Henrique and Isadora), Alex and Valéria (+ Gabriel and Vinícius), Lu and Marisa, César and Sílvia (+ Vìtor), Hervé and Ana (+Pierre), Olliand Sílvia, Erik and Roberta, Gilberto and Elisa (+ Júlia), Marcos and Caína, James, Edu and Cláudia, and Manu;

- Família Veeck, pelo carinho e amizade que me receberam dentro de casa. Não fazem idéia de como foram importantes!!

- Meus pais, pela vida e por estarem presentes sempre que precisei. E minhas irmãs, pela amizade e felicidade de ser um irmão;

- And the two most important persons, without who I would not finish at all. Lu e Artur, eu amo vocês!!! Muito obrigado por fazerem parte da minha vida!!

ACRONYMS

ACCE	Atlantic Circulation and Climate Experiment
ADEOS	Advanced Earth Observing Satellite
ATLAS	Autonomous Temperature Line Acquisition System
ATSR	Along-Track Scanning Radiometer
AVHRR	Advanced Very High Resolution Radiometer
BC	Brazil Current
CCM3	NCAR Community Climate Model
COADS	Comprehensive Ocean-Atmosphere Data Set
COARE	Coupled Ocean Atmosphere Response Experiment
cSEC	central South Equatorial Current
CW	Central Waters
DAS	Data Assimilation System
DWBC	Deep Western Boundary Current
ECMWF	European Centre for Medium-Range Weather Forecasts
ENSO	El Niño Southern Oscillation
EOF	Empirical Orthogonal Functions
eSEC	equatorial South Equatorial Current
EUC	Equatorial Undercurrent
FOCAL	Français Océan Climat Atlantique Equatorial
GARP	Global Atmospheric Research Program
GATE	GARP Atlantic Tropical Experiment
GC	Guinea Current
GEOS	Goddard Earth Observing System
GHRSST-PP	GODAE High Resolution Sea Surface Temperature Pilot Project
GODAE	Global Ocean Data Assimilation Experiment
ITCZ	Intertropical Convergence Zone
NAO	North Atlantic Oscillation
NASA	National Aeronautics and Space Administration
NBC	North Brazil Current
NCAR	National Center for Atmospheric Research
NCEP	National Centers for Environmental Prediction
NEC	North Equatorial Current
NECC	North Equatorial Countercurrent
NSCAT	NASA Scatterometer
nSEC	northern South Equatorial Current

NWP	Numerical Weather Prediction
PIRATA	Pilot Research Moored Array in the Tropical Atlantic
PMEL	Pacific Marine Environmental Laboratory
RT	Radon Transform
SEC	South Equatorial Current
SECC	South Equatorial Countercurrent
SEQUAL	Seasonal Response of the Equatorial Atlantic
SEUC	South Equatorial Undercurrent
SMMI	Special Sensor Microwave/Imager
SMMR	Scanning Multichannel Microwave Radiometer
sSEC	southern South Equatorial Current
SST	Sea Surface Temperature
SVD	Singular Value Decomposition
TAO	Tropical Atmosphere/Ocean
TIW	Tropical Instability Waves
TMI	TRMM Microwave Imager
TOGA	Tropical Ocean Global Atmosphere
TRMM	Tropical Rainfall Measuring Experiment
TSW	Tropical Surface Water
VOS	Volunteer Observing Ship
WMO	World Meteorological Organization
WOCE	World Ocean Circulation Experiment
ZZD	Zeng, Zhang and Dickinson algorithm

Chapter 1

Introduction

1.1. General introduction

The tropical oceans are generally characterised by a relatively shallow thermocline (about 100 m deep) separating a layer of warm, light fluid from a cooler, heavier one. The tropical ocean’s upper layer can be defined by two parameters: surface temperature and thermocline depth. The depth of the thermocline is considered as the dynamic response of the ocean to the global wind forcing, and the surface temperature is mostly considered as the thermodynamic response of the ocean to the local thermodynamic atmospheric forcing. Maintained by permanent easterly tradewinds, the annual mean thermocline is deeper on the western than on the eastern side of the tropical ocean (Merle and Arnault, 1985; Carton and Zhou, 1997).

Since the 1960's, the Tropical Atlantic Ocean has drawn the attention of many authors in different fields of research (Brown, 1961). The Tropical Atlantic Ocean is geographically located between the latitudes of 30^o N and 30^o S and from 70^o W to the African coast. As a natural link for Europe, Africa and America, its climatic influence over these continents is well known today (Hastenrath and Heller, 1977; Moura and Shukla, 1981; Servain, 1991; Nobre and Shukla, 1996; Enfield and Mayer, 1997; Yu and McPhaden, 1999; Ruiz-Barradas et al., 2000; Pezzi and Cavalcanti, 2001). However, there are still many open questions, especially concerning the oceanic climate variability. It is now established that the key to world climatic variations lies at least partly in large-scale ocean atmosphere interactions occurring in the tropics. In the tropical Atlantic, particular emphasis has been given to the study of the sea surface temperature (SST) oscillation known as the tropical Atlantic dipole (Servain, 1991) and its relation to the regional and world climate.

The lack of in situ data in the Tropical Atlantic has always been one of the major obstacles to a better understanding of the variability in the region. The first two major projects set up to consistently collect and analyse oceanographic and meteorological data in this region were the Global Atmospheric Research Program (GARP) Atlantic Tropical Experiment (GATE) in 1974, and the Français Océan Climat Atlantique Equatorial / Seasonal Response of the Equatorial Atlantic (FOCAL/SEQUAL) project, established in 1982. In the late 1990's, the establishment of research projects such as the Atlantic Circulation and Climate Experiment (ACCE) (WOCE, 1997) and the Pilot Research Moored Array in the Tropical Atlantic (PIRATA) (Servain et al., 1998) has increased the number and quality of data in the tropical Atlantic.

The PIRATA program began in late 1997 with the full array in place by the year 2000. It was envisioned as part of a multinational effort involving Brazil, France, and the United States. The array consists of 13 Next Generation ATLAS (Autonomous Temperature Line Acquisition System) moorings spanning 15°N – 10°S, 38°W – 0° (Figure 1.1). Of these 13 buoys initially proposed to be deployed, only 11 are still acquiring and transmitting the data. The loss of the other 2 buoys (2°N and 2°S at 10°W) is due to vandalism associated with tuna fishing, which takes place in the eastern equatorial Atlantic. The specific configuration of the PIRATA array (Figure 1.1) has been chosen to provide coverage along the equator of regions of strong wind forcing in the western basin and significant seasonal-to-interannual variability in SST in the central and eastern basin. The spacing of moorings near the equator (10° – 15° zonally and 2° meridionally) has been chosen to resolve the rapid equatorial Kelvin wave responses to abrupt wind changes in the western Atlantic.

Of the various oceanographic parameters obtained by all these observing programmes, the one with best coverage is the SST. This is because of the Volunteer Observing Ship (VOS) System (WMO, 1998). This programme utilises merchant ships of opportunity to make in situ oceanographic measurements in the sea, the simplest of all being SST. The size of the fleet taking part of the programme is currently estimated at about 4000 ships worldwide. As might be expected, realtime reports from the VOS are heavily concentrated along the major shipping routes, primarily in the North Atlantic and North Pacific Oceans. Therefore, these data are not sufficient to give the proper temporal and spatial resolutions required to study the tropical rapid and large-scale variations.

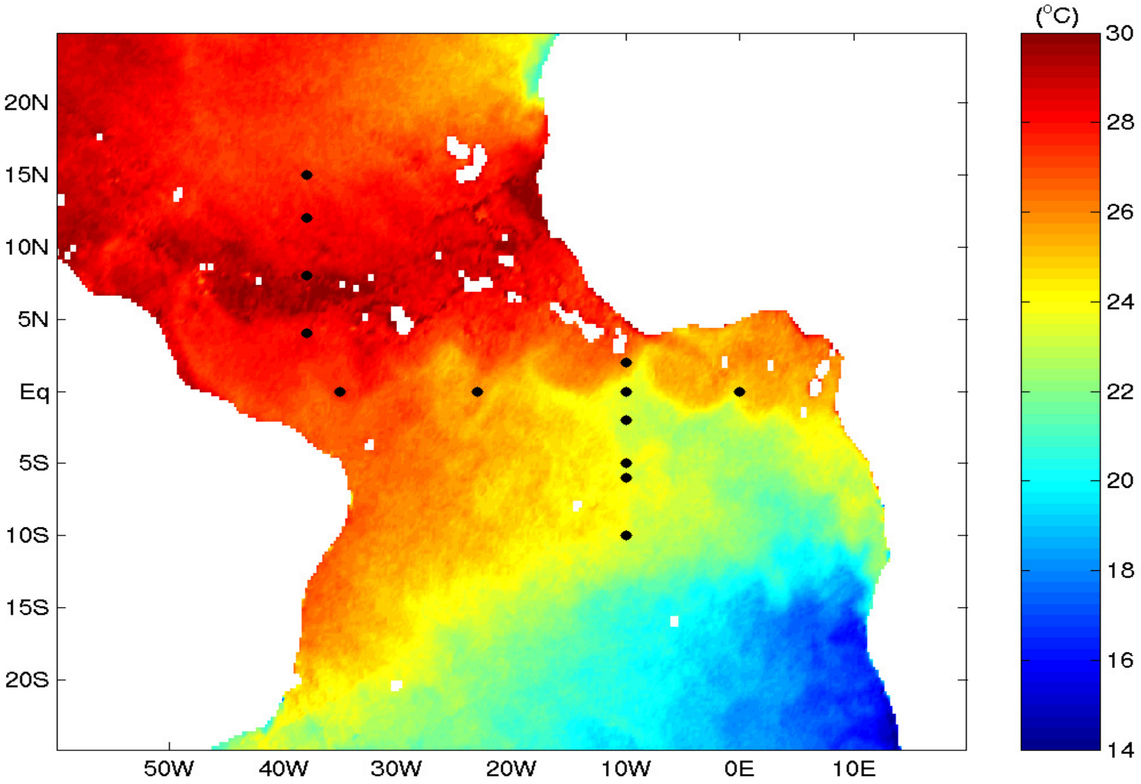

Figure 1.1 – Position of the buoys in the PIRATA array (black points) overlaying TMI SST (colour) on a 3-day mean composite starting on 19/09/2001. SST is in °C.

Satellite sensors provide an alternative approach to measuring SST from ships, and provide the higher spatial and temporal coverage needed to generate climatology more capable of characterizing local and seasonal SST changes, over time scales of days to years and spatial scales of a few kilometres. If used in conjunction with in situ data, i.e. from ships, moored buoys and drifters, the measurements from satellite sensors become a very powerful tool to understand many oceanographic phenomena.

However, caution is needed when using satellite-derived SST. One needs to clarify the meaning of the term "sea surface temperature". It becomes necessary to distinguish between “bulk” and "skin" SST. Skin SST is the radiometric temperature of the sea surface, and refers to the temperature at the air-sea interface, in a thin layer of the upper microns of the ocean. Bulk SST refers to the temperature of the upper ocean mixed layer, below the oceanic skin layer. The bulk SST determined from buoy measurements is typically obtained at a depth of 1 metre. Ships of opportunity generally obtain SST from a layer of about 5 – 10 metres deep. This is an important point because the temperature of the surface skin can differ by up to several degrees from the bulk SST (Yokoyama et al., 1995; Soloviev and Lukas, 1997; Donlon et al., 1999), being typically slightly cooler than the water millimetres below it by 0.17^{o}C (Donlon et al., 2002). As these previous studies have clearly shown that the diurnal signal has the potential to add bias and noise to measurements supposed to represent the mixed layer SST, Donlon (2004), through the GODAE High Resolution Sea Surface Temperature Pilot Project (GHRSST-PP), suggested a new definition for SST to describe the true mixed layer surface temperature, called Foundation Temperature. The project also recommends that all in situ measurements should be defined with their depth. For the present work, the term of bulk SST always refers to buoy measurements at 1-m depth.

The difference between bulk and skin SST is mainly due to the combined effects of diurnal warming and the “skin effect” (which is due to the effects of radiative and evaporative heat loss). The radiative, latent, and sensible heat exchanges between the atmospheric and oceanic boundary layers depend on the actual skin temperature of the ocean, making the skin temperature the critical SST for examining air-sea interactions (Webster et al., 1996).

Most of the databases that contain satellite infra-red SST data have their calibration algorithms built in reference to in situ SST measured by buoys or ships of opportunity. Once this is done, important processes such as the skin effect are incorporated to the data set (Robinson et al., 1984). Casey and Cornillon (1999) compare climatologies based on three data compilations: in situ only, blended satellite-in situ, and satellite-derived only. They showed that, although an 11-year base period for the satellite-derived climatology is somewhat shorter than the 30 years generally used for in situ climatologies, the abundance of the satellite data allowed the generation of nearly complete mean fields for each calendar month at a very high spatial resolution (approximately 9 km). They also found that the satellite SST data were more representative of spatial and seasonal SST variability than the traditional in situ and blended SST climatologies.

One of the aspects of research that has not been extensively covered in the tropical Atlantic is the diurnal cycle of the SST fields. In addition, the influence of the diurnal cycle variability on the differences between SST measured by buoys and satellites also need to be addressed. The spatial extent and the amplitude of the SST diurnal cycle in the tropical Atlantic is not well documented, especially because of the lack of high temporal resolution data for the region.

A diurnal warming is well known to occur in the upper ocean whenever the solar heating at noon exceeds the heat loss from the ocean surface (Imberger, 1985). Also, advection of warm water masses can also produce large day-night differences. As an example, regions of high surface variability (eddies, western boundary currents) can produce rapid shifts in SST over very short periods of time. Since the SST is a key parameter to calculate air-sea fluxes, it is necessary to address the difference between skin and bulk SST and their diurnal variations. The skin SST (SSST) data needed for such flux calculations differ little over a daily average from the measured bulk SST (BSST) but have diurnal variations departing substantially from those of the BSST. Hence, the examination of the diurnal flux patterns requires an adjustment of the BSST to SSST (Zeng et al., 1999).

Although synoptic and mesoscale air-sea flux variability in the tropics has a smaller magnitude in comparison to mid- and high latitudes, it may play an important role in some key processes in the tropical boundary layer. Large synoptic diurnal variations of tropical evaporation can affect cumulus convection (Soden, 2000). Also, in the tropics, the diurnal cycle in the air-sea fluxes becomes important, especially under calm conditions and considerable insolation (Weller and Anderson, 1996). These diurnal surface fluxes are most likely to be significant for atmospheric models, which are now generally forced by weekly or monthly average measured bulk temperatures (Reynolds and Smith, 1994), or by ocean model surface temperatures that neither resolve the diurnal cycle nor distinguish between bulk and skin temperatures.

A very powerful tool that can help to improve our understanding of the SST diurnal cycle in the tropical Atlantic is the SST data retrieved from the Microwave Imager (TMI) on the joint US/Japan Tropical Rainfall Measuring Mission (TRMM). Because the atmosphere and the clouds are transparent to microwaves the sensor has an enormous advantage over infrared radiometers such as the Advanced Very High Resolution Radiometer (AVHRR) and the Along Track Scanning Radiometer (ATSR), for example. The tropical regions, especially, suffer the chronic problem of high cloud coverage and data interpolation is often needed to fill gaps in AVHRR and ATSR data. Moreover, due to the low inclination of the satellite orbit, the TMI sensor can give an optimal sampling rate for monitoring diurnal variations. TMI has been used to estimate precipitation over the oceans (Imaoka and Spencer, 2000), in addition to and in recent years it has been intensively used to study Tropical Instability Waves (TIW), especially in the tropical Pacific.

TIW are cusp-shaped frontal waves (Figure 1.1) and have been observed very often in the tropical Pacific region, more developed north of the equator. They were first studied by Legeckis (1977) using radiometers on geostationary satellites. Since then, they have been extensively studied by other orbital infrared sensors (Allen et al., 1995), in situ data (Halpern et al., 1988; Hayes et al., 1989) and ocean models (Philander et al., 1986; Stockdale et al., 1993; Masina and Philander, 1999; Masina et al., 1999). Most recently, several studies have been performed using SST data retrieved from an orbital microwave sensor (Chelton et al., 2000; Liu et al., 2000; Chelton et al., 2001; Hashizume et al., 2001). In the Atlantic, however, the study of TIW is still a new and active field of investigation, and their spatial and temporal characterisation needs to be addressed.

Most recent studies of equatorial ocean dynamics explore interactions at the lower end of the frequency spectrum, such as connections between the El-Nino Southern Oscillation (ENSO) signal and the seasonal cycle (Enfield and Mayer, 1997; Yu and McPhaden, 1999; Ruiz-Barradas et al., 2000), in addition to interannual modulation and phase locking with TIW (Qiao and Weisberg, 1995; Cronin and Kessler, 2002). However, cross-scale interaction with the high end of the spectrum has not been fully explored. Understanding how high frequency mixed layer processes are modulated by, and in turn affect lower frequency seasonal and interannual variability is crucial for developing correct parameterizations of these processes.

With the possibility of combining the complementarity and mitigating the disadvantages of using the high temporal resolution of in situ data in conjunction with the excellent spatial coverage of satellite based data, this work aims to improve the understanding of the high-frequency variability in the tropical Atlantic Ocean.

1.2. Objectives

The main goal of this thesis is **to study and characterise the diurnal and other short timescales variability of the sea surface temperature and associated fields in the tropical Atlantic Ocean using a combination of in situ and satellite data.**

As mentioned before, little is known about the full spectral characteristics of the TIW in the tropical Atlantic. There are still some questions that remain open about TIW in the Atlantic: do TIW spectral characteristics in the tropical Atlantic vary from year to year? Where are they more active? Also, the hypotheses of ocean-atmosphere coupling on the properties of TIW have not been fully discussed for the tropical Atlantic. As the study of TIW in the Atlantic is still an active field of investigation, this thesis will explore the temporal and spatial variabilities associated with the TIW in the tropical Atlantic, and their spectral characteristics. Moreover, it will investigate multi-year variations of the TIW in the Atlantic basin using high-quality satellite data. These datasets also allow a complete assessment of the co-variability of geophysical fields measured by satellite and that can be affected by the instability waves. Therefore, we aim:

- to characterise the propagation of Tropical Instability Waves in the Tropical Atlantic, relating it with the SST, wind and air-sea fluxes variability.

It is already evident that the PIRATA array provides an incomparable source of data, especially high-frequency measurements that are useful for studies relating to diurnal variability. As there were no previous datasets similar to the PIRATA array, some scientific questions remain with incomplete or without answers. What is the magnitude of the diurnal cycle of SST, wind and air-sea fluxes in the tropical Atlantic Ocean? Are there differences in the diurnal signal between different regions (equatorial, extra-equatorial, western and eastern side) of the tropical Atlantic basin? What is the relationship between the measured met-ocean variables and calculated air-sea fluxes in a short time-scale for the tropical Atlantic Ocean? To try to answer those questions, the work has been guided by the following specific objectives:

- to characterise the geographical distribution of the diurnal variability of SST, wind and air-sea fluxes in the tropical Atlantic Ocean;

- to evaluate the interrelationship between SST, wind and air-sea fluxes in the tropical Atlantic Ocean at short time-scales;

As remote sensing is to be used as a major tool for oceanographic studies, especially in regions with lack of in situ data, it is important to validate the present retrievals of geophysical variables as “seen” by satellite. This subject will be addressed by the follow specific objective:

- to evaluate the difference between air-sea fluxes calculated using in situ and satellite-retrieved data;

1.3. Structure of the document

This document is organised as follows: Chapter 1 presents an introduction and the main objectives of the research. Chapter 2 presents background knowledge of the variability in the tropical Atlantic for several parameters, as well a review about the TIW. A description of the data and analytical methods used in this work is presented in Chapter 3. In Chapter 4 a complete validation of the dataset used in this work is performed by comparing in situ and satellite data.

The following three chapters present the main original contributions contained in this thesis. Chapter 5 exhibits and assesses the results of analyses of the diurnal cycle of met-ocean variables and heat fluxes in the tropical Atlantic, observed using the PIRATA dataset, and discusses them in relation to the relevant literature. Chapter 6 presents a complete analysis of the temporal and spatial distribution of the propagation of Tropical Instability Waves in the tropical Atlantic, and evaluates their influence on the atmospheric fields. The results achieved introduce new knowledge about this topic, covering some of the gaps identified in the relevant literature. Chapter 7 seeks to examine the existence of cross-scale interactions between diurnal cycle and TIW variability signals in the tropical Atlantic. And finally, Chapter 8 will present a general discussion, conclusions and suggestions for future work.

Chapter 2

Variability of the Tropical Atlantic

2.1. Introduction

It is well known that the largest ocean-atmosphere signal in the tropical Atlantic is the seasonal cycle which is in equilibrium with the wind (Philander and Chao, 1991). Most of the variability in the upper ocean in this region is associated with the meridional motion of the Intertropical Convergence Zone (ITCZ) from its mean position (near 8°N at 28°W). The ITCZ follows the seasonal cycle of the thermal equator, located around 3°N (Hastenrath and Lamb, 1978; Enfield and Mayer, 1997; Servain et al., 1999), and is characterised by strong convection and the constant presence of clouds.

This chapter will describe the long-term variability observed in the tropical Atlantic, in particular wind, SST currents and air-sea fluxes. Those main variables are the ones involved in coupling processes that can be associated with the modulation of high-frequency variability, and mesoscale processes, such as the Tropical Instability Waves, which are the main focus of this thesis. The background knowledge of the TIW is also highlighted in this chapter.

2.2. Winds

The wind field of the Atlantic Ocean is characterized by the northeasterly and southeasterly trade winds, which converge to form the ITCZ (Figure 2.1). Seasonally, the winds at the equator are intense during the northern summer and autumn when the ITCZ is farthest north and are weak in February, March and April when it is closer to the equator (Philander and Chao, 1991). As a consequence, the variability of the wind stress is determined by the seasonal displacements of the ITCZ. When the ITCZ reaches its northernmost position in September (about 10° – 15°N) the wind stress at the equator is maximum.

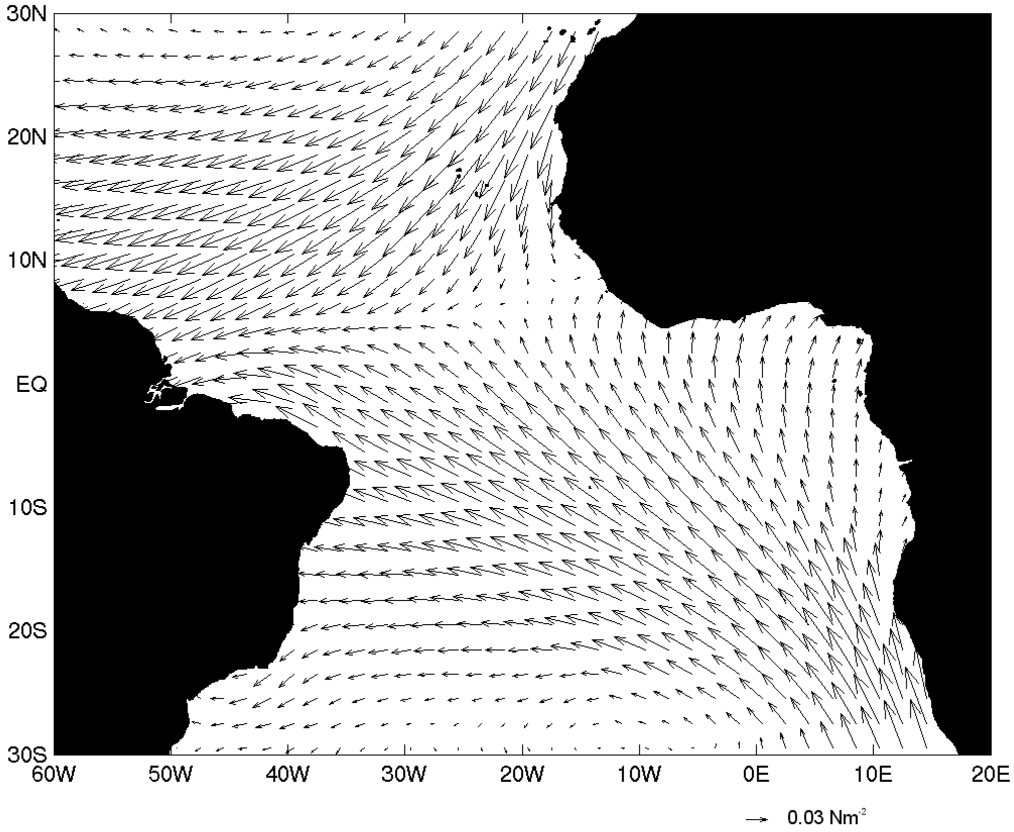

Figure 2.1 - Wind stress annual mean.
Source: SOC Climatology (http://www.soc.soton.ac.uk/JRD/MET/fluxclimmon.php)

The seasonal variability of the northeast trade winds is different from that of the southeast trades, as was shown by Hellerman and Rosenstein (1983) and Servain and Lukas (1990). In the atlas presented by Picaut et al. (1985), the mean seasonal cycle of wind stress shows that the northeast trade winds are stronger in February, in a large area centred around 10°N, 45°W. A second, smaller peak in magnitude occurs slightly farther northwest in June. These northeast trades are weak from August to November and their minimum occurs in October-November. The magnitude of the southeast trade winds is greatest in June-July and limited to an area around 10°S, 20°W.

In the western part of the tropical Atlantic basin, the wind is mainly zonal and has a strong annual amplitude. In the Gulf of Guinea (5° N – 5° S, 5° W – 10° E), the wind is more meridionally oriented with an eastward component at its easternmost part due to a low pressure system over the African continent (du Penhoat and Treguier, 1985). The winds weaken in July and August but then intensify again in November. Owing to that the large scale wind field has a significant semiannual signal (Philander and Pacanowski, 1986b).

Because the width of the equatorial Atlantic is small compared to the equatorial Pacific, the adjustment time to a change in the winds is lower than the seasonal time scale. This means that the response to the seasonal forcing should be mostly in equilibrium and should correspond to a succession of steady states. This idea has already been confirmed by the measurements of Katz (1987b). They found that seasonal variations in the intensity of the zonal wind stress along the equator, and in the oceanic zonal pressure gradient maintained by the wind, are practically in phase in the western equatorial Atlantic.

In this overview of the behaviour of the winds in the Tropical Atlantic, it is also necessary to point out that the response of the ocean in this region to the seasonally varying surface winds includes some other striking phenomena: the seasonal reversal of the North Equatorial Countercurrent in the western side of the ocean basin (Garzoli and Katz, 1983; Merle and Arnault, 1985), and the seasonal upwelling along the northern and eastern coasts of the Gulf of Guinea where the local winds do not vary seasonally (Picaut, 1983).

Observations made by Houghton (1989) suggested that the upwelling event in the Gulf of Guinea is associated with neither the local winds nor the local ocean circulation. A possible explanation is the mechanism of remote wind forcing in the western equatorial Atlantic that generates equatorial Kelvin wave pulses travelling eastward (Katz, 1987a; Verstraete, 1992). According to Weisberg and Tang (1987), the manner in which the wind stress changes from year to year is therefore crucial to the equatorial ocean's response. However, Philander and Pacanowski (1986b) found that the oceanic response to the winds is surprisingly local. Those authors show that the wind variations to the east of 30° W have smaller amplitude than those to the west and also have a distinct semiannual harmonic with maxima in June/July and in November.

Weisberg and Tang (1990), following the study performed by Weisberg and

Tang (1985), tried to clarify this issue with model simulations. Using a coherence analysis, the authors found that the entire basin responds to the wind stress distribution used to force the model, although with largest values at the western boundary and minimum values in the Gulf of Guinea. With these results, they conclude that the Gulf of Guinea is responding to remote forcing; however, it is the localized distribution of wind stress within the Gulf of Guinea that determine the location of maximum upwelling.

However, one topic that has received little attention in the literature is how the wind is responding to changes in the temperature fields rather than forcing the changes in the tropical Atlantic, in particular on intraseasonal scales that might be associated to TIW variability. This air-sea coupling is a very interesting issue that has not been fully investigated and results of this coupling will be presented in Chapter 6.

2.3. Sea surface temperature

Sea surface temperature is the most important physical parameter of the ocean affecting the atmosphere and because of this, it is the most studied parameter in the tropical Atlantic so far. The annual cycle of SST presents two distinct regions, one north and one south of the thermal equator at approximately 3° N (Figure 2.2). To the north, SST reaches its peak in September, while to the south the SST peaks in March-April. The largest amplitudes in both hemispheres occur in the east, where the thermocline is shallow. Off northwest and southwest Africa the amplitude of the annual cycle exceeds 3° C. Along the equator, SST follows the annual cycle of the Southern Hemisphere SST, with a maximum temperature in March and a minimum temperature in September. The cold water first appears along the equator between 10° W and 0° W and then expands westward (Carton and Zhou, 1997).

Unlike the tropical Pacific, the tropical Atlantic is not dominated by any single mode of climate variability such as the El Niño-Southern Oscillation (ENSO). Rather, this region is subject to multiple competing influences of comparable importance. There are three important SST pattern modes and associated responses. The first one is a remote response to SST in the Pacific. A prominent feature of this response is that during El Niño events the northeast trade winds in the Atlantic basin weaken, particularly during boreal winter (Curtis and Hastenrath, 1995).

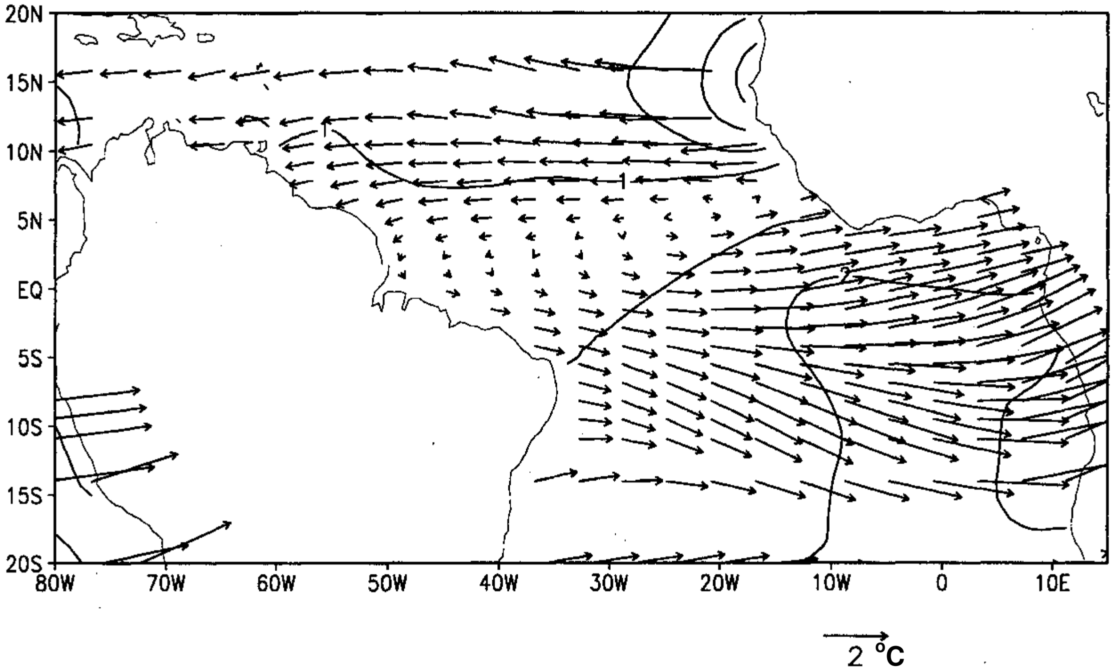

Figure 2.2 – SST annual cycle with amplitude (contours and length of vectors) and phase (direction of vectors). An arrow that is pointing straight up indicates maximum occurs in January. Phase increases clockwise. Contour interval is 1° C. Source: Carton and Zhou (1997).

Enfield and Mayer (1997) analysed a record of SST for the period 1950-1992 and found that the Atlantic is significantly correlated with ENSO in the region 10° – 20°N with a time lag of about 4-5 months. The second pattern is very similar to the ENSO phenomenon. The same physical mechanism that produces the ENSO mode in the Pacific can also produce an ENSO-like mode in the Atlantic. An eastward shift of warm water, a relaxation of the equatorial trade winds in the central basin, and a southward shift of convection accompany the warming of SST in the eastern basin. This picture resembles El Niño. But due to the different basin geometry the phenomenon is expected to be much weaker than in the Pacific (Philander and Pacanowski, 1986a; Carton and Huang, 1994). These equatorial SST fluctuations may be associated with air-sea interactions within the tropical Atlantic region (Zebiak, 1993) or atmospheric disturbances in the tropical Atlantic sector caused by the ENSO (Horel et al., 1986).

The most controversial pattern of variability of the tropical Atlantic is the so-called “Atlantic dipole” (Servain, 1991). The spatial representation of this pattern is a region of maximum SST gradient near the thermal equator, with two zones of maximum anomaly with opposite signs in the northern and southern extra-equatorial regions. This mode has considerable variability on decadal timescales and has its largest fluctuations in the subtropics. Analyses of rainfall data over Northeast Brazil suggest that an interhemispheric dipole in the tropical Atlantic SST anomalies have a major impact on the rainfall in this region (Moura and Shukla, 1981; Nobre and Shukla, 1996).

Nevertheless, Houghton and Tourre (1992) have argued that the Atlantic dipole is actually forced by the mathematical constraints of the spatial orthogonality in the EOF analysis which identifies it. These authors have used EOF modes rotated by the varimax method and simple correlation of area-averaged SST. They claimed that the SST anomalies to the south and north of the ITCZ region are not significantly correlated. On the other hand, Nobre and Shukla (1996) demonstrated that the SST dipole does appear as the first mode in a combined EOF analysis of SST and surface wind stress, which is not only free from the restriction of spatial orthogonality but is also physically consistent with the pattern of the surface wind.

Mehta and Delworth (1995) analysed box averaged SST anomalies in the tropical Atlantic from a 100 years data set and a 100 years simulation with a global general circulation model. They found a type of variability with a time scale of approximately 12 to 20 years, which spatially consists of a dipole. However, by performing a reanalysis of the 100 years of SST observations of the tropical Atlantic, Mehta (1998) found in a later study that there is no cross-equatorial dipole mode at any time scale in this area.

Dommenget and Latif (2000) conducted EOF analyses of annual mean SST from observations for the period 1903-1994 and from four different Global Coupled Models (GCM). They conclude, with coupled model experiments, that the interhemispheric dipole in the tropical Atlantic does not exist and that this pattern results from methodological constraints of the EOF analysis. In the absence of a strong and well-organised signal in the tropical Atlantic, the EOF analysis would give a monopole for the first mode and two anti-symmetric poles in the second mode, and the rotated EOF analysis would yield two separate modes. Those authors, reproducing these expected results from the Complex EOF (CEOF) analyses, argued against the occurrence of a dipole mode in the tropical Atlantic.

However, as mentioned before, there is still a discussion on the existence of a SST dipole mode in the tropical Atlantic. Other authors (Servain et al., 2000; Pezzi and Cavalcanti, 2001) have analysed distinct datasets and found degrees of relationship between the modes of interannual variability in the tropical Atlantic. Recently, to add more debate on this field, Andreoli and Kayano (2004) established that the modes of interannual variability in the tropical Atlantic (dipole-like and el-nino-like) can be seen as evolving modes. The authors suggest that the establishment of the SST anomaly patterns in the region depends crucially on the meridional propagation of those SST anomalies. Therefore, the results above can well illustrate the complexity of the SST variability in the region.

Particular attention has been given to long-term variability of the SST in a way to better understand how the coupled mechanisms interact, so long-term predictions could be made for climate change purposes. However, much of the SST variability in the tropical Atlantic can be linked to local and short timescales processes, varying from diurnal to intraseasonal, which have not been properly characterised, and can affect the long term variability. Another topic that presents interesting questions and needs to be further discussed is the cross-scale interaction between different high-frequency variability processes. An important contribution towards this issue will be presented in Chapter 7, with particular attention given to the interaction between the diurnal signal and variability associated with TIW. Understanding the roles played by these different processes and their interactions in producing the observed SST variability is a major issue in understanding the nature of the climate variations in this region and its potential predictability.

2.4. Currents

Circulation patterns within the tropical Atlantic Ocean play an important role in the interhemispheric transport of mass, heat and salt (Schmitz and Richardson, 1991). The Deep Western Boundary Current (DWBC) transports cold North Atlantic Deep Water toward the Southern hemisphere. The North Brazil Current (NBC) transports warm surface waters northward to close the thermohaline overturning cell. The authors estimate that the magnitude of this cross-equatorial exchange is about the order of 13 Sv.

In addition to those two currents, the presence of zonal countercurrents and other western boundary currents complicate the mean circulation in this region. These currents may also have a role in the regional and global climate. Figure 2.3 shows the horizontal distribution of the major tropical currents for the Tropical Surface Water layer at about 0 – 100 m depth. From north to south, they are the following: the North Equatorial Current (NEC), the North Equatorial Countercurrent (NECC), the South Equatorial Current (SEC) with the northern (nSEC), equatorial (eSEC), central (cSEC) and southern (sSEC) branches, the Guinea Current (GC), the Equatorial Undercurrent (EUC), the North Brazil Current (NBC), the South Equatorial Countercurrent (SECC), the South Equatorial Undercurrent (SEUC) and the Brazil Current (BC).

The seasonal cycle of the surface currents reflects their response to the seasonally varying wind field and the migration of the ITCZ. As the seasonal changes of the wind field lead to variations of the circulation in the tropical Atlantic, we can also see the difference between the fields for both boreal spring and boreal autumn in Figure 2.3. Most prominent is the well-known existence of the eastward flowing NECC during the northern autumn with maximum velocities in August, when the ITCZ is located at the northernmost position. The NECC is weaker or even reverses to a westward flow in the western tropical Atlantic during the boreal spring (Stramma and Schott, 1999).

The seasonal changes of the southeastern North Atlantic subtropical gyre were investigated by Stramma and Siedler (1988). For the NEC the authors described a small northward shift of the NEC in the upper 200 m of about 3° north of the Cape Verde Islands in autumn compared to spring, probably related to the northward shift of the ITCZ.

In the Gulf of Guinea region, the coastal Guinea Current transports low-salinity, warm waters eastward from its western Atlantic origin, as an extension of the NECC (Hisard and Merle, 1980). The other important surface flow in the Gulf of Guinea is the SEC, which is separated from the Guinea Current by the northern tropical convergence along the 3°N parallel. At the equator, the thickness of the SEC sharply decreases due to the presence of the EUC.

Molinari (1982) described the SEC as divided into three bands in the South Atlantic, separated by the SEUC and the SECC, respectively. The flow north of the SEUC was called northern SEC (nSEC), the flow between the SEUC and SECC was called central SEC (cSEC) and the flow south of the SECC was called southern SEC (sSEC). As the nSEC is further separated by the EUC, we will refer to the flow situated between the EUC and the SEUC as the equatorial SEC (eSEC) and only the flow north of the equator as the nSEC. Stramma (1991) described the sSEC as a broad and sluggish flow between 10°S and 25°S east of 30°W. Only the southern part of the sSEC turns south into the Brazil Current when reaching the Brazilian shelf between 10°S and 20°S, and direct observations (Evans and Signorini, 1985) show the existence of the well established Brazil Current south of 20°S.

The vertical structure of circulation of the NBC is a well-studied and well-understood phenomenon and clearly summarized by Bourles et al. (1999). The NBC and its subsurface component, the NBUC advect southern hemispheric waters across the equator and feed subsurface eastward currents at different latitudes and different depths. These zonal currents include the North Equatorial Countercurrent, located in the near-surface layer, the Equatorial Undercurrent, centered at the thermocline, and the North Equatorial Undercurrent (NEUC), located below the thermocline, and shown in Figure 2.4, together with the main currents for the Central Water layer at about 100-500 m depth.

In the equatorial Atlantic west of 44°W, a large fraction of the NBC retroflects and feeds the EUC. The EUC crosses the entire Atlantic although reducing its strength. Part of the EUC upwells in the equatorial region. In the eastern tropical Atlantic one might expect a seasonal variation of the EUC, because the easterly component of the wind stress (responsible for setting up the eastward zonal pressure gradient force believed to drive the EUC) undergoes a distinct seasonal cycle with a maximum between May and November. However, equatorial current meter moorings at 28°W and 4°W do not indicate significant changes in the EUC transport, but rather a seasonal variation in the depth of the maximum eastward flow (Wacongne and Piton, 1992).

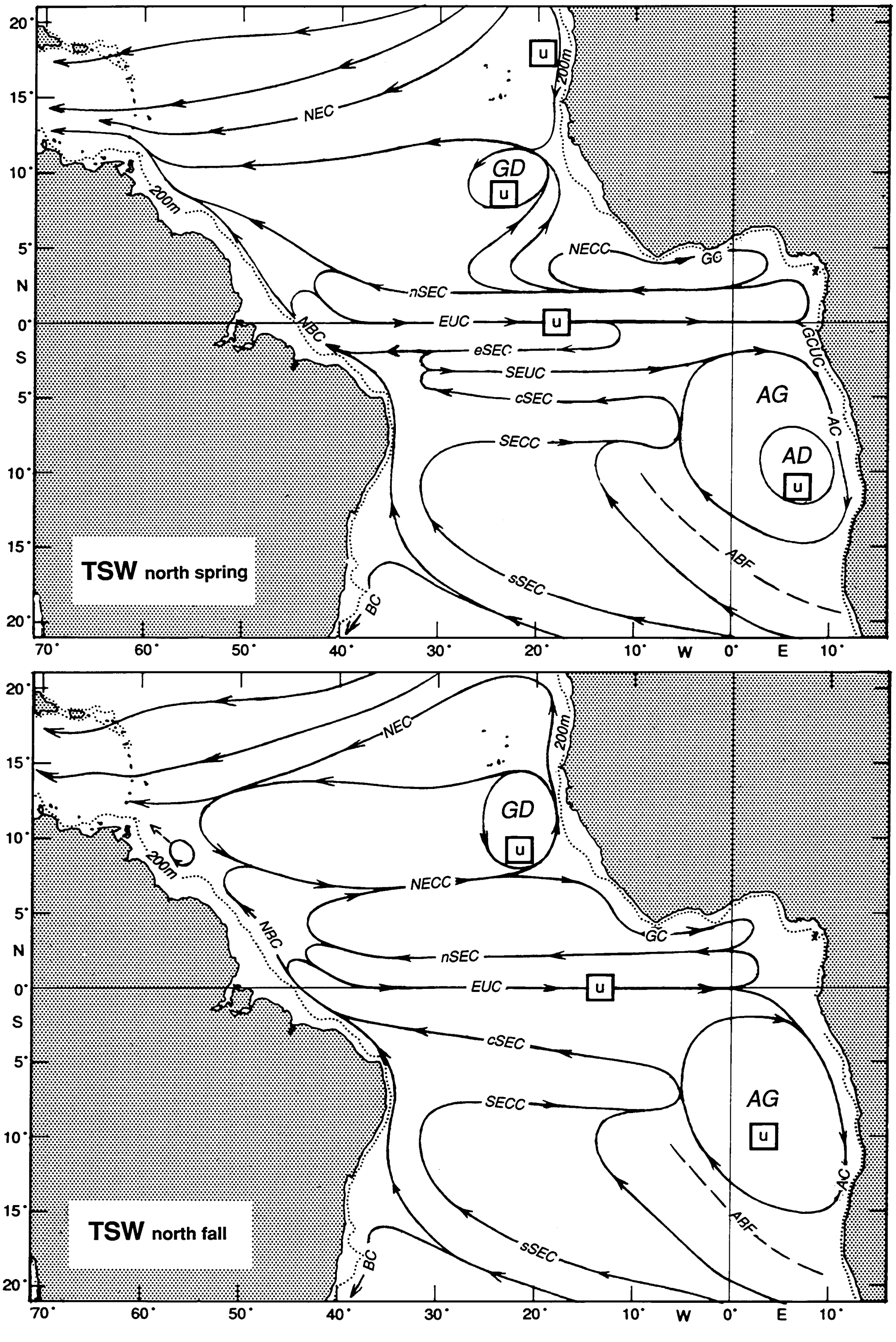

Figure 2.3 – Schematic diagram of the tropical surface water layer (TSW) in the Atlantic Ocean during boreal spring (upper panel) and boreal autumn (lower panel). Adapted from Stramma and Schott (1999).

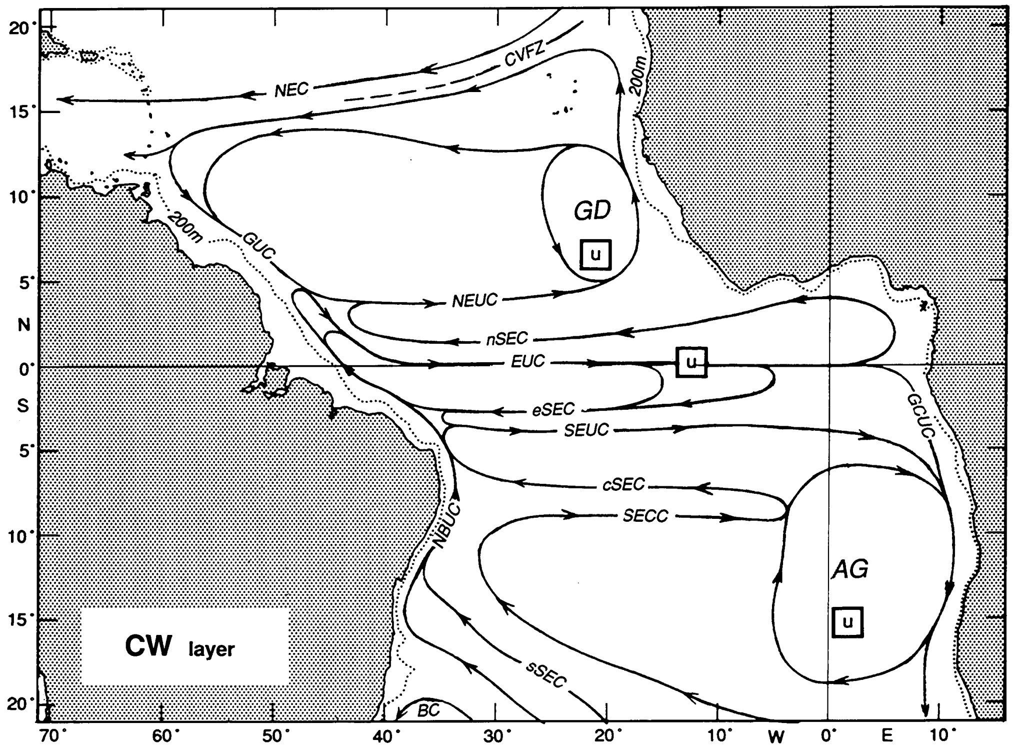

Figure 2.4 – Schematic diagram of the mean Central Water layer (CW) in the Atlantic Ocean. Adapted from Stramma and Schott (1999).

In boreal spring part of the NBC retroflects into the EUC, while part of the NBC continues its northwestward flow. This results in water from the tropical Atlantic reaching the northwestern part of the South American continent. The northwestward flow along the South American coast is known as the Guiana Current. Schott et al. (1998) reported a northwestward alongshore transport of about 10 Sv of waters from the southern hemisphere along the Guiana boundary. During boreal autumn, part of the NBC flows along the South American coast and feeds the NECC through a retroflection, which merges with water from the NEC. Wilson et al. (1994) estimated that the two-thirds of the NECC transport (16 Sv) is composed of NBC waters retroflected from the coast between 6°N and 8°N and one third (8 Sv) is supplied by the NEC. Tsuchiya et al. (1992) observed high salinities in the NECC at 25°W, which do not exist in the North Atlantic north of the NECC. They concluded that a significant amount of South Atlantic water is carried in the NECC. At the retroflection region of the NBC into the NECC at about 10°N, anticyclonic eddies detach from the NBC and move towards the Caribbean (Goni and Johns, 2001; Garraffo et al., 2003).

Although the rings in the NBC are well documented, Foltz et al. (2004) suggest that negative potential vorticity associated with tropical instability waves originated in the eastern tropical Atlantic may give rise to some of the instability and ring formation observed in the North Brazil Current system. This shows the complexity of the current systems in the tropical Atlantic, and indicates possible interactions related to processes between both sides of the Atlantic.

2.5. Air-sea fluxes

As mentioned before, the impact of the tropical Atlantic SST anomalies over the countries surrounding the basin is well-known (Moura and Shukla, 1981; Nobre and Shukla, 1996; Mehta, 1998). The finding that the regional climate variability and the tropical Atlantic SST are significantly correlated implies that the latter exert a considerable influence on the atmospheric circulation. However, one of the central issues concerning tropical Atlantic climate variability is to discover how much of the variability can be attributed to the air-sea feedback processes that are local to the tropical Atlantic and how much can be explained in terms of remote forcing. The El-Niño-Southern Oscillation (ENSO) in the tropical Pacific (Saravanan and Chang, 2000) and the North Atlantic Oscillation (NAO) in the high latitude Atlantic may both influence the tropical Atlantic variability, although how much direct influence the tropical Atlantic SST exert back on the atmosphere is not entirely clear.

Air-sea feedbacks have been hypothesized to be an important contributing factor to tropical Atlantic variability. A positive feedback means that the atmosphere and ocean are mutually reinforcing each other and thereby the two media are coupled. A negative feedback usually indicates that the atmosphere is merely forcing the oceans.

Two different types of positive air-sea feedbacks have been proposed to have potential impacts on tropical Atlantic climate variability. One of these feedbacks involves interactions between near equatorial meridional SST gradient, cross-equatorial atmospheric circulation and wind-induced latent heat flux anomalies (Hastenrath, 1984; Carton et al., 1996). At the heart of this mechanism lies a thermodynamic ocean-atmosphere interaction, which can be described as follows: in response to an anomalous, positive, meridional SST gradient across the equator, a northward wind-anomaly will develop near the equator due to an increase in the local sea level pressure gradient. Because of the Coriolis effect, the equatorial southerlies will evolve into southwesterly wind anomalies in the northern subtropics. These anomalous winds act to reduce the northeasterly mean trade winds in the north. As a result, the surface heat flux into the ocean is increased in the Northern Hemisphere due to a reduction of evaporation caused by a decrease in total wind speed. The anomalous heat flux thus tends to reinforce the initial north-south SST difference, which will in turn strengthen the cross-equatorial wind anomalies.

Chang et al. (1997) formulated the feedback mechanism explicitly in an attempt to explain the decadal variability of interhemispheric SST gradient in the tropical Atlantic. Dynamically, this feedback mechanism is consistent with the relationship between the rainfall variability and surface circulation revealed by the empirical analyses (Hastenrath and Heller, 1977; Moura and Shukla, 1981; Hastenrath, 1984; Nobre and Shukla, 1996; Wainer and Soares, 1997). However, at the present, the importance of this positive feedback process in the tropical Atlantic climate variability remains controversial.

The other feedback mechanism involves dynamic interactions between wind and SST anomalies along the equatorial wave guide, operating in a similar fashion to that of Pacific ENSO as originally proposed by Bjerknes (1969). In response to a warm (cold) SST anomaly in the eastern equatorial Atlantic, a westerly (easterly) wind anomaly forms in the western equatorial basin. This wind anomaly reduces (increases) upwelling along the equator and deepens (shoals) the thermocline depth in the east, and thus warms (cools) surface temperature of the oceans, causing initial perturbations to grow. Zebiak (1993) suggests that this feedback plays a role in determining the structure of the interannual variability of near-equatorial SST in the Atlantic basin.

Carton et al. (1996) demonstrated that wind-induced latent heat flux is a major contributing factor to the variability of the SST dipole, whereas wind forcing is the main source of the interannual SST variability associated with the “Atlantic El-Niño”. Chang et al. (1997), using a joint singular value decomposition (SVD) analysis based on 30-year COADS observations from 1960 to 1990 in a tropical Atlantic domain, revealed that the most dominant mode has a pattern characterized by opposite polarity of SST on the two sides of the equator. The surface heat flux pattern is consistent with the surface atmospheric circulation, having positive (negative) flux anomaly in the region where trades are weakened (strengthened). This circulation pattern agrees very well with the positive feedback mechanism for the interhemispheric SST anomaly. The principal component of the first SVD has a dominant spectral peak at 12-13 years. Interestingly, the surface heat flux anomaly near the equator coincides in location with the SST anomaly, but tends to be out of phase, implying a negative feedback. Zhou and Carton (1998) recently examined the effect of surface heat flux on ocean-atmosphere interaction on interannual time scale and found that surface heat flux anomalies mainly act to damp equatorial SST perturbations.

Chang et al. (2000), using an atmospheric general circulation model (AGCM) forced with differently configured SSTs, showed that the dominant atmospheric response to SST forcing is largely confined within the tropical Atlantic sector and may be associated with the variation in location and intensity of the ITCZ in response to changes in SST gradient near the equator. In the western tropical Atlantic warm pool region, there is an indication of a positive feedback between surface heat flux and SST anomalies. In this warm SST region, the latent heat flux tends to dominate surface heat flux variability, and the positive feedback takes place between the wind-induced flux and SST. A strong negative feedback is found off the coast of west Saharan Africa, where the mean SST is cold and the surface heat flux variability is largely induced by the air-sea temperature difference. In regions like that, surface heat flux generally tends to dampen the SST, which would indicate the negative feedback.

More recently, Foltz et al. (2003) analysed model outputs in conjunction to the PIRATA dataset, with the aim to calculate the seasonal heat budget in the tropical Atlantic and possible influence on the seasonal variability of the SST. They found that along the equator (10^{o}W – 35^{o}W), seasonal contributions from latent heat loss are diminished, while horizontal temperature advection and vertical entrainment contribute significantly. Zonal temperature advection is especially important during boreal summer near the western edge of the cold tongue, while horizontal eddy temperature advection, which most likely results from tropical instability waves, opposes temperature advection by the mean flow. However, what is the contribution, if any, of the TIW variability to the diurnal signal of the fluxes? And on these timescales, how do the SST fields interact with the heat fluxes? Is SST forcing heat flux changes rather than being modulated by the fluxes? These questions are interesting for the understanding of high-frequency variability in the tropical Atlantic, and will be further discussed in Chapter 7.

2.6 Current knowledge of TIW

The phenomenon of TIW has generally been attributed to intense latitudinal shears between the various components of the equatorial current system that cause the currents to become unstable (Philander, 1978; Cox, 1980). Observations confirm that these TIW act to reduce the shears of mean oceanic currents (Hansen and Paul, 1984; Weisberg, 1984). The instabilities cause large perturbations of the SST front between the colder upwelling water of the Pacific equatorial cold tongue and the warmer water to the north (Miller et al., 1985; Flament et al., 1996; Kennan and Flament, 2000). Qiao and Weisberg (1995) estimated that TIW in the equatorial Pacific propagate westwards with periods of 20 – 40 days, wavelengths of 1000 – 2000 km and a phase speed of ~0.5 ms^{-1}.

Although of oceanic origin, TIW variability can project onto the atmosphere, affecting the formation of cloud (Deser et al., 1993; Hashizume et al., 2001), changing the heat flux (Thum et al., 2002), and causing wind variations (Hayes et al., 1989; Chelton et al., 2000; Liu et al., 2000; Wentz and Schabel, 2000; Hashizume et al., 2002) with similar 20 – 30-day periodicities.

TIW-induced oceanic eddy heat flux towards the equator has been shown to be comparable to the Ekman heat flux away from the equator and the large-scale net air-sea heat flux over the tropical Pacific (Hansen and Paul, 1984; Swenson and Hansen, 1999; Wang and McPhaden, 1999). TIW are thus an important component of the large-scale heat balance of the equatorial cold tongue. These modifications of heat flux induce perturbations of the surface wind stress field that are controlled by perturbations of the underlying SST field.

Hayes et al. (1989) investigated the relationship between TIW-induced perturbations of SST and surface wind. They found a strong correlation between the meridional gradient of SST and the meridional gradient of the northward wind component. The importance of SST-induced modifications of atmospheric stability has been further investigated from satellite observations of the geographical distribution of low-level cloudiness in relation to the SST signatures of TIW (Deser et al., 1993). That study proposed that as the southeasterly trades blow across the meandering equatorial front, thermal convection may occur over the warm sector and help form clouds.

There are two main hypotheses concerning the relation between SST and surface winds over the tropical oceans. In the first hypothesis, SST couples with sea level pressure and changes the wind (Lindzen and Nigam, 1987). Lower and higher pressures are found over warmer and cooler water, respectively. As zonal winds move down the pressure or up the temperature gradient, the zonal winds always remain 90°

out of phase with SST and in phase with the zonal gradient of SST. The meridional component is accelerated northward at both the crest (north) and trough (south) of the waves. At the crest, the ocean is cold and meridional wind is 180° out of phase with SST. At the trough, the ocean is warm and meridional wind is in phase with SST. The strongest wind should be found at the highest pressure or SST gradient.

In the second hypothesis (Wallace et al., 1989), SST is coupled with wind through the stability (density stratification) change in the atmospheric boundary layer. Over warm water, air is more buoyant, mixing increases, and wind shear is reduced in the boundary layer. Surface winds increase as consequence. The opposite is true over cold water.

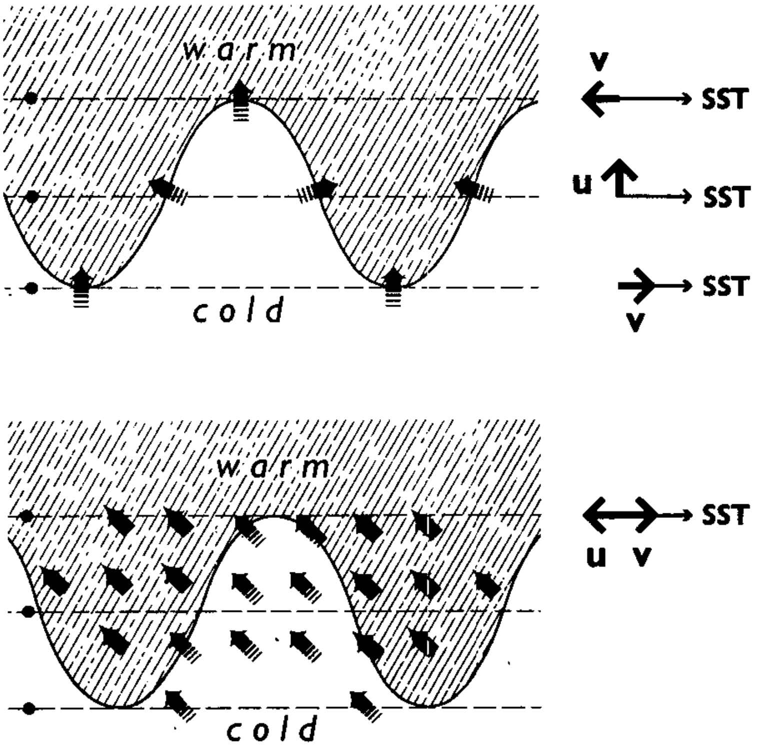

Figure 2.5 – Schematic representation of perturbation of the surface wind field (U = zonal wind, V = meridional wind) associated with a TIW, following the hypothesis suggested by Lindzen and Nigam (1987) (top panel) and Wallace et al. (1989) (bottom panel). Arrows in the figure represent wind. Figure modified from Hayes et al. (1989)

The two hypotheses that could explain the perturbation of the surface wind speed by a westward propagating SST field associated with TIW are summarised in Figure 2.5. The top panel assumes principal forcing is through the hydrostatic influence on the atmospheric sea-level pressure (SLP) as discussed in Lindzen and Nigam (1987). Warm SST is associated with low SLP, cool water with high SLP. Near the equator surface winds tend to flow down the SLP gradient. As summarised by the diagram on the right, zonal wind (U) perturbations are 90° out of phase with the SST while meridional wind (V) changes tend to be either in phase or 180° out of phase depending upon the latitude. Bottom panel assumes that the principal coupling of SST and wind is through modification of the boundary layer shear as discussed in Wallace et al. (1989). In this case surface winds are stronger over warm SST. For the southeasterly winds shown, zonal winds are 180° out of phase with SST perturbations and meridional winds are in phase with them.

These two hypotheses have not been investigated in the tropical Atlantic during events of TIW activity. In this work, this will be investigated by using the TMI dataset, which provides simultaneous measurements of SST, integrated water vapour (VAP), rain and cloud liquid water (CLD), in conjunction with zonal (U) and meridional (V) wind from QuickSCAT. The results will be shown and discussed further in Section 6.3.

2.6.1 TIW in the tropical Atlantic

Most of the works cited above were performed using data from the tropical Pacific. In the tropical Atlantic, due to the lack of in situ data, there are only a few studies. Duing et al. (1975) were the first to notice TIW in the tropical Atlantic during the GATE programme. Weisberg (1984) found that the seasonal appearance of the waves coincided with that of the off-diagonal horizontal Reynolds stress. Weisberg and Weingartner (1988), using current meter data from surface moorings deployed during the SEQUAL/FOCAL programs, described the TIW properties in the tropical Atlantic. They found a packet of waves with central periodicity of 25 days, zonal wavelength around 1100 km and phase speed of 0.5 ms^{-1}.

Weisberg and Weingartner (1988) also found that, thermodynamically, the waves effect a southward heat transport during the period when the North Equatorial Countercurrent (NECC) is most rapidly gaining heat, suggesting that the waves act to regulate the heat stored in the NECC. Also, the Reynolds' heat flux convergence upon the equator appears to halt the upwelling induced cooling and to increase SST. Dynamically, the waves decelerate the South Equatorial Current (SEC) north of the equator and reduce its shear. This occurs simultaneously with deceleration of the SEC by the basinwide adjustment of the zonal pressure gradient (ZPG). The seasonal modulation of the waves is therefore a consequence of both the ZPG response to seasonally varying wind stress as well as the instability itself since both are stabilizing.

Hashizume et al. (2001) used satellite data to describe the variability of several parameters associated with the TIW in the tropical Pacific and tropical Atlantic basins. They found that, in the Atlantic, the TIW signals are strongly trapped near the equator, with a wavelength of about 9^o in longitude, slightly shorter than the Pacific ones. Also, in the Atlantic, the TIW have a rapid development/decay, unlike the Pacific counterpart which has much more gradual development. This is presumably because the Atlantic is more strongly influenced by its neighbouring continents. Nevertheless, the authors used only a very short time series of the TMI and QuikSCAT dataset, which prevented any interannual comparison.

Recently Menkes et al. (2002) showed the effects of tropical vortices in the Atlantic Ocean, which are associated with TIW, and their influence on phytoplankton, zooplankton and small pelagic fish communities. Cold, nutrient and biologically rich equatorial waters are advected northward and downward to form sharp fronts visible in all tracers and trophic levels. The equatorward recirculation experiences upwelling at depth, with the pycnocline and ecosystem progressively moving toward the surface to reconnect with the equatorial water mass. The observations thus indicate that it is a fully three-dimensional circulation that dominates the distribution of physical and biological tracers in the presence of tropical instabilities and maintains the cusp-like shapes of temperature and chlorophyll observed from space.

The study of the TIW in the Atlantic is the main focus of this thesis. In addition to the characterisation of the spectral characteristics of the baroclinic component of the TIW, Chapter 6 will address the impact of the coupling patterns of these oceanic instabilities with atmospheric fields in the Atlantic.

2.7 Summary

This chapter presented the background knowledge of the long-term variability in the tropical Atlantic for SST, wind, current systems and air-sea fluxes, as well as the current understanding about TIW. It has shown that most of the studies in the region were based, until recently, in models or in regional datasets, since there was no similar dataset as the one provided by the PIRATA array. Also, possibly due to the lack of in situ data, most of the studies were concentrated on seasonal or longer timescales.

Although it is necessary to acknowledge the importance of understanding these long-term processes and their interactions, the existence of possible links with intraseasonal variabilities has also been suggested, for instance those associated with tropical instability waves. Some of the studies indicate the significant contribution that these processes can have on the seasonal cycle, which in turn might modulate variabilities of longer timescales.

As will be shown in the next chapters, it is intended to characterise the high frequency variability in the tropical Atlantic, as well as the variability associated with tropical instability waves, with the aim to make an important contribution in understanding climate variations in this region. For this, it is planned to make use of the interaction of high-resolution in situ datasets and high quality satellite data, which after careful validation, can complement each other. With the use of the analytical methods presented and described in the next chapter, it will be possible to characterise the temporal and spatial variability associated with the processes mentioned above.

Chapter 3

Dataset and methods of analysis

3.1. Introduction

This study aims to investigate the diurnal cycle of some of the met-ocean variables in the tropical Atlantic, as well as the variability associated with TIW, as mentioned in Chapter 1. Moreover, it plans to show the relationship between these two processes that have different timescales, which has not been fully investigated yet. To achieve the temporal resolution requirements to characterise the diurnal cycle, and the necessary spatial coverage to assess the variability of TIW, complementary datasets available from moored buoys and retrieved from satellite will be used. This work is based on observational data covering January 1998 to December 2001, and this chapter will make a complete description of these datasets.

The PIRATA array dataset will be mainly used for: i) the validation process of the satellite data, as further discussed in Chapter 4, ii) the characterisation of the diurnal cycle in the tropical Atlantic, which will be further analysed in chapter 5, and iii) the analysis of the relationship between the diurnal signal and TIW variability. The satellite dataset is derived from two missions: the Tropical Rainfall Measuring Mission (TRMM), which carries the TMI sensor, and the QuikSCAT mission, which carries the scatterometer sensor Seawinds. These data will be used mainly in the characterisation of the properties of TIW, and to assess the co-variability of air-sea fields, as discussed in Chapter 6.

However, to investigate the air-sea interaction in the tropical Atlantic, heat fluxes need to be parameterised using the basic measured variables. Therefore, a description of the bulk flux algorithms used in the parameterisations of the heat fluxes will also be made in this chapter. In addition, this thesis will explore processes that are multiscale and nonstationary. The choice of the analytical methods has to be based on the ability of the methods in highlighting those characteristics. This chapter will describe the two methods that will be used in the analysis of the data: i) the Radon Transform has been revealed to be a perfect tool for showing the spectral characteristics of propagating features, such as TIW, and ii) Wavelet analysis, although not new, is the modern approach for studying nonstationary spatial or time-dependent signal characteristics.

3.2. Dataset

3.2.1. In situ data

The moorings used in the PIRATA array are primarily Next Generation ATLAS (Autonomous Temperature Line Acquisition System) moorings (Figure 3.1) like those used in the equatorial Pacific as part of the TAO Array (McPhaden et al., 1998). All the data are relayed to shore in near-real time via Service Argos utilizing the NOAA polar-orbiting satellites. The design lifetime of the moorings is 1 year. The variables measured are (height/depth of sensors in brackets): surface winds (4m), SST (1m), sea surface conductivity (1m), air temperature (3m), relative humidity (3m), incoming shortwave radiation (3.5m), rainfall (3.5m), subsurface temperature (20, 40, 60, 80, 100, 120, 140, 180, 300 and 500m), subsurface conductivity (20, 40 and 120m), and subsurface pressure (300 and 500m).

Table 3.1 shows the types of sensors used on PIRATA moorings and lists their accuracies. Most instrumental accuracies listed are based on pre-deployment and post-recovery calibrations. The array consists of 13 ATLAS moorings spanning 15°N – 10°S, 38°W – 0° (Figure 3.2). Of these 13 buoys initially proposed to be deployed, only 11 are still acquiring and transmitting the data. The dataset used in this thesis spans from January 1998 to December 2001 but the buoys have variable record length. The availability of the data used is shown in Figure 3.3.

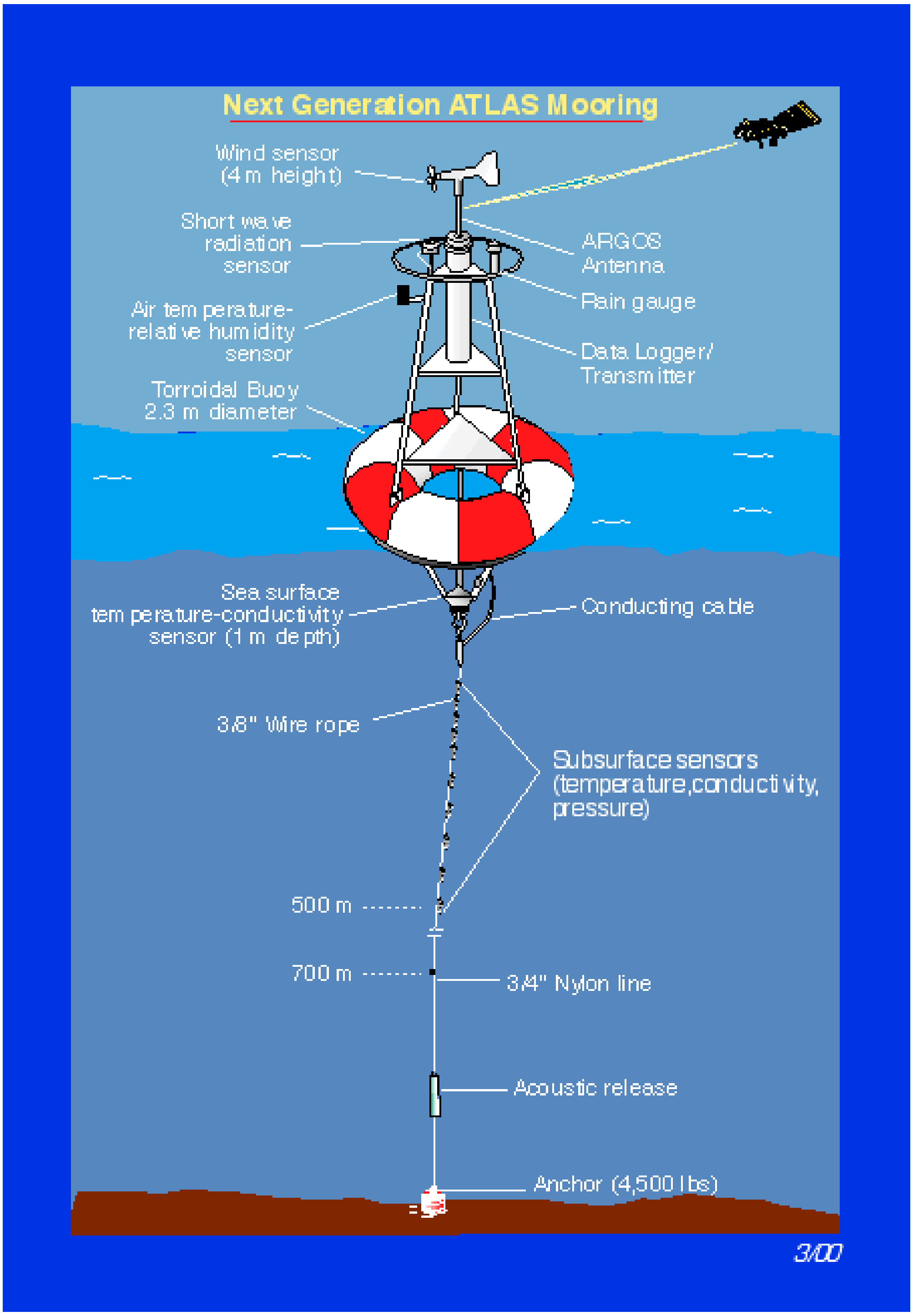

Figure 3.1 – The Next Generation ATLAS mooring
(Source: TAO Project website)

Table 3.1 – Details of sensors at the Next Generation ATLAS moorings
Source: TAO Project website

Measurement	Sensor type	Resolution	Range	Accuracy
Wind speed	Propeller	0.2 ms^{-1}	1 –20 ms^{-1}	±0.3 ms^{-1} or 3%
Air temperature	Pt-100 RTD	0.04°C Std	14 – 32 °C	±0.2°C
Relative humidity	Capacitance	0.4% RH (real time) 0.02% RH (delay mode)	55 – 95% RH	±2.7%
Rainfall	Capacitance	0.2 mm hr^{-1}	0 – 50 mm	±0.4 mm hr^{-1} (10 min. filtered data)
Downwelling shortwave radiation	Pyranometer	0.4 Wm^{-1}	200 – 1000 Wm^{-2}	±1%
Sea surface and subsurface temperature	Thermistor	0.001°C	1 – 31 °C	±0.003°C
Salinity	Internal field conductivity cell	0.0001 Sm^{-1}	3 – 6 Sm^{-1}	±0.02 psu

Once a year, the buoys are recovered and replaced with new instrument sensors. The instruments that have been recovered are then delivered to the PMEL (Pacific Marine Environmental Laboratory) in Seattle, USA, for post-calibration and retrieval of the high-frequency data, which are stored in the instruments' data loggers. These data are recorded at intervals of 10 minutes and will be used in this work with two objectives: (i) to describe the diurnal cycle over the Equator and in the two regions of high variability associated with the SST dipole mode; and, (ii) to show skin-bulk SST differences and their relation with local wind.

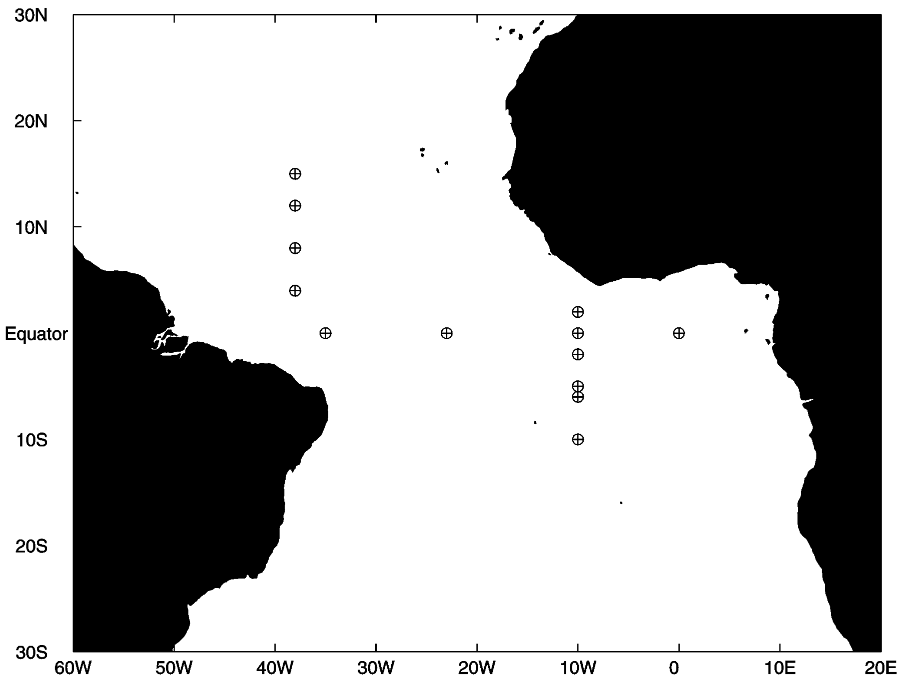

Figure 3.2 – Position of the buoys in the PIRATA array.

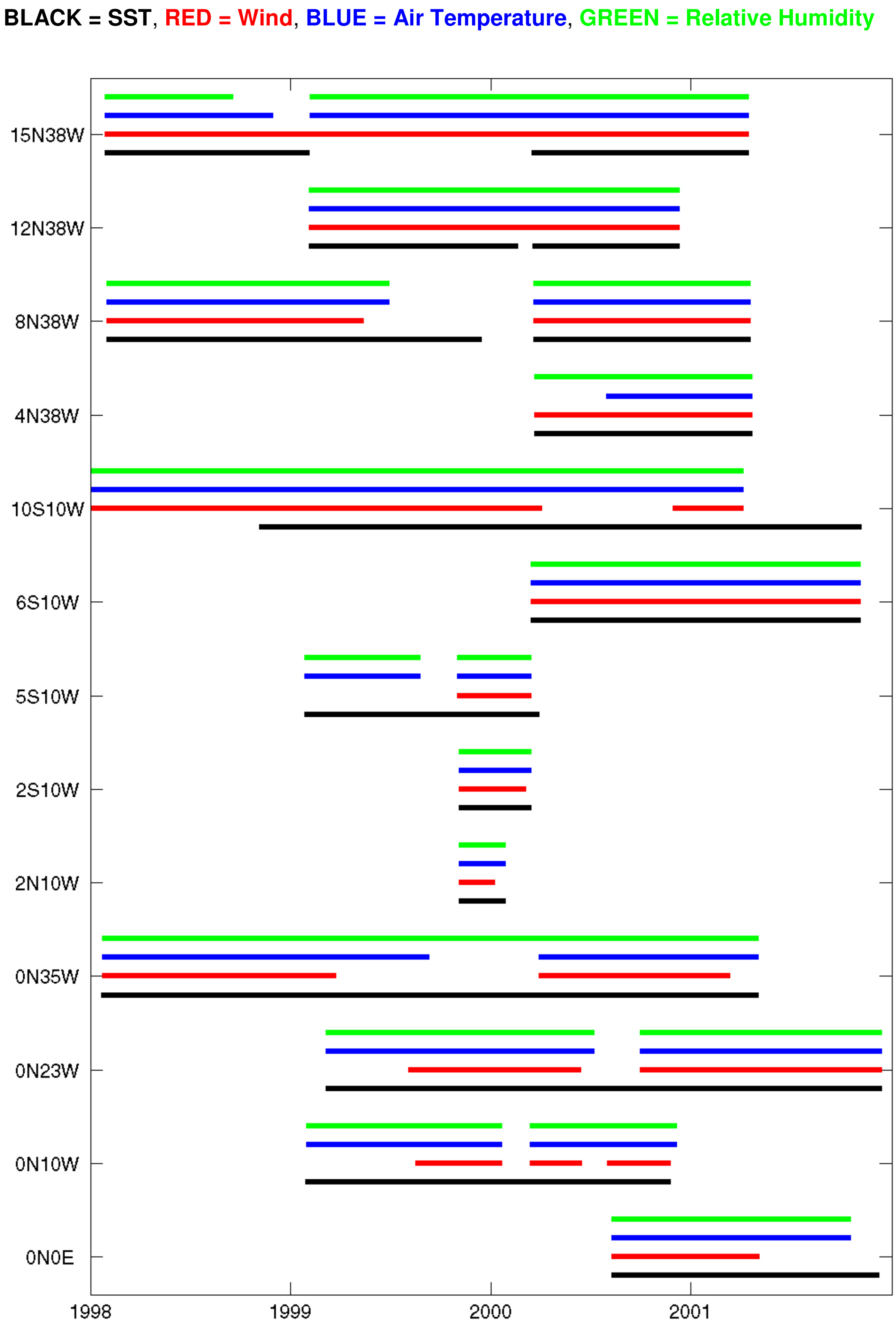

Figure 3.3 – Availability of the PIRATA dataset

3.2.2. Satellite data

3.2.2.1. Tropical Rainfall Measuring Mission (TRMM)

The Tropical Rainfall Measuring Mission is a joint mission between USA and Japan, and it is the first satellite earth observation mission to have as the main goal the monitoring of tropical rainfall. TRMM was launched by the H-II rocket from NASDA/Tanegashima Space Center in November 1997, and has gone into a circular non-sun-synchronous orbit of altitude 350 km, inclination angle 35^o and period 90 min, which gives a latitudinal coverage from 38^oS to 38^oN. After launch, rainfall observation from TRMM began, and the designed routine operation period of 3 years expired at the end of January 2001. Currently, TRMM is continuing observation for enhanced scientific studies, and its mission life is expected to extend for about 3 further years.

The satellite instrumentation package consists of the precipitation radar (PR), the TRMM Microwave Imager (TMI), the visible-infrared scanner (VIRS), the lightning imaging sensor, and the Clouds and the Earth's Radiant Energy System. Because of the characteristics of the orbit, the equatorial crossing time gradually varies, providing information on the diurnal variation of geophysical parameters, such as SST, surface wind speeds, atmospheric water vapour, liquid cloud water, and precipitation rates.

3.2.2.1.1 TRMM Microwave Imager (TMI)

The TMI is a multi-channel dual-polarized passive microwave radiometer. TMI utilizes nine channels with operating frequencies of 10.65 GHz, 19.35 GHz, 21.3 GHz, 37 GHz, and 85.5 GHz. (Kummerow et al., 1998; Nirala and Cracknell, 2002) give a complete description of the system. The instrument provides data related to the rainfall rates over the oceans, but less reliable data over land, where non-homogeneous surface emissions make interpretation difficult.

The measurement of sea-surface temperature through clouds by satellite microwave radiometers has been an elusive goal for many years. The early radiometers in the 1980's (e.g., Scanning Multichannel Microwave Radiometer – SMMR) were poorly calibrated, and the later radiometers (i.e., Special Sensor Microwave/Imager – SSM/I) lacked the low frequency channels needed by the retrieval algorithm. The TMI provides an unprecedented view of SST. Its lowest frequency channel (10.65 GHz) penetrates non-rain clouds with little attenuation, giving a clear view of the sea surface under all weather conditions except rain. This is a distinct advantage over the traditional infrared SST observations that require a cloud-free field of view. Ocean areas with persistent cloud coverage can now be viewed on a daily basis. Furthermore, at this frequency, microwave retrievals are not affected by aerosols and are insensitive to atmospheric water vapour, making it possible to produce a very reliable SST time series for climate studies. However, the disadvantages of using microwave sensors to retrieve SST are the poor spatial resolution (50 km compared to 1.1 km of infrared), and sensitivity to sea-surface roughness, unlike infrared retrievals. A primary function of the TRMM SST retrieval algorithm is the removal of surface roughness effects. The early results for the TMI SST retrievals were quite impressive and led to improved analyses in a number of important scientific areas, including tropical instability waves (Chelton et al., 2000).

The main reason for choosing the TMI dataset for this study is because of the enormous advantage of microwave retrievals over thermal radiometers, such as the Advanced Very High Resolution Radiometer (AVHRR) and the Along Track Scanning Radiometer (ATSR), regarding the chronic problem of high cloud coverage in the tropics. This advantage, associated with the satellite characteristic non-sunsynchronous orbit, gives a complete coverage in 3 days, with gaps only remaining in areas of strong and persistent rain. However, microwave and infrared SST retrievals are very complementary and can be combined to obtain a reliable global data set. Besides, TMI can also retrieve other geophysical variables that are important for the analysis of ocean-atmosphere interaction.

While not specifically designed as a wind speed retrieval instrument, TMI has made it possible to examine the benefits of the 11 GHz band to radiometric wind estimates. The TMI uses the same collection of brightness temperature channels as SSM/I with the addition of vertically and horizontally polarized channels at 10.65 GHz. As mentioned above, these channels provide a more transparent window to the ocean surface, while still maintaining sensitivity to the wind-modulated ocean surface brightness temperatures. However depending on the meteorological conditions, although the 11 GHz channels are less sensitive to the atmosphere, the 37 GHz can give better wind retrieval results as it will be more sensitive to wind speed at lower wind speeds, especially if compared with buoy measurement data.

The TMI 11GHz surface wind speed and sea surface temperature data have small regions of missing data that occur. These regions are located where the sunlight reflects off the ocean surface (also called “sun glint”) and affects the 11 GHz channel. Where this occurs, the data are removed through the processing scheme implemented by Remote Sensing Systems (http://www.ssmi.com). The whole TMI dataset used in this work is the product version 3 and distributed by Remote Sensing Systems.

TMI SST and wind speed products will be validated against the in situ measurements, and the results of the validation process are presented in the next chapter. TMI SST, in addition to other TMI products (atmospheric water vapour, liquid cloud water and precipitation rates) will be used in the characterisation and analyses of TIW variability in the tropical Atlantic, as presented in Chapter 6. TMI wind speed will be applied to fill the gaps in the in situ wind speed time series. However, it is not used in the study of TIW variability, as this requires vector wind data, as supplied by scatterometers such as the SeaWinds sensor on the QuikSCAT mission, described below.

3.2.2.2. QuikSCAT mission

The QuikSCAT (Qscat) satellite was launched in June 1999 by the U.S. Air Force Titan II launch vehicle from Space Launch Complex 4 West at California's Vandenberg Air Force Base. It is in a Sun-synchronous orbit at 803 km and with a 98.6° inclination. The scientific objectives of the mission are to acquire all-weather, high-resolution measurements of near-surface winds over global oceans, determine atmospheric forcing, ocean response, and air-sea interaction mechanisms on various spatial and temporal scales, and study daily/seasonal sea ice edge movement and Arctic/Antarctic ice pack changes. The mission development was a rapid response to the unfortunate loss of the Advanced Earth Observing Satellite-I (ADEOS-I) spacecraft in June 1997. ADEOS-1 carried the NASA scatterometer (NSCAT) and several other instruments.

The primary sensor on board of the Qscat is the microwave scatterometer SeaWinds, which operates at Ku-band (13.4 GHz). The single swath of the SeaWinds radar has a width of 1800 km, providing approximately 90% coverage of Earth's oceans every day, with wind vector estimates averaged over each 25 x 25 km^2 area within it. Surface wind speed measurements are made for a range of 3 to 20 m/s, with an accuracy of 2 m/s, and direction measurements have an accuracy of 20°. The instrument uses a rotating dish antenna with two spot beams that sweep in a circular pattern, and receive horizontal polarization at 46.25° and vertical polarization at 54°.

Rain can have a substantial influence on SeaWinds observations. Rain influences radar returns through three processes: backscatter from the rain, attenuation of the signal passing through the rain (Moore et al., 1979; Weissman et al., 2002), and changes in sea surface roughness (Craeye et al., 1997) by raindrop impacts (Sobieski and Bliven, 1995; Sobieski et al., 1999). The influence of these considerations on the accuracy of winds is a function of scatterometer design. Rain has a greater influence at large incidence angles (the beam interacts with more rain) as demonstrated by Craeye (1998). As an example, Craeye (1998) shows that when the wind speed is 6 ms^{-1}, a rain rate of 5.5 mm h^{-1} will cause the vertical polarization radar cross section to increase by 2dB at an incidence angle of 35°. However if the incidence angle is 50°, the radar cross section will increase by 7dB for this rain rate. This work highlights that the problem of rain-induced errors is a more serious issue for SeaWinds than it was for NSCAT, which collected signals from a range of incidence angles, from 18° to 59°.

The SeaWinds data used in this work is the product Version 2 made available by Remote Sensing Systems. For a question of consistency with most of the literature, the SeaWinds dataset will be referred in this work as Qscat data The geophysical model function (GMF) used for this dataset is called Ku-2000 and was developed as an improvement over the NSCAT-2 model function. The model function improvements can be characterized in two ways. First, at low winds (below 7 m/s) the model is a more accurate representation of the directional modulation of the backscatter power. Second, at high wind speeds (> 20 m/s) the relationship of backscatter versus wind speed has been modified to better agree with observations in tropical storms and hurricanes. The Ku-2000 model is capable of retrieving winds from 0 to 70 m/s.

Qscat data processing uses contemporaneous microwave radiometer measurements for rain flagging (F13 SSMI, F14 SSMI, F15 SSMI, and TMI) and sea ice detection (all the above except TMI). The Qscat dataset contains four rain flags, well designed for combination into a single rain flag. For the best quality data from Qscat, all cells for which the scatterometer rain flag is set have been removed to avoid rain contamination to the data.

3.3. Parameterisation of turbulent fluxes

Parameterisation formulae are used for determining the turbulent fluxes from the basic variables such as wind speed and air temperature. Thus these formulae are fundamental to heat flux estimation and therefore will be discussed in this section. Latent heat flux (Q_{lat}), sensible heat flux (Q_{sen}) and wind stress (τ) will be parameterised in this work by the algorithm developed by Zeng et al. (1998), hereafter denoted as ZZD and described in Section 3.3.3, and use the basic variables measured by the PIRATA moored buoys. However, as the ZZD algorithm does not include a correction for the cool-skin layer, so the input data for the algorithm must be either measured or derived skin SST. Therefore, an algorithm developed by Zeng et al. (1999) derives skin SST from the measured SST by the buoys. This algorithm is described in Section 3.3.2.

3.3.1. Definition of turbulent fluxes

In recent years there has been significant progress in the knowledge of the surface heat fluxes (WGASF, 2000). Air-sea interaction experiments have refined the formulae used for flux calculation and there is a better understanding of the errors in data and the corrections needed. Also, methods of obtaining fluxes from satellite data have been developed and weather forecast models have been used to produce a consistent re-analysis of the past state of the atmosphere.

The basic set of physical fluxes between the atmosphere and ocean are the transfers of shortwave radiation (Q_{sw} – wavelength 0.3 to 3 μm), longwave radiation (Q_{lw} – wavelength 3 to 50 μm), sensible heat (Q_{sen}), latent heat (Q_{lat}), and momentum (τ - wind stress). The air-sea fluxes can be obtained in several ways. The most straightforward, but also most difficult, is the direct measurement of the fluxes. Due to its complexity, direct measurements of fluxes are limited in space and time. However, it provides valuable data for developing formulae to estimate fluxes and for the validation of fluxes derived from other sources.

The sensible heat Q_{sen} can be parameterised by the relation:

$$Q_{sen} = C_h \rho c_p U (\theta - T_s) \qquad (3.1)$$

where C_h is the heat flux coefficient, ρ is the air density, U is the mean wind speed at the standard height of 10m, c_p is the specific heat capacity of air at potential temperature θ immediately above the sea surface, and T_s is the SST.

The latent heat Q_{lat} takes the form:

$$Q_{lat} = C_l \rho L U (q_a - q_s) \qquad (3.2)$$

where C_l is the latent heat coefficient, L is the latent heat of evaporation of sea water, q_s is the water vapour mixing ratio of the sea surface, and q_a is the water vapour mixing ratio at the air-water interface that is computed from the saturation mixing ratio for pure water at SST, following the Teten's formula for saturation vapor pressure from Buck (1981)

$$q_a = 0.98\, q_{sat} (T_s) \qquad (3.3)$$

Since relative humidity (RH) is measured for moisture, the water vapour mixing ratio, q_s, is obtained by

$$q_s = RH\, q_a (T_{air}) \qquad (3.4)$$

The following relationship defines the surface wind stress, ô:

$$\tau = C_d\, \tilde{n}\, U^2 \qquad (3.5)$$

where C_d is the drag coefficient. In this work, C_d values are estimated following Smith (1988).

The next sections describe briefly the algorithms that are used in this work. The first one is to account for the cool-skin SST from bulk SST measurements, following Zeng et al. (1999), and the other is the bulk formulae used to calculate turbulent fluxes, which follow ZZD.

3.3.2. Zeng's bulk-to-skin algorithm

Although the definitions have been given in Chapter 1, it is always important to remember the difference between skin and bulk temperatures, in particular when dealing with the diurnal cycle. The skin temperature refers to the temperature in a thin layer of the upper microns of the ocean. For the present work, bulk SST is always referred to buoy measurements at 1-m depth.

Previous modelling studies (Price et al., 1986; Fairall et al., 1996a; Webster et al., 1996) have shown how the net surface heat flux and wind speed determine the temporal variation of skin temperature, and also largely the temporal variation of bulk temperature through surface layer mixing. Therefore the temporal variation of the bulk temperature should be highly correlated with the net surface heat flux and hence, along with wind speed, can be used to derive skin temperature.

All these methods require knowledge of the net surface heat flux and near-surface wind speed. Diurnal averaged precipitation is required in addition for the Webster et al. (1996) regression algorithm for the diurnal amplitude of skin temperature. Ship and buoy observations, however, generally provide only the bulk temperature and environmental conditions (i.e., wind, temperature, and humidity) and not the net heat flux over the diurnal cycle except during field experiments. Consequently, it has not been possible to derive skin temperature data over the diurnal cycle for a large region.

Zeng et al. (1999) developed an algorithm and inferred an empirical approximation to the actual oceanic diurnal variation, including multiple frequencies, complex mixing processes in the near surface ocean, and the molecular sublayer. This was done through use of the actual diurnal shape of the observed bulk temperature and by allowing some coefficients to be determined independently by statistical fitting as a function of wind speed. That is, they assumed that

$$T(0,t) = < T_0 > + f(t), \qquad (3.6)$$

where, with the bracket denoting a 24 hour averaging, $< T_0 >$ is the mean skin temperature for an individual day and f is the variation of temperature around $< T_0 >$. To show that the bulk temperature will vary with depth they have

$$T(z,t) = < T_z > + e^{-bz} f(t - c_z), \tag{3.7}$$

where

$$< T_z > = < T_0 > + a_z + d \tag{3.8}$$

is the mean temperature at depth z for an individual day, and a, b, c, and d are coefficients with the first three being functions of wind speed. The term d is included to capture the daily averaged temperature difference across the molecular sublayer. Equations (3.7)-(3.8) mean that the skin temperature can be obtained from the temporal variation of bulk temperature by adjusting the daily mean value (using (3.8)), diurnal amplitude (through the exp(-b_z) term), and phase (through the –c_z term).

Let t_1 and t_2 denote the times when observed skin and bulk temperatures reach their maximum values T_{0max} and T_{zmax}, respectively. The coefficients a, b, c, and d are obtained from observational data by:

(1) computing d from $< T_z > - < T_0 >$ when the wind is sufficiently strong that $< T_z >$ can be assumed to be almost independent of depth in the ocean mixed layer (i.e., the a_z term in Eq. (3.8) can be omitted);
(2) computing a from Eq. (3.8);
(3) equating c to $(t_1 – t_2) / z$, and;
(4) computing b as $\ln[(T_{0max} - < T_0 >) / (T_{zmax} - < T_z >)] / z$.

Provided the coefficients have been so determined, skin temperature is computed from the bulk temperature at depth z by:

(1) obtaining $< T_0 >$ from Eq. (3.8);
(2) obtaining $f(t – cz)$ from Eq. (3.7);
(3) linearly interpolating $f(t – cz)$ to $\pi(t)$ at each hour, and;
(4) obtaining the skin temperature from Eq. (3.6).

3.3.3. Zeng et al. (1998) algorithm

The algorithm described by ZZD takes essentially the same path as the Coupled Ocean Atmosphere Response Experiment (COARE) algorithm (Fairall et al., 1996b), but uses different stability functions for the velocity and scalar profiles, and a different form for the scalar roughness lengths. The various empirical constants are given values, which ensure reasonable agreement with observation over the wind speed range 0 –18 ms^{-1}. The observations used are the COARE Moana Wave dataset for low to moderate wind speeds (0-12 ms^{-1}) and the Humidity Exchange Over the Sea (HEXOS) program data up to 18 ms^{-1}.

Like Fairall et al. (1996b), ZZD use the Kansas expressions for near-neutral atmospheric stability and the stable case but, as stability increases beyond z/L = 1, the expression of Holtslag et al. (1990) is adopted:

$$\Phi_m = \Phi_t = \Phi_q = 5 + z/L \qquad (3.9)$$

where Φ_m, Φ_t and Φ_q are the dimensionless profiles of wind, temperature and humidity, respectively, derived using dimensional considerations and similarity theory (Geernaert, 1990), and L is the Monin-Obukhov length as defined by Stull (1988). ZZD match the near-neutral to convective forms at z/L= -1.574 for momentum and z/L = -0.465 for the scalars.

They also use the functional form of Smith (1988) for the momentum roughness length, but their analysis of the Moana Wave COARE data suggests a value for the Charnock constant α_c= 0.013. For the scalar roughness length of humidity and temperature, they use the expression given by Brutsaert (1982):

$$\ln\left(\frac{z_0}{z_{0T}}\right) = \ln\left(\frac{z_0}{z_{0Q}}\right) = b_1 \mathrm{Re}^{1/4} + b_2 \qquad (3.10)$$

where *Re* is the roughness Reynolds number, and the constants determined empirically by the authors (b_1 = 2.67 and b_2 = -2.57) differ slightly from those given by Brutsaert (1982). This is partly because they are optimised to provide a continuous fit to both the COARE and HEXOS datasets.

Other similarities with the COARE algorithm include allowance for the 2% reduction in saturated specific humidity over sea water, which ZZD find decreases latent heat flux by 20% at 14 ms^{-1}, and the “gustiness” correction at low wind speeds. However, they adopt a value ®=1.0, rather than the value 1.2 which Fairall et al. (1996b) prefer. As explained earlier, ZZD algorithm does not include the contributions to sensible heat and momentum due to rainfall, nor models for the cool skin and diurnal thermocline, so input data for the algorithm must be either measured or derived skin SST.

ZZD have compared the performance of their algorithm with five other different algorithms: the COARE algorithm, version 2.5, the algorithm used in the National Center for Atmospheric Research (NCAR) Community Climate Model version 3 (CCM3), the ECMWF forecast model, the National Centers for Environmental Prediction (NCEP) medium-range fore-cast model, and the Goddard Earth Observing System (GEOS) Data Assimilation System (DAS). They conclude that for moderate wind conditions (3 to 6 ms^{-1}), the different algorithms provide similar results.

Brunke et al. (2003) have recently evaluated and ranked twelve bulk flux algorithms using direct turbulent flux measurements determined from covariance and inertial-dissipation methods from 12 ship cruises over the tropical and midlatitude oceans. ZZD algorithm has been classified as one of the least problematic, as well as the COARE version 3.0, and those used at the European Centre for Medium-Range Weather Forecasts (ECMWF) and the National Aeronautics and Space Administration (NASA) Data Assimilation Office for version 1 of the Goddard Earth Observing System reanalysis (GEOS-1). Therefore, the choice of the ZZD algorithm seems to be justified. In addition, its use for the tropical Atlantic region has not yet been reported in the literature.

3.4. Analytical methods

As mentioned earlier in this chapter, this work will explore processes that are multiscale and nonstationary. This section will describe the two methods that will be used in the analysis of the data, in order to highlight those characteristics: i) Radon Transform which will be used in Chapter 6 to determine the propagation speed of TIW in the tropical Atlantic, and ii) Wavelets, which will be used in Chapter 5 to show the seasonal variability of the diurnal cycle. In addition, Chapter 7 will explore the filtering properties of wavelets, essentially acting as bandpass filter.

3.4.1. Radon Transform (RT)

Radon transform has been successfully used in determining the Rossby waves characteristics observed in altimeter dataset (Chelton and Schlax, 1996; Polito and Cornillon, 1997). As only more recently it has been applied in SST (Hill et al., 2000) and ocean colour data (Cipollini et al., 2001), its use still needs to be disseminated in these fields. Thus, this work will also estimate the usefulness of identifying the propagation characteristics of TIW in the SST data by using the RT technique, which is explained below.

Let f (V), the wavefield in the longitude–time plot, be a function of the 2D vector V = (x, y), where x and y are longitude and time, respectively. If L is an arbitrary line at an angle θ with respect to the x axis, the RT (Deans, 1983) is defined as the projection of f (V) on L; that is,

$$p(s,\theta)=\int_{\tilde{o}} f(V)du \qquad (3.11)$$

where *u* is the direction orthogonal to L (along which the integral summation is performed) and *s* is the co-ordinate on L. Note that for a given θ*,* the RT is a 1D function of the line coordinate *s.* We can rewrite Equation 3.11 in terms of coordinates *x* and *y*,

$$p(x',\theta)=\int_{y'} f(x,y)\Big|_{\begin{cases} x=x'\cos\theta-y'\sin\theta \\ y=x'\sin\theta+y'\cos\theta \end{cases}} dy' \qquad (3.12)$$

The Radon Transform has many varied applications: in medical imaging, in the processing of seismic data to find subsurface rock interfaces, and in the detection of ship wakes in satellite images. In all these applications, in addition to the applications in remote sensing of the oceans described earlier, the essential method is to transform two-dimensional images with lines into a domain of possible line parameters (e.g., slope, which equates to speed in a longitude–time plot), whereby each line in the image will yield a peak at the corresponding line parameter in the transform domain

(Figure 3.4). When the focus of the analysis is on the propagation speed, rather than on the wavelength and period characteristics of the single components, the Radon Transform is more appropriate than the Fourier Transform.

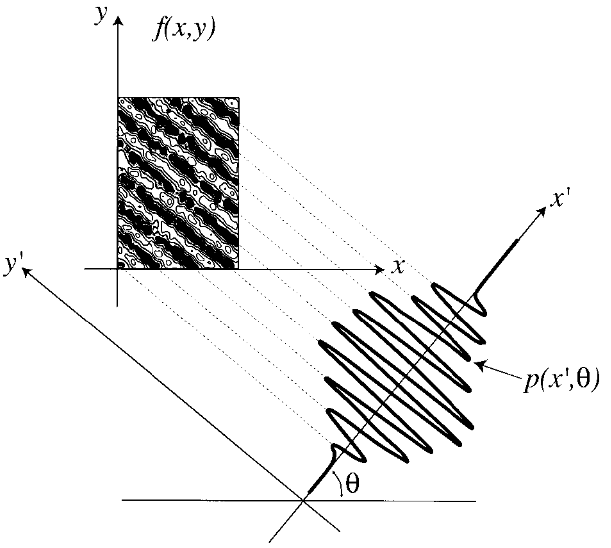

$$p(x',\theta) = \int_{y'} f(x,y)\Big|_{\substack{x = x'\cos\theta - y'\sin\theta \\ y = x'\sin\theta + y'\cos\theta}} dy'$$

Figure 3.4 – Schematic of the 2D RT of a longitude-time section modified from Challenor et al. (2001)

3.4.2. Wavelets

Engineers, physicists, astronomers, geologists, medical researchers, and others have already begun exploring the extraordinary array of potential applications of wavelet analysis, ranging from signal and image processing to data analysis. In oceanographic and atmospheric research, the volume of work that uses this technique has increased in the last five years (Torrence and Compo, 1998; Masina and Philander, 1999; Cromwell, 2001; Yan et al., 2001; Wainer et al., 2003). This work will also explore the potentialities of the wavelets, by determining the seasonal variability of the diurnal cycle. However, little attention has been given to a major advantage of wavelets, which is its use as a bandpass filter. This work will explore this convenience of the method in order to isolate the temporal band of the variability associated with TIW, aiming to identify its influence in the diurnal signal, as will be demonstrated in Chapter 7.

Wavelet methods, in contrast to Fourier analysis, use approximating functions that are localized in both time and frequency space (Foufoula-Georgiou and Kumar, 1994). It is this unique characteristic that makes wavelets particularly useful, for example, in capturing, identifying, and analyzing local, multiscale, and nonstationary processes.

Wavelet analysis is based on the convolution of a time series *F(t)* with a set of functions $G_{ab}(t)$ using parameters *a* and *b*, derived from a "mother wavelet" *G(t)*, where:

$$G_{ab}(t) = \frac{1}{a^{1/2}} G\left(\frac{t-b}{a}\right) \qquad (3.13)$$

The real scalar *b* is called the "translation" parameter, and corresponds to the central point of the wavelet in the time series. The real and positive scalar *a* is the "scale dilation" parameter and determines the width of the wavelet. The factor $1/a^{1/2}$ normalises the wavelets so that they have unit energy and hence are comparable for all scales *a*.

The convolution of *f(t)* with the set of wavelets is the "wavelet transform":

$$T_g(b,a) = \frac{1}{a^{1/2}} \int g\left(\frac{t-b}{a}\right) f(t) dt \qquad (3.14)$$

This is known as the continuous wavelet transform since *a* and *b* may be varied continuously. However, according to Meyer and Xu (1997), to be a mother wavelet both formally and in practice, *g(t)* must have the following properties:

(i) It must be a function centred at zero and in the limit as $|t| \to \infty, g(t) \to 0$ rapidly. This condition produces the local nature of wavelet analysis, since the coefficients $T_g(b,a)$ are affected only by the signal in the "cone of influence" about t = b. In practice, the radius of the cone of influence is the point $|t| = r_c$ beyond which $g_{ab}(x)$ no longer has significant value.

(ii) Also, *g(t)* must have zero mean. Known as the admissibility condition, this implies the invertability of the wavelet transform. That is, the original signal can be obtained from the wavelet coefficient using

$$f(t) = \frac{1}{C} \iint \frac{T_g(b,a) g_{ab}}{a^2} da db \tag{3.15}$$

where

$$\frac{1}{C} = \int_{-\infty}^{\infty} \frac{|\hat{g}(\omega)|^2}{\omega} d\omega \tag{3.16}$$

(iii) Wavelets are often regular; that is, $\hat{g}(\omega < 0) = 0$. This simplifies the interpretation of the transform because it eliminates confusion of measurements at ω with those at $-\omega$. Wavelets that are regular are also called progressive.

(iv) Higher-order moments should vanish, allowing for the study of high-order variations in the data. This requirement can be relaxed depending on the application.

The principles behind the wavelet transform, as explained above and well described by Grossmann and Morlet (1984) and Daubechies et al. (1992), is to hierarchically decompose an input signal into a series of successively lower resolution reference signals and their associated detail signals. At each decomposition level, L, the reference signal has a resolution reduced by a factor of 2L with respect to the original signal. Together with its respective detail signal, each scale contains the information needed to reconstruct the reference signal at the next higher resolution level. Wavelet analysis can therefore be considered as a series of bandpass filters and be viewed as the decomposition of the signal into a set of independent, spatially oriented frequency channels. Using the orthogonality properties, a function in this decomposition can be completely characterised by the wavelet basis and the wavelet coefficients of the decomposition.

Once we have decomposed the signal into coefficients, we can remove any frequency band by setting the respective wavelet coefficients towards zero, while preserving the other frequency features. The method can be described as a three step procedure: 1) data are transformed into a set of wavelets coefficients applying the discrete wavelet function; 2) coefficients of the required band are set to zero; 3) the wavelet coefficients left are transformed back in the domain of the original data.

3.5. Summary

This chapter has described the dataset that is used in this work, covering January 1998 to December 2001, as well as explained the analytical methods that will be explored in the data analyses. It is already evident that the PIRATA array provides an incomparable source of data. However, this dataset has been used in studies analysing seasonal and interannual timescales. The high-frequency measurements that are useful for studies relating to diurnal variability have been neglected. Therefore, this work plans to exploit these high-frequency measurements in order to characterise the diurnal cycle in the tropical Atlantic.

The use of high quality satellite data, in particular data retrieved from microwave sensors, which provides data of the sea surface under all weather conditions except rain, is essential for tropical regions. To achieve the necessary spatial coverage to assess the variability of TIW, data from two sensors, TMI and Qscat, are used in this work. These two sensors retrieve measurements of SST, wind speed, atmospheric water vapour, liquid cloud water and precipitation rates (TMI) and wind speed and direction (Qscat). TMI wind speed will be applied to fill the gaps in the in situ wind speed time series. However, it is not going to be used in the study of TIW variability, as vector wind data would be necessary, as supplied Qscat.

Turbulent heat fluxes, as they are not measured directly by the PIRATA buoys, need to be parameterised. The method chosen to be used is the one developed by Zeng et al. (1998), which has been extensively compared with other algorithms and ranked as one of the least problematic (Brunke at al. (2003). However, as it does not have a correction for the cool-skin layer, skin SST data is derived using the algorithm developed by Zeng et al. (1999).

As this work aims to investigate processes that are multiscale and non-stationary, the analytical methods used in the analysis of the data, will emphasize those characteristics. Radon Transform has already been successfully used with altimeter data, and here will show its usefulness with SST data, planning to resolve the propagation speed of TIW in the tropical Atlantic. And finally, wavelets will be used to show the seasonal variability of the diurnal cycle. However, as little attention has been given to the filtering capability of the technique, this work will explore the convenience of the method in order to isolate the temporal band of the variability associated with TIW.

Chapter 4

Validation of the dataset

4.1. Introduction

As satellite data has become an essential part of any large scale study, its validation has also become crucial for the purpose of having good quality data. Many works have been devoted to such an important issue, by validating satellite retrieved wind data (Freilich, 1997; Dickinson et al., 2001; Ebuchi et al., 2002; Bourassa et al., 2003) and SST (Donlon and Robinson, 1998; Donlon et al., 2002; Stammer et al., 2003). However, few works have validated satellite data for the tropical Atlantic region using the PIRATA array dataset. And more important, most of the studies have used the *in situ* data as a single dataset, not taking into account possible regional biases. As an example, Kelly et al. (2001) showed that the difference between the zonal components of TAO-based wind and QuikSCAT wind have a striking similarity with the tropical Pacific currents, especially with the South Equatorial Current (SEC) at 2^o N, and North Equatorial Countercurrent (NECC) at 7^o N.

Thus, this is the reason for this chapter to present a substantial amount of work, as the result of a complete validation of the satellite dataset used in this work, assessing each of the buoys individually. This makes an important contribution since it takes into account possible regional biases. It will also investigate the possible sources of error in the turbulent heat fluxes calculations due to instrumental inaccuracy.

4.2. Impact of availability of data

The availability of in situ data might become an important issue for validation and intercomparison studies with satellite data. As the buoys of an array are deployed in different regions of the oceanic basin, one can expect distinct oceanic and climatic conditions which might influence the instrument measurements. Distinct wave regimes are particularly significant as this might change the depth and/or height at which the instruments are measuring the variables. Moreover, seasonal variations of the above mentioned conditions can add inaccuracies in the measurements. To illustrate, results of intercomparison between satellite and in situ data will probably be different if the time series has data collected only during winter months or only during summer months.

As mentioned in the previous chapter, it is very unfortunate that the time series of the buoys of the PIRATA array do not present the same record length for each buoy, or even for each sensor on a single buoy. However, this is not a particular problem for the PIRATA dataset. This is a condition that affects all the other arrays, and is due mainly to instrumentation faults and vandalism. Figure 3.3 illustrated well the length difference among the variables for all the buoys, as well gaps in the time series.

In this work, we acknowledge these circumstances and discuss the results achieved in the light of this condition. With the exception of two buoys (2°N 10°W and 2°S 10°W), all the other buoys present SST time series approximately one year long. This certainly reduces, although does not fully eliminate, the seasonal influence that any oceanic condition can have on the dataset. Interannual variations could also interfere but are impossible to eliminate as the datasets are still not long enough. Short time series and frequent gaps are a particular problem for wind data, as described in the next section. For these data, we are particularly cautious with the interpretation of the results achieved for this work.

4.3. Wind data

Ocean vector winds, critical for determining the dynamical forcing of the ocean, are sensitive indicators of the surface manifestation of over-ocean atmospheric phenomena. Accurate measurements of surface stress are needed to understand air-sea coupling, and to improve predictions of climate variability (Huang and Schneider, 1995; Kessler et al., 1995).

Although satellite-based wind data provide a synoptic view from space, buoy data is still the main source for the calculations of air-sea fluxes. The largest problem with *in situ* data is that very often there are gaps in the time series due to technical problems and vandalism. Faulty instruments can cause large data gaps because maintenance cruises are performed only once per year. In this case, satellite data would be very useful in filling those gaps.

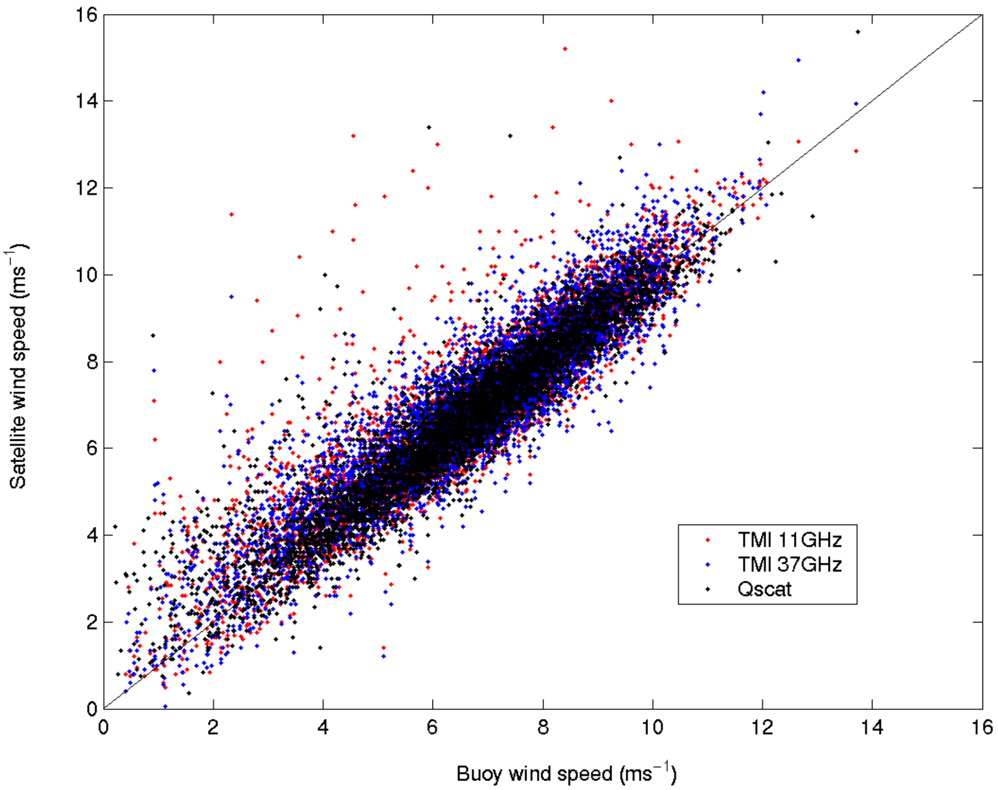

Figure 4.1 – Comparison between buoy wind speed and satellite wind speed. Satellite wind data is TMI 11GHz (red), TMI 37GHz (blue) and Qscat (black).

In this study, to make the most direct comparison, satellite-based (QuikSCAT, TMI 11 and 37GHz) and buoy data have been collocated within 30 min and 25 km of each other. Since each satellite model function produces a wind at 10 m, assuming a neutrally stratified atmosphere, the buoy wind data were converted from 4 m above sea level in the real atmosphere to 10 m in a neutrally equivalent atmosphere. The conversion was made using the bulk formulation of the log profile approximation in the atmospheric surface layer (Zeng et al., 1998).

Figure 4.1 show comparisons between wind data measured by the buoys and converted to 10-m, and satellite data: QuikSCAT, TMI 11 GHz and TMI 37 GHz. The largest scatter is most noticed at low wind speed, for all the missions. QuikSCAT has been shown to provide robust and good quality data (Ebuchi et al., 2002) . Regarding the TMI wind data, it is possible to observe a slightly better result for the 37 GHz dataset, although one might expect a better agreement with the 11 GHz channel, as it is less sensitive to the influence of the atmosphere. One possible explanation is that, although the 11 GHz is less susceptible to the influence of the atmosphere, the 37 GHz will be more sensitive to wind speed at lower wind speeds, which in general is what buoys measure well (Laurence Connor, personal communication).

Figures 4.2 – 4.4 follow the schematic diagram shown in Appendix A. They show comparisons between wind data measured by the buoys and converted to 10-m, and satellite data (QuikSCAT, TMI 11 GHz and TMI 37 GHz, respectively) for each individual buoy. In general, the wind speed derived from the satellites agrees well with buoy observations, although it is mostly overestimated by all the satellite sensors, with few exceptions. Tables 4.1 – 4.3 summarise statistics of the comparison for the three wind datasets. Despite this good agreement, it is important to notice that the buoys located at the latitudes 4° N, 8° N, 12° N and longitude 38° W, when compared with the other locations, show a larger rms difference (~ 1 ms^{-1}), but this is still smaller than the missions' specification of 2 ms^{-1}. Also, the same locations show some of the largest biases.

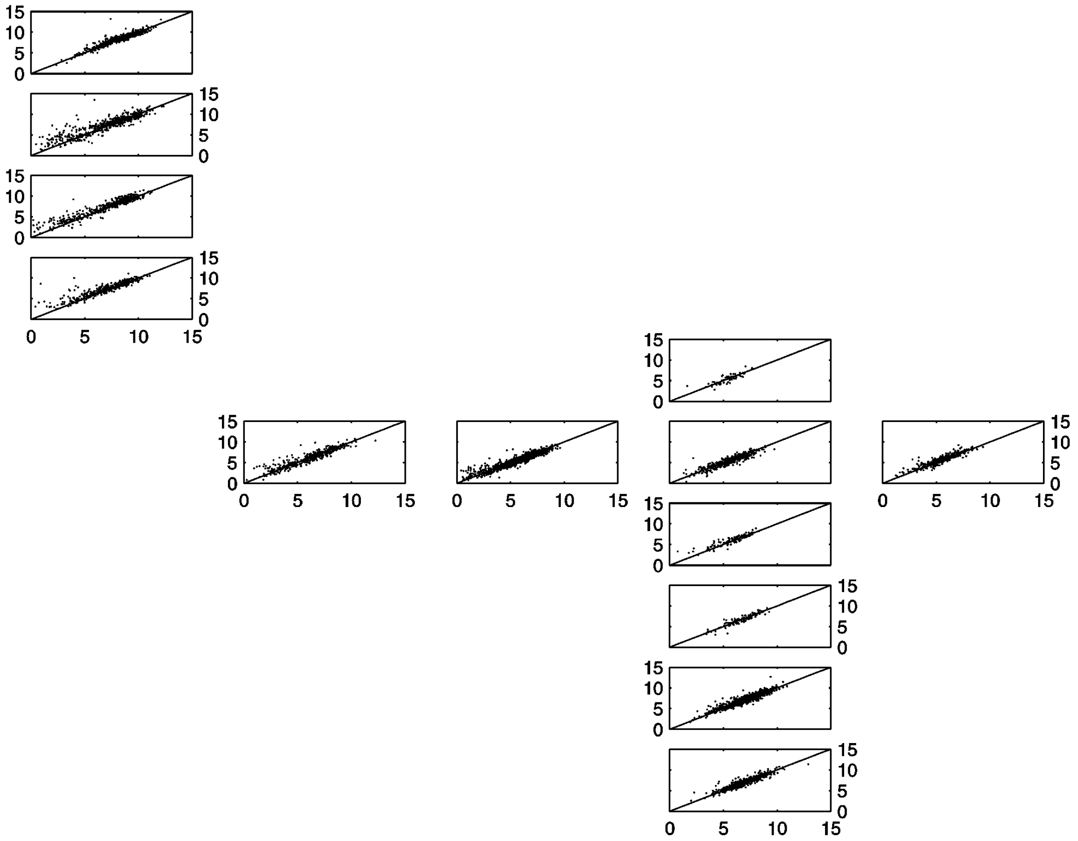

Figure 4.2 – Wind speed (ms^{-1}) measured by PIRATA buoys (X axis) and QuikSCAT (Y axis)

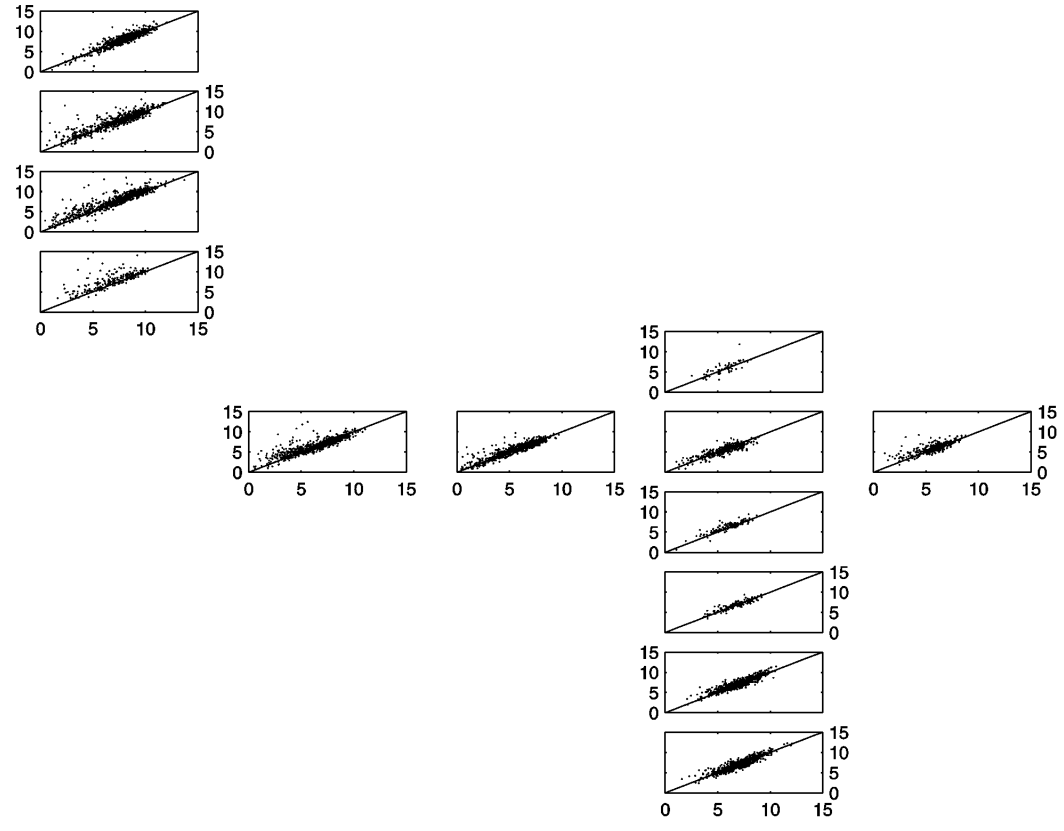

Figure 4.3 – Wind speed (ms^{-1}) measured by PIRATA buoys (X axis) and TMI 11 GHz (Y axis)

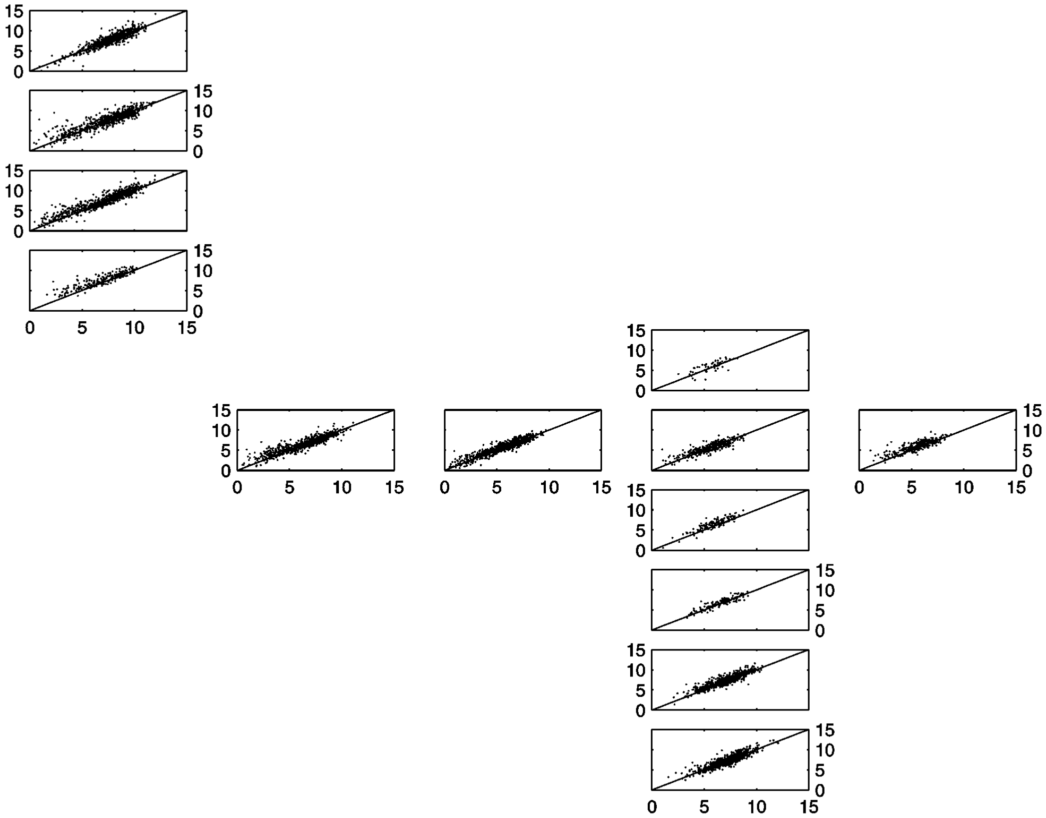

Figure 4.4 - Wind speed (ms^{-1}) measured by PIRATA buoys (X axis) and TMI 37 GHz (Y axis)

Table 4.1 – Statistics of comparison between wind speed (ms^{-1}) measured by PIRATA buoys and QSCAT

Buoy	r^2	rms diff	bias	No. obs.
0N 0W	0.8421	0.5884	-0.1784	353
0N 10W	0.8357	0.6246	0.1613	406
0N 23W	0.8829	0.6476	0.1186	900
0N 35W	0.8600	0.7622	-0.0660	417
10S 10W	0.8699	0.5425	-0.0470	441
12N 38W	0.8163	1.1198	-0.3631	518
15N 38W	0.8903	0.5688	-0.1745	501
2N 10W	0.7339	0.6546	-0.0276	55
2S 10W	0.8357	0.6221	-0.2442	115
4N 38W	0.8138	0.9933	-0.4204	350
5S 10W	0.8488	0.4933	-0.0139	126
6S 10W	0.8742	0.5584	-0.1693	805
8N 38W	0.9065	0.8789	-0.4350	455

Table 4.2 – Statistics of comparison between wind speed (ms^{-1}) measured by PIRATA buoys and TMI 11 GHz

Buoy	r^2	rms diff	bias	No. obs.
0N 0W	0.6119	0.9736	-0.3420	297
0N 10W	0.7588	0.7521	0.0951	334
0N 23W	0.8332	0.7517	-0.0384	762
0N 35W	0.7472	1.0556	-0.1736	682
10S 10W	0.8281	0.6146	-0.0196	761
12N 38W	0.8064	1.0350	-0.3228	669
15N 38W	0.8576	0.6720	-0.0809	675
2N 10W	0.5664	0.9961	-0.2124	57
2S 10W	0.8014	0.6974	-0.3335	126
4N 38W	0.5932	1.5683	-0.8561	238
5S 10W	0.8456	0.5308	-0.0977	139
6S 10W	0.8399	0.6420	-0.2023	617
8N 38W	0.8300	1.1174	-0.5257	762

Table 4.3 - Statistics of comparison between wind speed (ms^{-1}) measured by PIRATA buoys and TMI 37 GHz

Buoy	r^2	rms diff	bias	No. obs.
0N 0W	0.7053	0.9040	-0.4449	301
0N 10W	0.7479	0.7704	-0.0687	345
0N 23W	0.8745	0.6668	-0.1292	773
0N 35W	0.8321	0.8700	-0.1678	699
10S 10W	0.7979	0.6846	-0.0571	779
12N 38W	0.8005	1.0360	-0.2386	685
15N 38W	0.8148	0.7794	-0.0343	689
2N 10W	0.5524	0.9513	-0.2512	58
2S 10W	0.7959	0.8659	-0.5639	127
4N 38W	0.7948	1.1040	-0.6584	243
5S 10W	0.7996	0.6326	-0.1846	140
6S 10W	0.8056	0.7541	-0.3271	631
8N 38W	0.8776	0.9210	-0.3918	777

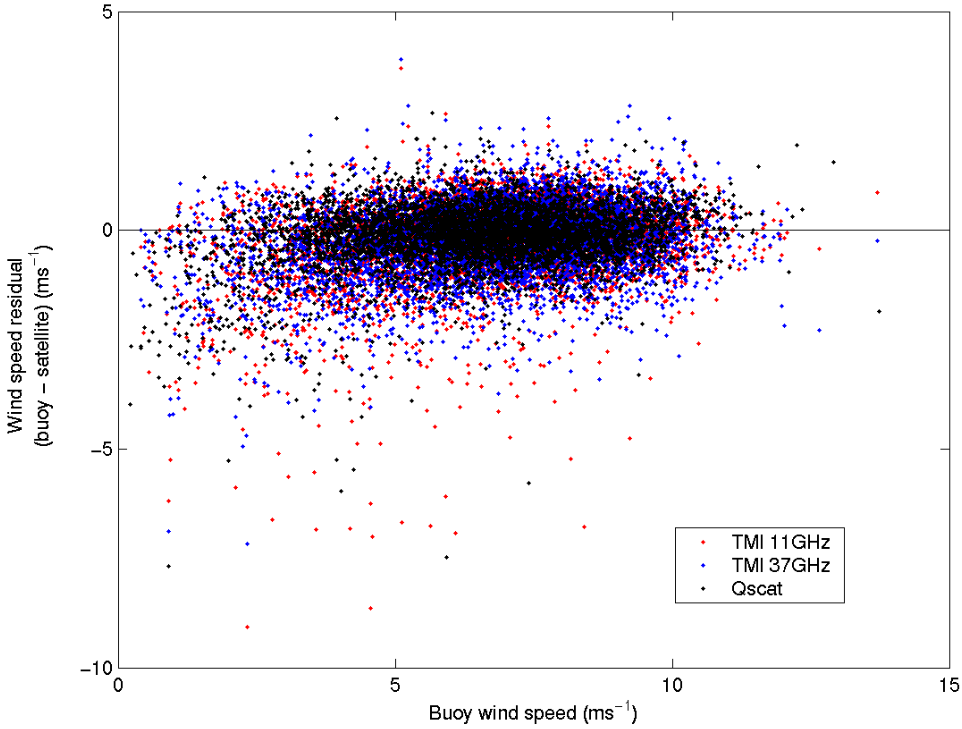

Figure 4.5 – Dependence of wind speed residual (Buoy – satellite) on the buoy wind speed. Satellite wind data is TMI 11GHz (red), TMI 37GHz (blue) and Qscat (black).

The dependence of wind speed residual (buoy-satellite) on the buoy wind speed is shown by Figures 4.5, for QuikSCAT, TMI 11 GHz and TMI 37 GHz. The largest scatter is observed for all the sensors at low buoy wind speed. TMI 11GHZ data seems to produce most of the largest negative residuals, indicating an overestimation of the wind speed measured by the 11 GHz sensor. Figure 4.6, which presents the number of data, averages and standard errors calculated in bins of buoy wind speed of 1 ms^{-1}, confirms this situation. Moreover, it shows that all the missions present the same behaviour. At low wind speeds (< 5 ms^{-1}), a negative bias is noticed, which could indicate a possible overestimation of the wind speed measured by the satellite. These results are corroborated by Freilich (1997), who showed that random component speed errors introduce positive wind speed biases at all true wind speeds, although the effect is greatest at low true winds. With the findings of Freilich (1997) showing that these errors are randomically introduced, it is possible to suggest that the results here presented would not imply a systematic overestimation of the wind speed. Furthermore, these analyses raise questions regarding proper instrument calibration and algorithm refinement when it is known that the magnitude data to be validated contain significant random errors.

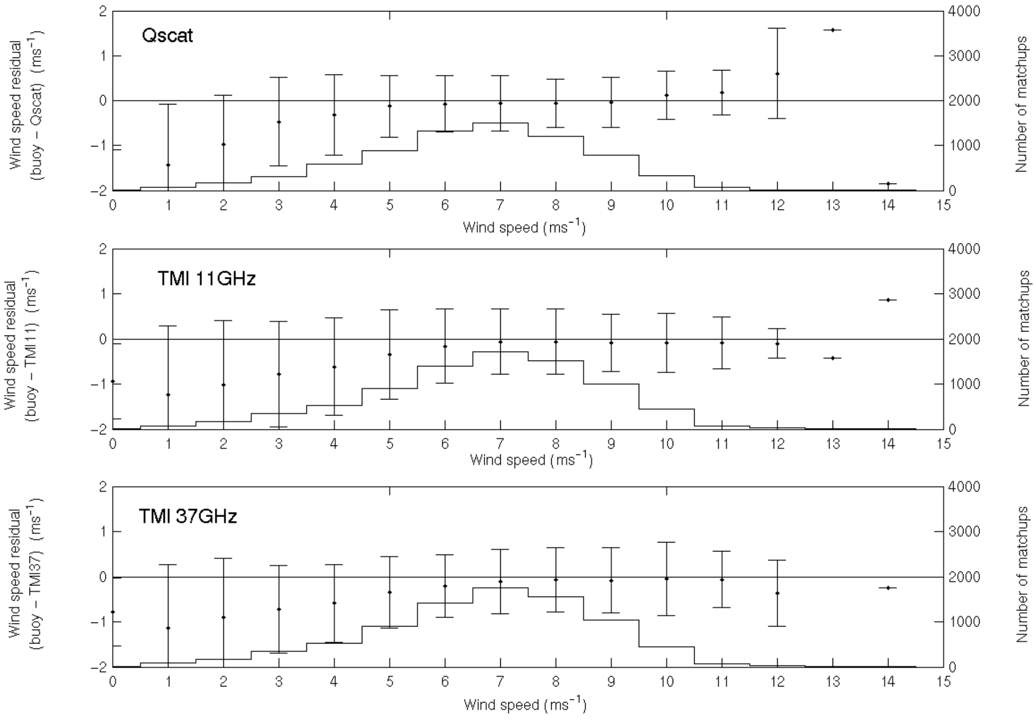

Figure 4.6 – Dependence of wind speed residual (buoy – satellite) on buoy wind speed. Number of data points (histograms), averages (points) and standard error (vertical lines) calculated in bins of buoy wind speed of 1 ms^{-1} for wind data retrieved from Qscat (top), TMI 11GHz (middle) and TMI 37GHz (bottom)

The results presented in the beginning of this section suggested the possibility of regional biases, thus Figures 4.7 – 4.9 analyse the dependence of wind speed residual on the buoy wind speed separated by each of the buoys. These figures follow the schematic diagram shown in Appendix A. For all these figures, the upper panels show scatterplot, and the lower panels show number of data, averages and standard errors calculated in bins of buoy wind speed of 1 ms-1. For most of the locations, the wind speed residual is almost zero and shows no systematic dependence on the buoy wind speed above 5 ms^{-1}.

As expected, a negative bias is noticed, which could indicate a possible overestimation of the wind speed measured by the satellite. However, this problem seems to be more critical for the buoys located at the latitudes 4° N, 8° N, 12° N and longitude 38° W. The biases at low buoy wind speed are larger at these locations, confirming what has been observed in Figures 4.2 – 4.4.

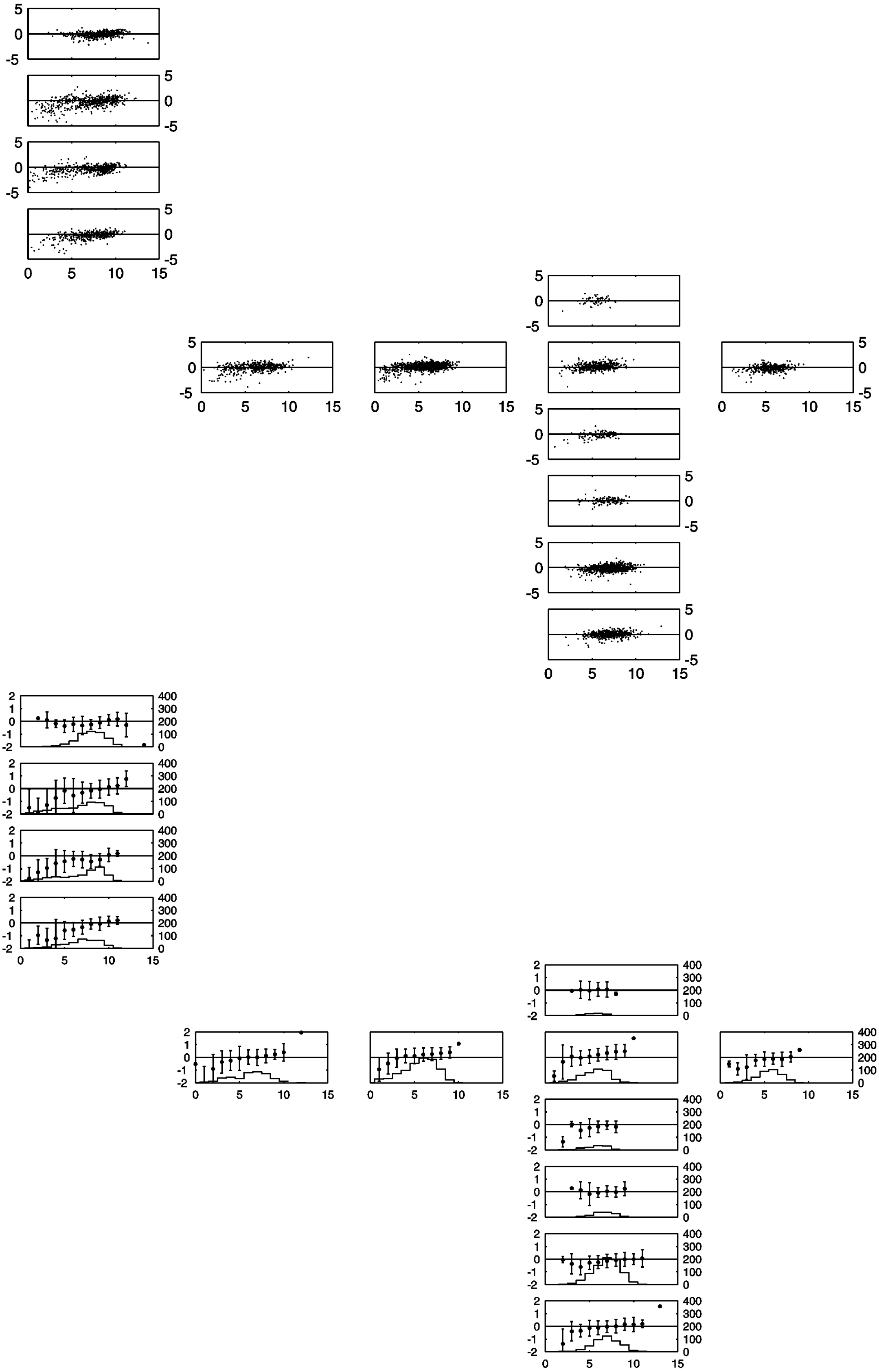

Figure 4.7 – Dependence of wind speed residual (Buoy – QuikSCAT) on the buoy wind speed. (Upper panels) Scatterplots and (lower panels) number of data points, averages (points) and standard error (vertical lines) calculated in bins of buoy wind speed of 1 ms^{-1}.

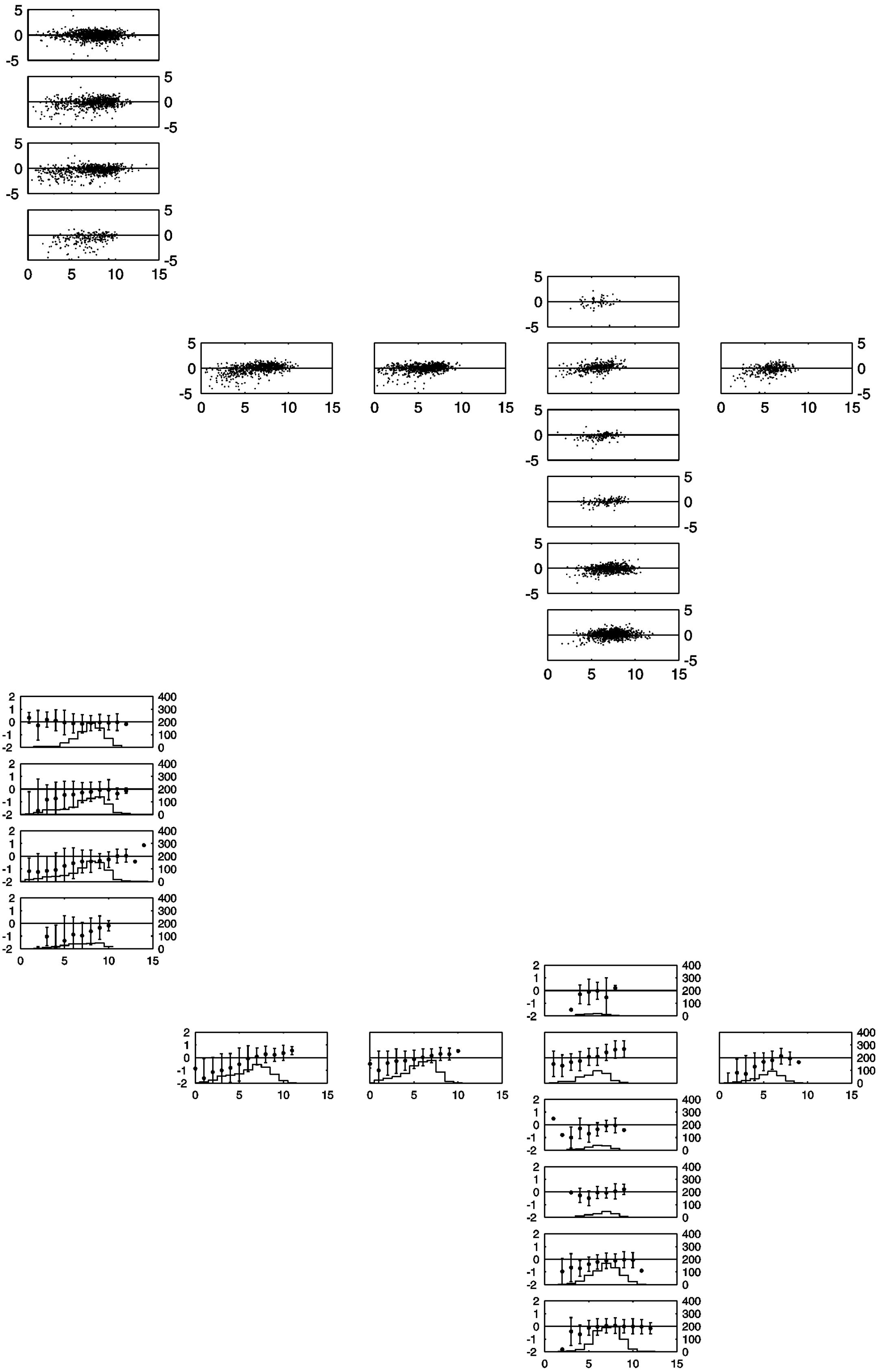

Figure 4.8 – Dependence of wind speed residual (Buoy – TMI 11 GHz) on the buoy wind speed. (Upper panels) Scatterplots and (lower panels) number of data points, averages (points) and standard error (vertical lines) calculated in bins of buoy wind speed of 1 ms^{-1}.

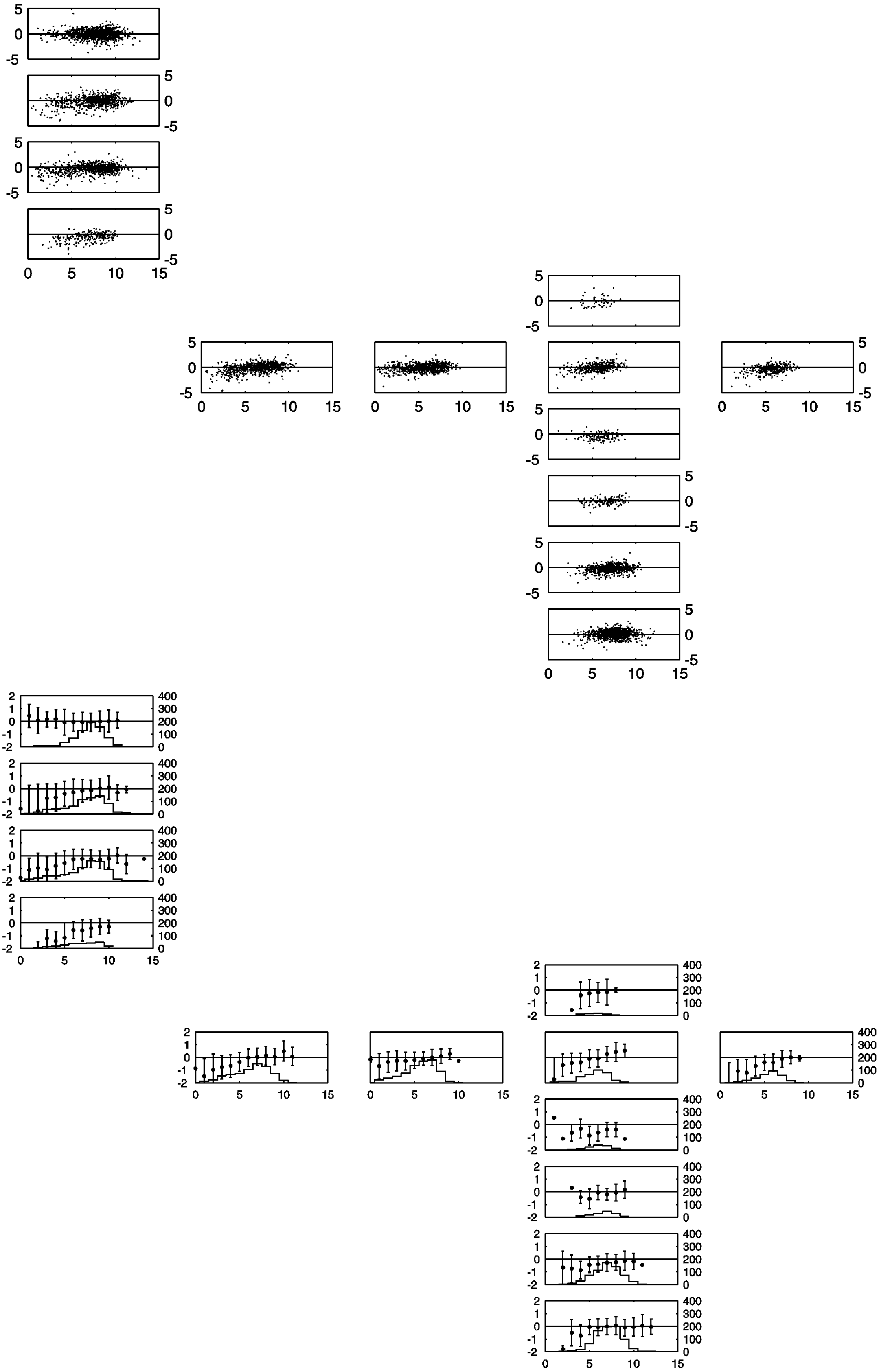

Figure 4.9 – Dependence of wind speed residual (Buoy – TMI 37 GHz) on the buoy wind speed. (Upper panels) Scatterplots and (lower panels) number of data points, averages (points) and standard error (vertical lines) calculated in bins of buoy wind speed of 1 ms^{-1}.

To assess the influence of the atmospheric and oceanic conditions on the algorithms used for wind retrieval from the satellites used in this study, the wind speed residuals have been compared with parameters (SST and air-sea temperature difference) observed by the buoys.

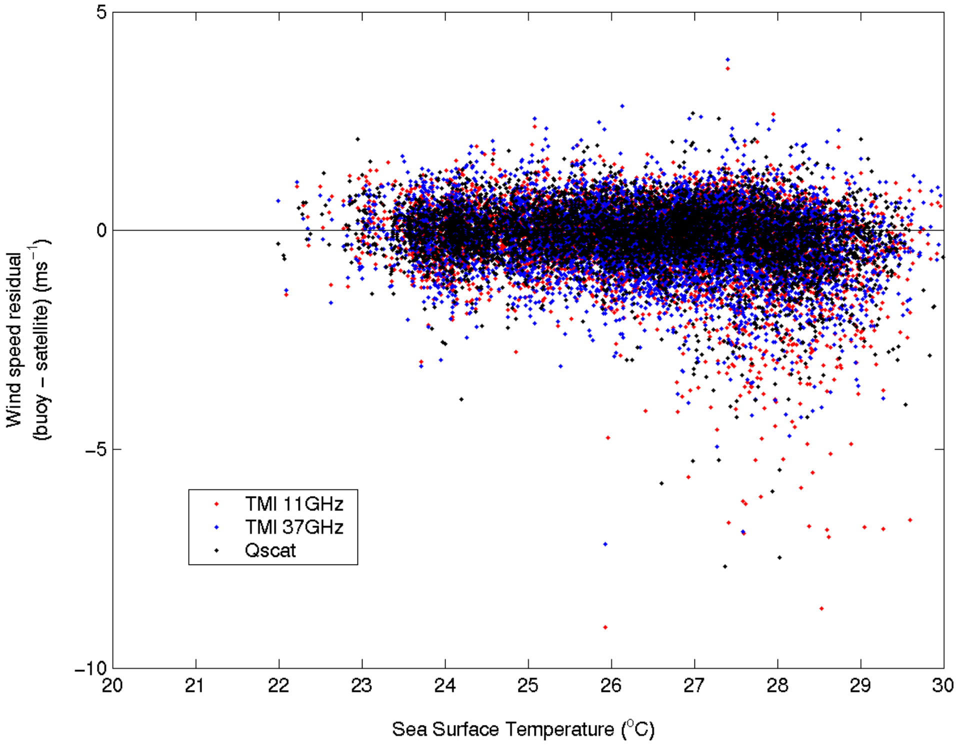

Figure 4.10 – Dependence of wind speed residual (Buoy – satellite) on the buoy SST. Satellite wind data is TMI 11GHz (red), TMI 37GHz (blue) and Qscat (black).

Figure 4.10 shows the scatterplot of data showing the dependence of wind speed residual on the buoy SST. The largest scatter is noticeable for all the missions at temperatures higher than 27°C, although TMI 11GHz data seems to present more variability. This possible dependence on SST is evident in Figure 4.11, showing that wind speed residuals may have weak dependency on SST. Analyses of dependence of wind speed residual on air-sea temperature difference show a weak dependence for the more negative of difference (Figures 4.12 – 4.13). However, as there are only few observations for those conditions, it is not possible to draw any final conclusions for the effect of the temperature difference on the wind speed.

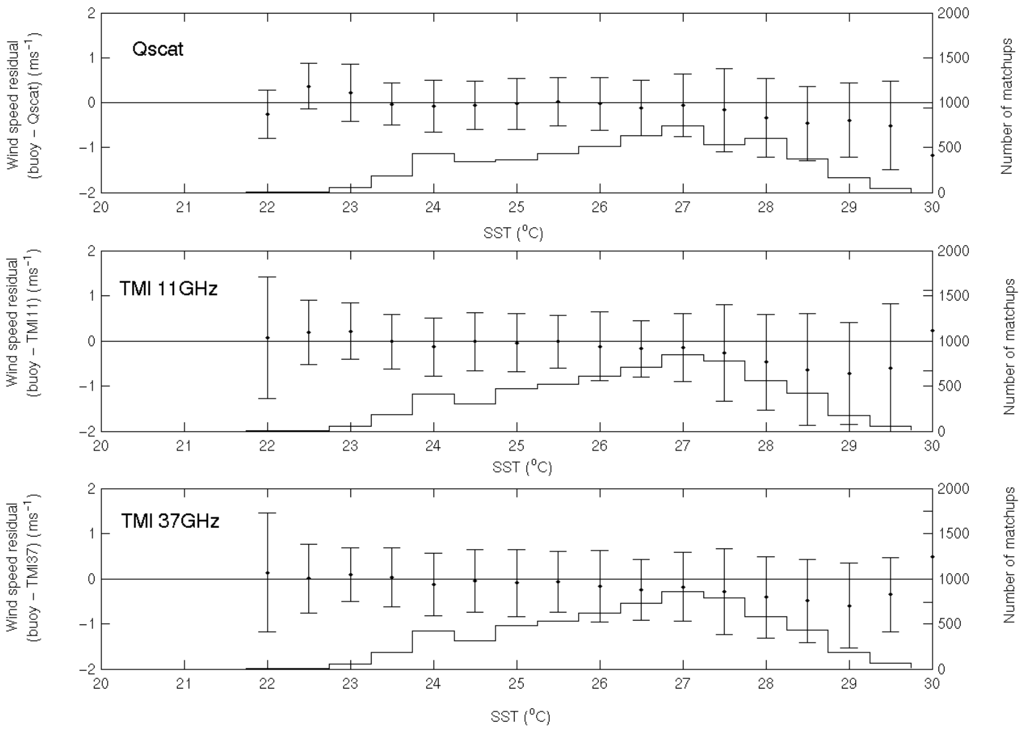

Figure 4.11 – Dependence of wind speed residual (buoy – satellite) on buoy SST. Number of data points (histograms), averages (points) and standard error (vertical lines) calculated in bins of SST of 0.5°C for wind data retrieved from Qscat (top), TMI 11GHz (middle) and TMI 37GHz (bottom)

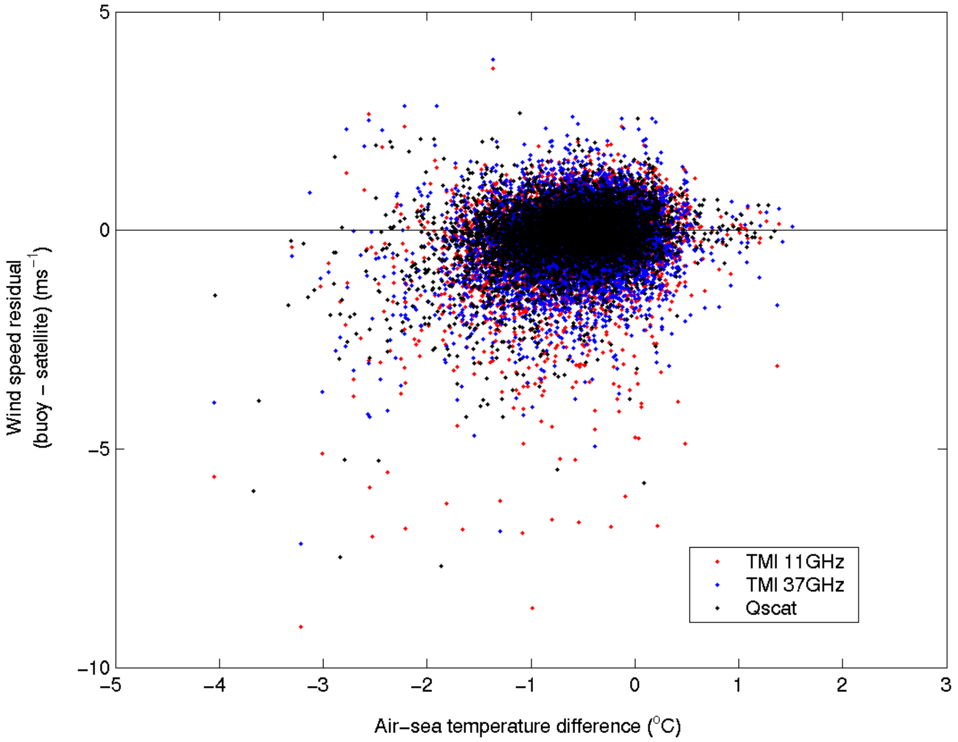

Figure 4.12 – Dependence of wind speed residual (Buoy – satellite) on the buoy air-sea temperature difference. Satellite wind data is TMI 11GHz (red), TMI 37GHz (blue) and Qscat (black).

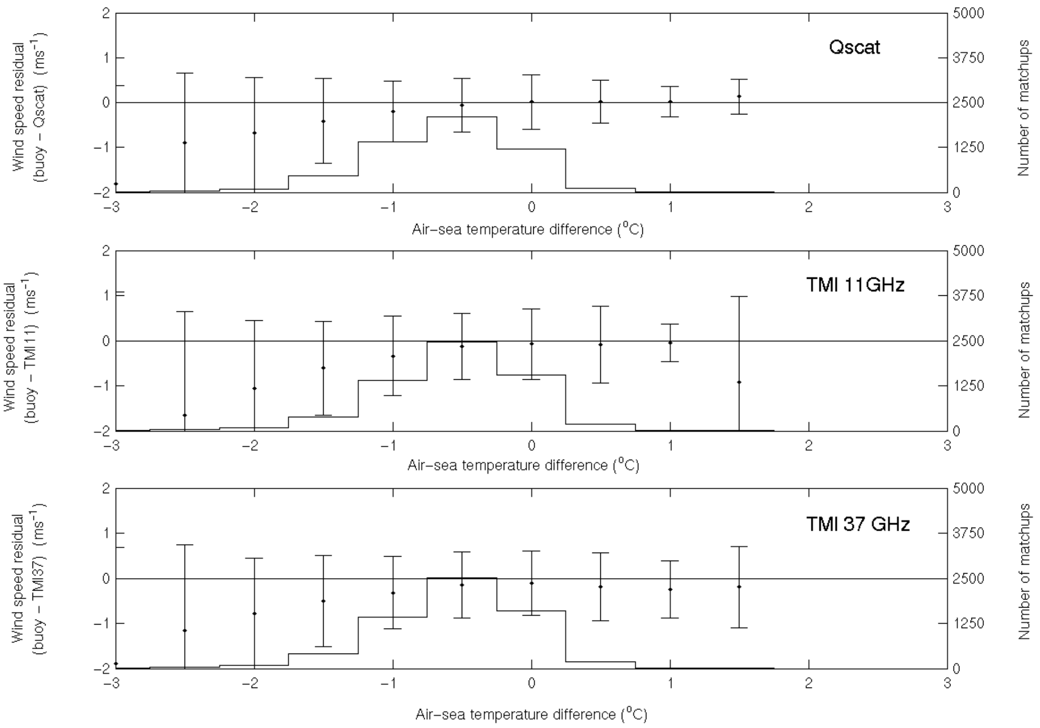

Figure 4.13 – Dependence of wind speed residual (buoy – satellite) on buoy air-sea temperature difference. Number of data points (histograms), averages (points) and standard error (vertical lines) calculated in bins of air-sea temperature difference of 0.5°C for wind data retrieved from Qscat (top), TMI 11GHz (middle) and TMI 37GHz (bottom)

Nevertheless, as one of the aims of this chapter is to investigate if there are any regional biases affecting the quality of the data, the same analyses shown in the previous figures are performed for each individual buoy. The results are presented in Figures 4.14 - 4.19. As in Figures 4.7 – 4.9, the upper panels show scatterplots, and the lower panels show the number of data, averages and standard errors calculated in bins of buoy SST (Figures 4.14 – 4.16) or air-sea temperature difference (Figures 4.17 – 4.19) of 1 °C. All these figures follow the schematic presented in Appendix A.

It is shown that wind speed residuals have weak dependencies on both SST and air-sea temperature difference. However, for the buoys located at the latitudes of 4° N, 8° N, 12° N and longitude of 38° W, it is possible to notice a negative trend of wind speed residual for SST higher than 27° C. Although some studies have reported that SST may influence the microwave backscattering from the sea surface (Donelan and Pierson, 1987), the results presented here do not support this hypothesis. If it were the case of microwave backscattering dependence on SST, it should be expected to find such relation in all locations. However, as mentioned above, only the buoys located meridionally at 38°W showed this behaviour. Most interesting is that those buoys are the ones that measure the seasonal migration of the ITCZ, with associated low winds and high SST. Additionally, those locations are the same that present some of the largest bias and rms difference between buoy-measured wind and satellite-retrieved wind (Tables 4.1 – 4.3).

This might suggest that the algorithms used for wind retrieved by the satellites are not working well in oceanic regions with low winds, as mentioned before in this section. However, this suggestion is carefully assessed as differences in the record length of the time series, as explained in Section 4.2, can add some of the observed variability. The problems at low wind speed could also be due to the comparison of a large-scale average to a local average. At these wind speeds, boundary-layer convection and large eddies can cause large differences in surface wind within a few tens of kilometres. For such conditions, the satellite-derived winds are likely to be more representative of the average winds in the satellite footprint.

Moreover, the results here presented clearly highlight the need of a careful validation process, in particular for taking into account possible regional biases. Analyses made by using data collected from different regions as a single dataset can lead to inaccurate conclusions. Data under influence of distinct environmental conditions, if treated as a single dataset can mask overall results.

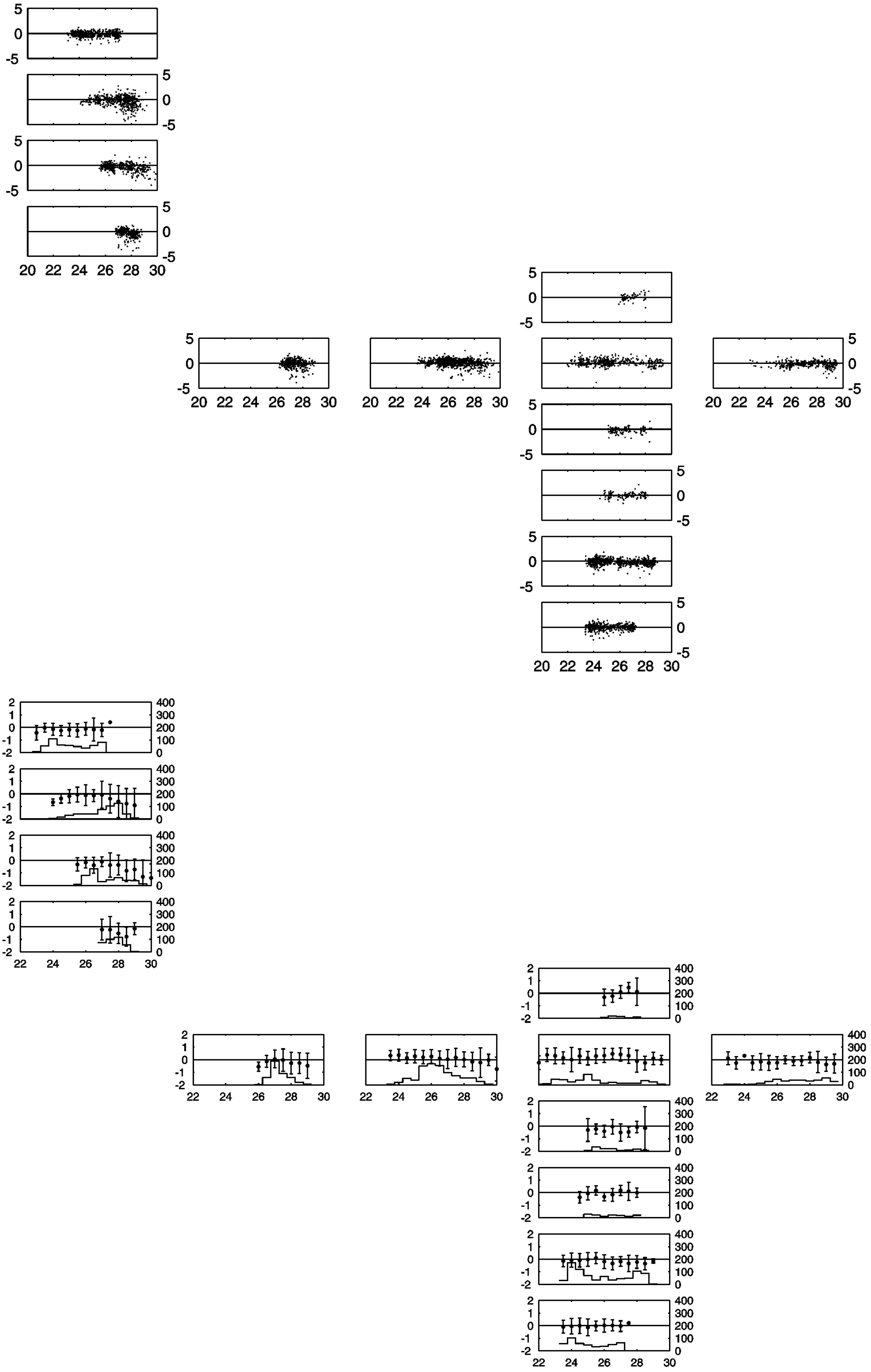

Figure 4.14 – Dependence of wind speed residual (Buoy – QuikSCAT) on the SST. (Upper panels) Scatterplots and (lower panels) number of data points, averages (points) and standard error (vertical lines) calculated in bins of SST of 0.5 ^{o}C

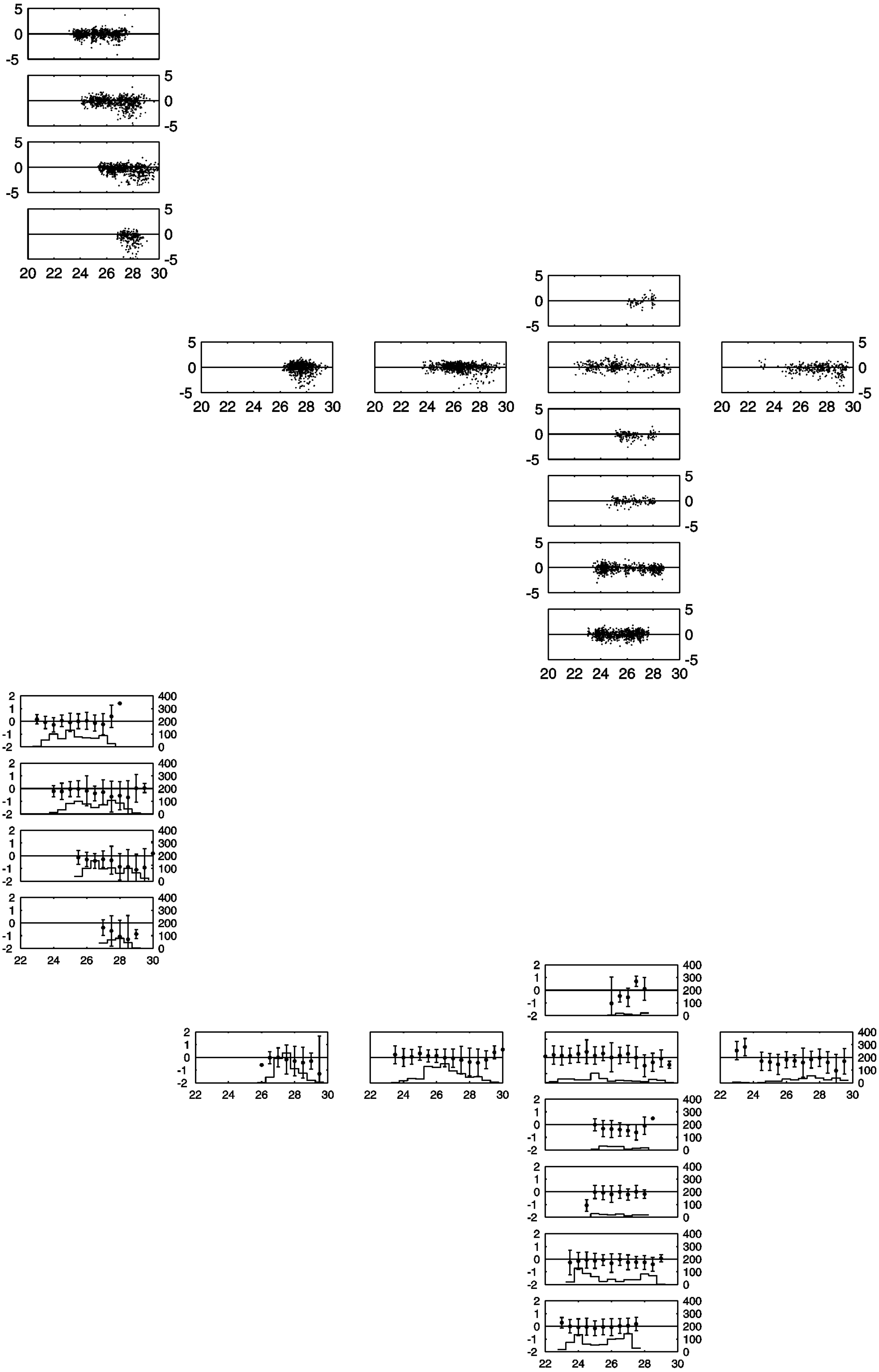

Figure 4.15 – Dependence of wind speed residual (Buoy – TMI 11 GHz) on the SST. (Upper panels) Scatterplots and (lower panels) number of data points, averages (points) and standard error (vertical lines) calculated in bins of SST of 0.5 °C

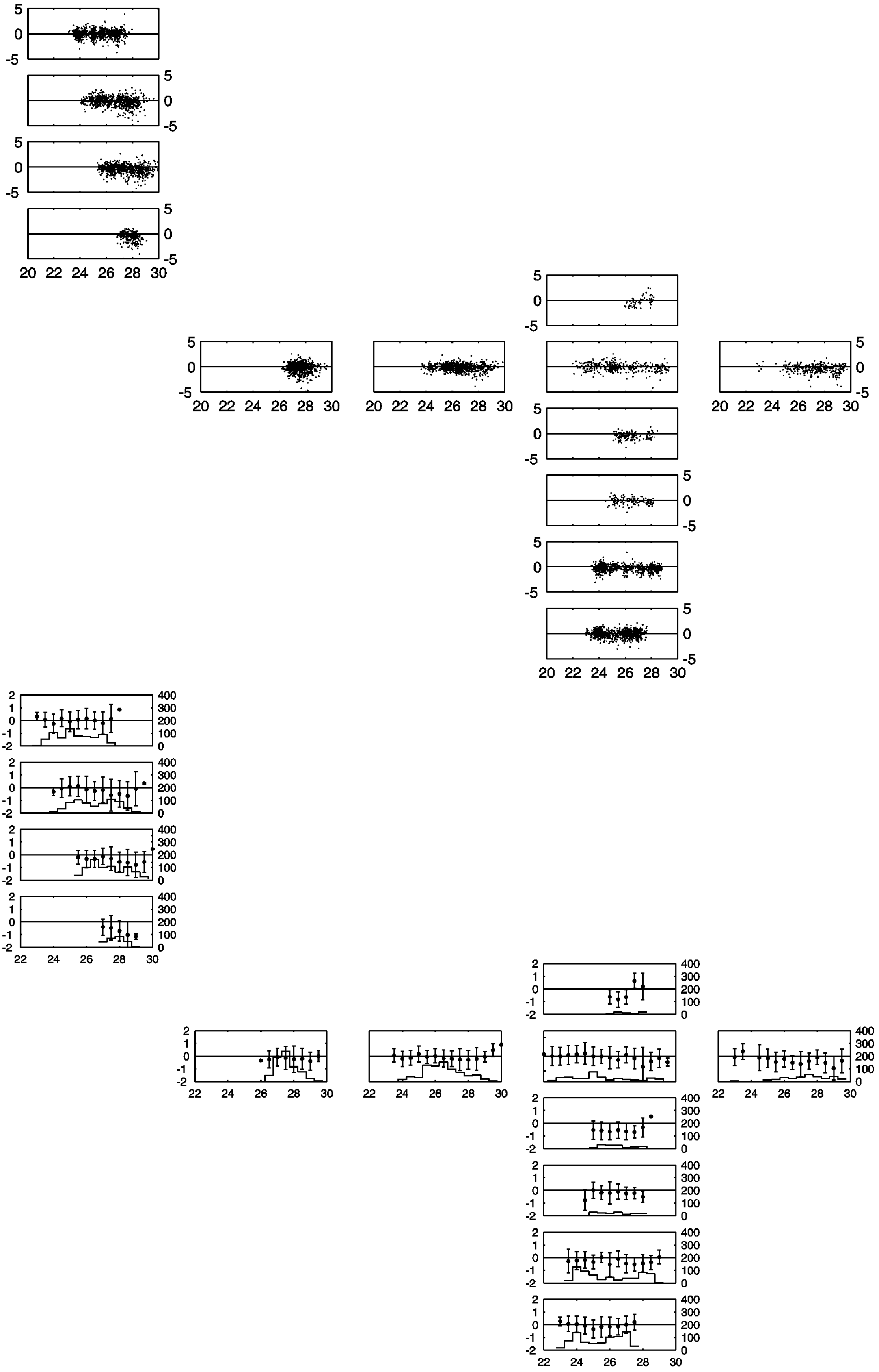

Figure 4.16 – Dependence of wind speed residual (Buoy – TMI 37 GHz) on the SST. (Upper panels) Scatterplots and (lower panels) number of data points, averages (points) and standard error (vertical lines) calculated in bins of SST of 0.5 °C

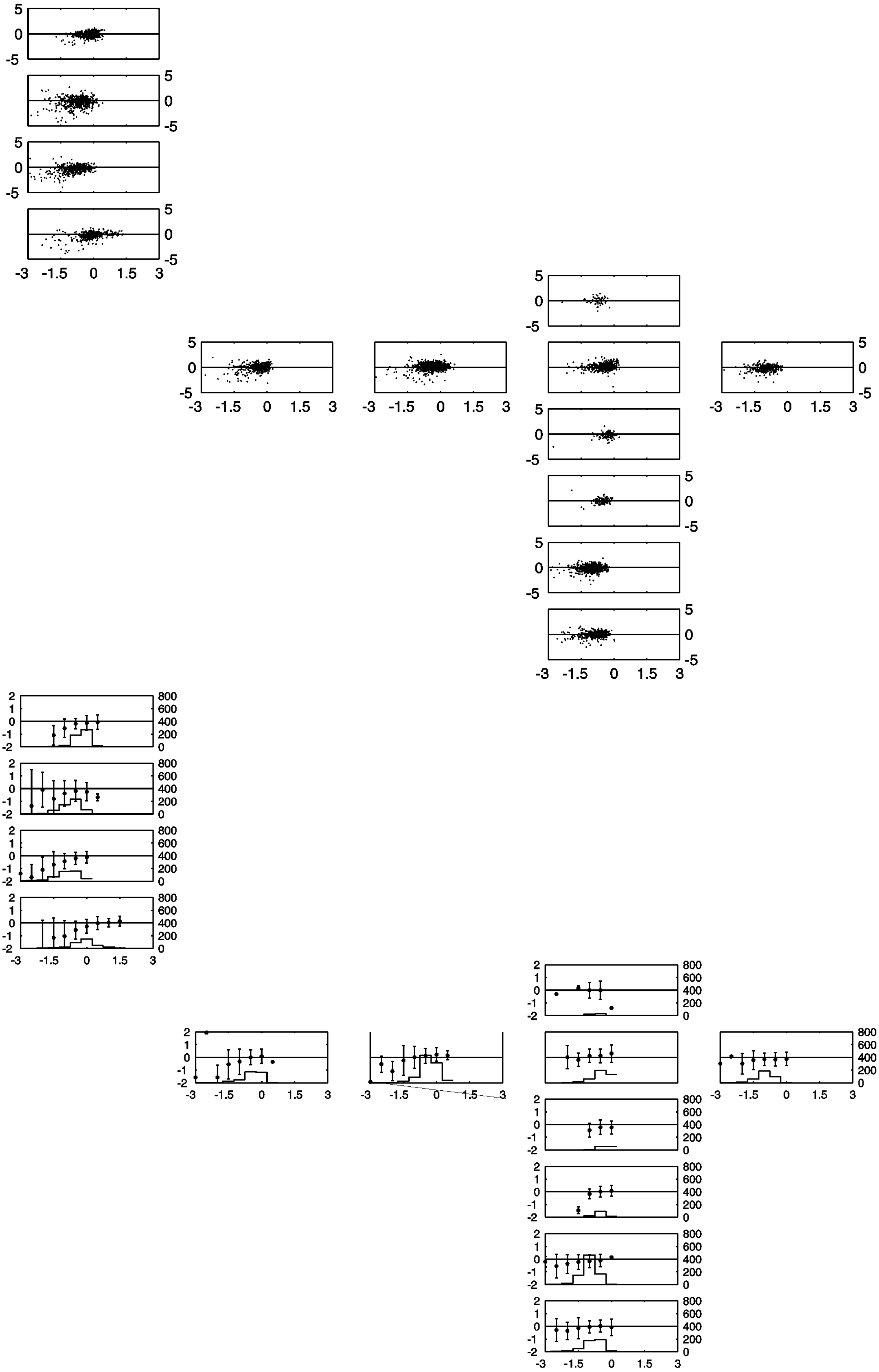

Figure 4.17 – Dependence of wind speed residual (Buoy – QuikSCAT) on the air-sea temperature difference. (Upper panels) Scatterplots and (lower panels) number of data points, averages (points) and standard error (vertical lines) calculated in bins of air-sea temperature difference of 0.5 °C

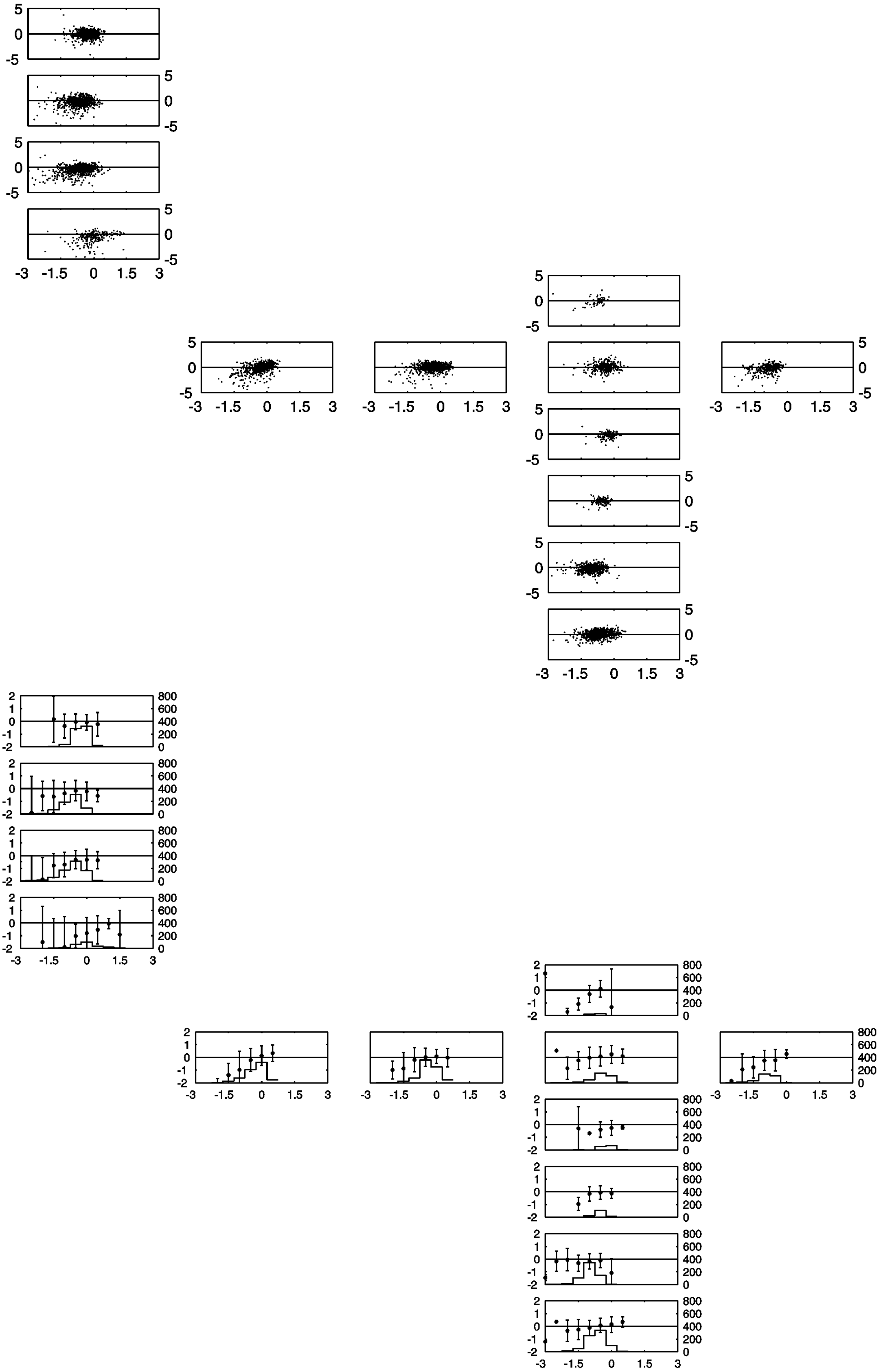

Figure 4.18 – Dependence of wind speed residual (Buoy – TMI 11 GHz) on the air-sea temperature difference. (Upper panels) Scatterplots and (lower panels) number of data points, averages (points) and standard error (vertical lines) calculated in bins of air-sea temperature difference of 0.5 °C

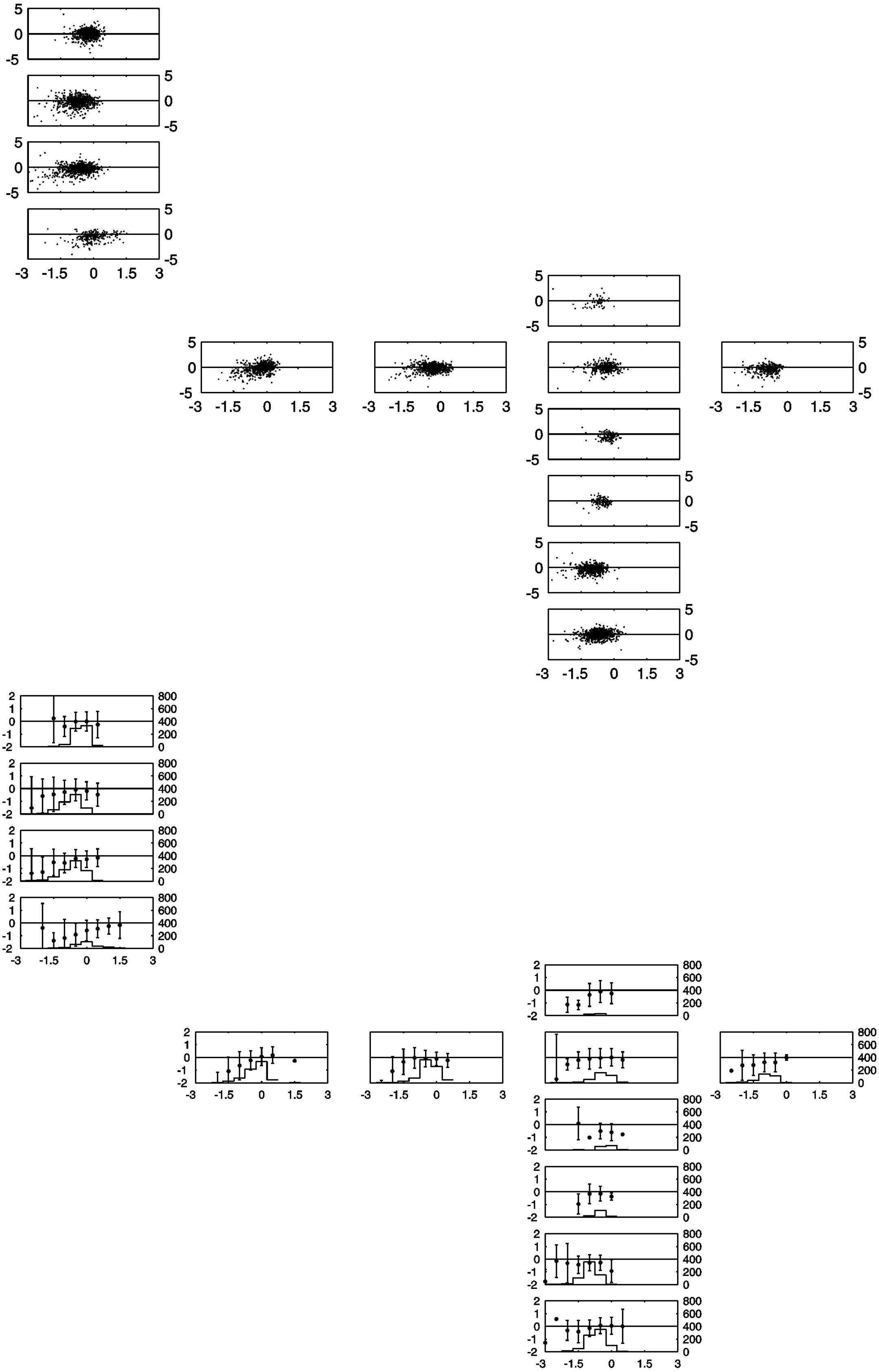

Figure 4.19 – Dependence of wind speed residual (Buoy – TMI 37 GHz) on the air-sea temperature difference. (Upper panels) Scatterplots and (lower panels) number of data points, averages (points) and standard error (vertical lines) calculated in bins of air-sea temperature difference of 0.5 °C

4.4 Sea surface temperature

As stated before, SST is of vital importance as a boundary condition for numerical weather prediction, climate modelling, ocean circulation, and air-sea interaction studies. Nowadays, this variable can be measured with very good accuracy, either by *in situ* sensors or satellites. However, the measurements by *in situ* and satellite sensors each suffer from a number of drawbacks. Buoy measurements do not have the global coverage offered by satellites, and microwave SST measurements, in particular, are limited by errors such as decreased sensitivity at high wind speeds and by a relatively poor spatial resolution. However, by combining the advantages of each of the measurements, e.g., high temporal resolution for *in situ* measurements and high spatial coverage for satellite products, the studies that attempt to integrate both datasets are expected to be of considerable importance.

Nevertheless, validation of the data is necessary in order to verify the quality of the dataset. The main consideration to take into account in validation is the depth to which the measurements refer. The temperature difference across the skin layer has direct relevance to both remote sensing of SST and interactions between the ocean and atmosphere (Castro et al., 2003). For heat flux calculations, it is critical to use the actual skin SST because the main heat exchanges between the atmospheric and oceanic boundary layers occur in the top 10 to 100 μm of the ocean surface.

This section shows the result of the comparison between the SST datasets used in this study: buoy-measured at 1 metre, skin-derived, and TMI retrievals. Like the validation of the wind dataset in the previous section, the satellite-based (TMI) and buoy data are collocated within 30 min and 25 km of each other. The skin SST is derived from the SST measured by the sensor fixed at the moored buoys, using Zeng et al. (1999) algorithm as described in Section 3.3.2. The validation of the skin-derived SST is necessary because the algorithm used for this purpose has its coefficients set to the tropical Pacific region, and this is the first attempt to use a product derived from it in the tropical Atlantic region.

It is important to recall that the skin SST is the temperature of the top 10 μm of the sea surface. TMI measures the integrated temperature of the top 1.2 mm and it is believed to represent the SST at the base of the skin SST layer. However, only during periods when the wind speed is below 6 ms^{-1} are significant skin deviations and warm layer effects expected to occur, while at higher wind speeds the small differences may be accounted for by assuming a skin temperature deviation of 0.17 K, as suggested by Donlon et al. (2002).

Figure 4.20 shows the comparison between buoy-measured and skin-derived SST, as well as the dependence of ∆T (skin – buoy) on the buoy wind speed. The results show a very good agreement between both datasets and with a mean bias around –0.20 °C. As this is the first assessment of Zeng's bulk-to-skin algorithm for the PIRATA array, this result is very important as it has considerable observational evidence to confirm it (Schluessel et al., 1990; Fairall et al., 1996; Wick et al., 1996; Donlon and Robinson, 1997; 1998; Zeng et al., 1999; Donlon et al., 2002).

From these results, it is possible to make observations about the behaviour of Zeng's bulk-to-skin model. Although this model only uses "bulk" temperature and wind speed to derive skin SST, it seems to be very reliable as the dependence of ∆T on wind speed follows the theoretical and observational expected pattern. The skin SST has a cold bias in relation to the SST for a typical wind speed (> 5 ms^{-1}). At lower wind speeds, the stratification of the upper ocean layer may complicate the relationship. For those values, it is still possible to observe a slightly cooler skin SST. Because for this validation analysis the time of the day is not taken in account, on average the skin SST is expected to be colder than SST for all wind speed values (Figure 4.20b). For daytime data only, the plot shows the expected shape of the curve, with skin-derived temperature warmer than SST at 1-metre (Figure 4.20c). For nighttime data only, SST at 1-metre is colder that the average for low wind speed (3 ms^{-1}).

Figure 4.21 shows the comparison between buoy-measured and skin-derived SST for each individual buoy, and Table 4.4 summarises statistics. Bias in the table is calculated as skin SST minus SST at 1-metre. The outliers observed in the scatterplots for buoys at latitudes of 8° N and 15° N, longitude 38° W are due to a bad adjustment of the algorithm for a specific subset of the data. A more detailed inspection (not shown) demonstrated that they refer to only one specific day. However, the cause of the bad adjustment could not be identified. These "bad" data have been excluded from all future analyses.

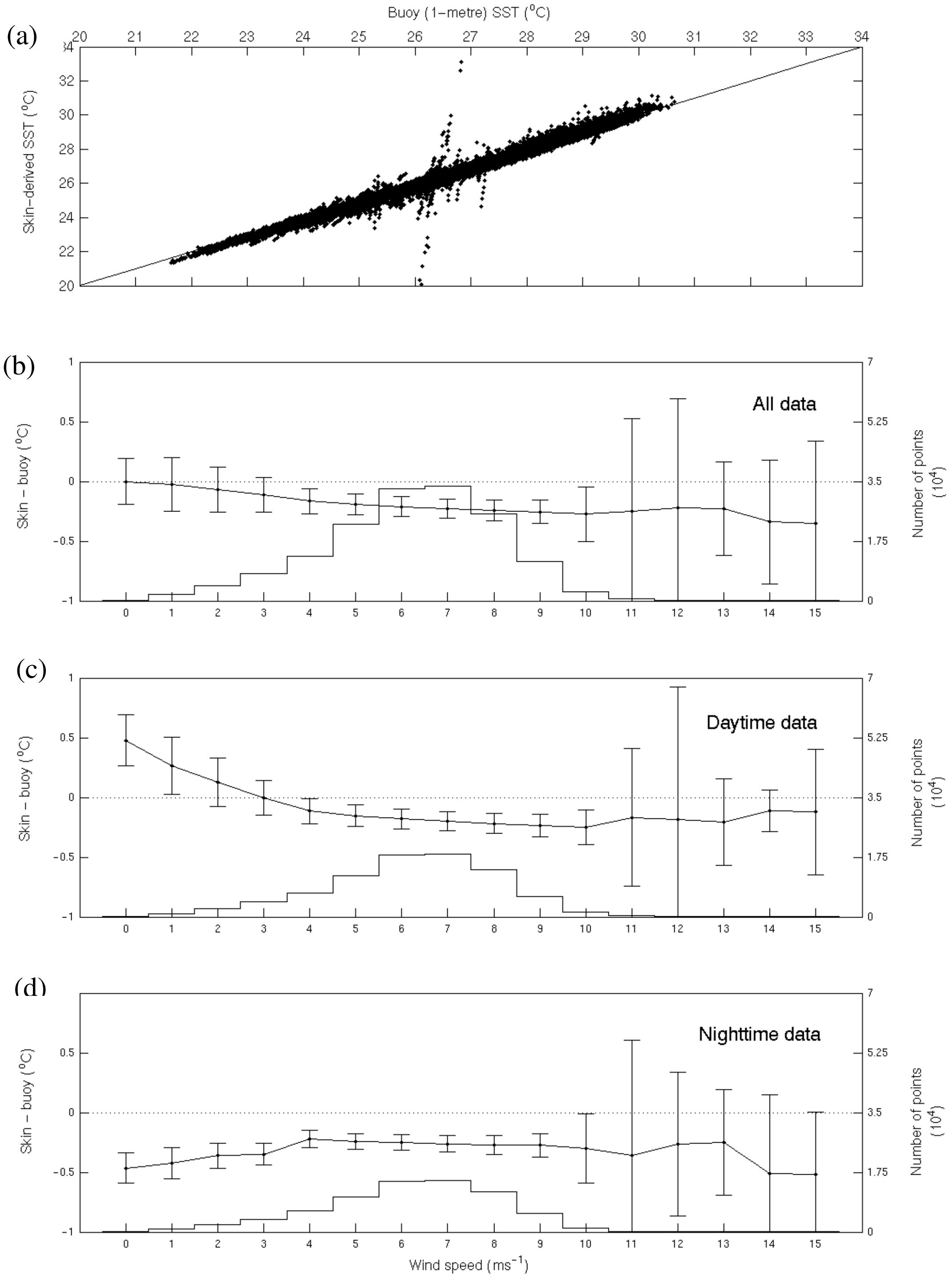

Figure 4.20 – (a) Comparison between buoy-measured SST at 1 metre and skin-derived SST. (b) Dependence of ΔT (skin – buoy) on buoy wind speed with number of data in units of 10^4 (histogram), averages (points) and standard error (vertical lines) calculated in bins of buoy wind speed of 1 ms^{-1} for all data. (c) As (b) but only for daytime data. (d) As (b) but only for nighttime data (d).

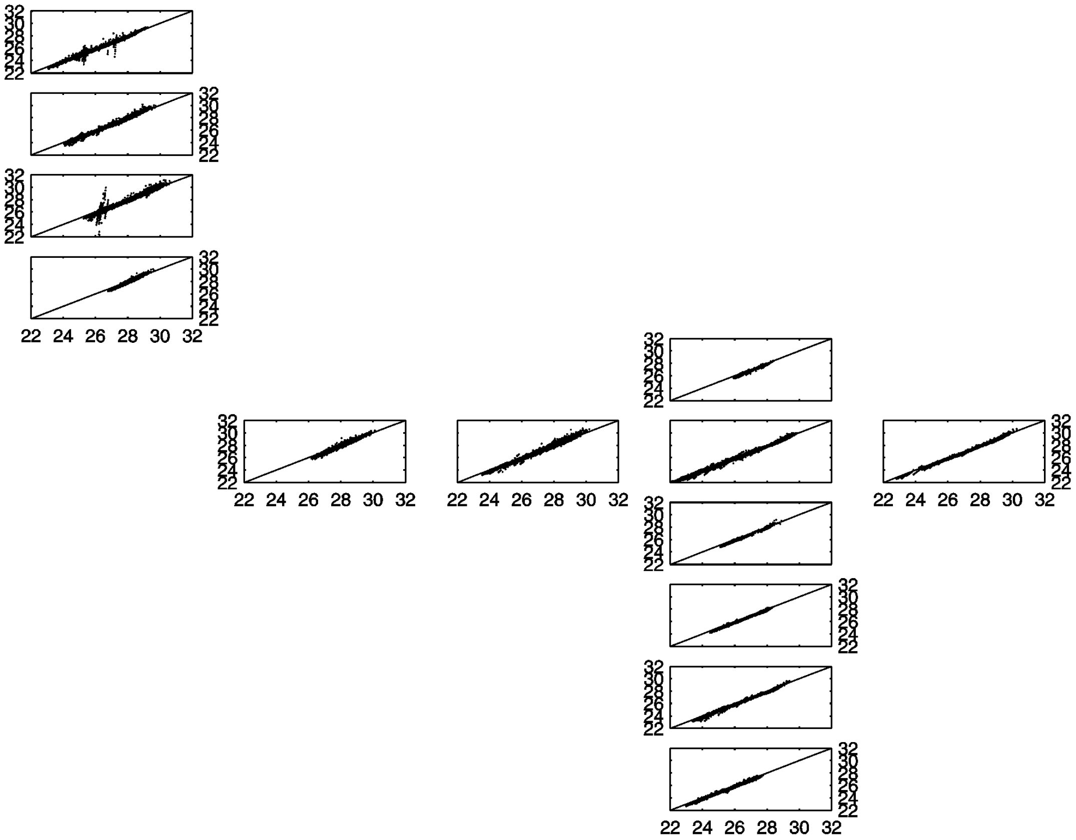

Figure 4.21 – Comparison between buoy-measured SST (X axis) at 1 metre and skin-derived SST (Y axis) for each individual buoy.

Table 4.4 – Statistics of comparison between SST and skin-SST (°C)

Buoy	r^2	rms diff	bias	No. obs.
0N 0W	0.9962	0.2094	-0.1894	7670
0N 10W	0.9957	0.2263	-0.1884	8867
0N 23W	0.9895	0.2261	-0.1775	18586
0N 35W	0.9772	0.2256	-0.1953	18399
10S 10W	0.9967	0.2358	-0.2231	17589
12N 38W	0.9925	0.2454	-0.2152	15540
15N 38W	0.9928	0.2548	-0.2308	18424
2N 10W	0.9828	0.2153	-0.1927	1553
2S 10W	0.9897	0.2198	-0.1960	2973
4N 38W	0.9695	0.2196	-0.1969	9514
5S 10W	0.9934	0.2304	-0.2143	3304
6S 10W	0.9977	0.2342	-0.2196	14406
8N 38W	0.9743	0.2854	-0.2085	20458

igure 4.22 shows the mean ΔT (skin SST - SST) plotted as a function of the buoy wind speed and binned at intervals of 1 ms^{-1}. Error bars show ± 1 standard error. Its results support the information presented in Table 4.4. The investigation of these results did not show any particular regional biases linked to the calculation of skin-SST.

The comparison between the buoy-measured and satellite SST is shown in Figure 4.23. In these analyses, ΔT is TMI minus buoy dataset. The sensors installed at the buoys measure warmer temperatures (~ 0.09 °C). Comparisons made by Chelton et al. (2001) between TMI and TAO SST showed ΔT (TMI – buoy) with a small positive bias (~ 0.15 °C), indicating that buoys measured colder temperatures. Their results report ΔT with an opposite sign of that presented above. As they used a former version of the TMI dataset than used in the present work, but also provided by Remote Sensing Systems, it is suggested here that their results show wind speed effects on the microwave brightness temperature that had not been completely removed in the first TMI SST retrieval algorithm. The results shown here clearly indicate that the dataset processed with the new version of the algorithm produced a much better result.

It is important to notice, however, that TMI SST appears to overestimate the SST at higher temperatures, over 28° C. As higher concentrations of water vapour can be expected at higher temperatures, this bias could indicate either an inaccuracy of the 21-GHz channel in correcting SST for water vapour biases or inability to account for absorption of the 10.6-GHz channel. But this could simply indicate that TMI has an error dependent on SST. Either way, this dependence on higher temperatures requires further investigation.

Figure 4.24 shows the comparison between buoy SST and TMI SST for each individual buoy, and the results are summarised in Table 4.5. Bias in Table 4.5 is TMI minus buoy SST. The agreement between the two datasets is very good with low rms difference values, and agree well with previous results (Stammer et al., 2003; Donlon et al., 2004). The buoys positioned at (2°N, 10° W), (0°N, 35°W) and (4°N, 38°W) do not yield such good results. The problem at the first of the locations is clearly due to small numbers of matchups. The other two problem locations have a small bias but the largest rms differences. One possible explanation could be that these two locations have the highest values of SST for the entire region. Because the TMI seems to overestimate the SST at higher temperatures, the difference between the matchups becomes higher and the relation between the datasets is poorer. Also, these poorer results observed for the buoys at (2°N, 10° W), (0°N, 35°W) and (4°N, 38°W) can also indicate different sampling periods, where distinct oceanic and climatic conditions might influence the instrument measurements, as mentioned in Section 4.2.

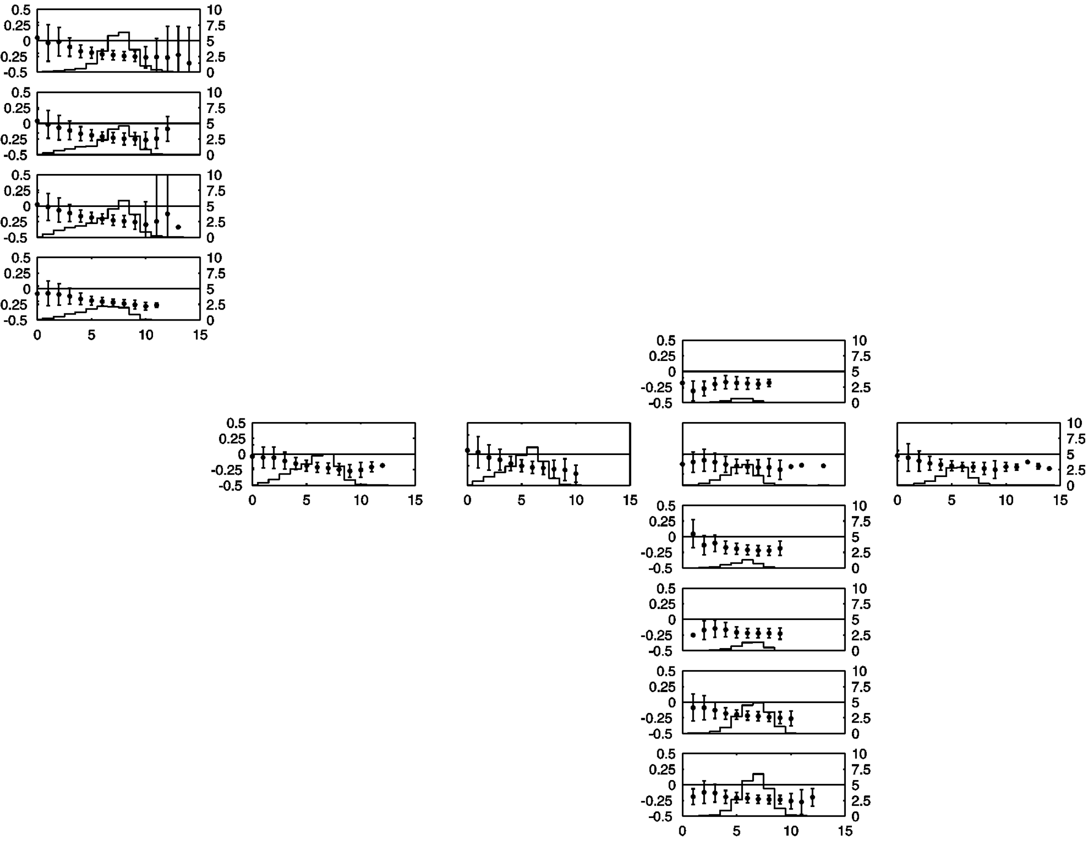

Figure 4.22 - ΔT (skin SST – SST) as function of buoy wind speed.
Number of data points (right-Y axis) in 10^3 units, averages (points) and standard error (vertical lines) calculated in bins of buoy wind speed of 1 ms^{-1}.

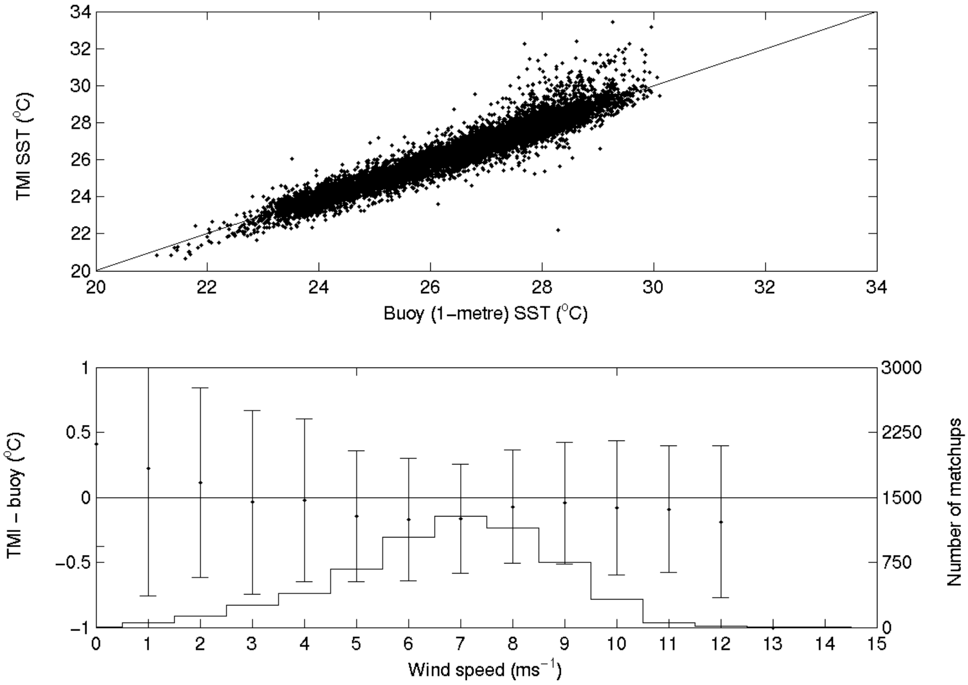

Figure 4.23 – Comparison between buoy-measured SST at 1 metre and TMI SST (upper panel). Dependence of ΔT (TMI – buoy) on buoy wind speed with number of data (histogram), averages (points) and standard error (vertical lines) calculated in bins of buoy wind speed of 1 ms^{-1} (lower panel).

The mean ΔT (TMI - buoy) has been plotted as a function of the buoy wind speed and binned at intervals of 1 ms^{-1} (Figure 4.25). Error bars show ± 1 standard error. It can be seen that, as observed for the difference between skin SST and buoy data, there is a tendency of TMI SST to be warmer than buoy SST for low wind speed. The graphs indicate, and are supported by the values in Table 4.5, that the bias for TMI minus buoy data (~ -0.09 °C) is smaller than the bias for skin SST minus buoy (~ -0.2 °C). This can be accounted for largely by a skin temperature deviation of around 0.14 °C (Donlon et al., 1999; Donlon et al., 2002)

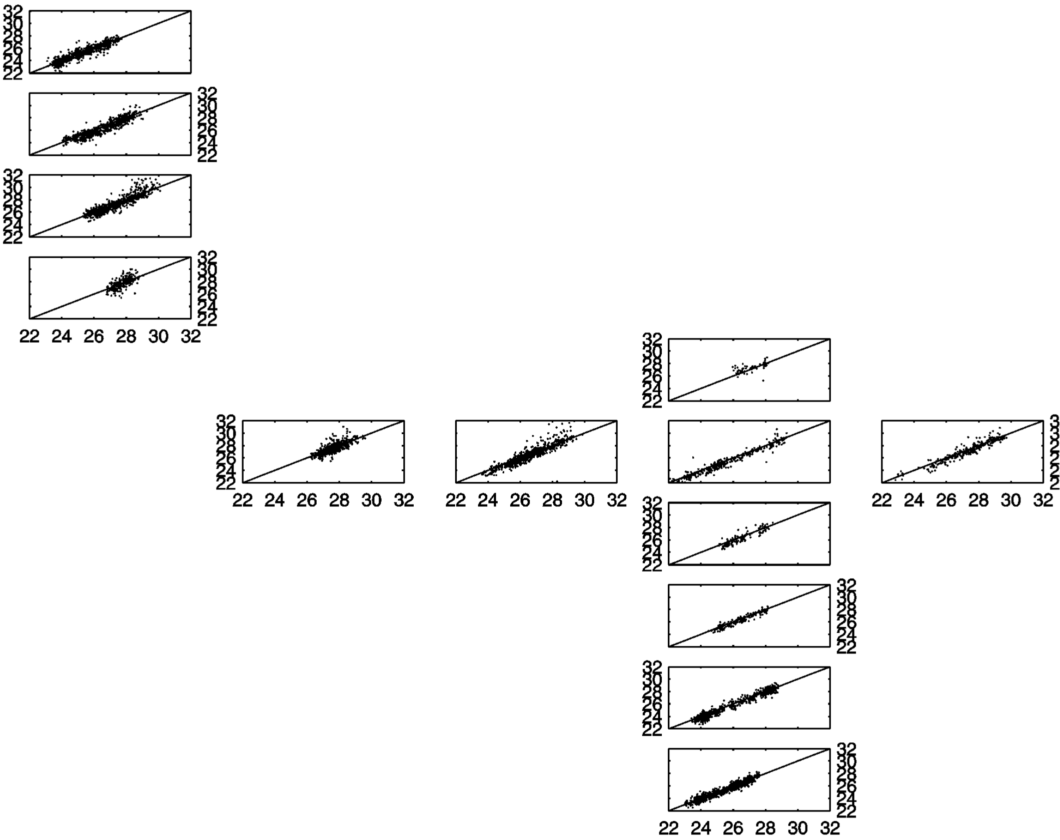

Figure 4.24 – Comparison between buoy-measured SST (X axis) at 1 metre and TMI-retrieved SST (Y axis) for each individual buoy.

Table 4.5 – Statistics of comparison between SST and TMI (^{o}C)

Buoy	r^2	rms diff	bias	No. obs.
0N 0W	0.9069	0.4994	-0.1417	298
0N 10W	0.9455	0.5059	-0.2214	336
0N 23W	0.8357	0.6113	-0.0988	765
0N 35W	0.6234	0.4963	-0.0469	682
10S 10W	0.9257	0.3789	-0.0839	763
12N 38W	0.8649	0.5339	-0.1936	671
15N 38W	0.8551	0.4611	-0.0313	676
2N 10W	0.3724	0.6482	0.1934	57
2S 10W	0.8234	0.4799	-0.1969	126
4N 38W	0.4771	0.6453	-0.0442	240
5S 10W	0.9028	0.3610	-0.1534	139
6S 10W	0.9533	0.4318	-0.1664	617
8N 38W	0.8139	0.5923	-0.0536	764

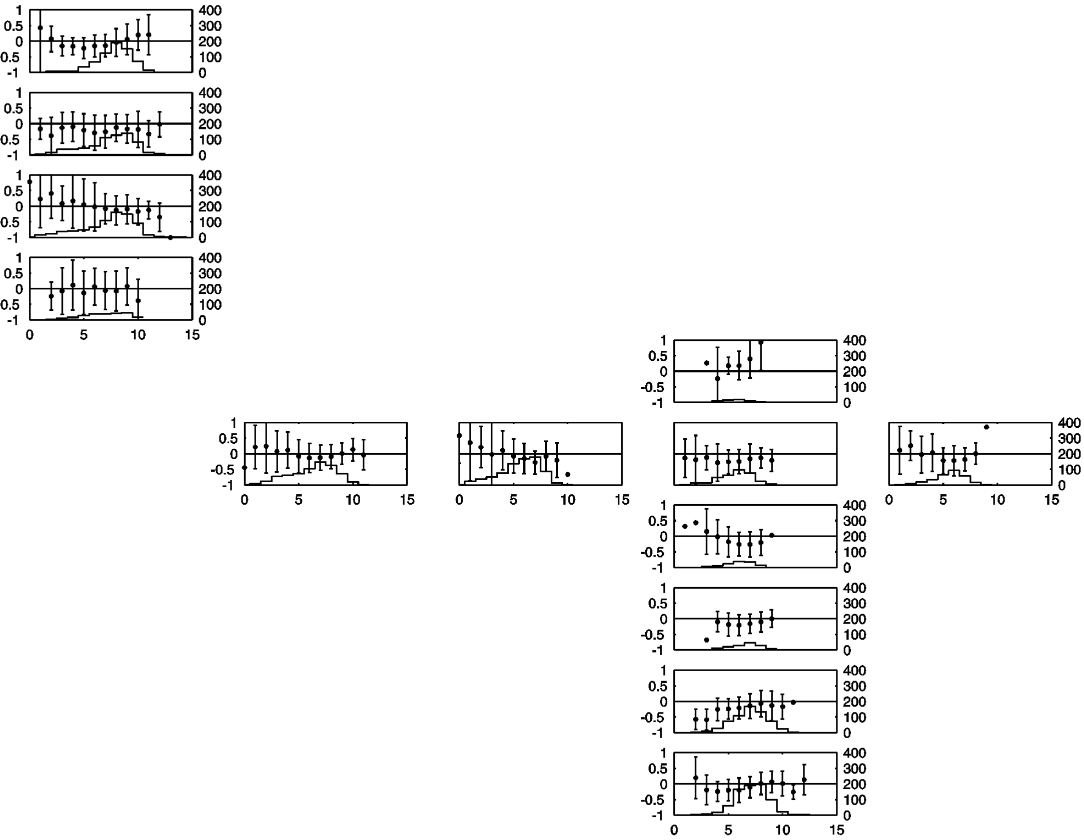

Figure 4.25 - ΔT (TMI – buoy) as function of buoy wind speed. Number of data points (right-Y axis), averages (points) and standard error (vertical lines) calculated in bins of buoy wind speed of 1 ms^{-1}.

In order to complete the assessment among the temperature datasets, Figure 4.26 show the results for the comparison between TMI SST and skin SST. In this analysis, ΔT is TMI minus skin SST. Overall, the TMI has a warm bias of around 0.11 °C when compared with the skin SST dataset, which is consistent with Donlon et al. (2002). The analysis of ΔT (TMI – skin SST) as a function of buoy wind speed indicates that there is no systematic dependence of ΔT on wind speed. At low wind speeds, the behaviour of ΔT is similar to typical and high wind speeds, which could indicate that in this situation it is very likely that the skin and sub-skin layer of the ocean are warmed up by the same degree. It is possible that the skin SST may heat up more than the sub-skin under low winds, although the results shown in Figure 4.26 show that, on average for low winds, sub-skin is warmer that skin. These small differences are due to competing effects of heating and cooling at the surface, and there is not enough detailed information and understanding of these processes, which makes these results particularly significant since there are few comparisons of skin and sub-skin showing the relationship between these two layers.

The analysis of comparison between TMI SST and skin-derived SST for each individual buoy is presented in Figure 4.27, and statistics are summarised in Table 4.6. Bias in Table 4.6 is TMI SST minus skin SST. As for the preceding analysis between TMI SST and buoy (1-metre) SST, the agreement between these two datasets is also good. Once again, the buoys situated at (2°N, 10°W), (0°N, 35°W) and (4°N, 38°W) yield a poorer result, possibly due to the same characteristics: few matchups for (2°N, 10°W) and the overestimation of the SST by the TMI. And as highlighted in Section 4.2, this could also be due the influence of distinct oceanic conditions that affect the buoys located at different regions of the basin. Figure 4.28 shows the dependence of ΔT (TMI – skin) on buoy wind speed. Error bars show ± 1 standard error. No systematic dependence on wind speed has been observed in this analysis.

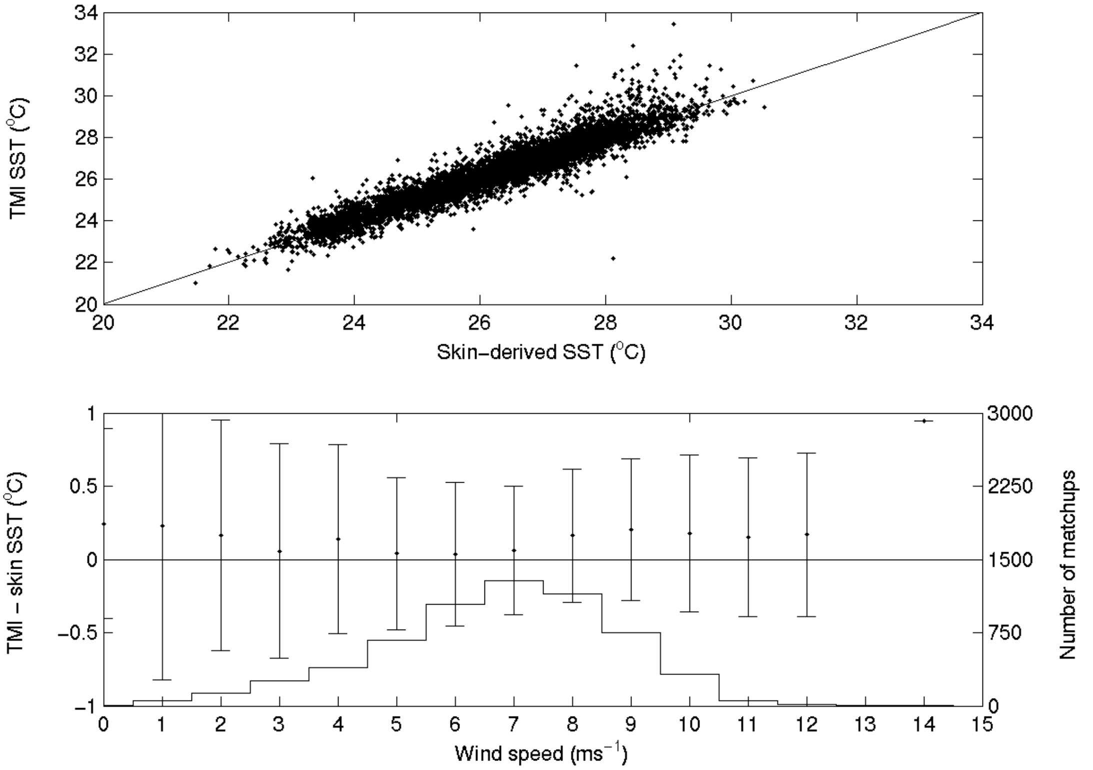

Figure 4.26 – Comparison between skin-derived SST and TMI SST (upper panel). Dependence of ΔT (TMI – skin) on buoy wind speed with number of data (histogram), averages (points) and standard error (vertical lines) calculated in bins of buoy wind speed of 1 ms^{-1} (lower panel).

Table 4.6 – Statistics of comparison between TMI-retrieved and skin-SST (^{o}C)

Buoy	r^2	rms diff	bias	No. obs.
0N 0W	0.8955	0.5052	0.0497	298
0N 10W	0.9389	0.4819	-0.0295	336
0N 23W	0.8199	0.6226	0.0849	765
0N 35W	0.5921	0.5365	0.1463	682
10S 10W	0.9175	0.4136	0.1391	763
12N 38W	0.8519	0.5231	0.0183	671
15N 38W	0.8436	0.5185	0.1972	676
2N 10W	0.3492	0.7496	0.3798	57
2S 10W	0.8075	0.4540	0.0006	126
4N 38W	0.4516	0.6738	0.1702	240
5S 10W	0.8880	0.3592	0.0661	139
6S 10W	0.9461	0.4293	0.0607	617
8N 38W	0.8011	0.6227	0.1605	764

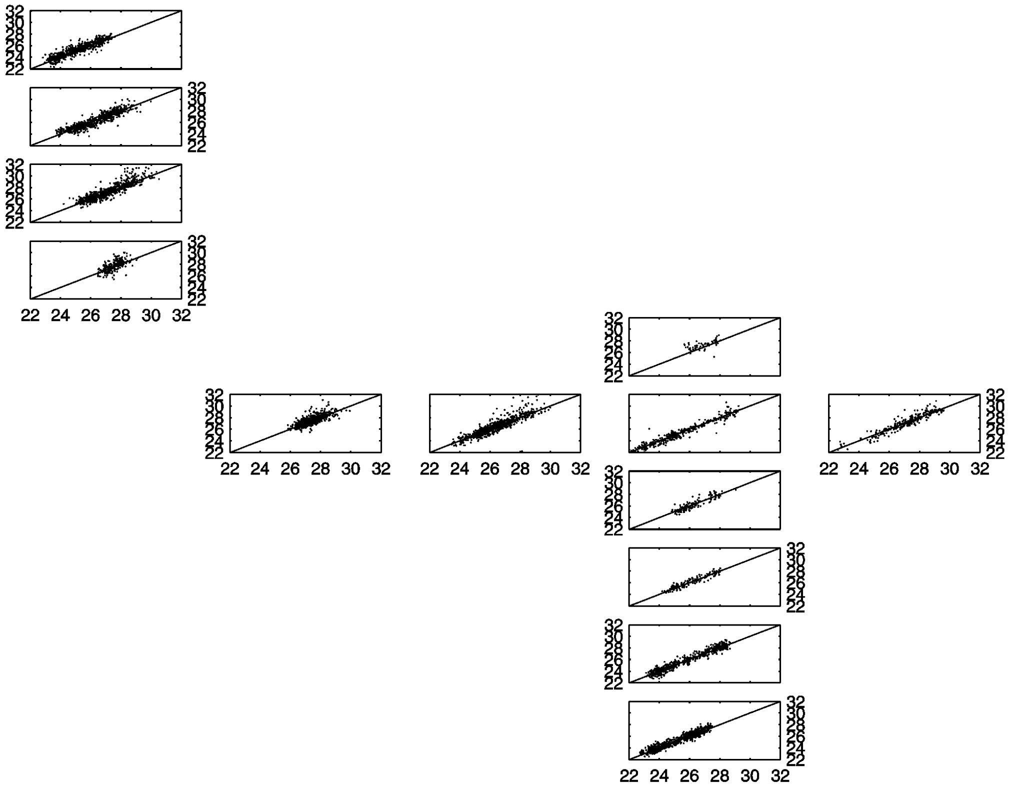

Figure 4.27 – Comparison between skin-derived SST (X axis) and TMI-retrieved SST (Y axis) for each individual buoy.

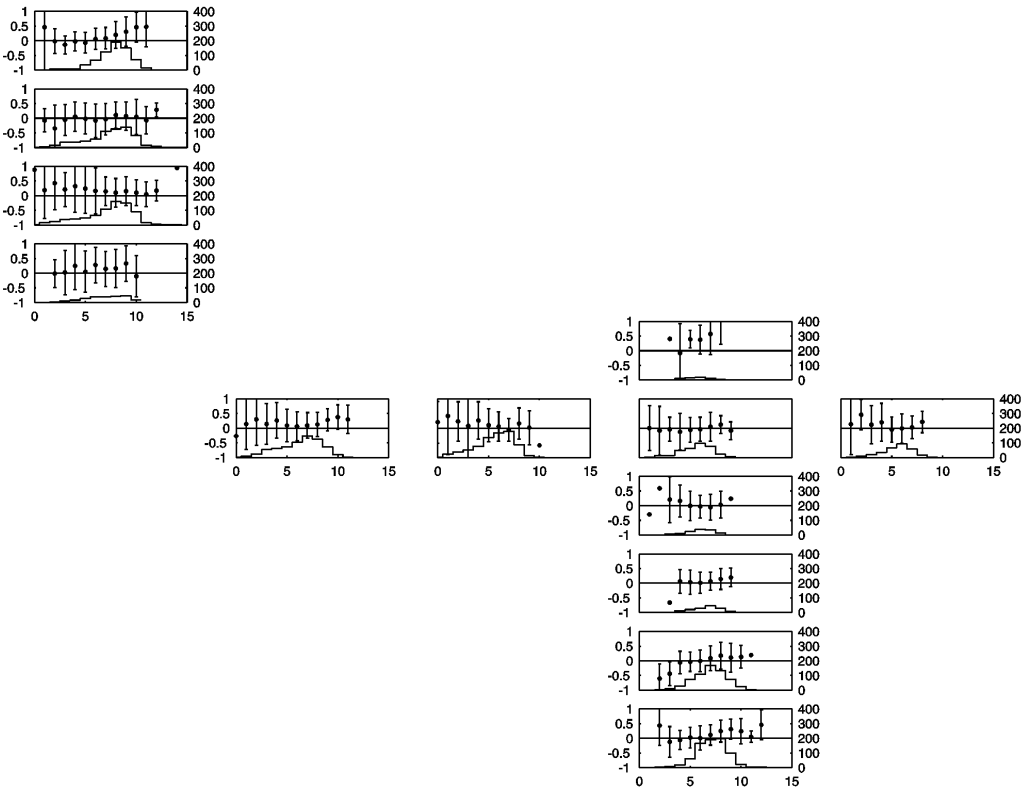

Figure 4.28 - ΔT (TMI – skin SST) as function of buoy wind speed. Number of data points (right-Y axis), averages (points) and standard error (vertical lines) calculated in bins of buoy wind speed of 1 ms^{-1}.

4.5. Heat fluxes

As shown in Section 4.1, there is very good agreement between satellite-based and in situ wind data, which would enable the filling of gaps in the in situ wind time series with satellite-based winds in order to extend the length of the heat flux time series. However, the error introduced in the heat flux calculations would be a disadvantage. With the aim of estimating the sources of error in the turbulent heat fluxes due to typical errors in the bulk variables (SST, wind speed, air temperature and relative humidity), we followed the procedure described by Cronin and McPhaden (1997), and summarised below.

The bulk flux algorithm was run sequentially, substituting the values of SST, wind, air temperature (Tair) and relative humidity (RH) by adding up and subtracting the respective instrument accuracy as shown in Table 3.1. The errors listed in Table 4.7, were then computed as one-half the rms difference between the flux time series estimated with values of SST, wind, Tair and RH added up by the respective instrument accuracy, and the flux time series estimated with values of SST, wind, Tair and RH subtracted by the respective instrument accuracy. Errors due to inadequate parameterisation are not included, so these error estimates of the turbulent fluxes should be considered as lower bounds. Equation 4.1, where F are the calculated fluxes time series, as function of wind speed (*w*), SST (*t*), air temperature (*tair*), and relative humidity (*rh*), *a1, a2, a3, a4* are the accuracy of the instruments measuring wind, SST, air temperature and relative humidity, respectively, and *n* is the number of observations, summarises the approach used.

$$\frac{1}{2}\left(\frac{\sum[F(w+a1,t+a2,tair+a3,rh+a4)-F(w-a1,t-a2,tair-a3,rh-a4)]^2}{n}\right)^{1/2} \qquad (4.1)$$

Latent heat flux (Q_{lat}) is sensitive primarily to errors in relative humidity and to a lesser extent to errors in air temperature and wind speed. Sensible heat flux (Q_{sen}) is most sensitive to measurements of air temperature. These errors for latent and sensible heat flux are highlighted in bold in Table 4.7. These results are corroborated by those found by Cronin and McPhaden (1997). They presented similar values for most of the variables, and the main differences are for latent flux errors associated with inaccuracy of air temperature and relative humidity measurements. However, it is important to remember that those results are based on a 4-month time series for only one buoy in the tropical Pacific, whereas this thesis covers 12 buoys over 4 years.

Through the results observed at Tables 4.1 – 4.3 in Section 4.1 when satellite-retrieved wind speed is compared with *in situ* data, and results of the effect of bulk variables on turbulent heat flux, it is possible to say that the use of satellite-retrieved wind speed data to fill gaps in the wind speed series is acceptable. The mean bias between satellite-retrieved wind speed and *in situ* data is of the same order as the accuracy of the buoy wind speed sensor. Since the heat fluxes are more sensitive to relative humidity and air temperature, the errors that could be introduced by the satellite-retrieved wind speed would not have a large impact on the fluxes. Therefore, the impact of using satellite-retrieved wind speed on turbulent heat fluxes should be minimal.

Table 4.7 – Rms difference of Q_{lat} and Q_{sen} associated with errors in the measurement of bulk variables.

Buoy	SST		Wind		Tair		RH	
	Q_{lat}	Q_{sen}	Q_{lat}	Q_{sen}	Q_{lat}	Q_{sen}	Q_{lat}	Q_{sen}
0N 0W	0.09	0.03	4.87	0.45	5.33	**1.84**	**12.91**	0.02
0N 10W	0.09	0.03	3.46	0.28	5.03	**1.81**	**12.00**	0.01
0N 23W	0.09	0.03	3.58	0.29	5.16	**1.79**	**12.44**	0.02
0N 35W	0.10	0.03	4.40	0.34	5.98	**2.01**	**15.03**	0.02
10S 10W	0.11	0.03	6.06	0.34	5.76	**2.33**	**15.01**	0.01
12N 38W	0.11	0.04	5.55	0.39	5.38	**2.45**	**16.50**	0.02
15N 38W	0.11	0.04	4.89	0.20	6.42	**2.51**	**16.63**	0.01
2N 10W	0.09	0.03	4.37	0.42	5.32	**1.82**	**12.81**	0.02
2S 10W	0.09	0.03	3.41	0.17	5.40	**1.85**	**13.05**	0.01
4N 38W	0.11	0.03	4.93	0.42	6.49	**2.17**	**16.77**	0.02
5S 10W	0.10	0.03	5.10	0.23	5.79	**2.13**	**14.59**	0.01
6S 10W	0.11	0.03	6.32	0.45	5.82	**2.31**	**15.07**	0.02
8N 38W	0.12	0.04	5.99	0.49	6.53	**2.38**	**16.97**	0.02

4.6. Summary

The use of satellite data plays an essential role in studies of large scale dynamics. And more and more, these datasets are being used in operational forecast, where they are assimilated into models for climate prediction. Therefore, the accuracy of satellite-retrieved data became an important issue, which requires an appropriate validation. By acknowledging the importance of validation processes in pursuing data of higher quality, this chapter shows the results of validating the satellite data against the in situ data used in this work. It also takes into account that distinct oceanic and climatic conditions observed in different regions where the buoys are located, can influence the instrument measurements.

Overall, the wind dataset agrees well with buoy observations, with no observed systematic dependence on the atmospheric and oceanic conditions. It showed, however, that for low wind speeds, large biases are present. This would suggest that the algorithms used for wind retrieved by satellite are not working well in oceanic regions with low winds.

SST dataset validation present important results as this is the first study that uses Zeng et al. (1999) bulk-to-skin algorithm for the tropical Atlantic region. Furthermore, it also shows the improvements made by the re-processing of TMI data, included in the data version 3.

The results here presented show that skin SST, derived using Zeng's model, has a colder bias of around 0.20 ^{o}C in relation to the buoy SST, measured at 1-meter depth. This imply that the model, which only uses "bulk" temperature and wind speed to derive skin SST, is reliable as there has been considerable observational evidence to confirm it. The comparison between TMI and skin SST shows that TMI SST has a warm bias of around 0.11 ^{o}C, with no systematic dependence of ΔT (TMI – skin SST) on wind speed, which would indicate that it is very likely that the skin and sub-skin layer are warmed up by the same degree. This is still a hot topic of research as the understanding of the processes involved is not clear yet.

Wind speed time series are problematic for the calculation of turbulent heat fluxes due to frequent gaps. In order to evaluate if these time series could be filled in by satellite retrieved wind speed, without effect on the heat fluxes, it was necessary to assess what are the sources of errors in the calculation of those heat fluxes. The analyses showed that latent heat flux (Q_{lat}) is sensitive primarily to errors in relative humidity and to a lesser extent to errors in air temperature and wind speed. Sensible heat flux (Q_{sen}) is most sensitive to measurements of air temperature. As the mean bias between satellite-retrieved wind speed and in situ data, as shown in Section 4.3, is of the same order as the accuracy of the buoy wind speed sensor, the errors that could be introduced by the satellite-retrieved wind speed would not have a large impact on the fluxes. This result indicates that it is possible to fill in the wind speed time series gaps with satellite derived wind speed.

Chapter 5

Diurnal cycle in the tropical oceans

5.1. Introduction

Meteorologists studying the tropical regions have noted for a long time the existence of daily variations of a variety of weather elements including wind, cloudiness, rainfall, and barometric pressure over the open ocean. Semidiurnal fluctuations have been identified most prominently in sea level pressure records (Hamilton, 1981), but also in the tropospheric zonal winds (Williams et al., 1992), light rain and associated stratiform cloudiness.

Diurnal variations over the tropical oceans are strongly present in heavy rainfall and deep convective cloudiness, with an early morning maximum in most regions (Gray and Jacobson Jr., 1977). Recently, the large scale nature of the diurnal rainfall cycle over the tropical oceans has been revealed by global satellite data (Hendon and Woodberry, 1993; Imaoka and Spencer, 2000; Sorooshian et al., 2002).

The investigation of the diurnal cycle, in particular of SST, has become top of the agenda for the oceanography scientific community, as it is more aware of the importance of the diurnal cycle. However, for some regions, such as the tropical Atlantic, the complete understanding of this topic, taking into account shape, phase and seasonality of the diurnal cycle, is yet to be fully investigated. As mentioned in Section 1.3, this chapter will present and assess the results of the analyses of the diurnal cycle of met-ocean variables and heat fluxes in the tropical Atlantic, observed using the PIRATA dataset. First, in Section 5.2, the relevant literature on diurnal variability will be introduced as a way to identify the possible gaps of knowledge, and highlighting what will be investigated in this study.

5.2. Current knowledge of the diurnal cycle

5.2.1. Winds

Little is known about the magnitude and spatial patterns of the daily surface wind variations over the open ocean in the tropics. Research programmes such as the Global Atmospheric Research Program (GARP) Atlantic Tropical Experiment (GATE) and the Barbados Oceanographic and Meteorological Experiment (BOMEX) gathered useful but limited information on daily wind changes in the tropical Atlantic (Nitta and Esbensen, 1974; Gray and Jacobson Jr., 1977; Jacobs, 1978; Albright et al., 1981). They demonstrated the diurnal variations in the vertical profile of horizontal wind divergence and the related inferred upward motion of daily variations in the deep convective activity. However, these previous studies were restricted to some regions of the tropical Atlantic, thus they cannot be considered as a complete representation of the wind diurnal cycle in the region.

Diurnal wind variations at island stations in the western tropical Pacific were first examined by Hastenrath (1972). Another study in the Pacific was pursued by Williams et al. (1992), who documented the variations of the vertical structure of the diurnal zonal wind at Christmas Island in the central equatorial Pacific. Another two of the few studies available on the subject of the daily wind variability over the equatorial Pacific are those by Halpern (1987) and Deser and Smith (1998).

Deser and Smith (1998) showed a complete picture of the diurnal and semidiurnal variations of the surface wind field over the tropical Pacific using the TAO array data set. They relate the diurnal meridional wind variations along the equator to the diurnal cycle of the deep convection in the ITCZ to the north of the equator. In particular, surface wind divergence along the equator (which is dominated by the meridional component) exhibited a pronounced diurnal cycle, with the strongest divergence in the early morning time when the deep convection in the ITCZ is at its maximum.

Dai and Deser (1999), in a global analysis of diurnal variations of surface wind and divergence fields show that, over the ocean, the amplitude of the diurnal cycle is about 0.3 – 0.4 m/s for both the wind speed and the wind direction components and varies little from winter to summer. Over the tropical Atlantic and eastern and central portions of the tropical Pacific, a zonally coherent pattern exists with maximum convergence (divergence) north (south) of the equator in the morning around 09:00 – 12:00 LST. This is generally similar to the latitudinal profile of the mean daily divergence, being indicative of an enhancement of the local Hadley cell around 10:30 LST relative to the daily mean.

5.2.2. Sea Surface Temperature

A diurnal thermal cycle is well known to occur in the upper ocean whenever the solar heating at midday exceeds the heat loss from the ocean surface (Imberger, 1985). In the absence of wind effects, solar heating produces strong warming within a very thin surface layer. Observational studies (Price et al., 1986) have shown that diurnal signals can be detected in the thermocline due to ensuing processes of turbulence, water mass stratification, kinetic energy dissipation, and vertical mixing. These processes are primarily linked to the daytime warming due to solar insolation, the nighttime cooling due to longwave radiation, and the wind forcing. All these phenomena lead to diurnal variation of SST.

Until the seventies, it was generally assumed that diurnal temperature variations at the sea surface in the open ocean were small. Bruce and Firing (1974), however, observed that under light winds (2 – 4 m/s) a shallow layer (1 to 2 m) was 2^{o}–3^{o}C warmer than the main mixed layer underneath. Further research (Wick et al., 1996) pointed out that the intense diurnal warming of the surface of the ocean commonly occurs in low wind conditions, when the wind-driven turbulence is insufficient to erode the near surface stratification caused by the absorption of solar radiation.

The existence of a cool skin effect has been studied theoretically through models and empirically through observations. The cool skin is a layer in the upper few millimetres of the ocean caused by the combined cooling effects of the net longwave radiation, and the sensible and latent heat fluxes. The cool skin is almost always present, although its effect may be compensated by the presence of a warm layer. In the turbulent layer below the skin, a mixed layer is formed during the night due to free convection associated with heat loss from the sea surface and also to the forced convection caused by wind mixing (Kondo et al., 1979). During the day, roughly half the solar radiation reaching the sea surface is absorbed in the upper 2 m, and the warming leads to a stable stratified layer (warm layer). Therefore, one can affirm that the warm layer is a diurnal phenomenon. The upper warm layer is thinner in weaker wind conditions, and the temperature difference across the warm layer is also greater at these conditions (Fairall et al., 1996).

The bulk-skin temperature difference is highly variable. During the day it is larger than that during the night since the upper layer absorbs the solar radiation (Webster et al., 1996; Donlon and Robinson, 1997). It is showed that ΔT has a daytime mean value of 0.49 K ±0.39, and a nighttime mean value of 0.27 K ±0.28. However, their results do not agree with the results of Schluessel et al. (1990), which showed that the mean value of the bulk-skin temperature differences is about 0.3^{o} C during the night and 0.1^{o} C during the day. The different results are suggested to be partly due to different calibration of sensors used to measure skin SST, but mainly due to measurements taken in distinct regions. Although this thesis does not aim to study the skin-bulk difference as a topic, this stresses the necessity to study and acknowledge the regional differences of the diurnal cycle of SST.

Satellite thermal infrared measurements were compared with in situ data by Lynn and Svejkovsky (1984) during a period of two days and they found that the measurements differ significantly. However, Stramma et al. (1986), also using in situ data and model results, demonstrated conclusively that large diurnal warming seen in satellite-derived SST fields represents quite accurately the warming of the upper 1 m or so of the water column. They observed diurnal SST fluctuations of up to 3.5^{o}C from satellite data, in excellent agreement with in situ data from a thermistor at 0.6 m on a 2-year mooring.

One question demanding to be dealt with is the importance of resolving the diurnal cycle for correctly coupling the ocean and atmosphere for model predictions. The heat transfer between the atmosphere and the ocean is fundamental to the prediction of climate. Diurnal variations of SST may result in strong interaction of the ocean's surface layer with the overlying atmosphere through enhanced convection. The convective processes in the atmosphere, on the other hand, acts as a negative feedback by increasing the cloudiness and diminishing the net radiation that arrives at the sea surface (Webster et al., 1996).

In the tropical Pacific, many researches have been made considering the diurnal cycle (Flament et al., 1994; Bond and McPhaden, 1995; Zeng et al., 1999). Most were carried out in the tropical western Pacific (Lukas, 1991; Ravier-Hay and Godfrey, 1993; Soloviev and Lukas, 1997) where it is possible to find a large area characterised by high amplitudes of diurnal warming. In the tropical Atlantic, there is more uncertainty when we consider the diurnal cycle. What seems to be a lack of interest in the subject by the research community is probably owing to the lack of high-frequency SST data in the region that could make the basic research possible.

In the tropical Atlantic, most of the published works were undertaken in the Bermuda region where the largest warming zone in the north Atlantic (Bruce and Firing, 1974; Cornillon and Stramma, 1985; Stramma et al., 1986) seems to be located. In the eastern part of the tropical Atlantic, Halpern and Reed (1976) found diurnal warming amplitudes of up to 1.4^{o} C near the African coast in March. However, very little is known about differences of SST diurnal variability for the whole tropical Atlantic basin, especially when comparing data from similar sources, and common periods of measurements.

5.2.3. Air-sea fluxes

The diurnal cycle in the sea-air fluxes becomes important, especially under calm conditions and considerable insolation (Weller and Anderson, 1996). The diurnal variation of heat fluxes could have a significant impact on diurnal variation of clouds and precipitation. The enhancement of convection, and the reduction of the magnitude of the diurnal cycle, is responsible for the transition of tropical convection regimes from primarily continental to marine type. These effects were studied explicitly in the TOGA-COARE experiment (Slingo and Delecluse, 1999). An earlier study focusing on diurnal variation of air-sea fluxes in the tropical Atlantic was performed by Jacobs (1978), using the GATE dataset. The author showed that hourly flux values displayed modulations that are of the order of 20% of the mean value of the fluxes. Intra-diurnal variation in the total heat flux is approximately 47% of the variation of the total heat flux associated with the passage of an easterly wave disturbance in the region.

Numerical models commonly use daily to monthly mean sea surface bulk temperature, while near-surface wind, temperature, and humidity are usually updated at time step intervals of less than 1 hour (Zeng and Dickinson, 1998). These authors analysed the impact of diurnally varying temperature on surface fluxes. Use of either daily or monthly temperatures underestimates daytime latent heat flux by up 10 Wm^{-2} and sensible heat flux by 2 – 3 Wm^{-2} whereas at night latent and sensible heat fluxes are overestimated by 5 Wm^{-2} and 1 – 2 Wm^{-2}, respectively.

A commonly stated goal is that the surface energy balance of the tropical oceans must be known to within 10 Wm^{-2}, implying that the individual component fluxes must be known to accuracy better than 5 Wm^{-2} (Webster and Lukas, 1992). This is a difficult goal to achieve, even using in situ measurements of surface fluxes, because of instrumentation errors. Additionally, in situ measurements of ocean surface fluxes are very sparse and infrequent; consequently, because of the importance of episodic events like westerly wind bursts, sampling errors dominate the uncertainty even for values averaged over large space and time scales. Moreover, such poor sampling limits our understanding of the processes controlling these fluxes by precluding their observation at the scales on which they vary. Hence, it is desirable to determine all of the components of the surface heat and momentum balances from satellite observations.

Most previous satellite determinations of one or two components of the sea surface heat fluxes have been made for weekly or monthly timescales. Recently, attempts have been made to determine from satellite data the surface flux components on daily timescales or on scales that resolve the diurnal cycle. Chou et al. (1997) and Schulz et al. (1997) have determined daily values of the surface turbulent heat fluxes. Rossow and Zhang (1995) have determined all the components of the surface radiative fluxes on a timescale of 3 hrs for a spatial scale of 280 km.

Clayson and Curry (1996) and Curry et al. (1999) also determined values of turbulent fluxes of momentum, sensible, and latent heat on scales of 50 km and 3 hrs. By comparing the satellite-derived surface fluxes with in situ measurements, they found that the difference between them is dominated by satellite sampling; these are reduced when some averaging is done. Nevertheless, the fluxes are determined with a useful accuracy, even at the highest temporal and spatial resolution they have been derived.

It is important to notice that only the research performed by Jacobs (1978) was made in a restricted region of the tropical Atlantic. There is a lack of comparisons focusing on diurnal variability in different regions of the tropical Atlantic basin. Other researches, e.g., Webster et al. (1996) and Zeng and Dickinson (1998), were performed in the tropical Pacific, where there is a well developed understanding of the subject. Since the bulk formulae are also used in numerical models to calculate fluxes from the basic model variables, and all the bulk parameterisation formulae have their coefficients set and tuned for the tropical Pacific, it becomes necessary to understand the impact of those formulae in the calculation of diurnal variability in the tropical Atlantic, as suggested by WGASF (2000).

5.3. Diurnal variability in the Tropical Atlantic

5.3.1. Mean diurnal cycle

For this study on the diurnal variability in the tropical Atlantic, the full hourly data record of the PIRATA buoys have been used for each variable in each buoy. In order to compare the variability of the diurnal cycle in different locations at the tropical Atlantic, the daily mean of the variables have been removed from each location. This procedure was adopted to reduce the influence of the seasonal cycle in the tropical Atlantic. Once the daily mean was removed, the mean diurnal cycle of the residual was calculated, which is basically, for each hourly time step, the long term average of the deviation of the referred hour to the daily mean. For simplicity, this will be referred to this work as the mean diurnal cycle.

As mentioned previously in Section 4.2 and shown in Figure 3.3, the record lengths of the buoys time series are not the same. Also the sampling period for each of the buoys varies. With exception of the buoys located at 2^oN 10^oW and 2^oS 10^oW, all the other buoys have time series of approximately 1 year long for most of the variables. Wind speed time series are particularly problematic with gaps. Nevertheless, the number of days averaged should produce acceptable mean diurnal cycles for those variables. Also, the removal of the daily mean for each hourly time step reduces the influence of the low frequency signals, as the seasonal and interannual cycles.

Figure 5.1 shows the mean diurnal cycle for the measured SST at 1-metre (T_B) and derived skin-SST (T_S), calculated following Zeng et al. (1999), as explained in Section 3.3.2. Figure 5.1 follows the schematic diagram shown in Appendix A. The diurnal cycle of T_B presents a peak of maximum at mid-afternoon, around 15:00 hrs, and a minimum at around 08:00 hrs in all buoys. The mean diurnal cycle of T_S follows the same pattern but with a sharper rise of temperature from mid-morning until it reaches its maximum. The maximum and minimum of T_S is generally one hour before T_B. It is important to notice that these results are not evidence that T_S is warmer than T_B at mid-afternoon, although this can happen in calm and sunny conditions. The graphs illustrate that T_S has a larger deviation from its daily mean. Table 5.1 summarises the amplitude of the SST diurnal cycle for all the locations. The amplitude of the diurnal cycle of T_S increases toward the Equator and varies from 0.35 to 0.70 °C, while that of observed T_B has a similar spatial pattern but smaller amplitudes (from 0.17 to 0.41 °C). The diurnal amplitude of T_S is largest over the central and eastern Atlantic (rather than over the western Atlantic warm pool) because the diurnal amplitude of observed T_B reaches its maximum there. However, the T_S/T_B ratio of diurnal amplitude is still larger over the warm pool. Although amplitudes are smaller at (0°N 35°W), this higher ratio could indicate a larger influence on T_S for wind of similar magnitude.

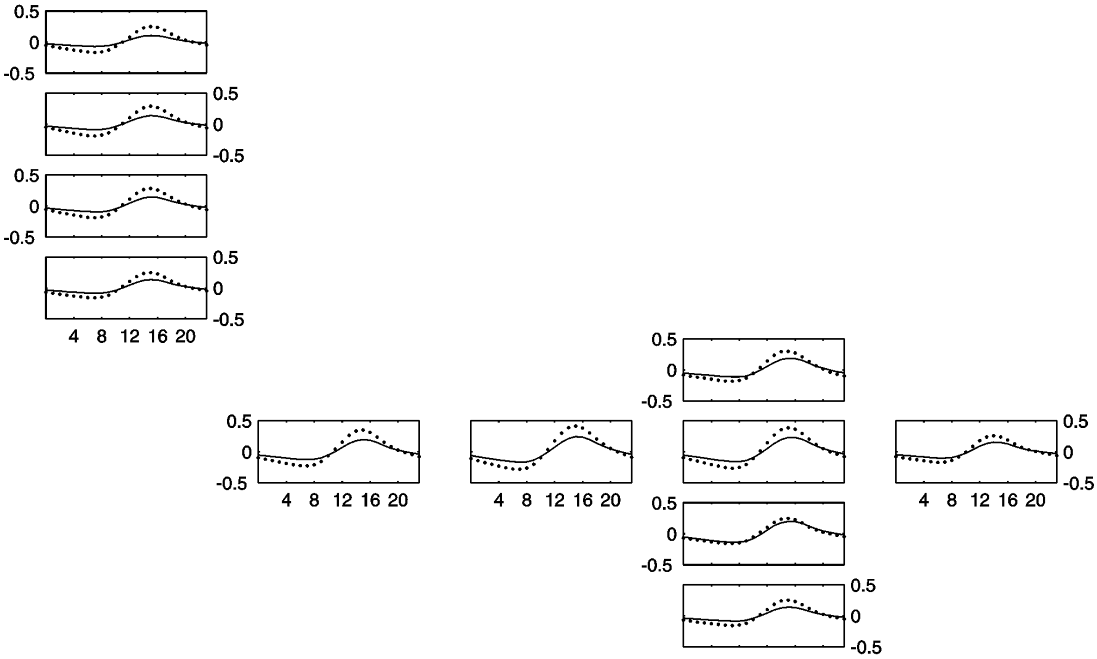

Figure 5.1 – T_B (solid line) and T_S (dotted line) mean diurnal cycle in the tropical Atlantic. Y-axis shows values in °C. X-axis is given in hours.

As can be observed, wind speed has a diverse diurnal variability through the tropical Atlantic basin (Figure 5.2). The buoys located at the western side of the basin and along the meridional line of 38° W tend to present a strong semidiurnal signal, with peak of maxima in the early morning and night, while the buoys located at the eastern side do not have or have a much weaker semidiurnal signal, with their lowest values at early morning and maximum at late evening. The semidiurnal fluctuations of the zonal wind are well evident in all sites with maxima at around 04:00 hrs and 16:00 hrs (Figure 5.3). For zonal wind, positive (negative) values indicate westerly (easterly) winds relative to the daily mean. These results are very similar to those found by Deser (1994) and Deser and Smith (1998) for the tropical Pacific. They explain that the zonal wind acceleration is due to the well-known semidiurnal variation of the sea level pressure in the Tropics (Haurwitz and Cowley, 1973; Hamilton, 1980).

Table 5.1 – T_B and T_S diurnal amplitude and their ratio

Buoy	**T_B amplitude**	**T_S amplitude**	**Ratio T_S amp/ T_B ampl**
0N 0E	0.26	0.43	1.68
0N 10W	0.39	0.65	1.67
0N 23W	0.41	0.70	1.70
0N 35W	0.32	0.57	1.77
10S 10W	0.17	0.35	2.06
12N 38W	0.23	0.48	2.13
15N 38W	0.18	0.42	2.36
2N 10W	0.30	0.48	1.60
2S 10W	0.33	0.60	1.80
4N 38W	0.22	0.41	1.87
5S 10W	0.22	0.41	1.82
6S 10W	0.20	0.41	2.02
8N 38W	0.24	0.47	1.95

The mean diurnal cycle of the meridional wind is shown in Figure 5.4. For meridional wind, positive (negative) values indicate northerly (southerly) winds relative to the daily mean. For most of the locations, there is a reasonably strong diurnal cycle, with little semidiurnal variability. A general tendency of midday maxima north of the equator and evening maxima south of the equator can be observed.

This spatial variability observed for the mean diurnal cycle of wind raises a question: how can the mean diurnal cycle of SST be so similar in shape and phase in all the tropical Atlantic basin, when there is such variability in the mean diurnal cycle of wind speed? In Figure 5.5, the mean diurnal cycle of SST, skin SST and wind speed are selected for four locations, representing four regimes in the tropical Atlantic: (8°N 38°W), (0^{n}N 35°W), (0°N 0°E) and (10°S 10°W). In a first inspection, the locations for the western side of the basin seem to present a strong out-of-phase relationship between the mean diurnal cycle of wind speed and the mean diurnal cycle of SST and skin SST. This situation is not completely true for the other two locations on the eastern side. Moreover, for lower wind speed in the morning, one could expect that SST would peak earlier than other locations.

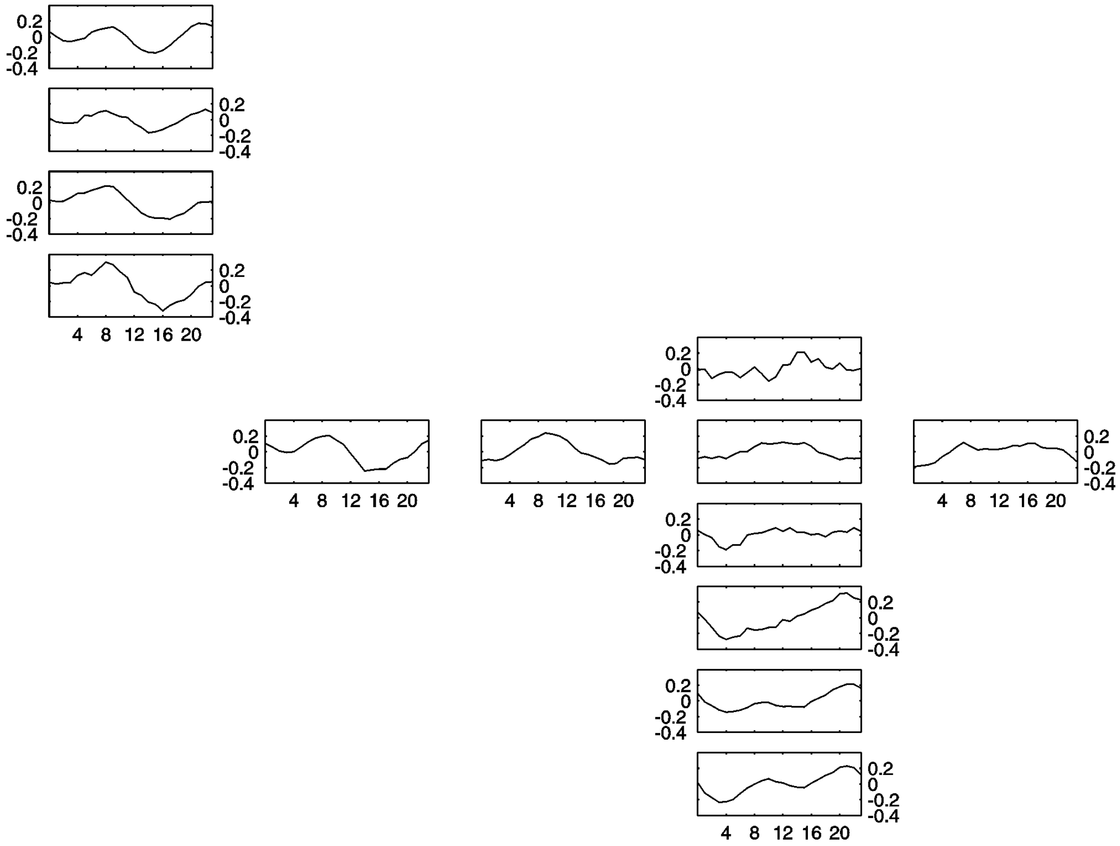

Figure 5.2 – Wind speed mean diurnal cycle in the tropical Atlantic.
Y-axis shows values in ms^{-1}. X-axis is given in hours.

However, if the relationship between the mean diurnal cycle of SST and wind change, here defined as ∂(wind)/∂t, is analysed, it is possible to observe a similar behaviour for all the locations (Figure 5.6). A comparable positive value in wind change can be observed at around 06:00 hrs. Also, a change of signal at around 08:00 hrs, indicating a reduction of the wind speed. In this case, it is suggested that the way at which the wind speed mean diurnal cycle changes would control the phase of the SST mean diurnal cycle, thus indicating that the morning winds are important in regulating the shape of the SST diurnal cycle. The results also suggest that the more negative the value of ∂(wind)/∂t at around 12:00 hrs, the higher the mid-afternoon amplitude. This indicate that, although the SST can react quickly to wind variations (Stuart-Menteth, 2004), the SST mean diurnal cycle will respond by the level of change in the wind speed.

Although the development of a parameterisation of the SST diurnal cycle is not one of the main objectives of this thesis, those results show that new parameterisation schemes could follow this approach. It is necessary to point out that this analysis is dealing with long term mean diurnal cycles and, therefore, different datasets could provide different results. Nevertheless, the results are encouraging since distinct datasets of buoys located at different regions on the basin provide similar results.

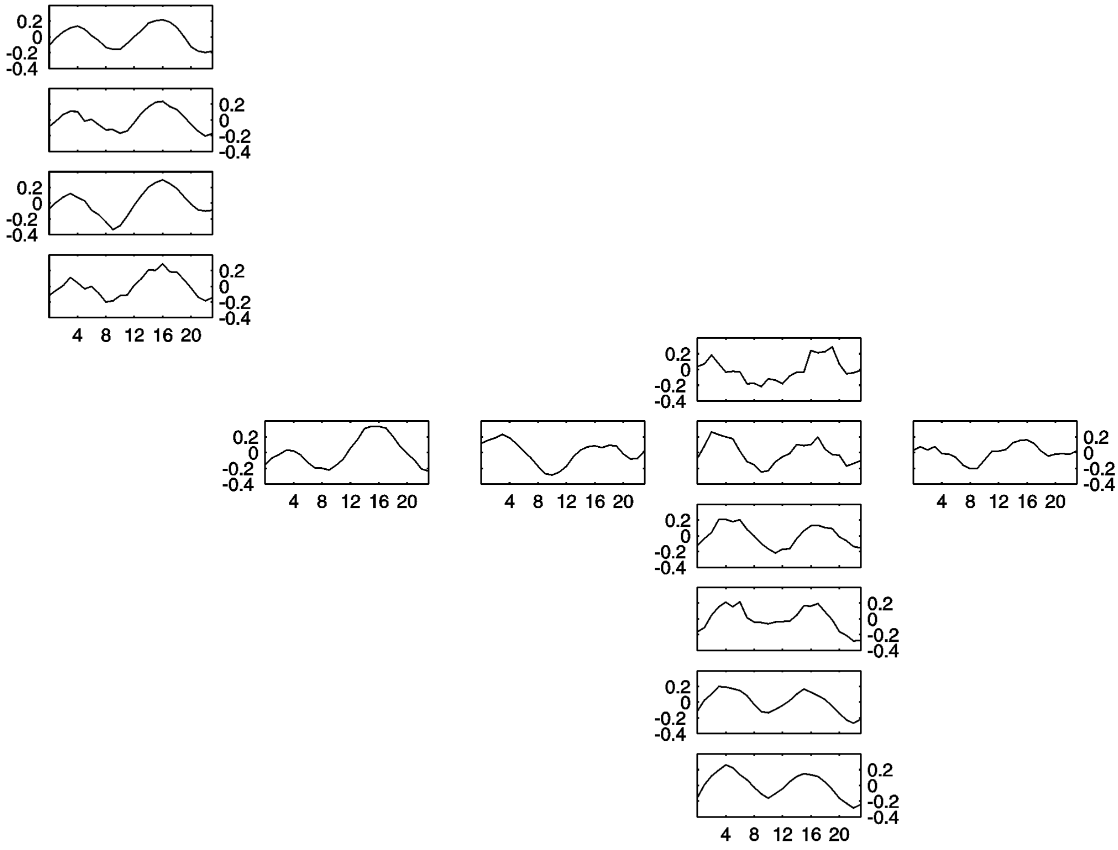

Figure 5.3 – Zonal wind mean diurnal cycle in the tropical Atlantic. Y-axis shows values in ms^{-1}. X-axis is given in hours.

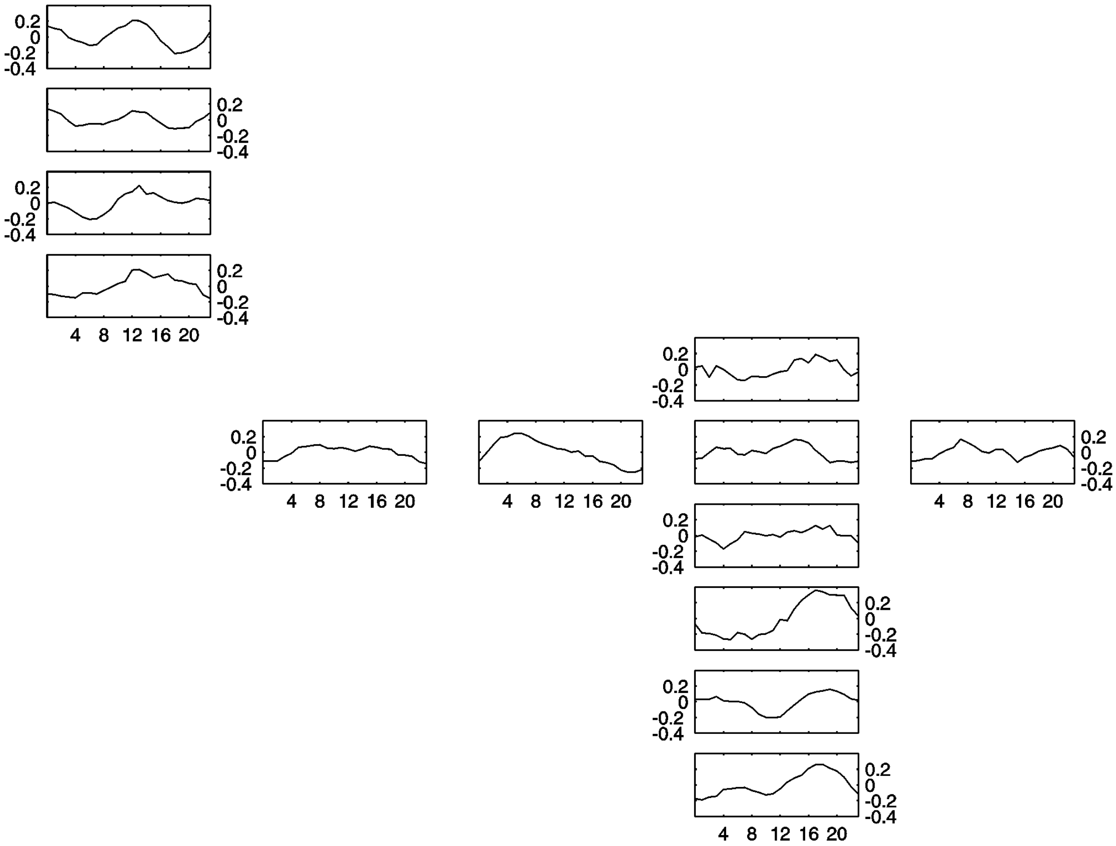

Figure 5.4 – Meridional wind mean diurnal cycle in the tropical Atlantic. Y-axis shows values in ms^{-1}. X-axis is given in hours.

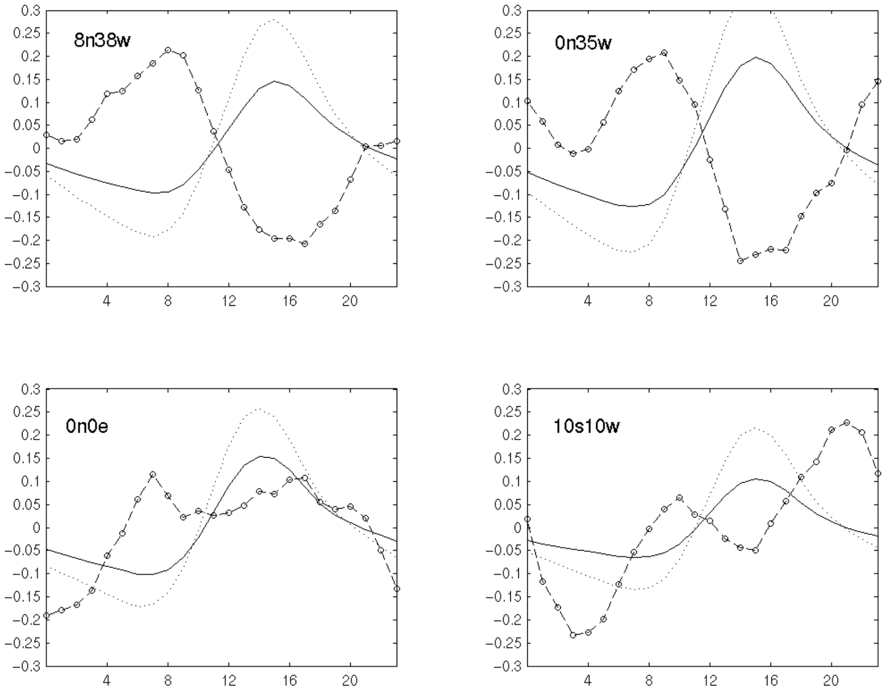

Figure 5.5 – Mean diurnal cycle of SST (solid), skin SST (dotted) and wind speed (dashed). Units are °C for SST and skin SST, and ms^{-1} for wind speed.

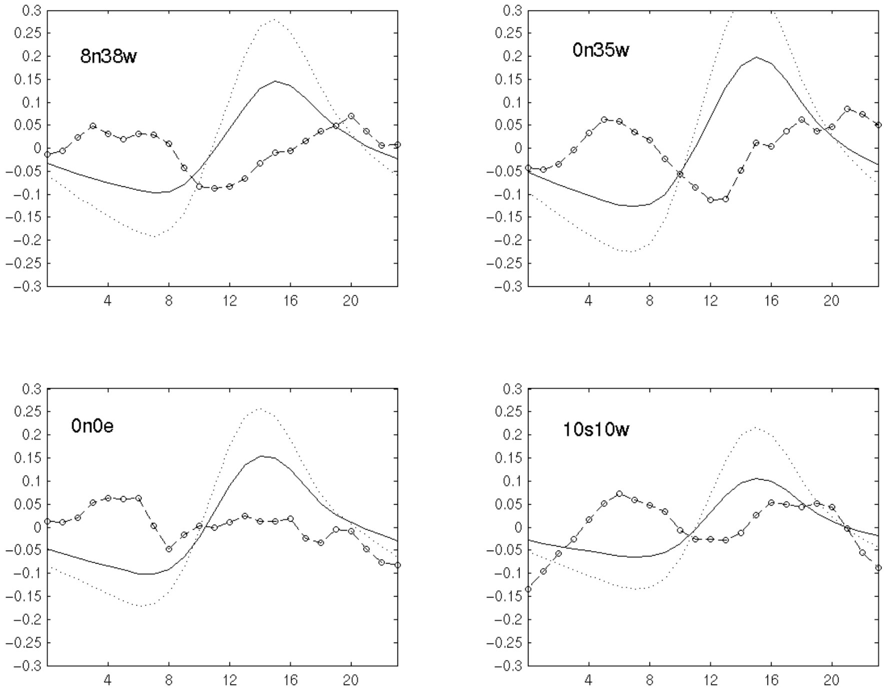

Figure 5.6 – Mean diurnal cycle of SST (solid), skin SST (dotted) and wind speed change (∂(wind)/∂t) (dashed). Units are °C for SST and skin SST, and ms^{-1} hr^{-1} for wind speed change.

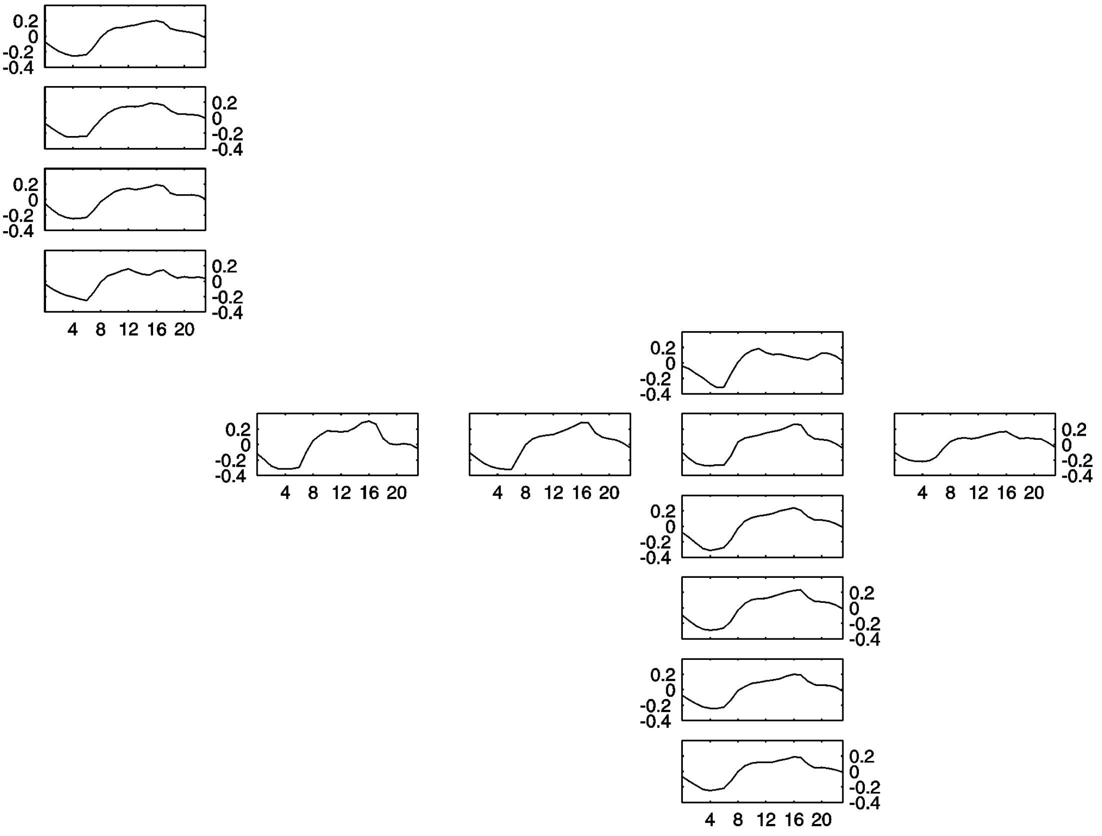

Figure 5.7 – Air temperature mean diurnal cycle in the tropical Atlantic. Y-axis shows values in °C. X-axis is given in hours.

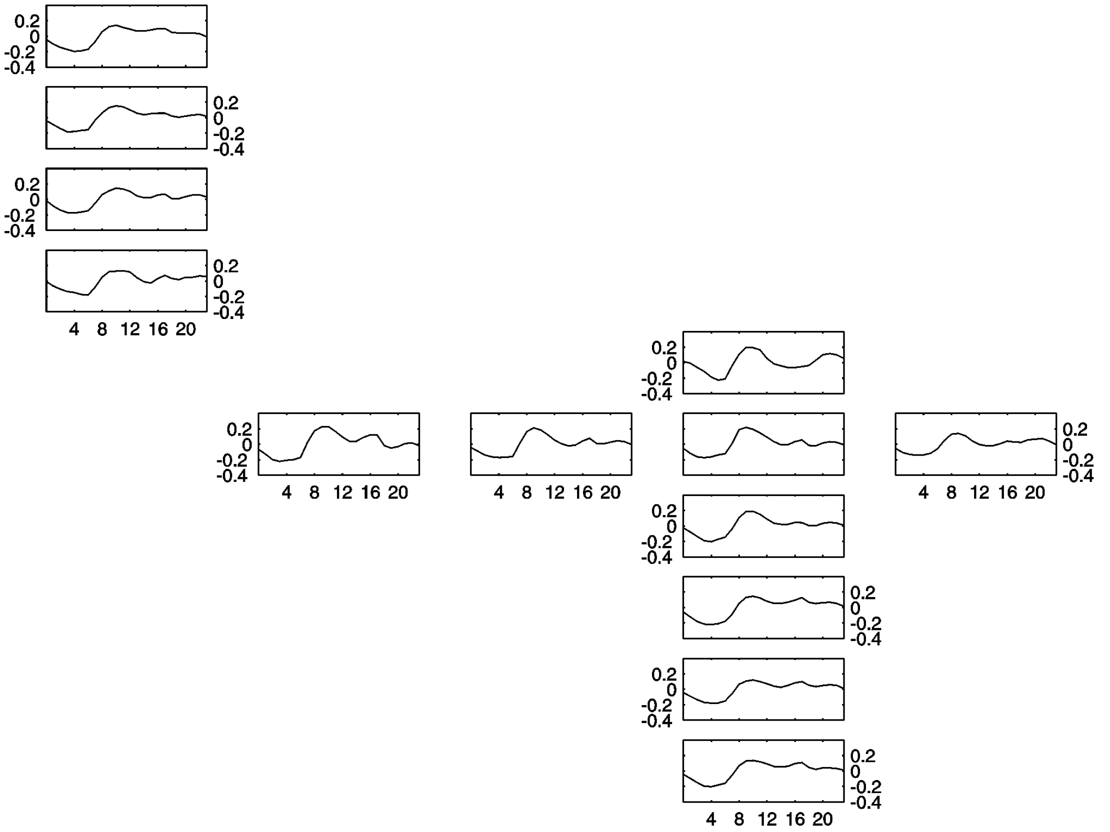

Figure 5.8 – Air-sea temperature difference mean diurnal cycle in the tropical Atlantic. Y-axis shows values in ^{o}C. X-axis is given in hours.

The diurnal cycle of air temperature (Figure 5.7) is similar to the SST diurnal cycle with the difference that, just after the sunrise, the air temperature rises sharply. It peaks at mid-afternoon and has minima at early morning. The shape of the diurnal cycle of air temperature will produce a very characteristic diurnal cycle of air-sea temperature difference (Figure 5.8), with three peaks of maxima difference: the main one at mid-morning, due to the sharp rising of air temperature after the sunrise, followed by two secondary ones, at mid-afternoon and late evening.

Relative humidity (Figure 5.9) presents a different pattern for the equatorial and extra-equatorial sites. The buoys located at the equator show a minimum relative humidity at around 16:00 hrs, with a constant decrease of relative humidity starting at around 8:00 hrs. After reaching its minimum, relative humidity rises very sharply. In contrast, the buoys in the extra-equatorial region have an accentuated decline of relative humidity, reaching its minimum at mid-morning and remaining at a constant, plateau-like value until mid-afternoon, when it starts rising again.

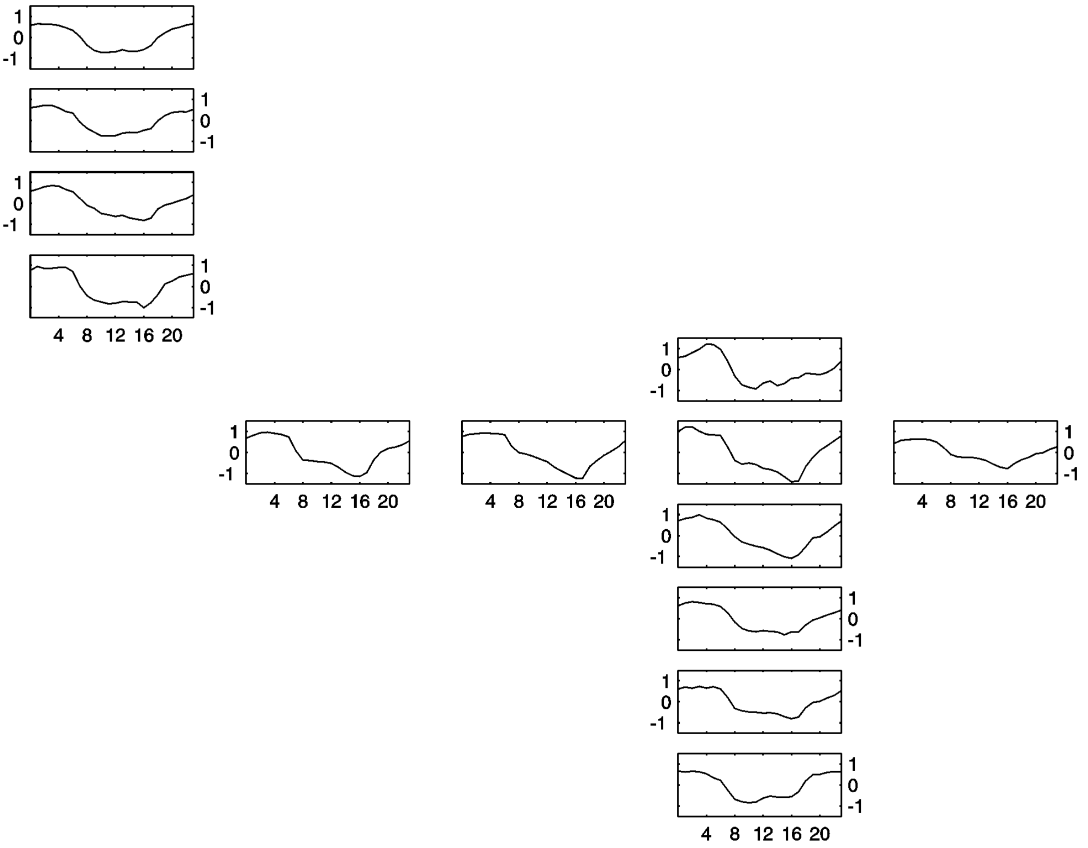

Figure 5.9 – Relative humidity mean diurnal cycle in the tropical Atlantic. Y-axis shows values in %. X-axis is given in hours.

5.3.2 Seasonal variation of the diurnal cycle

The PIRATA array provides an incomparable source of data and information about the tropical Atlantic. For the first time it is possible to show the seasonal variation of the diurnal cycle for met-ocean variables that have been measured by the moorings. To quantify the variability contained in these time series, the wavelet analysis was applied as described in Section 3.4.2. Morlet wavelet has been adopted in the analysis, as this is the most widely used in studies of geophysical processes (Torrence and Compo, 1998; Masina and Philander, 1999).

In order to assist the "reading" of the following figures, Figure 5.10 shows in detail the results of the wavelet analysis for one of the locations (0^{o}N 23^{o}W). The upper panel shows the power spectrum of the analysis, with colorbar in $^{o}C^{2}$ units. Black contour lines indicate the 95% confidence level. It is assumed that the time series has a mean power spectrum. If a peak in the wavelet power spectrum is significantly above this background spectrum, then it can be assumed to be a true feature with a certain percent confidence. The dotted lines have been plotted to separate the bands of different periods, identified in the y-axis. The diurnal signal is easily recognized for the band between 16 and 32 hours, as shown in the lower panel of Figure 5.10, and is clearly the most significant signal. Although the lower panel is not included in the subsequent figures, it highlights here the fact that the signal averaged between 16 and 32 hours is above the significance level.

Figures 5.11 – 5.14 show the power spectrum of the SST, wind speed, air temperature and relative humidity. Each of this figures are divided in three parts (a, b and c), where the panels show the time-variability of the PIRATA buoys on each of its lines. The figures part “a” corresponds to buoys located at 15°N, 12°N, 8°N, 4°N on 38°W. Figures part “b” are for the buoys at 35°W, 23°W, 10°W, 0°E on the equator, and figures part “c” are for the buoys located at 5°S, 6°S, 10°S on 10°W. Data from the buoys at 2°S and 2°N on 10°W have not been used in this analysis due to the short length (~ 3 month) of the dataset.

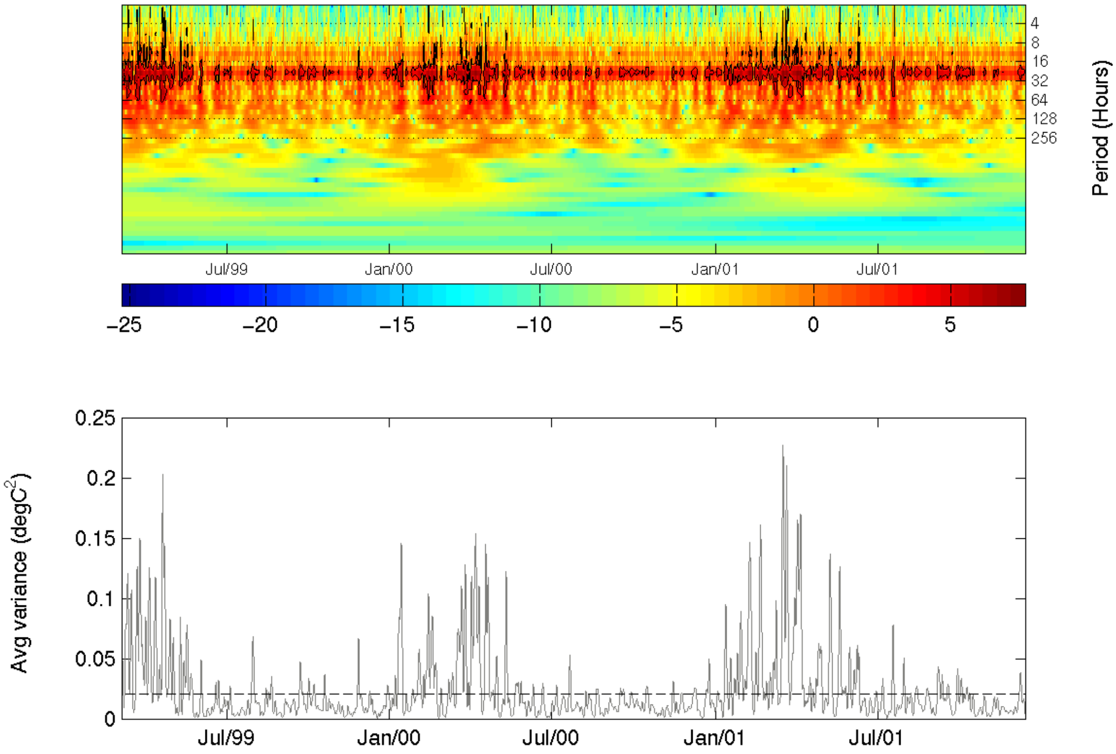

Figure 5.10 – Detail of SST wavelet power spectra for the buoy at 0°N 23°W (top panel). 16 – 32 hours band average time series (lower panel). Black contour lines in the upper panel and dashed line in the lower panel are the 95% confidence level. Units are (°C)^2.

All the buoys show the strongest diurnal cycle signal in the SST records during the summer of the respective hemisphere (Figure 5.11). The buoys north of the equator show a strong diurnal cycle starting in June. The signal can last almost until the end of the year. The buoys on the equator follow the season of the southern hemisphere with strong diurnal cycles starting in January, the same happening with the buoys south of the equator. It is very important to notice that, in particular for the buoys located on the equator, between July and January, which is generally the period of weaker diurnal signals, there are events when these diurnal signals are statistically significant. It is suggested that these events are modulated by processes at different timescales, in particular by Tropical Instability Waves. It is also worth mentioning that, although not statistically significant in the wavelet analysis, a semi-diurnal cycle is well visible in all the buoys. These signals are possibly due to the influence of the wind speed data, which shows a much stronger variability at higher frequencies (Figure 5.12).

It seems that north of the equator, the periods of strong diurnal SST signals are discernible, but intermittent, and also associated with signals of higher frequencies. This is probably due to the influence of the ITCZ, which can affect the diurnal cycle of winds, which in turn would affect the diurnal signals of SST. On the other hand, south of the equator, the periods of strong diurnal signals are more continuous, highlighting the impact of less variable winds on the diurnal signal of SST.

The diurnal cycle of the wind speed (Figure 5.12) follows the same seasonal pattern as the diurnal cycle of the SST, although with stronger diurnal (and higher frequency) signals during the summer of the respective hemisphere. However, for wind speed, in contrast to SST, this is the time of the year when the lowest wind speeds are noticed. The buoys south of the equator show fewer apparent periods of strong diurnal signal of wind speed, similarly to the SST power spectra, when compared with the locations north of the equator. As highlighted before, the number of gaps in the wind speed dataset is much higher than for other variables, especially for locations on the equator. As this is a critical problem for the calculation of heat fluxes, and with the possibility of using satellite-retrieved wind speed, a study of the impact of daily wind on hourly surface heat fluxes is done in the next section.

Figures 5.13 and 5.14 show the analysis for air temperature and relative humidity, respectively. These two variables do not follow the pattern observed for the other variables. For the northern hemisphere, the strongest diurnal signal is detected during summer time, following the seasonal displacement of the ITCZ. For the buoys in the southern hemisphere, the diurnal cycle of these variables seems to be controlled by the intrusion of the cold tongue. The cold tongue is well developed in July, which is southern hemisphere winter, leading to strong diurnal cycles of air temperature and relative humidity by this time.

As mentioned before, this is the first time that the seasonal variation of diurnal signals is observed for the whole tropical Atlantic. It clearly underlines the relationship of the mean diurnal cycle of SST and wind speed, and suggests possible modulations on the SST diurnal signal by processes of other timescales, which will be further investigated in this document.

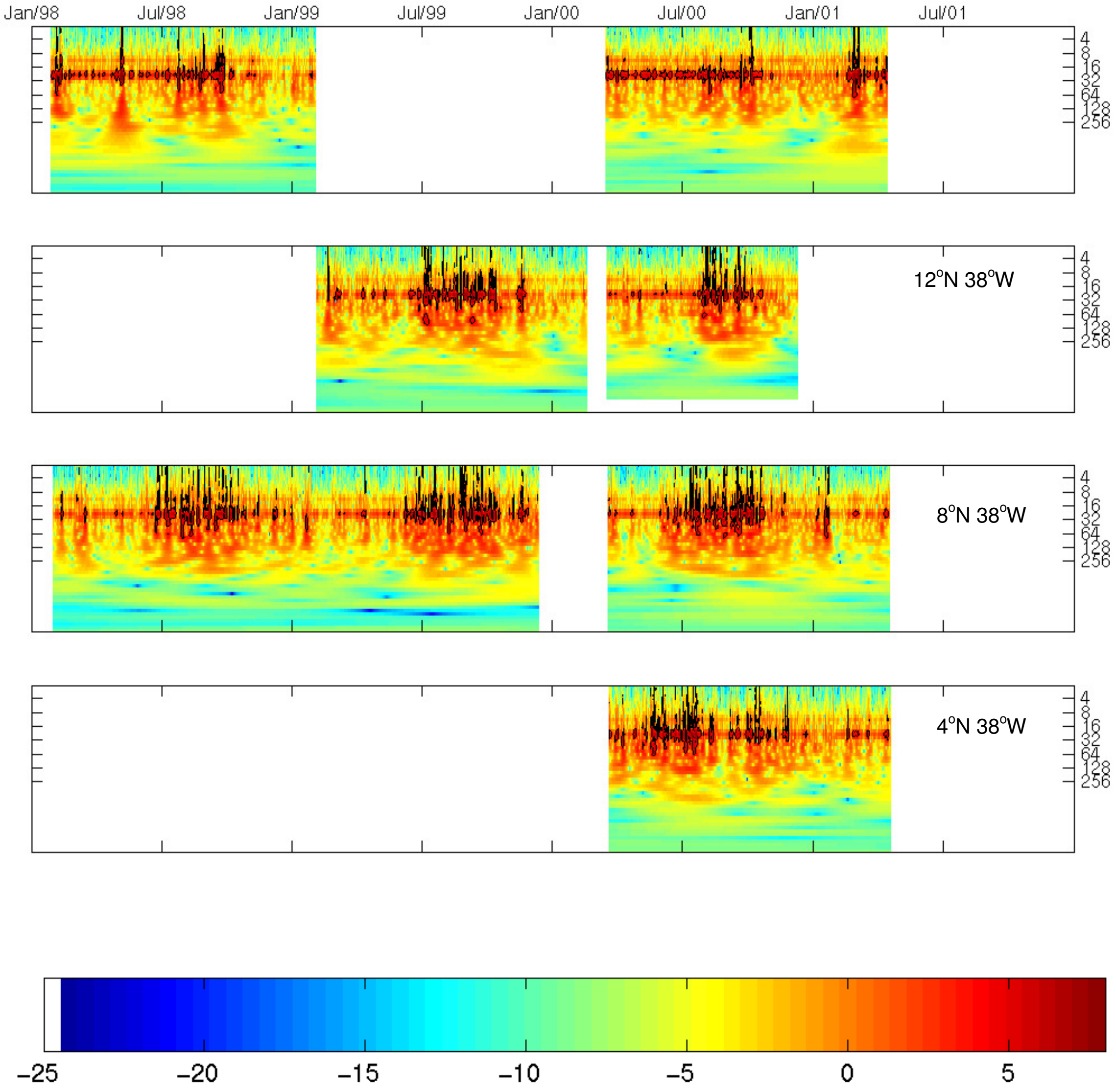

Figure 5.11a – SST wavelet power spectra for the PIRATA buoys. Y-axis is the period in hours. The colorbar unit is $(^{o}C)^{2}$. Black contour lines are the 95% confidence level.

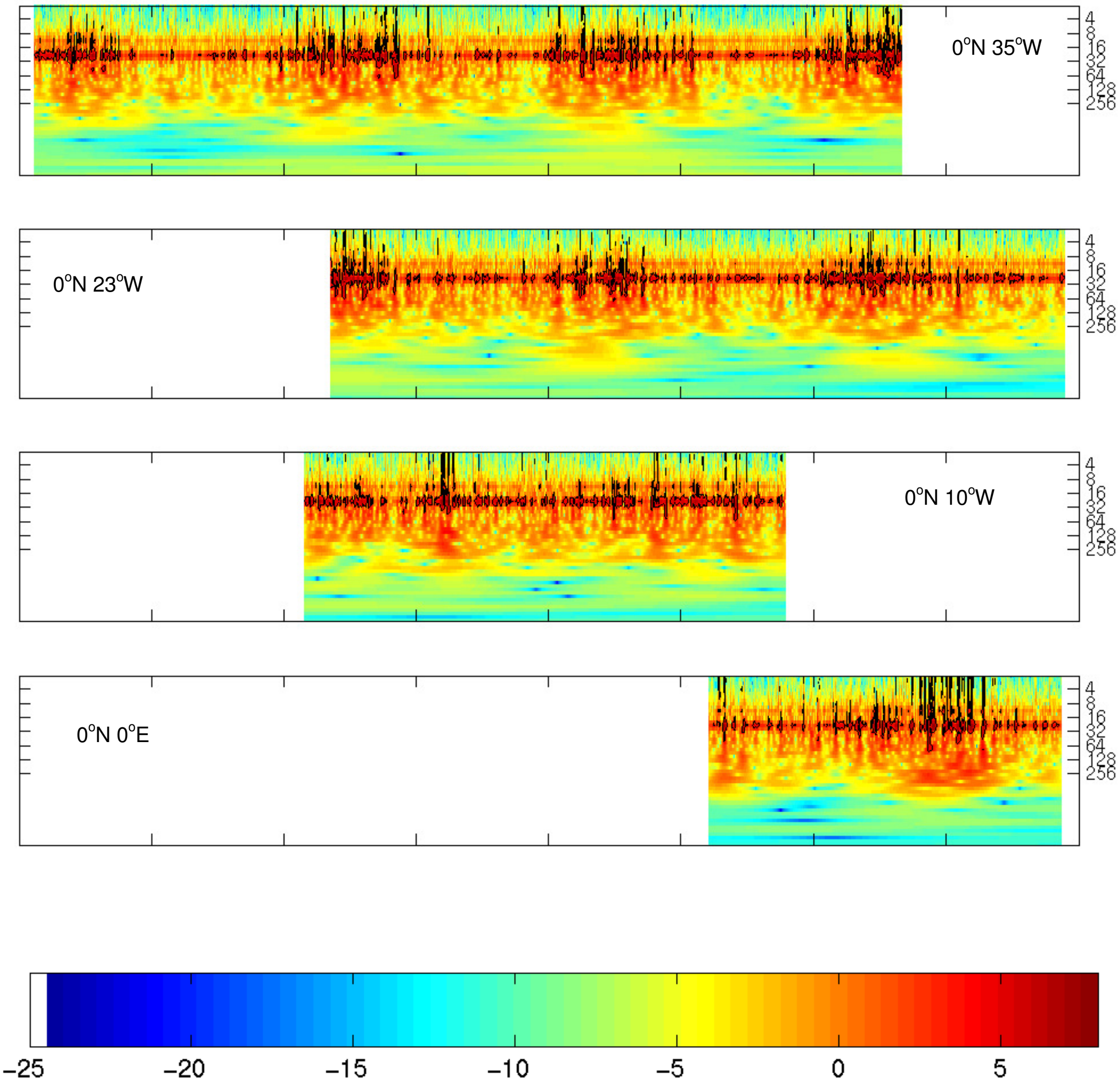

Figure 5.11b – SST wavelet power spectra for the PIRATA buoys. Y-axis is the period in hours. The colorbar unit is (°C) ^{2}. Black contour lines are the 95% confidence level.

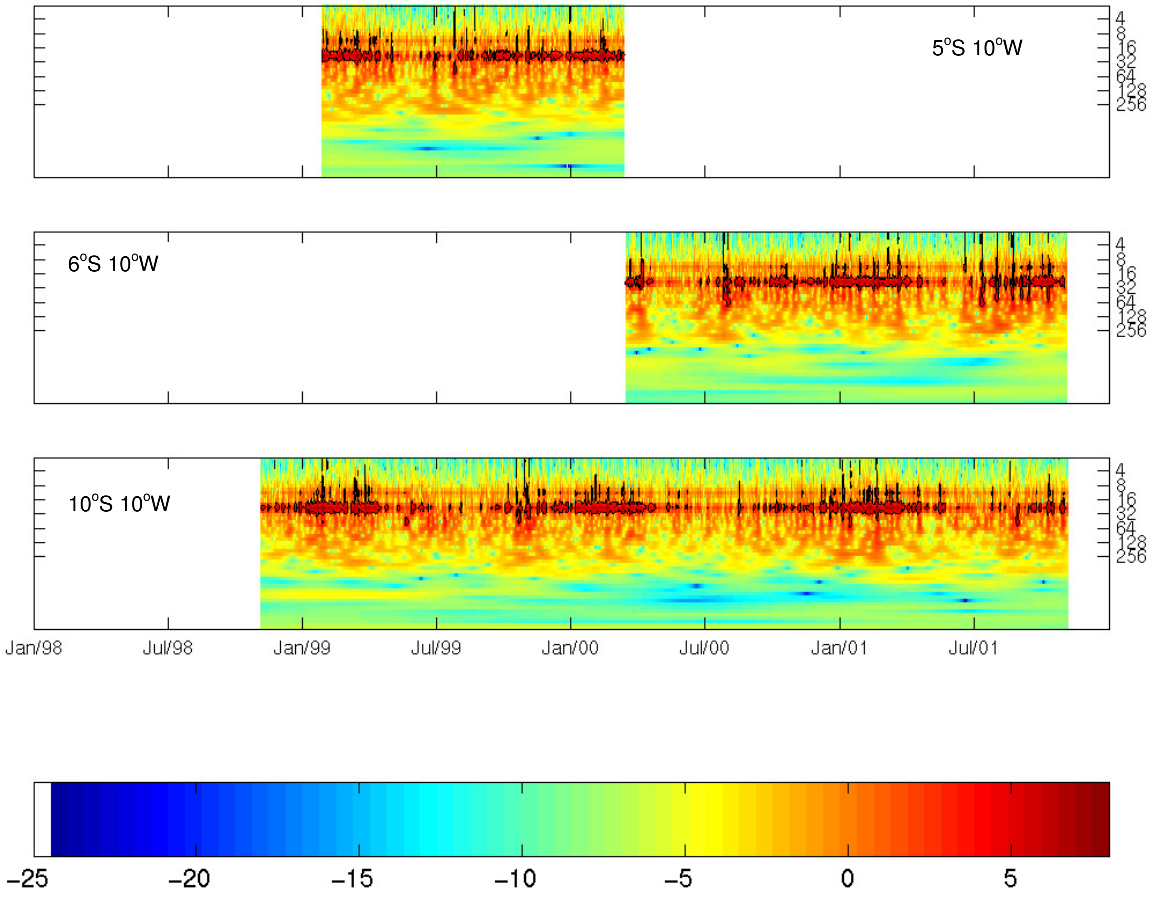

Figure 5.11c – SST wavelet power spectra for the PIRATA buoys. Y-axis is the period in hours. The colorbar unit is (^{o}C) ^{2}. Black contour lines are the 95% confidence level.

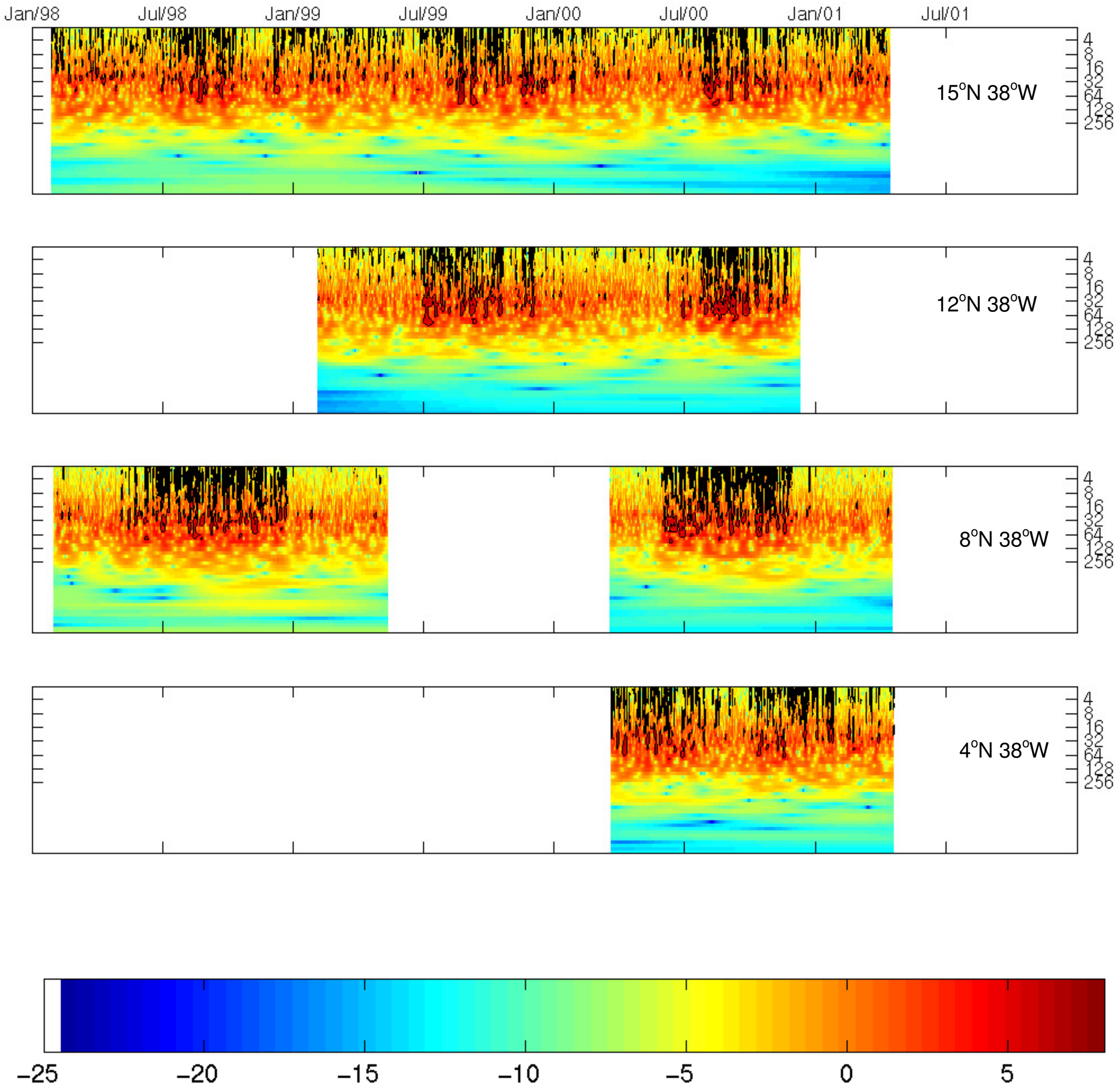

Figure 5.12a – Wind speed wavelet power spectra for the PIRATA buoys. Y-axis is the period in hours. The colorbar unit is $(m/s)^2$. Black contour lines are the 95% confidence level.

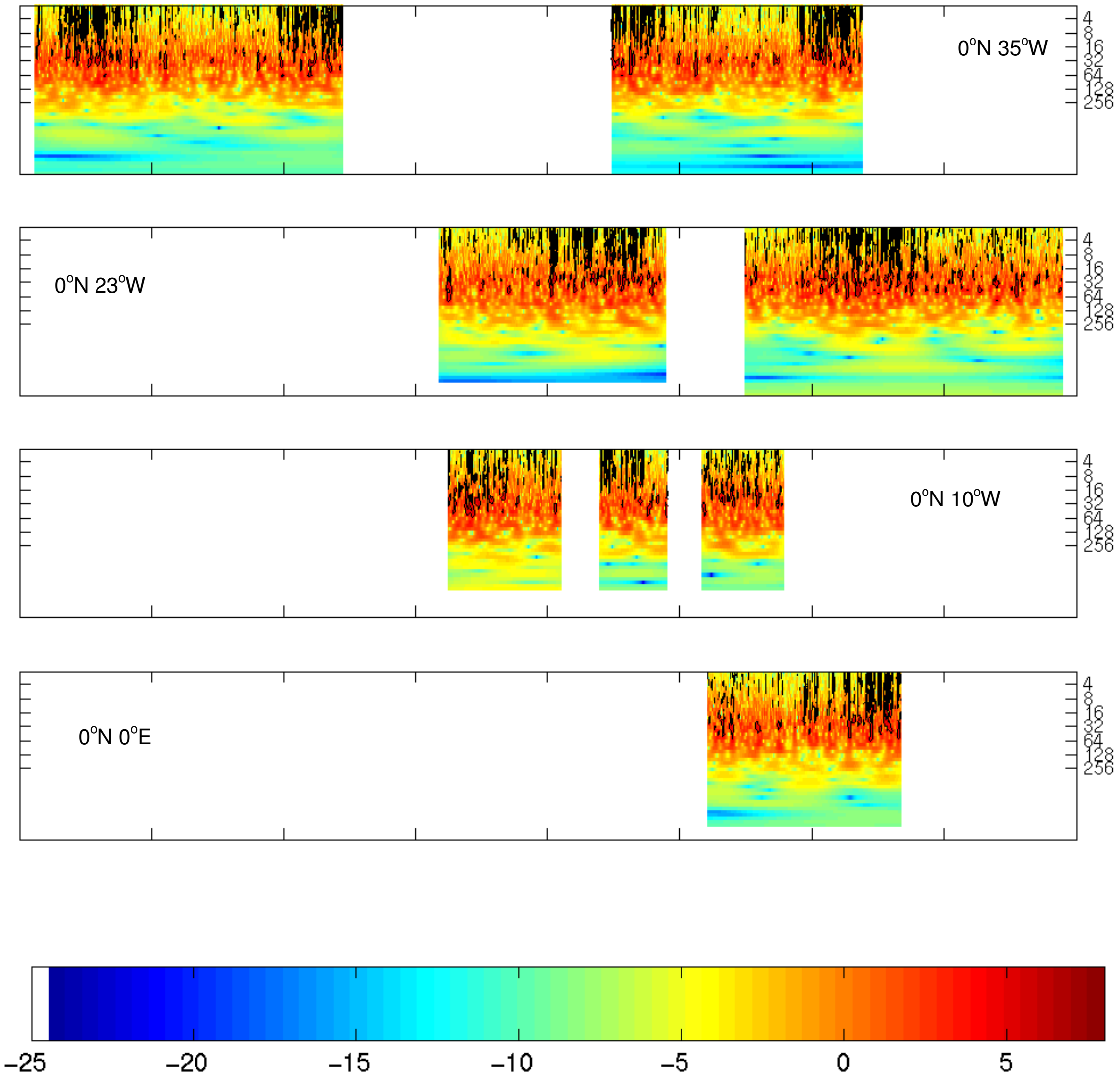

Figure 5.12b – Wind speed wavelet power spectra for the PIRATA buoys. Y-axis is the period in hours. The colorbar unit is (m/s) ^{2}. Black contour lines are the 95% confidence level.

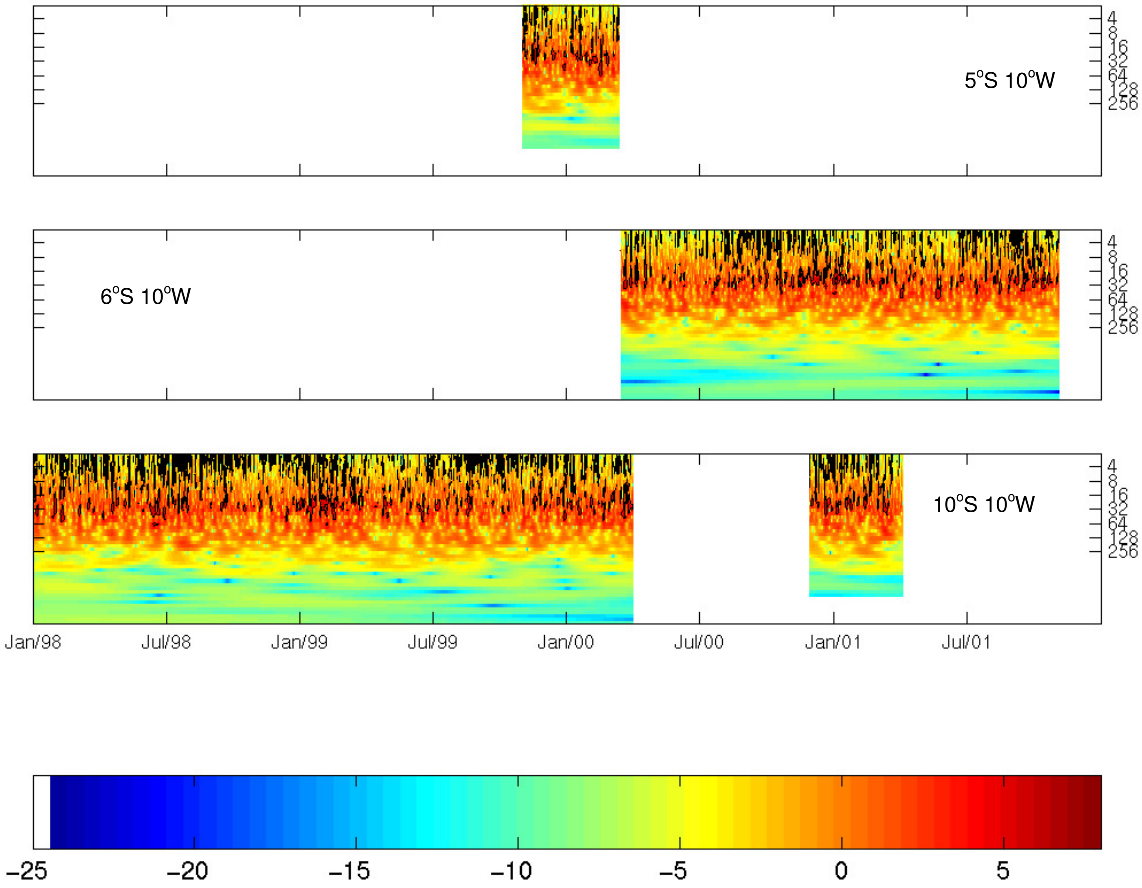

Figure 5.12c – Wind speed wavelet power spectra for the PIRATA buoys. Y-axis is the period in hours. The colorbar unit is (m/s) ^{2}. Black contour lines are the 95% confidence level.

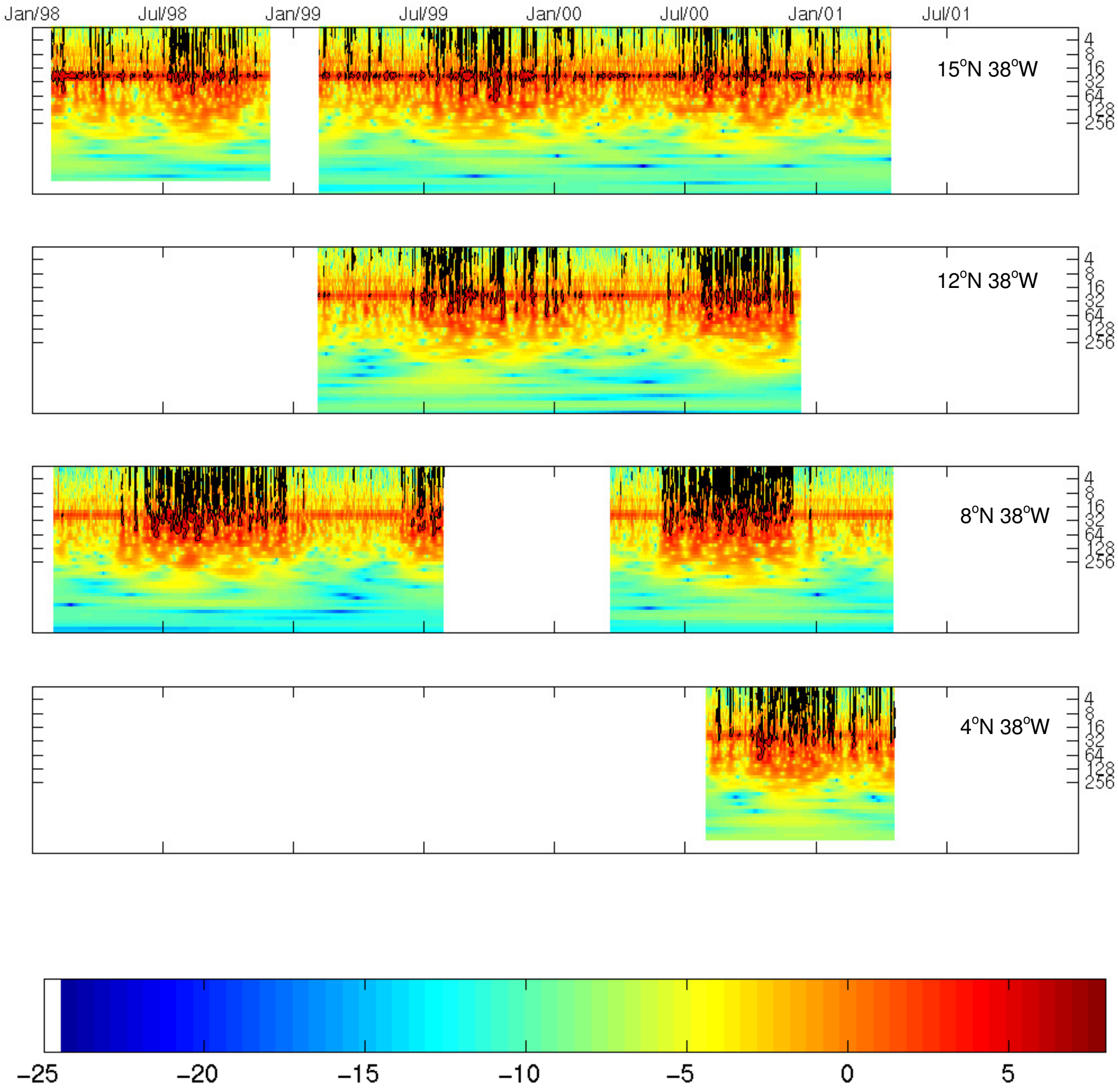

Figure 5.13a –Air temperature wavelet power spectra for the PIRATA buoys. Y-axis is the period in hours. The colorbar unit is (^{o}C) ^{2}. Black contour lines are the 95% confidence level.

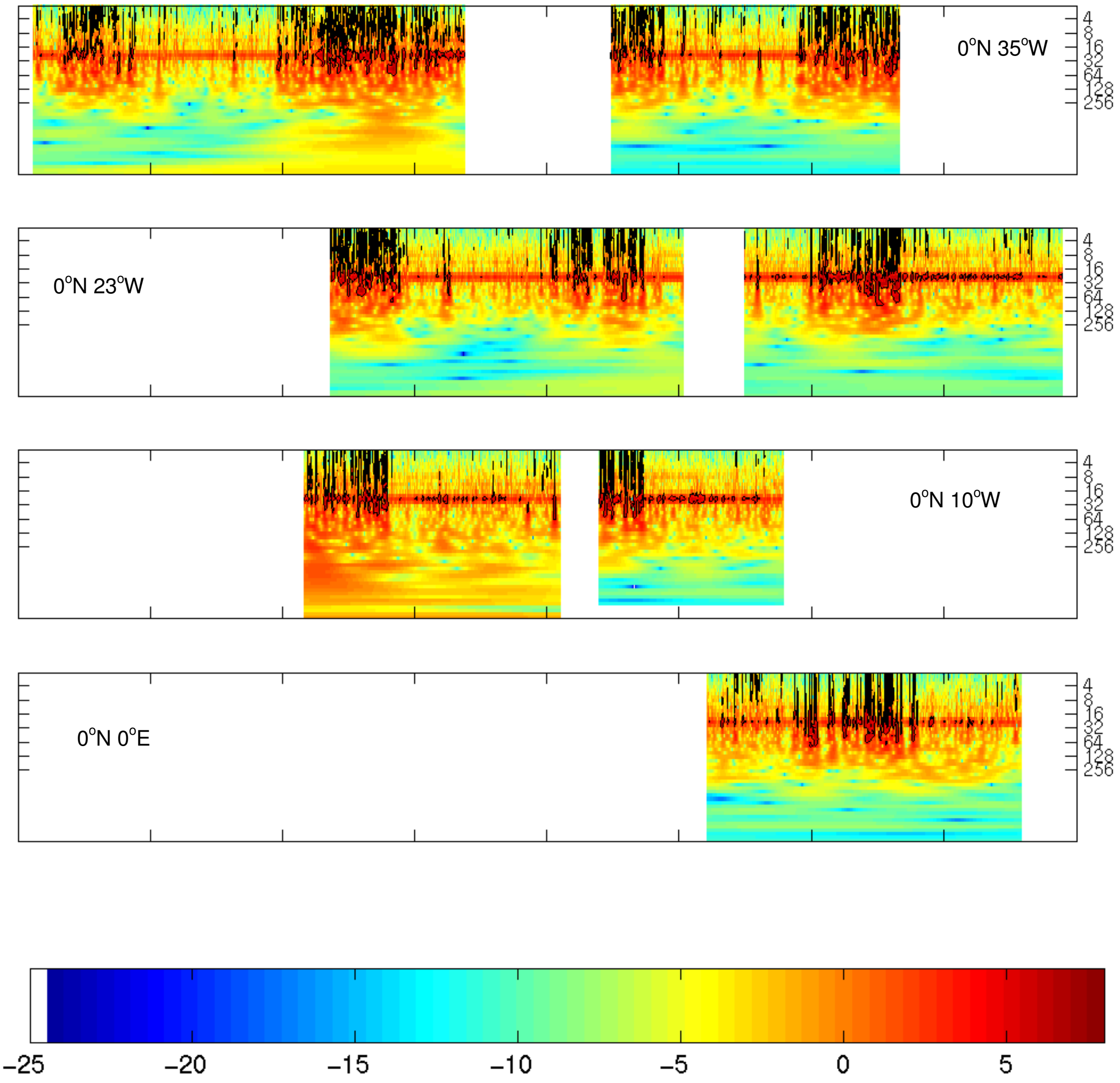

Figure 5.13b – Air temperature wavelet power spectra for the PIRATA buoys. Y-axis is the period in hours. The colorbar unit is $(^{o}C)^{2}$. Black contour lines are the 95% confidence level.

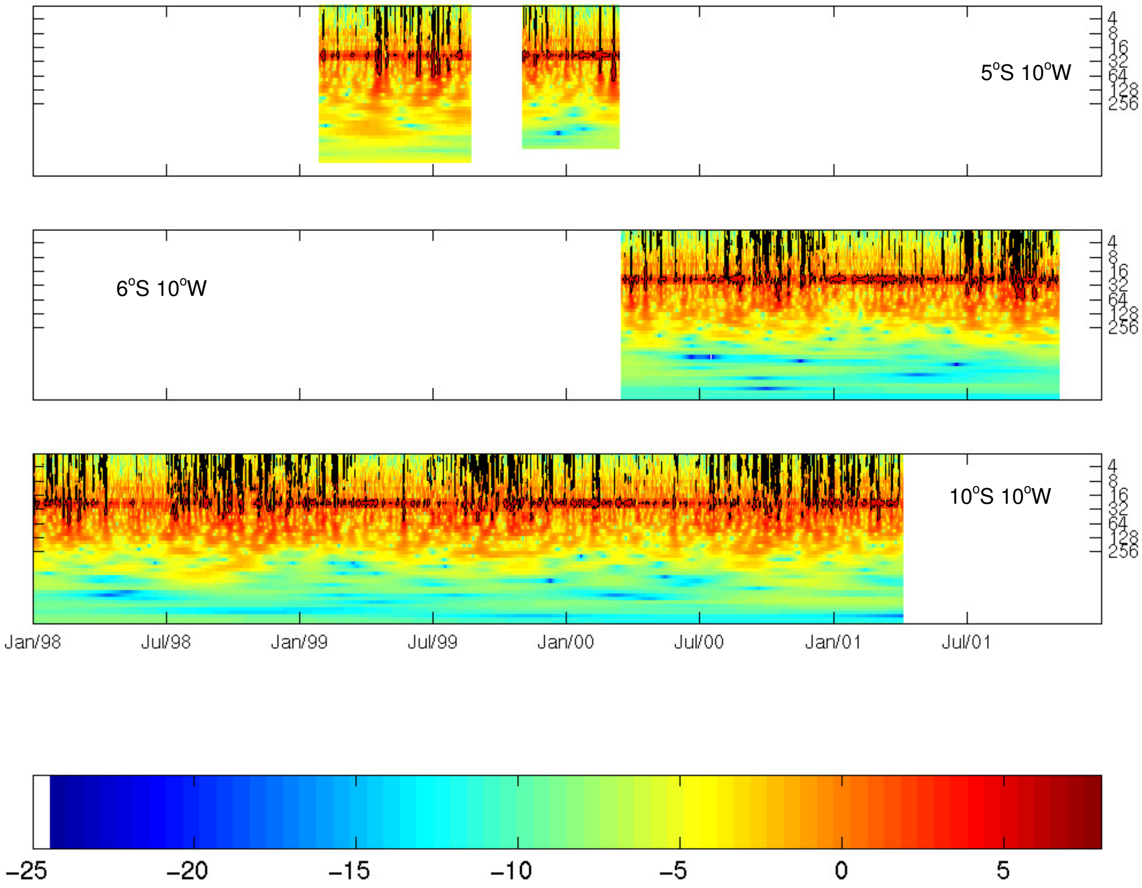

Figure 5.13c – Air temperature wavelet power spectra for the PIRATA buoys. Y-axis is the period in hours. The colorbar unit is $(^{o}C)^{2}$. Black contour lines are the 95% confidence level.

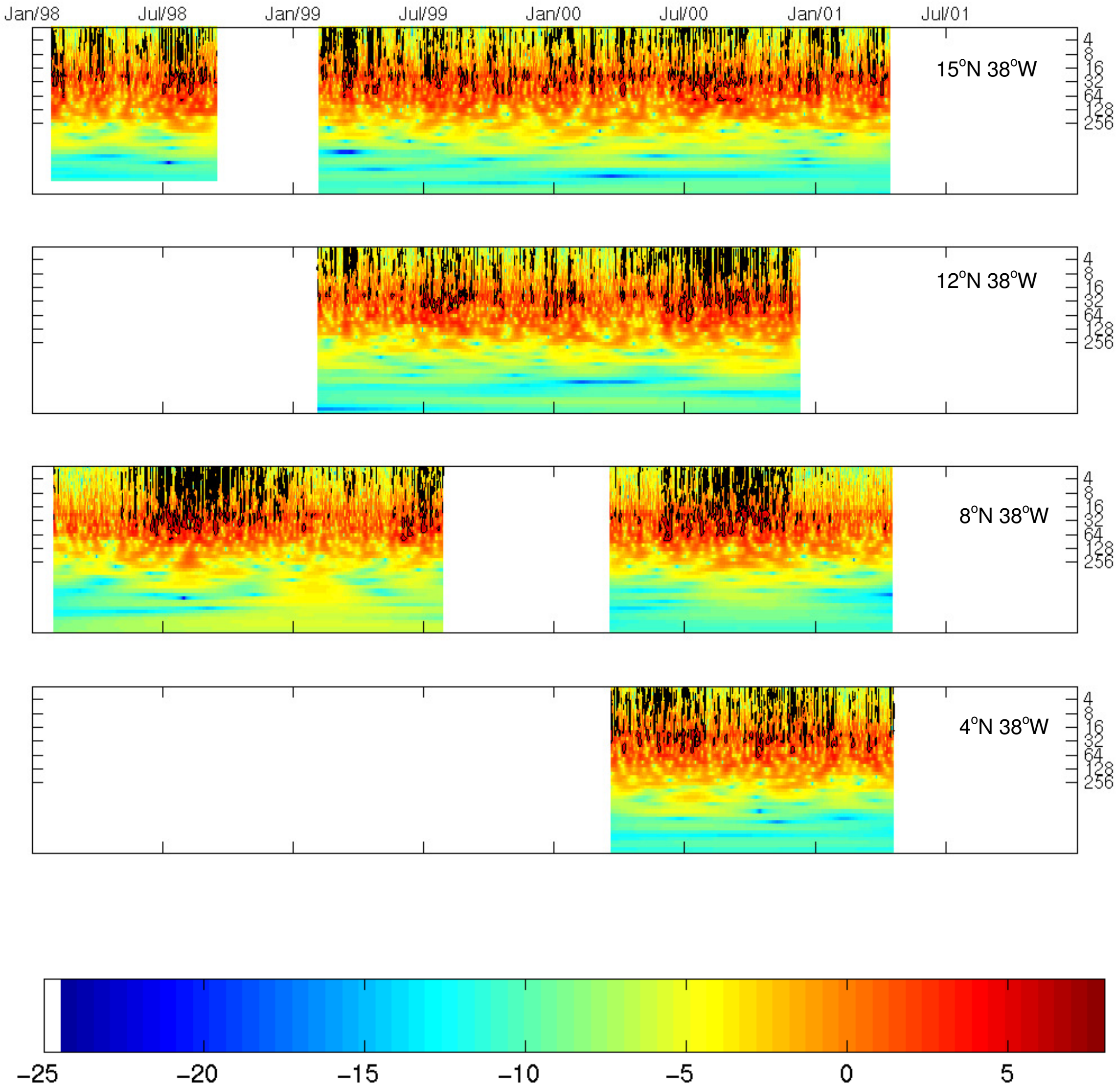

Figure 5.14a – Relative humidity wavelet power spectra for the PIRATA buoys. Y-axis is the period in hours. The colorbar unit is (%) ^{2}. Black contour lines are the 95% confidence level.

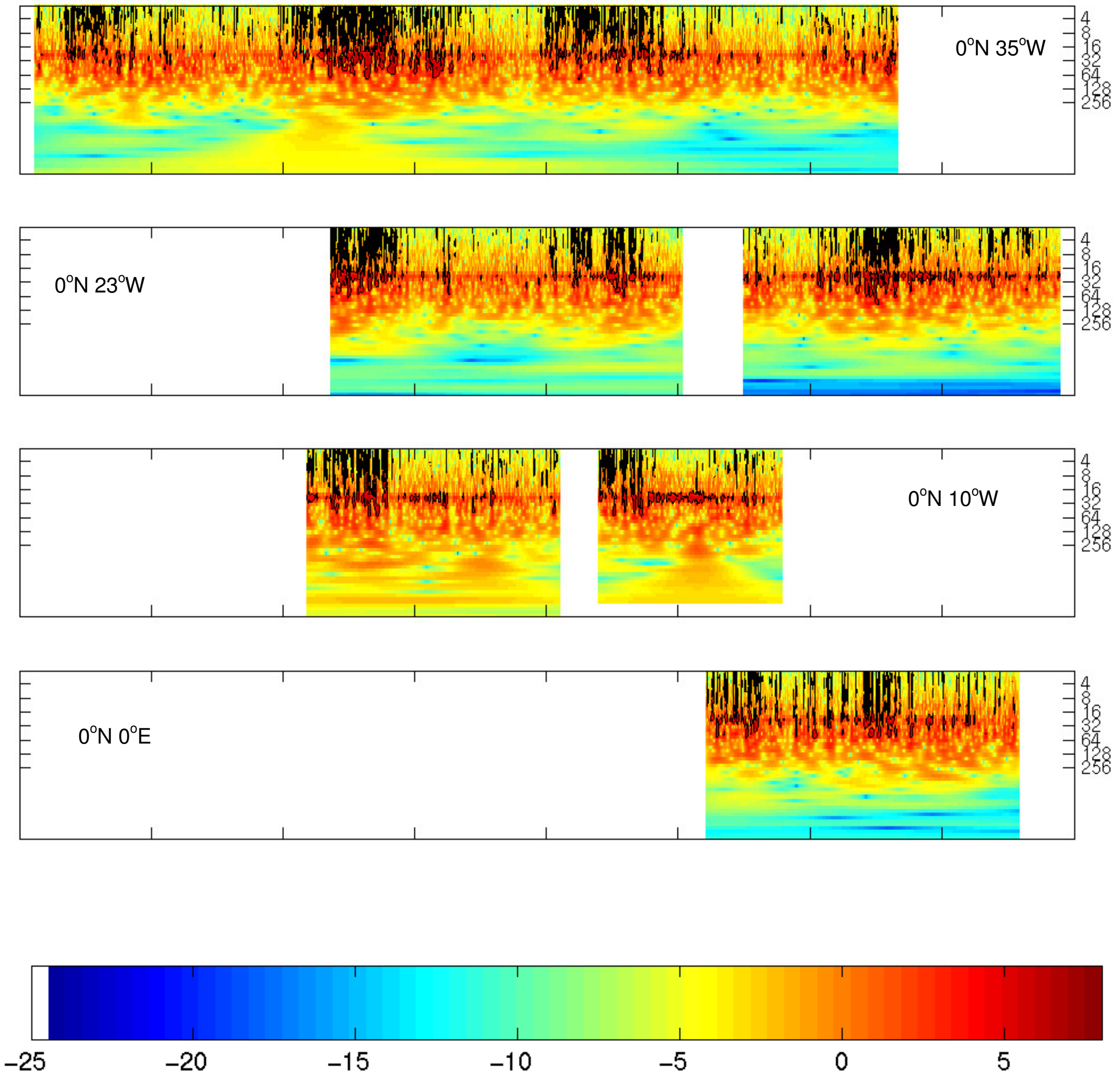

Figure 5.14b – Relative humidity wavelet power spectra for the PIRATA buoys. Y-axis is the period in hours. The colorbar unit is (%) ^{2}. Black contour lines are the 95% confidence level.

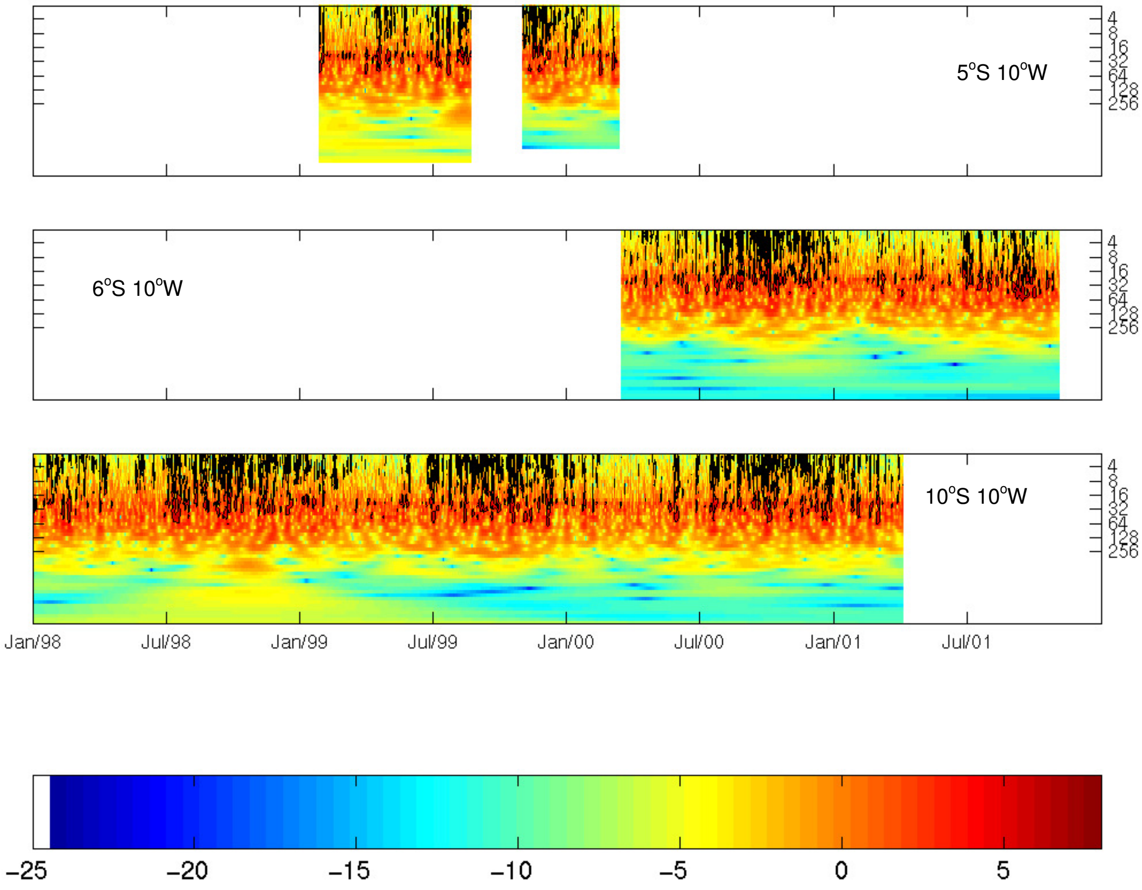

Figure 5.14c – Relative humidity wavelet power spectra for the PIRATA buoys. Y-axis is the period in hours. The colorbar unit is $(\%)^{2}$. Black contour lines are the 95% confidence level.

5.4. Impact of daily wind on hourly surface heat fluxes

As highlighted in Chapter 4, the main limitation in calculating surface heat fluxes using the PIRATA dataset is the gaps that exist in the data, most accentuated in the wind speed time series. In order to overcome this problem, and based on the encouraging results presented in the previous chapter, it was decided to use the wind-retrieved satellite data to fill those gaps. However, the satellite data only yield a few measurements during the day so it would not be possible to interpolate the series at every hourly time step. The solution was to calculate the hourly surface heat fluxes by using daily average wind speed.

Some studies have analysed the systematic biases of fluxes in the tropics, especially the tropical Pacific (Esbensen and McPhaden, 1996; Gulev, 1997; Zhang, 1997). These studies showed small differences in monthly heat fluxes calculated using hourly, daily, or monthly wind, humidity, and temperature sampling. These studies, however, have not dealt with the nature of the diurnal cycles of fluxes. Zeng and Dickinson (1998) addressed the impact of hourly, daily and monthly skin sea surface temperature on the calculations of the diurnal cycle of heat fluxes. The results below will address the impact of daily average wind speed on the diurnal cycle of heat fluxes as this is yet to be fully discussed in the literature. In this section, the hourly latent and hourly sensible heat fluxes are derived from Zeng et al. (1998), and use hourly SST, hourly air temperature and hourly relative humidity measured from the PIRATA buoys. SST has been accounted for the cool skin effect using the Zeng et al. (1999) algorithm.

The scatterplots presented in Figure 5.14 and 5.15 illustrate the comparison of hourly latent and hourly sensible heat fluxes, respectively, calculated using hourly and daily wind speed. For most of the buoys, the largest scatter is in the region of high latent and sensible heat fluxes. Latent heat flux shows a larger variability due to the nature of its calculation. Nevertheless, the performance of this comparison seems to be of very good quality.

Table 5.2 summarises the statistics of the comparison between latent and sensible heat fluxes calculated using hourly and daily wind speed. As in Section 4.3, the errors listed in the table were computed as one-half the rms difference. The agreement is very good, with a small bias for both Q_{lat} and Q_{sen}. The rms difference between Q_{lat} calculated with hourly and daily wind speed is larger than for Q_{sen}, as expected. Still, the errors have similar magnitudes to those estimated for inaccurate measurements of the bulk variables by the in situ sensors, as shown in Section 4.3.

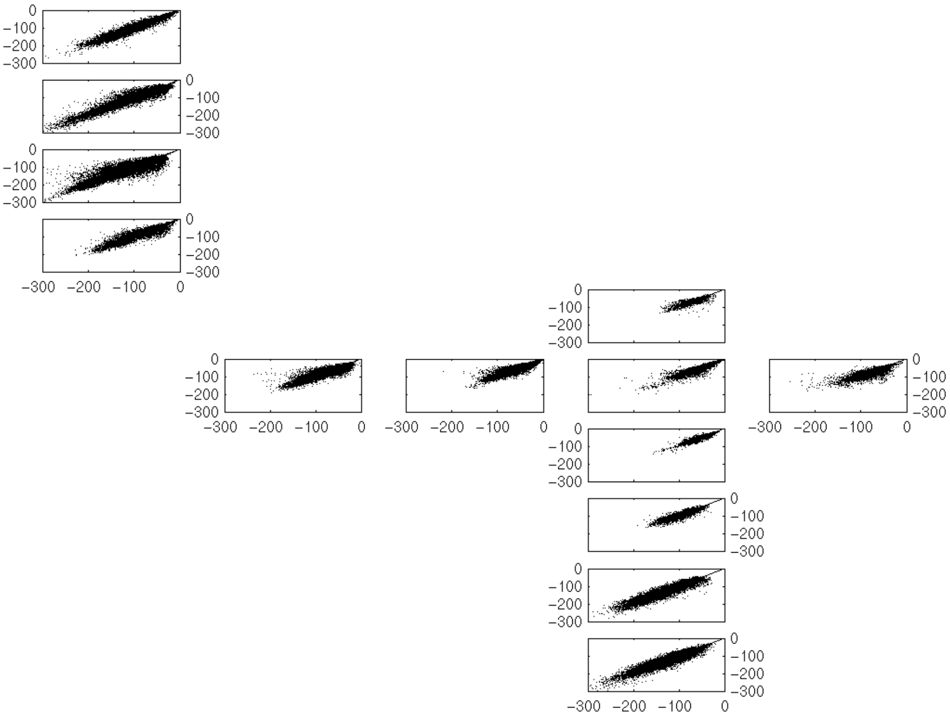

Figure 5.15 – Hourly latent heat flux (Wm^{-2}) calculated using hourly wind speed (X axis) and daily wind speed (Y axis).

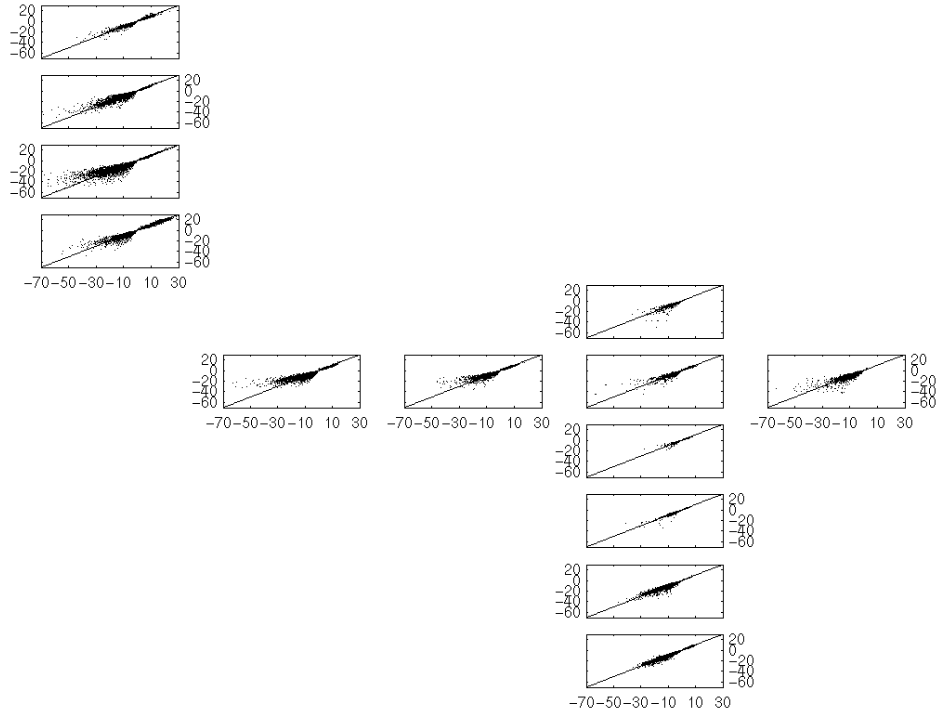

Figure 5.16 – Hourly sensible heat flux (Wm^{-2}) calculated using hourly wind speed (X axis) and daily wind speed (Y axis).

Table 5.2 – Statistics of comparison between Q_{lat} and Q_{sen} calculated with hourly and daily wind speed

Buoy	r^2		rms diff		bias		No. obs.
	Q_{lat}	Q_{sen}	Q_{lat}	Q_{sen}	Q_{lat}	Q_{sen}	
0N 0W	0.60	0.83	7.87	1.07	- 0.16	0.00	7660
0N 10W	0.87	0.91	5.20	0.69	- 0.37	- 0.02	8559
0N 23W	0.87	0.92	4.86	0.62	- 0.14	0.01	18461
0N 35W	0.80	0.91	6.66	0.89	- 0.15	- 0.01	18309
10S 10W	0.86	0.97	7.05	0.44	0.04	0.03	17546
12N 38W	0.89	0.94	7.83	0.81	- 0.07	0.02	15532
15N 38W	0.92	0.98	5.59	0.34	0.02	0.04	15045
2N 10W	0.66	0.79	6.55	1.08	- 0.36	0.10	1538
2S 10W	0.83	0.95	4.02	0.29	- 0.11	0.02	2949
4N 38W	0.83	0.94	7.80	1.00	- 0.27	0.16	7091
5S 10W	0.80	0.93	5.83	0.41	0.04	0.03	3274
6S 10W	0.88	0.93	7.09	0.60	- 0.01	0.03	14393
8N 38W	0.77	0.90	10.26	1.31	- 0.26	- 0.06	20405

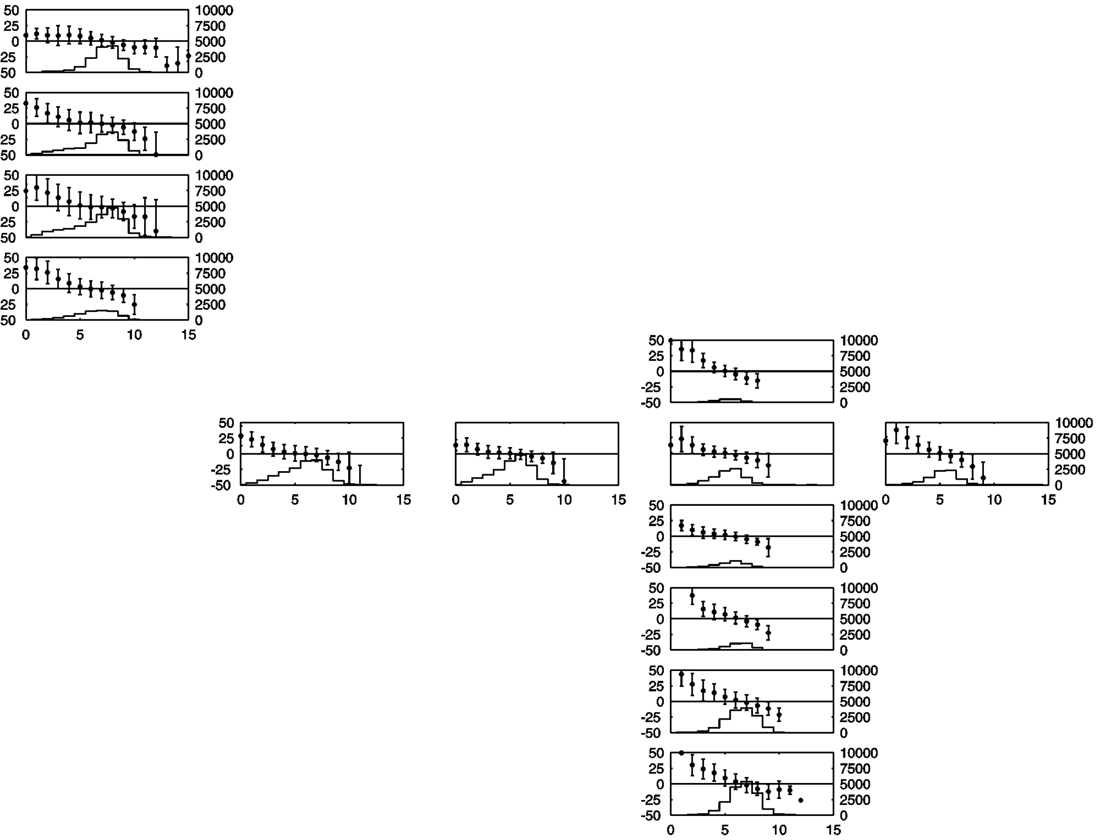

Figure 5.17 – Dependence of latent heat flux residuals on the buoy wind speed. Number of data points, averages (points) and standard error (vertical lines) calculated in bins of wind speed of 1 ms^{-1}.

In order to evaluate the influence of the atmospheric and oceanic conditions on the use of hourly or daily wind speed in the latent heat flux calculation, the relation between the residual latent heat flux, here defined as the latent heat flux calculated using hourly wind speed minus the latent heat flux calculated using daily wind speed, and buoy wind speed and SST is shown in Figures 5.17 and 5.18, respectively. As latent heat flux is more affected by the use of hourly or daily wind than sensible heat flux, the following analysis refers only to latent heat flux. At low wind speeds (< 3 ms^{-1}), it can be seen that the use of daily wind speed underestimates the calculation of latent heat flux by more than 25 Wm^{-2} for most of the buoys (Figure 5.17). However, this is not the typical wind speed in the region. For the typical wind speed measured in the tropical Atlantic (5 – 9 ms^{-1}), the residual is very small, with a slight tendency of latent heat flux calculated with daily wind speed to overestimate the flux calculation. In relation to SST (Figure 5.18), the only dependence is seen for high temperatures (above 28° C). For the large majority of sea surface temperature values, latent heat flux residuals exhibit no dependence on SST.

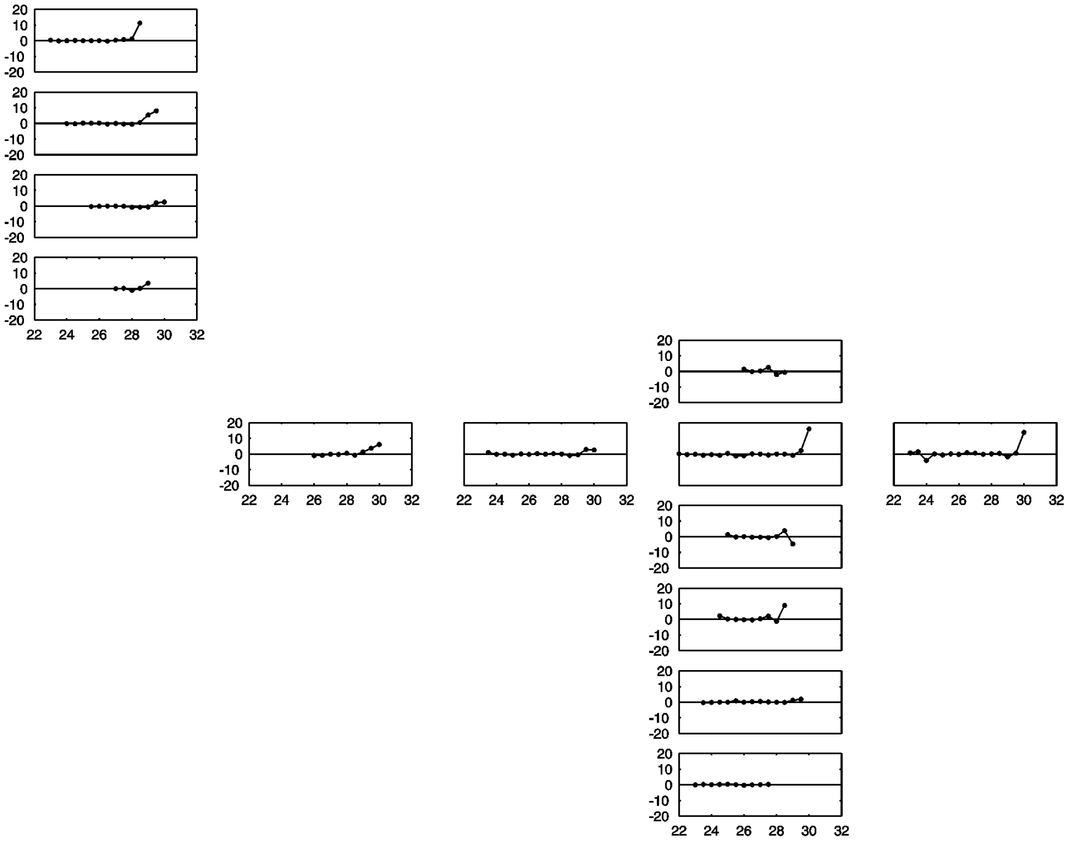

Figure 5.18 – Dependence of latent heat flux residuals on SST. Averages (points) calculated in bins of SST of 0.5 ^{o}C.

Figures 5.19 and 5.20 shows the comparison of mean diurnal cycles for sensible and latent heat fluxes, respectively, calculated using hourly and daily wind speed. As in Section 5.3.1, the daily mean of the variables have been removed from each location, and once it was removed, the mean diurnal cycle was calculated. Sensible heat flux (Figure 5.19) does not show large differences in the diurnal cycles, with a very good match for most of the buoys. The main differences can be seen in the diurnal cycle of latent heat flux (Figure 5.20). No difference in phase is observed. However, the difference between maximum and minimum becomes larger for most of the buoys.

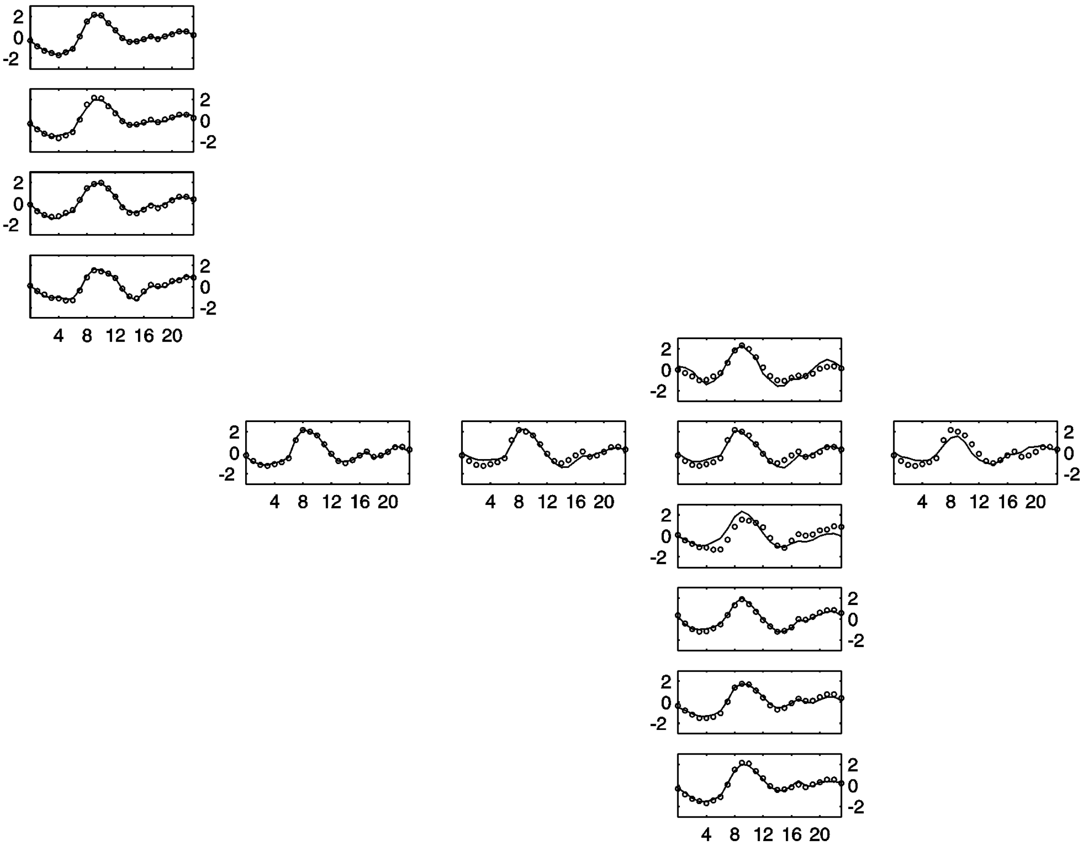

Figure 5.19 – Mean diurnal cycle of sensible heat flux calculated using hourly (solid line) and daily (circles) wind speed. X-axis is time (hours) and Y-axis is Q^{sen} (Wm^{-2})

The impact of using daily wind speed on the diurnal cycle of latent heat flux is illustrated in Figure 5.21. There is a marked difference between the western and eastern side of the basin, as there was for the diurnal cycle of wind speed (Figure 5.2). For the western side, the use of daily wind speed can underestimate Q_{lat} by up to 5 Wm^{-2} in mid-afternoon, coinciding with the time of lowest wind speed, while in the early morning, Q_{lat} is also overestimated by up to 5 Wm^{-2}. In contrast, the eastern side of the tropical Atlantic basin shows the largest underestimation of Q_{lat} at around 04:00 hrs if daily wind speed is used. Q_{lat} can be overestimated by up to 5 Wm^{-2} at around 21:00 hrs.

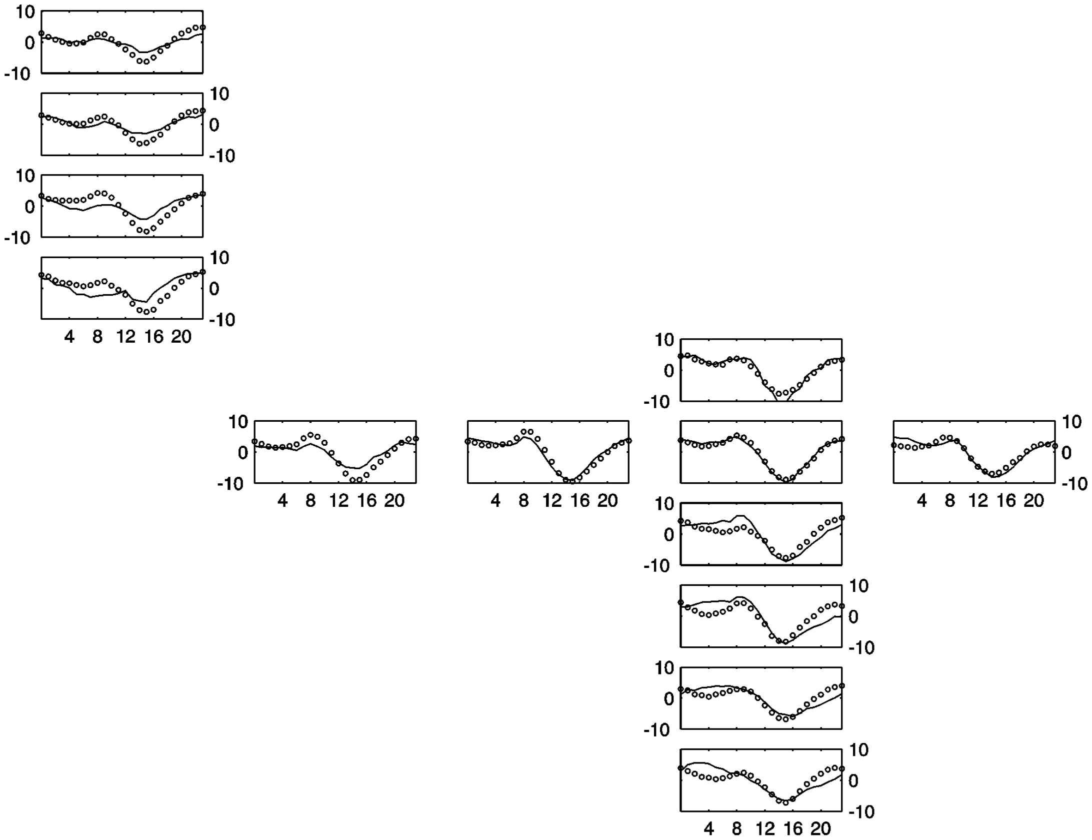

Figure 5.20 – Mean diurnal cycle of latent heat flux calculated using hourly (solid line) and daily (circles) wind speed. X-axis is time (hours) and Y-axis is Q^{sen} (Wm^{-2}).

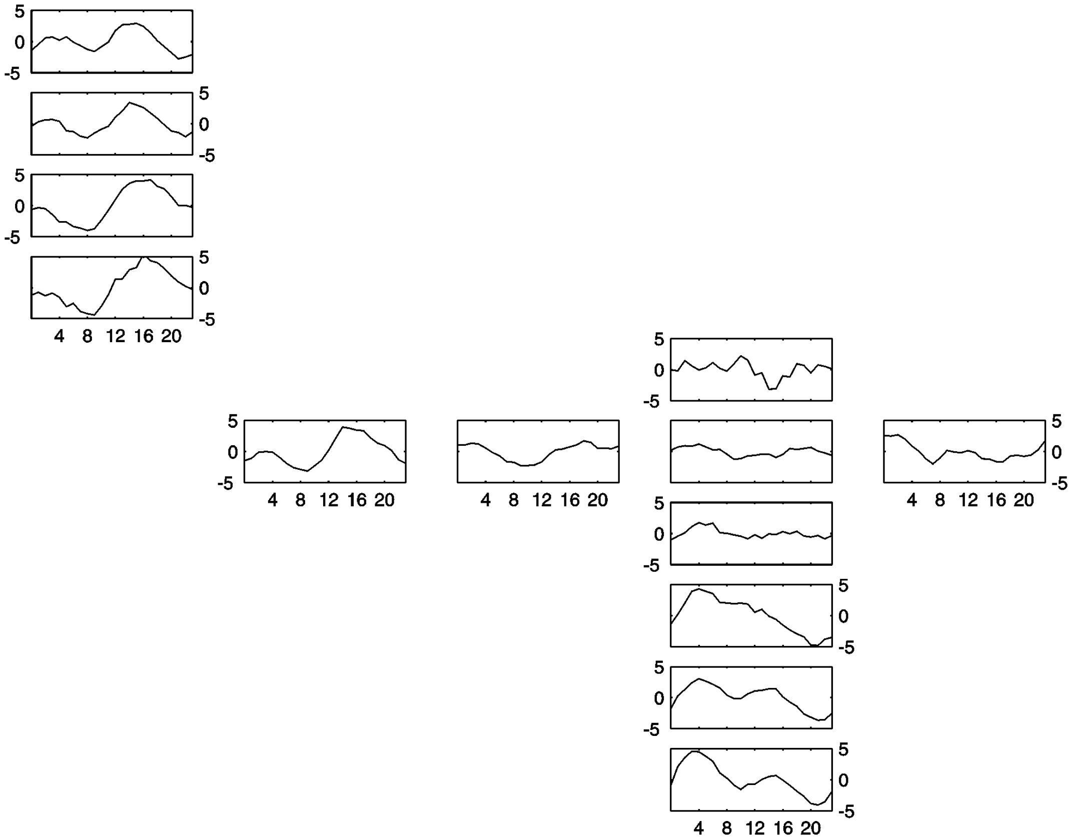

Figure 5.21 – Mean diurnal cycles of latent flux differences using hourly and daily wind speed. X-axis is time (hours) and Y-axis is Q^{lat} (Wm^{-2}).

5.5. Diurnal variability of heat fluxes in the Tropical Atlantic

5.5.1. Mean diurnal cycle

Air-sea fluxes derived from the observed variables (Figures 5.22 and 5.23) show some similarities with previous analyses performed in the tropical Pacific. Zeng and Dickinson (1998) showed that the diurnal cycle of Q_{sen} in the tropical Pacific has a minimum value at about 09:00 hrs with dual peaks on either side, closely correlated with the diurnal cycle of the surface-air temperature difference.

To calculate the diurnal cycle of heat fluxes in the tropical Atlantic, and based on the results obtained in Chapter 4 and in Section 5.4, the wind speed time series has the gaps filled by the average of the three satellite (QuikSCAT, TMI 11 GHz and TMI 37 GHz) wind speed retrievals for the day in question, which was then used as the mean daily wind speed. The sensible and latent heat fluxes were calculated using Zeng's algorithm (Zeng et al., 1998), as explained in Section 3.3.3. Hourly data time series for SST, Tair and RH were used, except for wind speed that was used as daily mean, following the discussions in the precious section. As in Section 5.3.1, the daily mean of the fluxes have been removed from each location, in order to isolate diurnal variations from other dominant signals such as the seasonal cycle in the tropical Atlantic. The mean diurnal cycle was calculated, which is basically the long term average for each hourly time step.

The maximum loss by Q_{sen} is at about 05:00 hrs, with a minimum loss at about 09:00 hrs (Figure 5.22). It is also noticeable that the two peaks in reduction of heat loss occur in early-evening (18:00 hrs) and late-evening (22:00 hrs). Those two peaks are also seen in the air-sea temperature difference diurnal cycle (Figure 5.7). It seems that the air-sea temperature difference controls the diurnal cycle of Q_{sen}.

In contrast, the diurnal cycle of Q_{lat} varies throughout the basin. The largest amplitudes of Q_{lat} (Figure 5.23) can be seen at the buoys located on the Equator, with maximum loss at mid-afternoon. The buoys at the extra-tropical region have the smallest amplitudes, with minimum loss of Q_{lat} in the mid-morning, probably associated with a small magnitude of SST diurnal cycle.

As the wind speed used in this calculation was daily wind speed, the role of sea surface temperature on the diurnal cycle of heat fluxes is apparent. The maximum loss of Q_{lat} is directly related to the mid-afternoon peak of SST. As SST increases, evaporation also increases and the ocean loses more heat. For Q_{sen}, the morning minima of SST is also directly related to the minimum loss as the air-sea temperature difference is minimised.

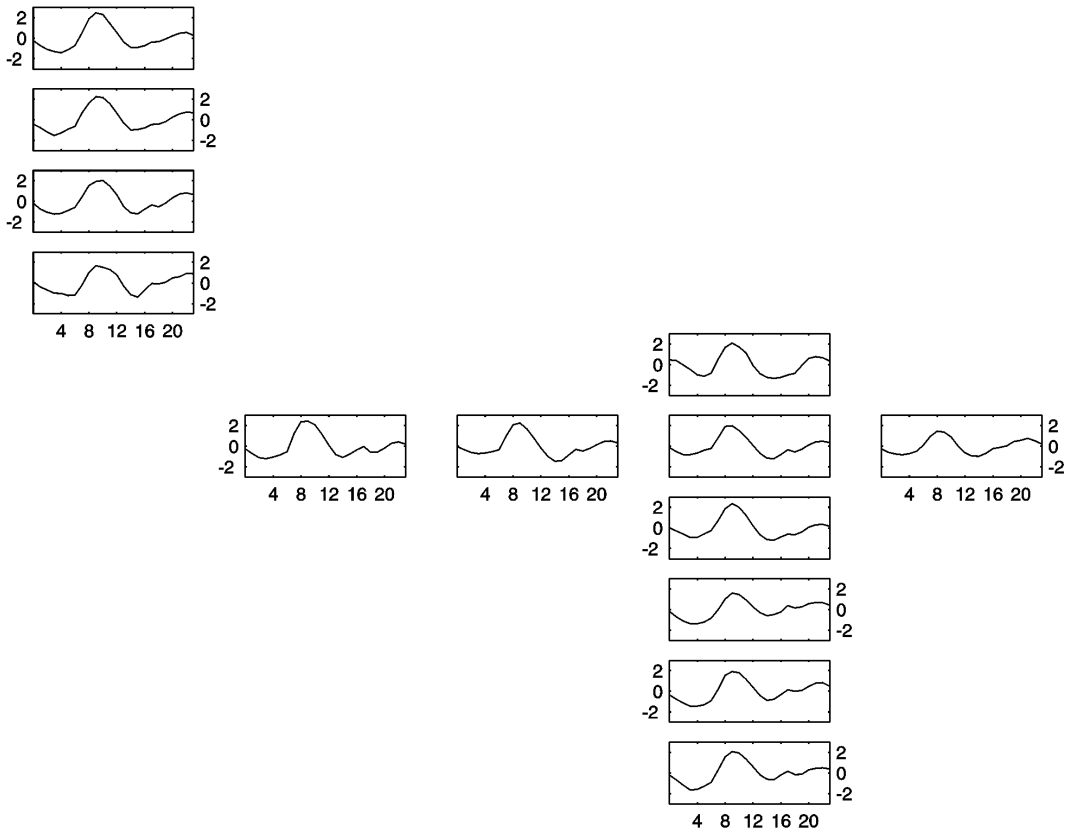

Figure 5.22 – Mean diurnal cycle of sensible heat flux in the tropical Atlantic. X-axis is given in hours. Y-axis shows values in Wm^{-2}.

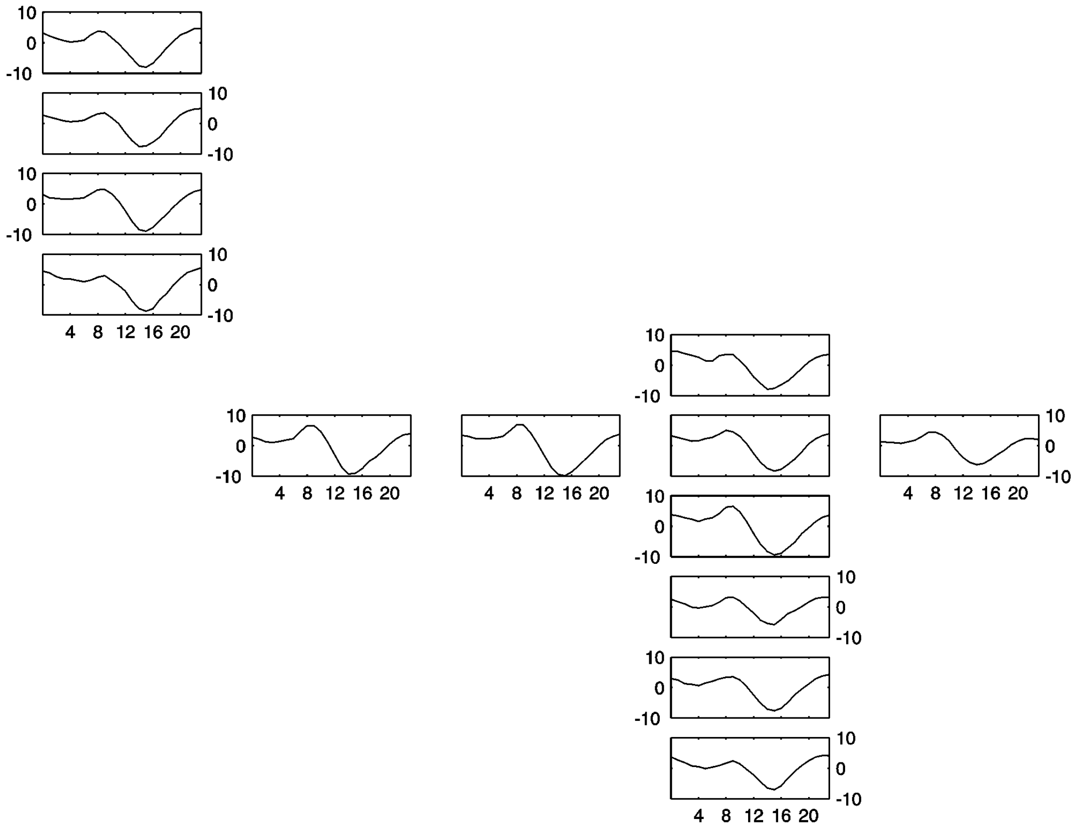

Figure 5.23 – Mean diurnal cycle of latent heat flux in the tropical Atlantic. X-axis is given in hours. Y-axis shows values in Wm^{-2}.

5.5.2 Seasonal variation of the diurnal cycle of heat fluxes

While the determination of seasonal periods of strong diurnal signal in met-ocean variables seems straightforward, with clear delimitation of parts of the year when strong diurnal variability occurs, the same does not happen with surface heat fluxes. Since the fluxes are an interaction of several variables, sometimes the periods of variability are not as obvious as might have been expected.

The analysis of the wavelet power spectrum for the sensible heat flux is shown in Figure 5.24. The diurnal signal of Q_{sen} can be seen clearly in the buoys located in the extra-equatorial region, and highly correlated with the air temperature diurnal signal (Figure 5.13), with periods of strong diurnal signal in summer in the northern hemisphere, and in winter in the southern hemisphere. The intrusion of the cold tongue in the southern hemisphere might lead to a stronger diurnal cycle of air temperature, which would increase the amplitude of air-sea temperature differences, due to day-warming and night-cooling. On the Equator, while it is still possible to discern periods of strong diurnal signal related to the diurnal cycle of air temperature, periods of weak diurnal cycle of air temperature seem to allow the diurnal cycle of sensible heat flux to be controlled by wind speed.

The latent heat flux diurnal cycle (Figure 5.25) presents a more composed pattern for the buoys in the extra-equatorial region, following the autumn-winter season of the respective hemispheres. During this time, the regions are characterised by a drop of incident heating and an increase of heat loss by latent heat. The strongest diurnal signals can be seen during September-March for the buoys in the northern hemisphere and April-September south of the Equator, following to some extent the diurnal cycle of relative humidity. On the Equator, the diurnal cycle of latent heat flux tend to be more uniform, due mainly to the low amplitudes of the seasonal cycle.

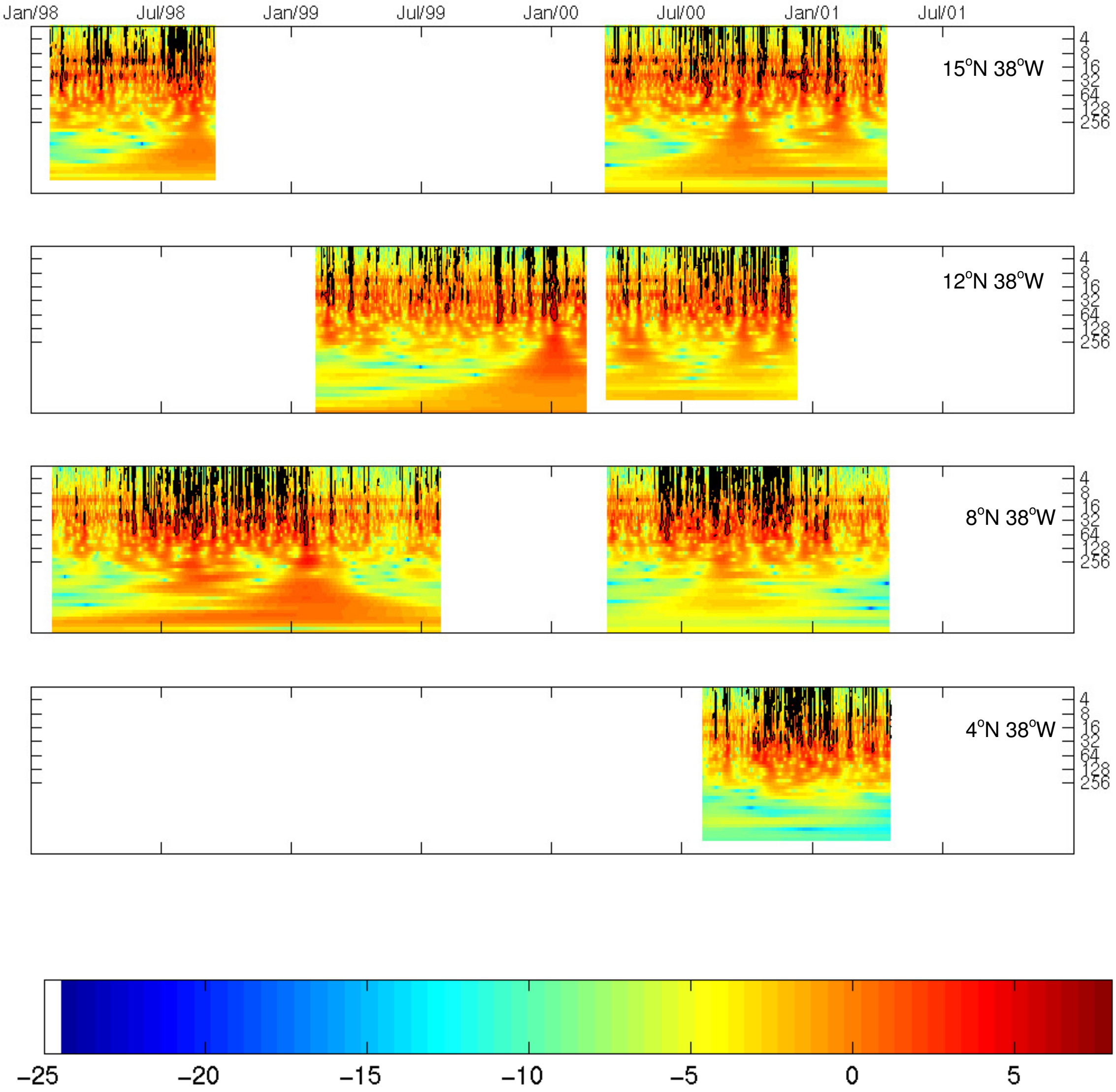

Figure 5.24a – Sensible heat flux wavelet power spectra for the PIRATA buoys. Y-axis is the period in hours. The colorbar unit is $(Wm^{-2})^2$. Black contour lines are the 95% confidence level.

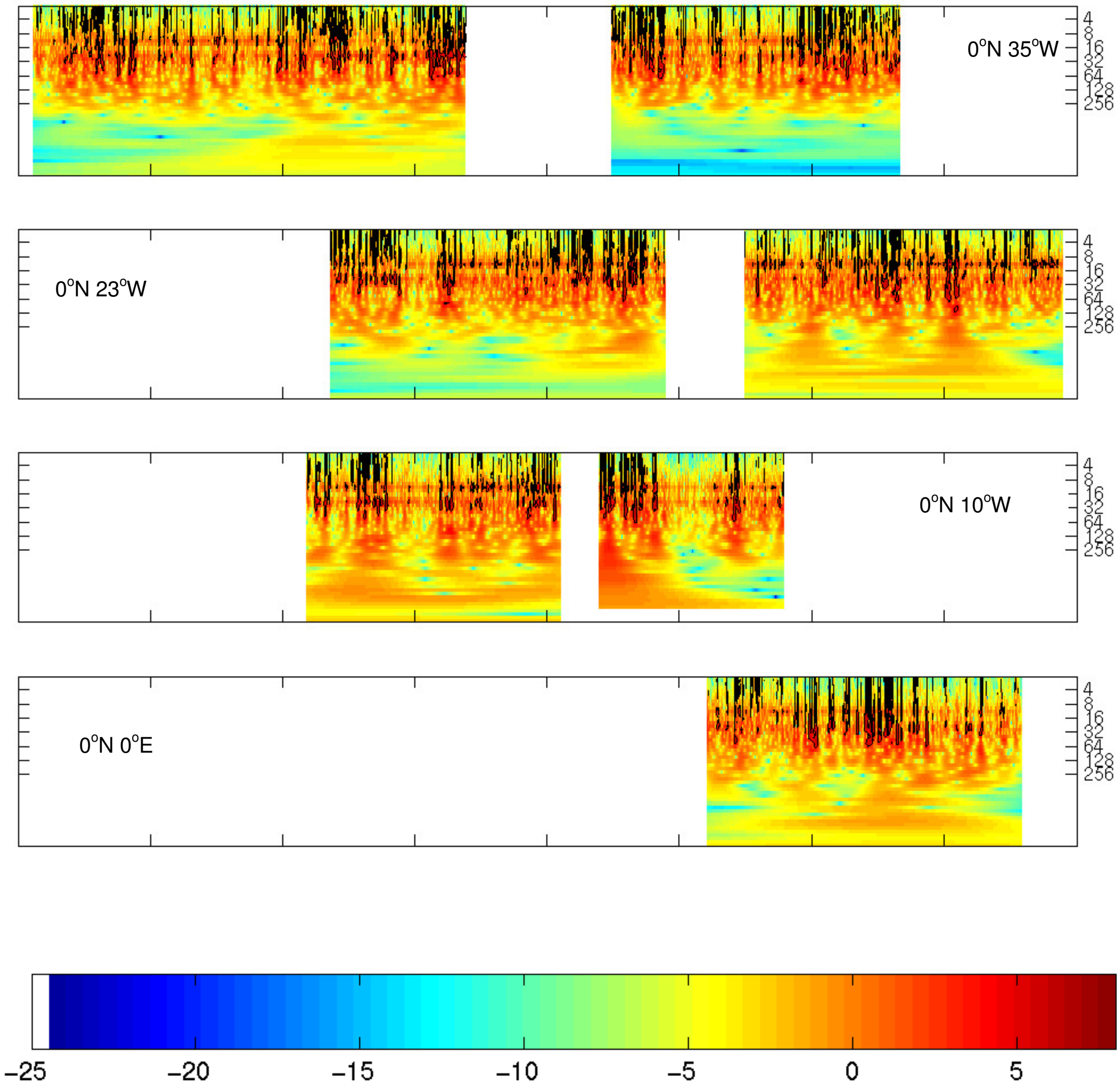

Figure 5.24b – Sensible heat flux wavelet power spectra for the PIRATA buoys. Y-axis is the period in hours. The colorbar unit is $(Wm^{-2})^2$. Black contour lines are the 95% confidence level.

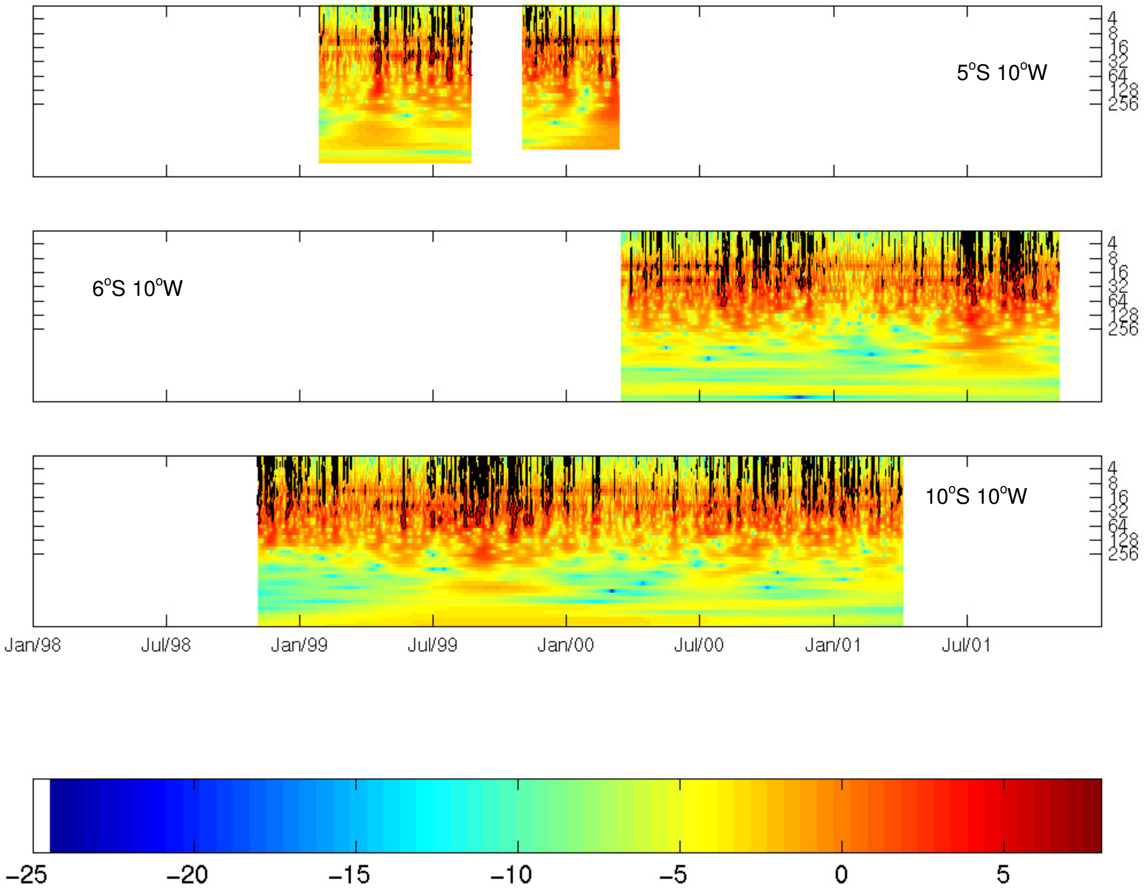

Figure 5.24c – Sensible heat flux wavelet power spectra for the PIRATA buoys. Y-axis is the period in hours. The colorbar unit is $(Wm^{-2})^2$. Black contour lines are the 95% confidence level.

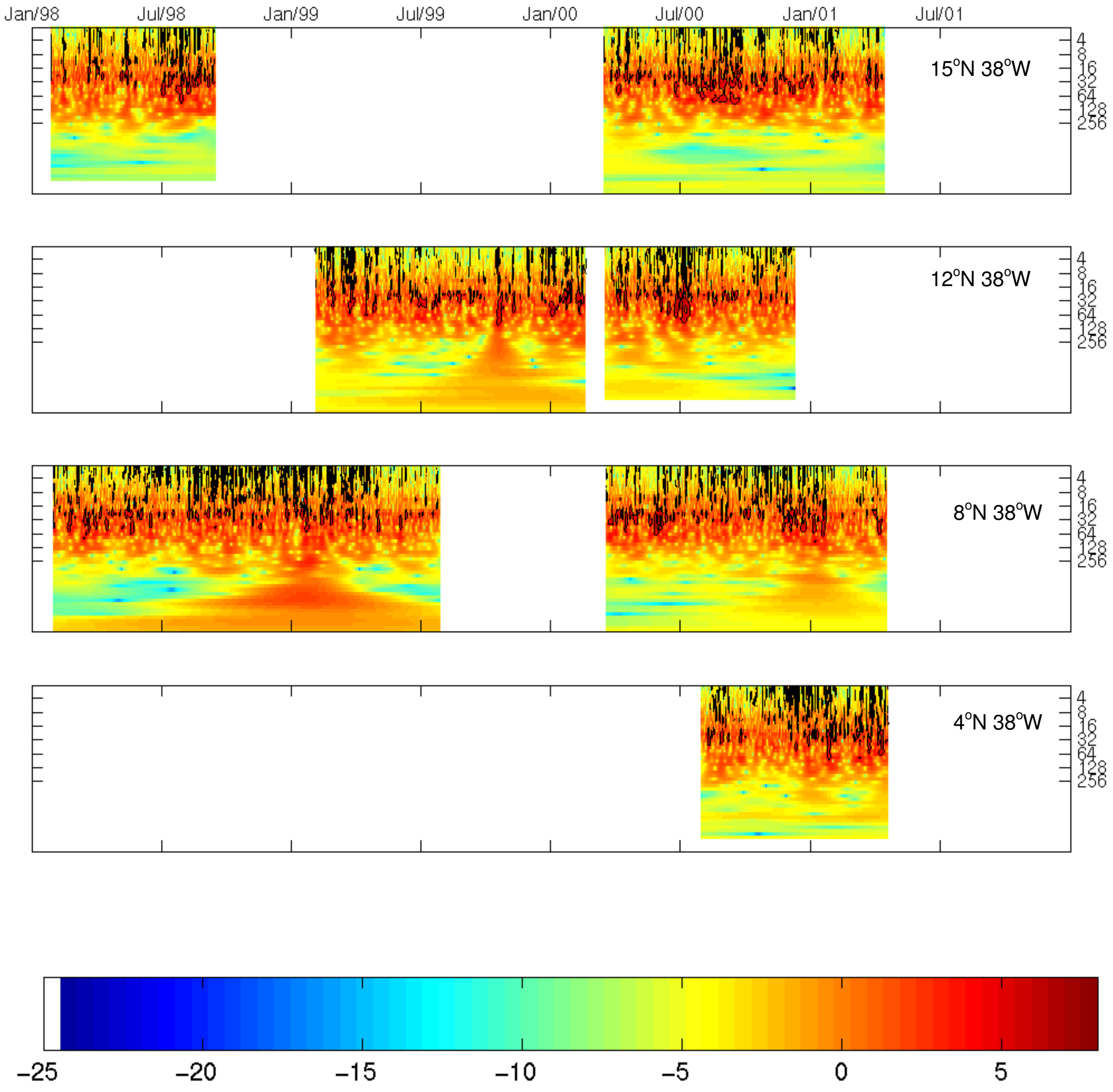

Figure 5.25a – Latent heat flux wavelet power spectra for the PIRATA buoys. Y-axis is the period in hours. The colorbar unit is $(Wm^{-2})^2$. Black contour lines are the 95% confidence level.

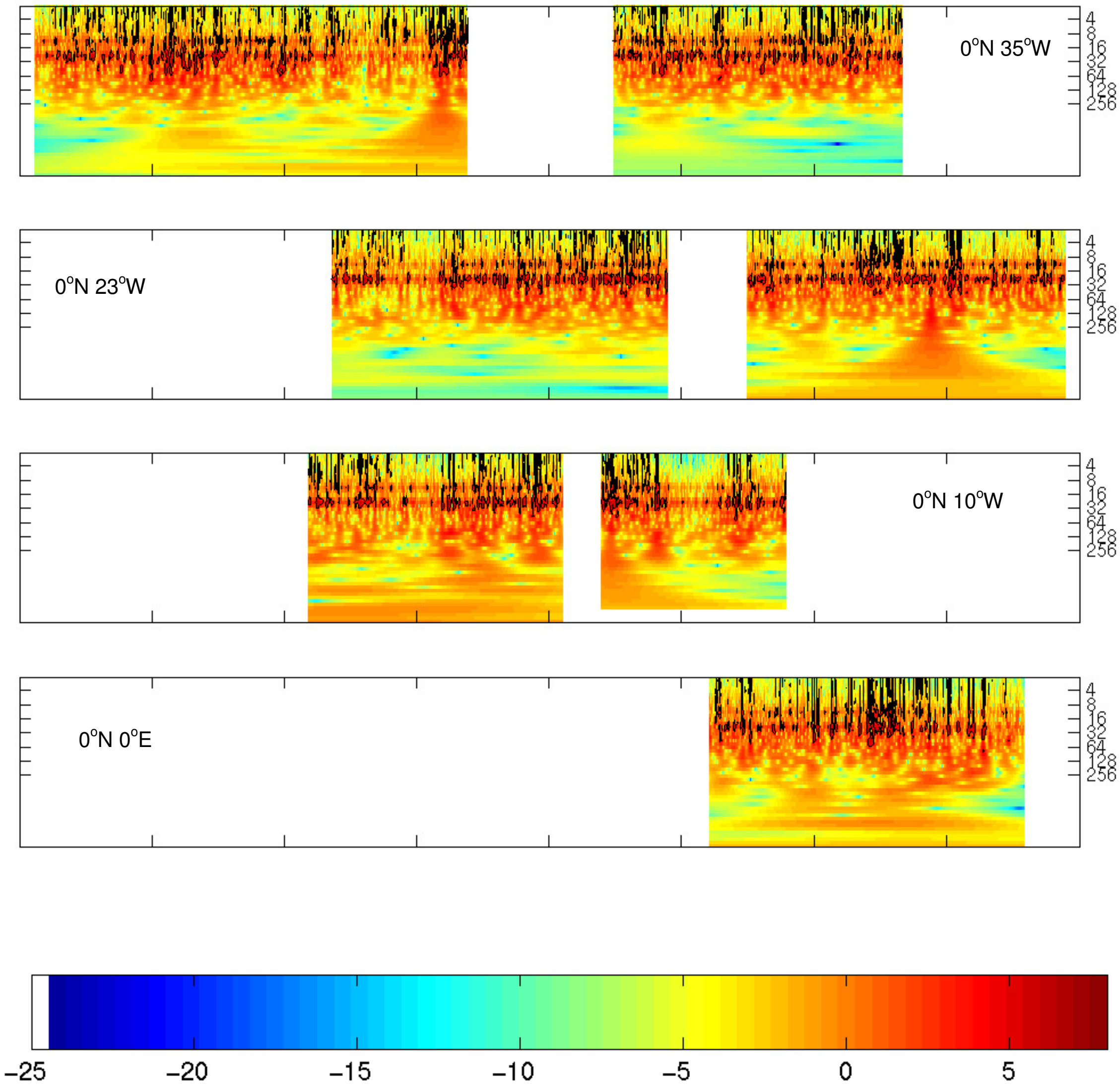

Figure 5.25b – Latent heat flux wavelet power spectra for the PIRATA buoys. Y-axis is the period in hours. The colorbar unit is $(Wm^{-2})^2$. Black contour lines are the 95% confidence level.

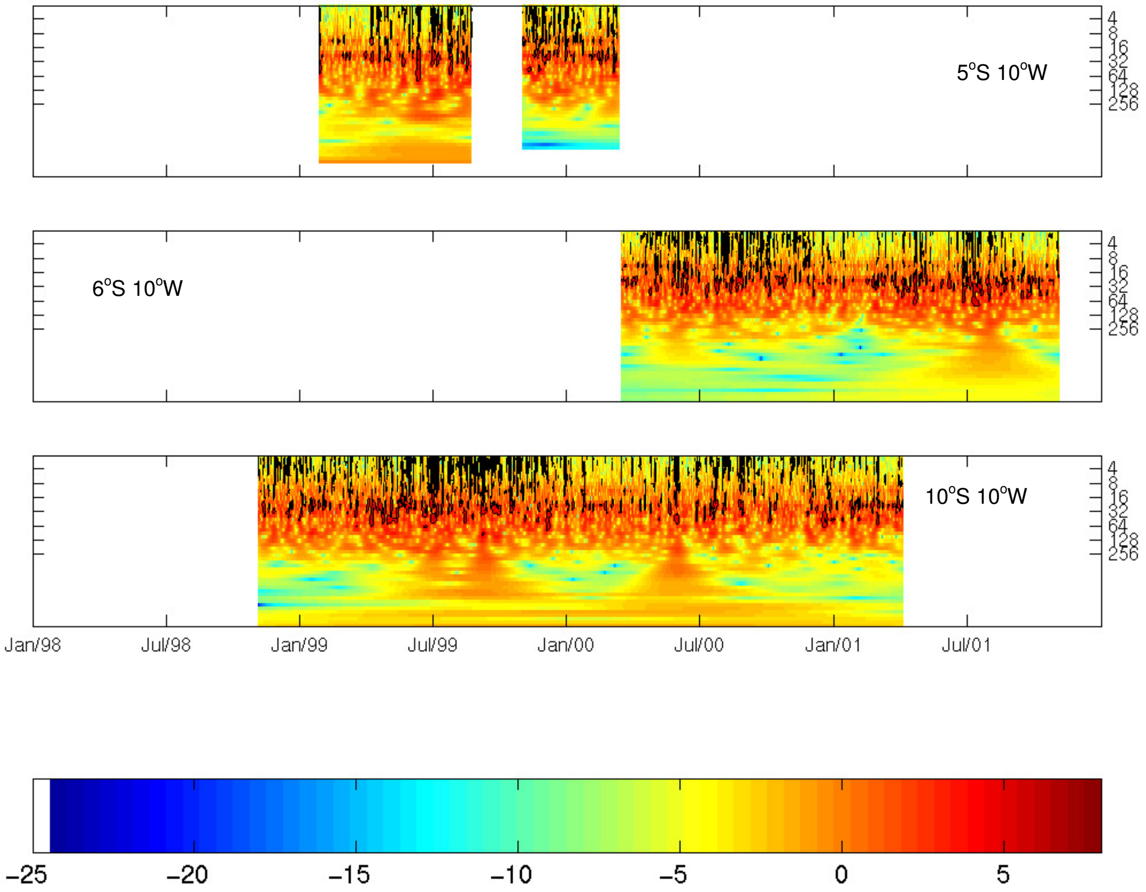

Figure 5.25c – Latent heat flux wavelet power spectra for the PIRATA buoys. Y-axis is the period in hours. The colorbar unit is $(Wm^{-2})^2$. Black contour lines are the 95% confidence level.

5.6. Summary

This chapter has analysed the diurnal cycle of meteo-ocean variables measured by the PIRATA buoys, in order to characterise for the first time the mean diurnal cycle in the tropical Atlantic. Moreover, the diurnal cycle of heat fluxes have also been shown.

One interesting characteristic observed was that, although the phase of the mean diurnal cycle of SST is almost the same for the whole basin, the mean diurnal cycle of wind speed is very variable, which could indicate that it cannot control the phase alone. However, the relationship of the wind speed change, defined as ∂(wind)/∂t, with SST is very similar for the buoys analysed, which would indicate that the way the wind speed changes, in particular the morning wind, tend to control the SST phase. The magnitude of the afternoon maximum of SST would then be tuned by insolation and local SST conditions.

A complete picture of the seasonal variability of the diurnal signal was also developed. The SST diurnal signal presents strong characteristics during the respective summer in both hemispheres. However, through the wavelet technique used in this analysis, significant diurnal signal could be noticed at the equator during the second half of the years, indicating a possible modulation of the diurnal signal by processes with different timescales. It is suggested that Tropical Instability Waves could be one of these processes and its influence on the diurnal signal will be analysed in Chapter 7.

Another important contribution achieved with the results in this chapter was the analysis of the Impact of the use of daily wind on the calculation of hourly surface heat fluxes. As gaps in the hourly wind speed time series from the buoys is a problem, especially in the calculation of heat fluxes, it has been tested the impact that daily winds have on the hourly heat fluxes, in order to validate the use of satellite winds to fill those gaps. It has been shown that the errors introduced have similar magnitudes to those estimated for inaccurate measurements of the bulk variables by the *in situ* sensors, as shown in Section 4.3.

Chapter 6

Tropical Instability Waves

6.1. Introduction

This thesis has so far investigated the diurnal cycle of meteo-ocean variables in the tropical Atlantic, characterising its spatial distribution in the region by using the high-resolution data available form the PIRATA moorings, and studying the seasonal variation. In the previous chapter, it was suggested that processes on other timescales may modulate the SST diurnal signal. One of these processes that are not yet fully investigated in the tropical Atlantic are the Tropical Instability Waves (TIW).

In this chapter, the temporal and spatial variabilities associated with the TIW in the tropical Atlantic are explored, and their spectral characteristics examined. Moreover, this is the first study that investigates interannual variations of the TIW in the Atlantic basin using high-quality satellite data. These datasets also allow a complete assessment of the co-variability of geophysical fields measured by satellite and that can be affected by the instability waves.

As explained in Chapter 2, there is still a vast field of research regarding TIW in the tropical Atlantic. This chapter, which will show results of an observational study of the TIW using satellite data, aims to make an important contribution for this field of research.

6.2 TIW signal in the sea surface temperature fields

The baroclinic component of the TIW is directly associated with the extension of the cold tongue and, in particular, with the thermal gradient generated between the cold tongue and the warmer waters in a north position of the cold tongue. Figure 6.1 shows examples of the TIW for different years on this study.

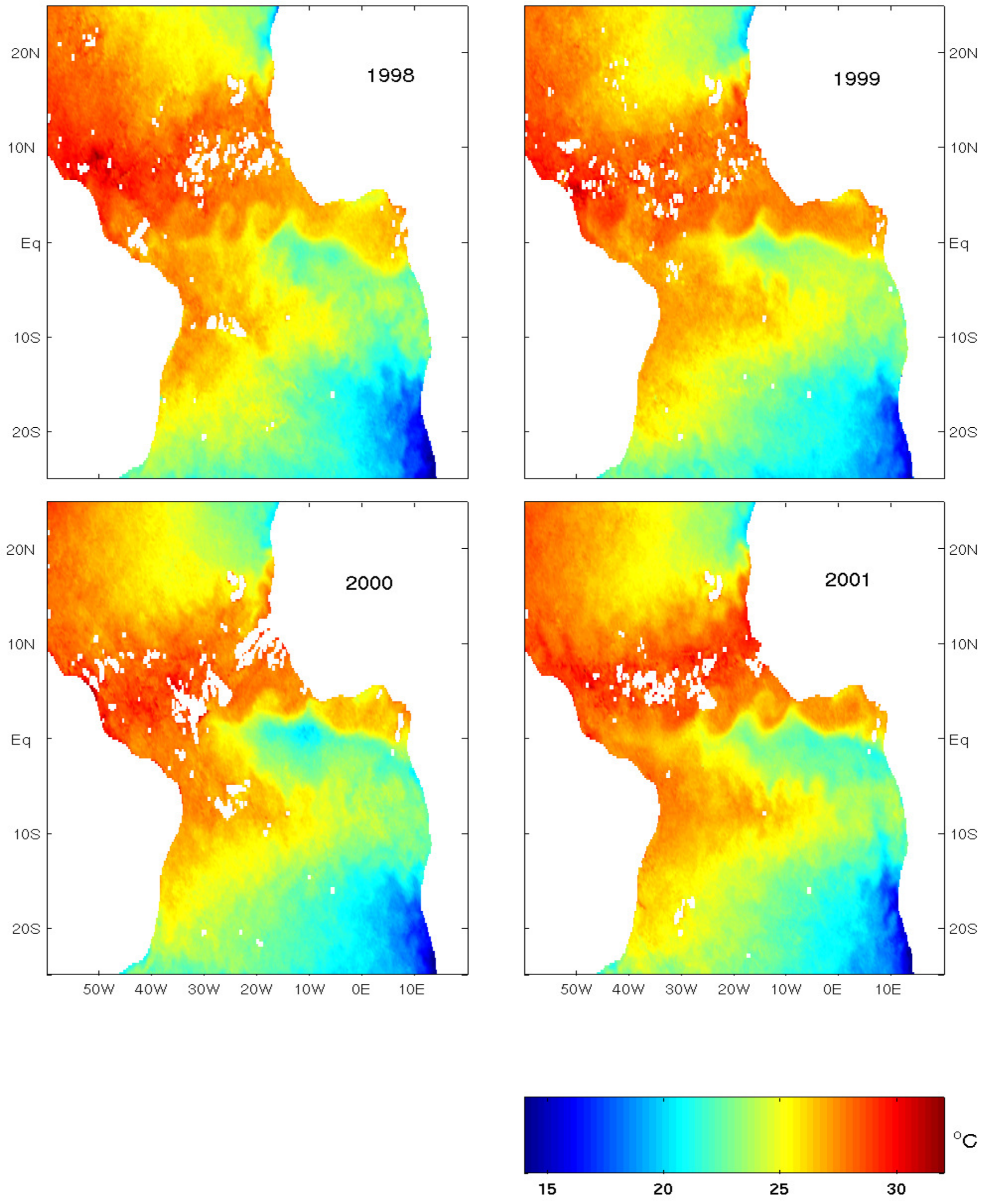

Figure 6.1 – Example of TMI SST 3-day mean composites for the years of 1998, 1999, 2000 and 2001.

Figure 6.2 presents the time-longitude plots of SST derived from TMI for five different latitudes (Equator, 1°N, 2°N, 3° N and 4°N) in the tropical Atlantic. For these analyses, SST daily maps were averaged in 3-day mean composites, spanning four years (1998 – 2001). The only processing needed to be applied to this dataset was to fill any gaps, existent due to strong rain, by applying a mean moving window of 3x3 grid points.

Even without any filtering, it is possible to see westward propagating features in the last six month of each of the years, when the Atlantic cold tongue is well developed. The variation with year and latitude of the TIW signatures can be clearly observed in the plots. In 1999, the cold tongue was not very well developed in which case the more energetic region of TIW is observed around 1° N and after July. However, in 2000, the cold tongue appears well developed. The regions where the high gradients and high instability can be observed are displaced somewhat further north (2° N) when compared to the previous years. Also, the cold tongue starts to develop earlier, in late May.

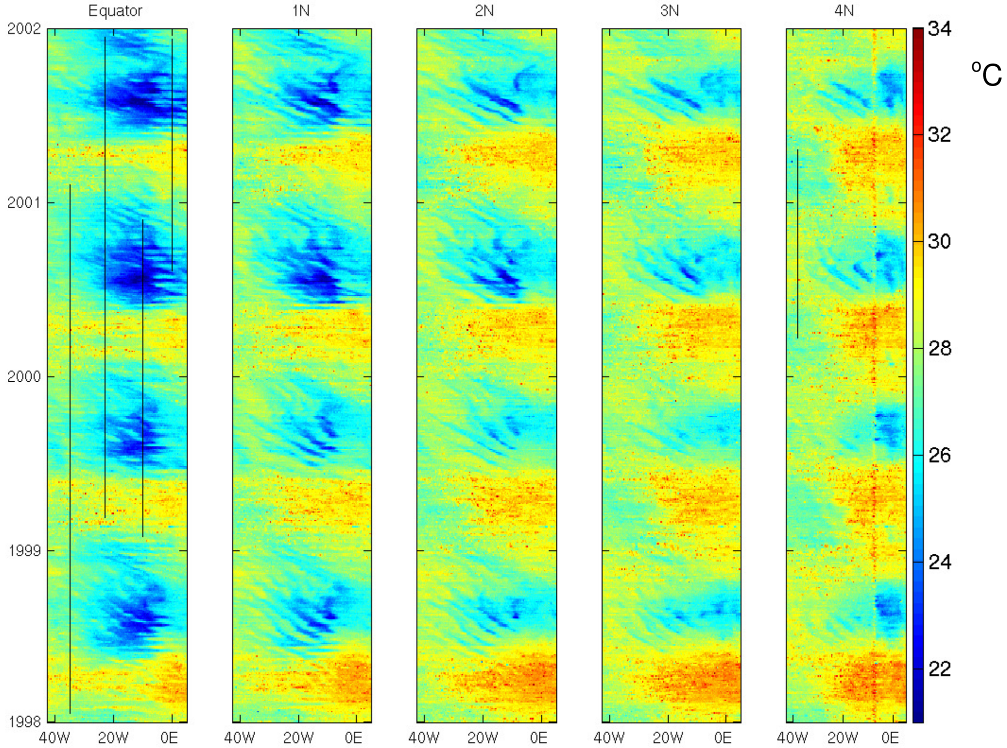

Figure 6.2 – Time-longitude plots of TMI SST data at the Equator, 1°N, 2°N, 3° N and 4°N. SST is in °C. Black lines show the position and length of the SST data from the PIRATA buoys.

In order to isolate the TIW variability from other strong temperature signals found in the region, such as the seasonal cycle, a filtering scheme was used. The filter applied was a westward-only 2-D finite impulse response (FIR) filter, following the method employed by Cipollini et al. (2001). The filter is designed using prior knowledge of the approximate range of the period and wavelength of the waves. This information is set as input and restricts the filter output to a particular region of the frequency-wavelength spectrum. It has a 1 / 4 length size sample kernel, with a bandpass of 5° to 20° in the longitude and 20 to 40 days in time.

Figure 6.3 shows the SST time-longitude filtered fields based on the same data as Figure 6.2. It shows that the filter effectively removes any signal propagating to the east and other variability signals, including the cold tongue itself. The results suggest that TIW in the tropical Atlantic have their largest variability at 1°N and 2°N and around 15°W. Northward, the TIW signals are still visible but less intense, with the exception of 2001 when the waves are still very active at 4°N. At the Equator, although that is the region where it is possible to find the largest development of the cold tongue (Figure 6.2), the TIW display a weaker signal. This is because the instabilities are created at the SST front between the colder upwelling water of the Atlantic equatorial cold tongue and the warmer water to the north, and not at the core of the cold tongue. This same mechanism has been observed in the tropical Pacific (Miller et al., 1985; Flament et al., 1996; Kennan and Flament, 2000).

TIW vary in exact location and phase velocity (Liu et al., 2000). With the intention of quantifying the TIW variability in space and time, the statistical standard deviation based on the entire period is calculated. The top panel on the lefthand side of Figure 6.4 shows the standard deviation completed for each latitude, derived from the entire period (1998-2001). The results confirm that the maximum SST variability occurs at 1°N and around 15°W.

The remaining panels in Figure 6.4 display the standard deviation of SST derived year-by-year, to show the TIW interannual variability at different latitudes and years. They show that the TIW variability in the tropical Atlantic is more active at 1°N, without much influence of the magnitude of the cold tongue. However, it should also be noticed that in 2001 at 2°N and 3°N, the signals associated with TIW were stronger than previous years at those latitudes. This shows that, in addition to a well developed cold tongue, the perturbations in the SST front were larger, therefore being visible further north.

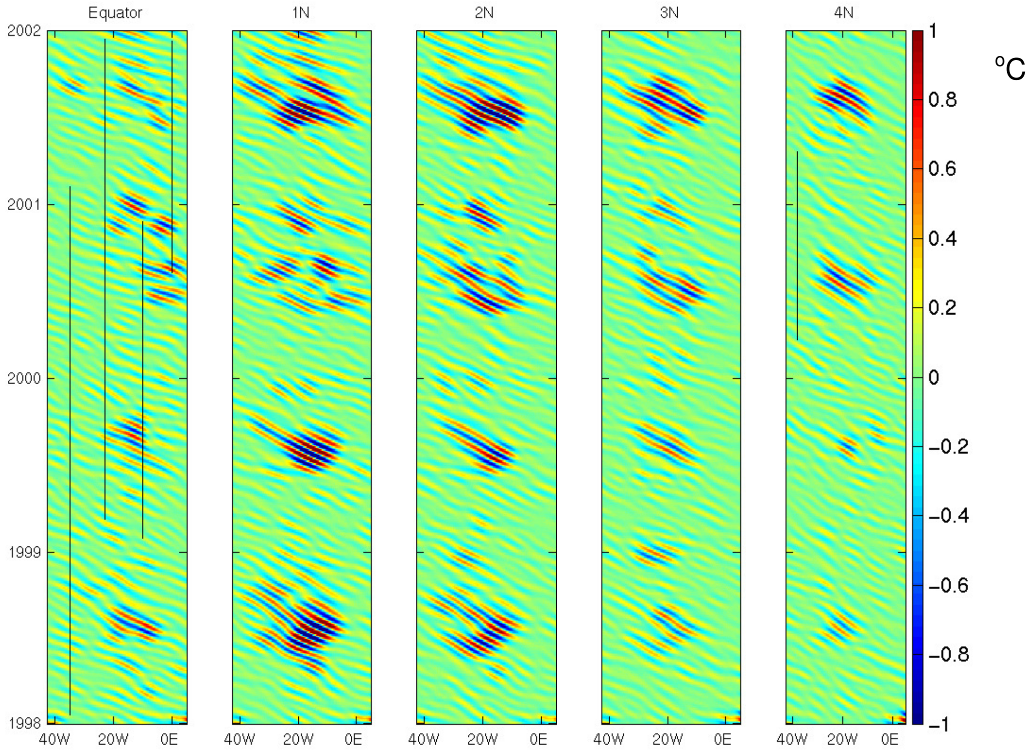

Figure 6.3 – Time-longitude plots of filtered TMI SST data at the Equator, 1°N, 2°N, 3° N and 4°N. SST is in °C. Black lines show the position and length of the SST data from the PIRATA buoys.

These interannual variabilities are summarised in Table 6.1, which shows the spectral characteristics of TIW for two latitudes. The waves have their largest amplitudes at 1°N. As can be seen, the characteristics vary from year to year, depending on the strength of the equatorial upwelling. It suggests that for periods of strong upwelling we can observe longer wavelengths and higher wave speed. The spectral characteristics at 4°N will differentiate from those at 1°N depending mostly on how well marked and developed are the waves themselves.

As a general rule, the more developed the waves, the more similar are the characteristics at these two different latitudes. The better examples are the results for 1998 and 2001, when the TIW signals can be distinguished further north (Figure 6.1) when compared with previous years. Due to the geographical features of the tropical Atlantic region, the condition of the TIW development will have a greater impact on the meteorological fields in the whole basin, in particular on the region of the ITCZ.

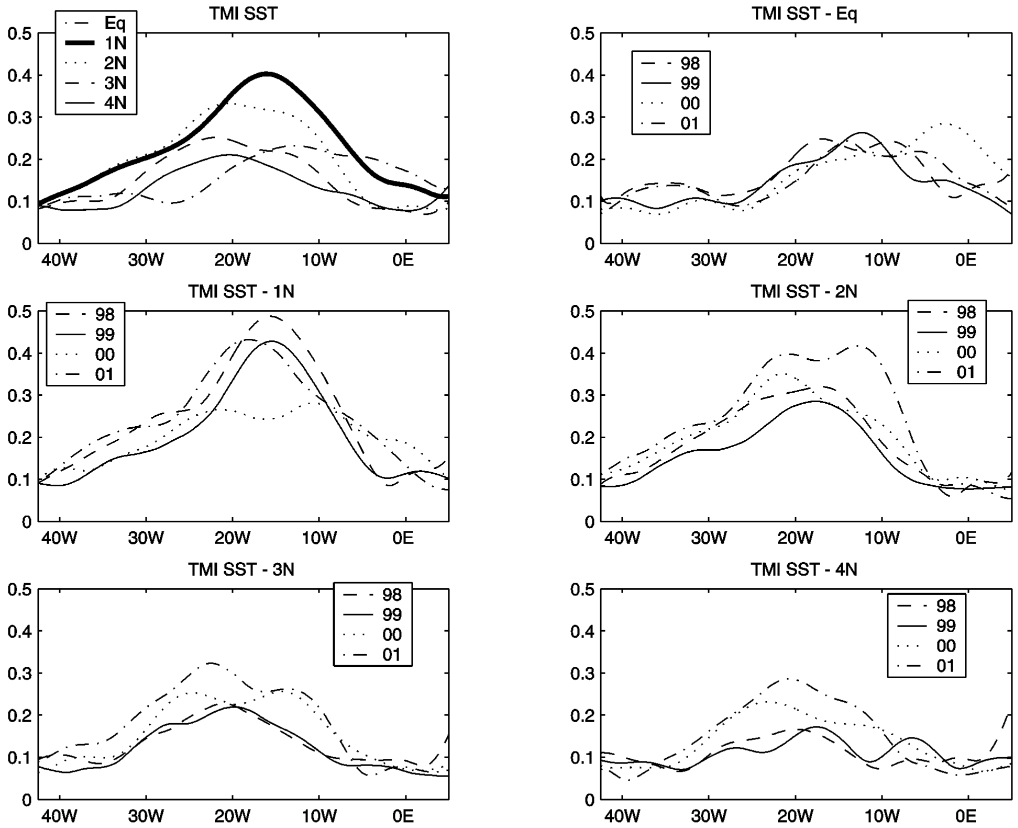

Figure 6.4 – Standard deviation of SST for several latitudes at the tropical Atlantic Ocean. Top left panel shows the standard deviation of the time series spanning from 1998 to 2001 for the latitudes of equator, 1°N, 2°N, 3°N and 4°N.The remaining panels are each zonally averaged for the same latitudes as above, and for the different years.

Table 6.1. – Spectral characteristics of TIW at 1°N and 4°N.

	1°N			**4°N**		
	Wave speed ($cm\ s^{-1}$)	**Wavelength (degrees)**	**Period (days)**	**Wave speed ($cm\ s^{-1}$)**	**Wavelength (degrees)**	**Period (days)**
1998	31	7.9	33	35	7.9	31
1999	40	9.5	31	67	11.9	21
2000	61	11.9	24	35	9.5	37
2001	40	9.5	33	43	9.5	30

As it can also be observed in Figure 6.1, for the years of 1999 and 2000, the waves are not well developed, and the spectral characteristics are highly distinct between 1°N and 4°N (Table 6.1). The difference between these two years is that the frontal thermal region is located at different latitudes: more south in 1999 and more north in 2000. For these two years, the spectral characteristics are similar two the other years depending on where the front is more active, i.e. at 1°N in 1999 and at 4°N in 2000.

The spectral characteristics of TIW in the Atlantic obtained by this study and presented in Table 6.1 are corroborated by previous observations. However, most of those observational studies are based on data from single locations, usually on the equator, and are derived from shorter records. Still, they yield information about the spatial extent of the TIW. Weisberg and Weingartner (1988) found that TIW have a central periodicity of 25 days, on the equator at 28°W, with phase speed between 10 – 50 cm s^{-1} and wavelengths of around 10°. Steger and Carton (1991) also showed similar results. Compared with the tropical Pacific, these characteristics are similar. Pezzi (2003) showed that TIW at 1°N in the Pacific presented in 1999 a phase speed of 55 cm s^{-1}, wavelength of 11° and period of 30 days, similar to the results presented by Hashizume et al. (2001). These slight differences between the two equatorial oceans are suggested to be due to the different shape of the oceans, with a higher influence of the continents in the Atlantic case.

Previous theoretical studies, Philander (1978) for the tropical Atlantic and Cox (1980) for the tropical Atlantic, showed that the westward propagating instabilities, generated by the shear between the North Equatorial Countercurrent (NECC) and the northern branch of the South Equatorial Current (nSEC), have a period of around 1 month and wavelength of 10°. More recently, Jochum et al. (2004) showed that the wavelength of the TIW can vary from 700 to 1100 km, with a phase speed variation of 30 to 50 cm s^{-1}. The physical reason to expect a certain range in the wave properties is that these instabilities are generated by barotropically unstable flows. Therefore it is possible for the TIW properties to have a range of values.

Moreover, the characteristics of TIW due to the thermal gradient north of the equator, as investigated in this work, have not been shown for the whole tropical Atlantic. These results show that the instabilities associated with the thermal gradient have the same characteristics of those generated by the shear of the surface currents, highlighting that they also contribute to the variability of the TIW.

6.3. TIW signal in the wind fields

In the tropics, surface wind and SST are tightly coupled and their interactions give rise to rich space-time structures of the tropical climate and its variability (Neelin et al., 1998; Xie et al., 1998). While it is well established that changes in tropical SST lead to changes in surface wind, the responsible mechanisms are not well understood, partly because of insufficient observations over the remote tropical oceans.

Global measurements of vector wind by satellite scatterometers allow the determination of space time structure of TIW-induced wind variability, as demonstrated by Xie et al. (1998) and Contreras (2002) with the European Remote Sensing (ERS) scatterometer. Also, by applying various statistical techniques to the QuikSCAT data, Liu et al. (2000), Chelton et al. (2001) and Hashizume et al. (2001) showed that the trade wind acceleration is more or less in phase with SST variability, in support of the vertical mixing mechanism.

Figure 6.5 shows the wind magnitude derived from QuikSCAT in a time-longitude plot. This shows that the TIW also have a westward propagating signal in the wind fields, although it is not as clear as in the SST plots. This was expected because of the more rapid changes observed in wind than in SST. Nevertheless, the TIW signals can be enhanced by filtering out the lower frequency component of the wind magnitude field as shown in Figure 6.6, applying the same filter as in Figure 6.3.

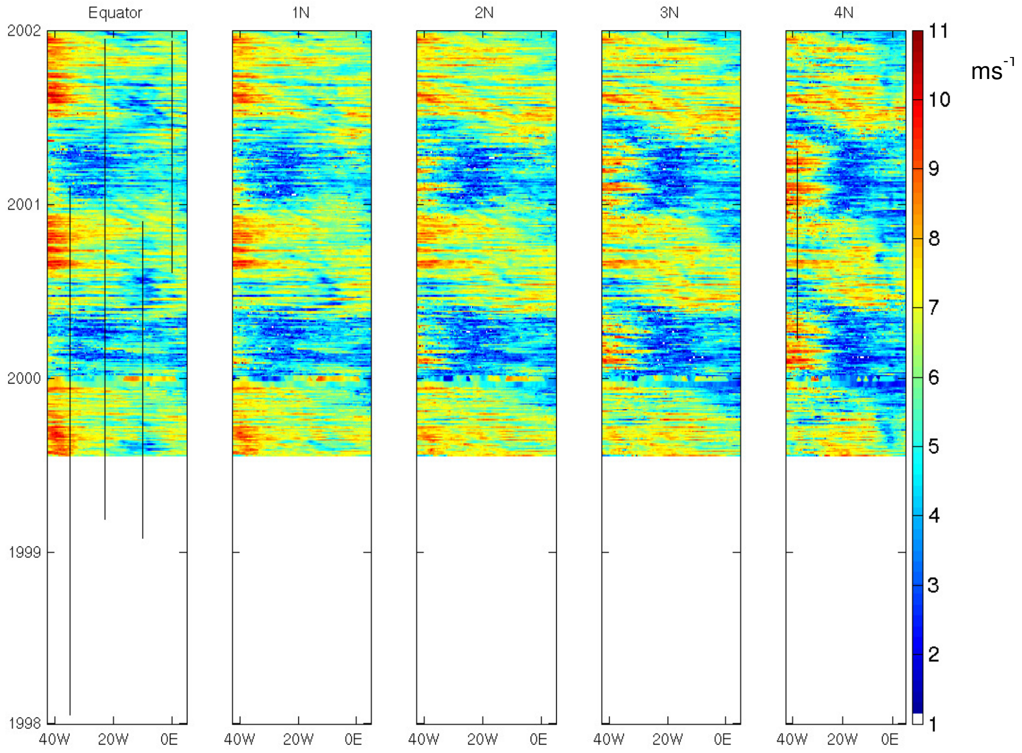

Figure 6.5 – Time-longitude plots of filtered Qscat wind speed data at the equator, 1°N, 2°N, 3° N and 4°N. Wind speed is in ms^{-1}. Black lines show the position and length of the SST data from the PIRATA buoys.

It is noticeable that the imprints of TIW in the wind speed fields are clearer in 2000 and 2001, when the cold tongue was well established. Spatially, the centre of maximum variability is displaced further north, at around 3°N, as shown by the plots in Figure 6.7. Unfortunately, this analysis is limited by the QuikSCAT data used in this study, spanning from the second half of 1999 until the end of 2001, leaving only two complete years of data. As explained in Section 3.2.2.1.1, and because further analyses will require vectorial wind data, TMI wind speed is not used here. Temporally, it does not show large differences between those two years. On the other hand, it highlights the features observed in Figure 6.4, where in 2001, it is possible to observe the influence of TIW signals reaching regions located at 4°N.

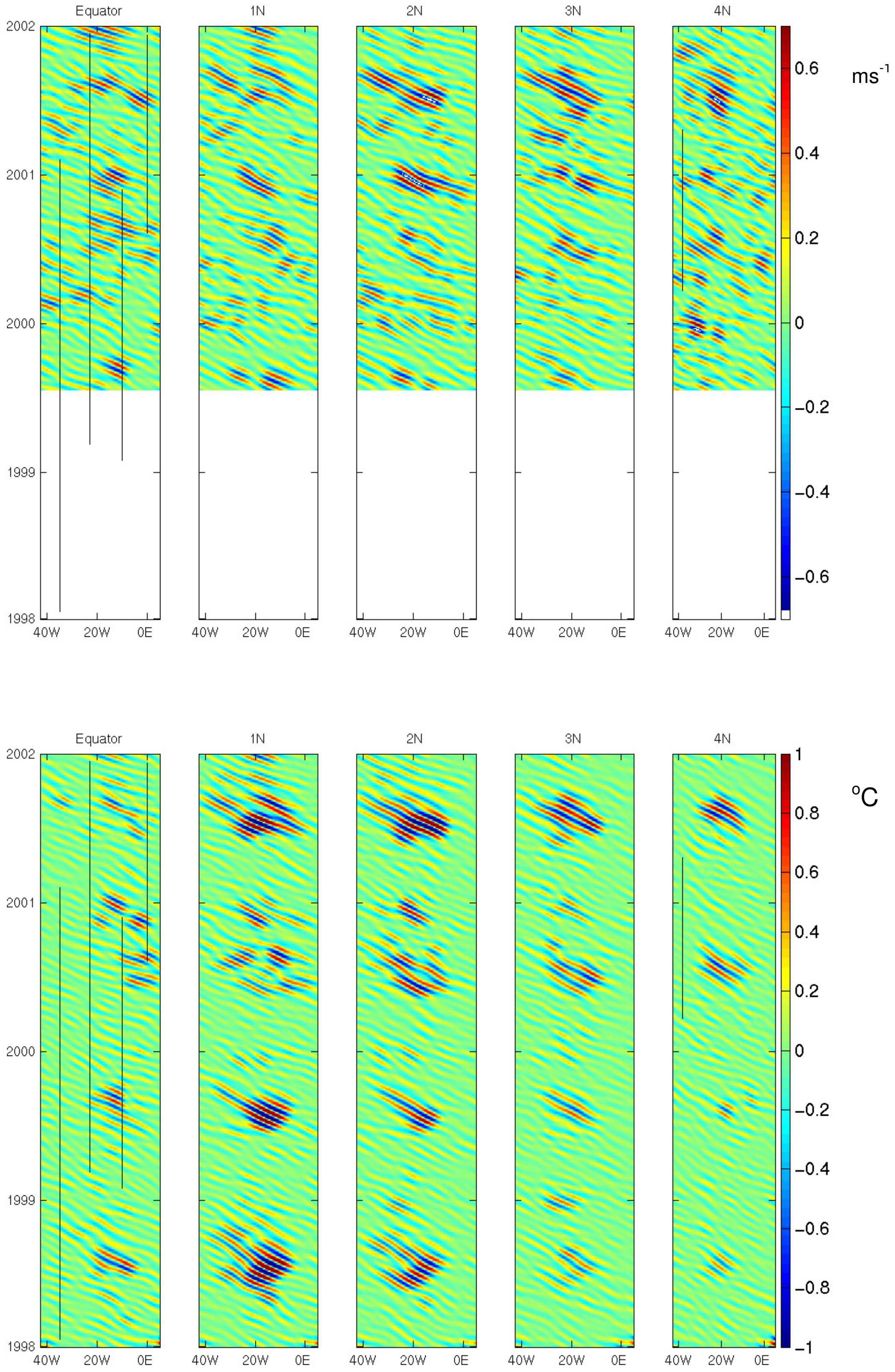

Figure 6.6 – Time-longitude plots of filtered data at the Equator, 1^{o}N, 2^{o}N, 3^{o} N and 4^{o}N for QuikScat wind speed in ms^{-1} (top panels) and TMI SST in ^{o}C (bottom panels). Vertical black lines show the position and length of the SST data from the PIRATA buoys.

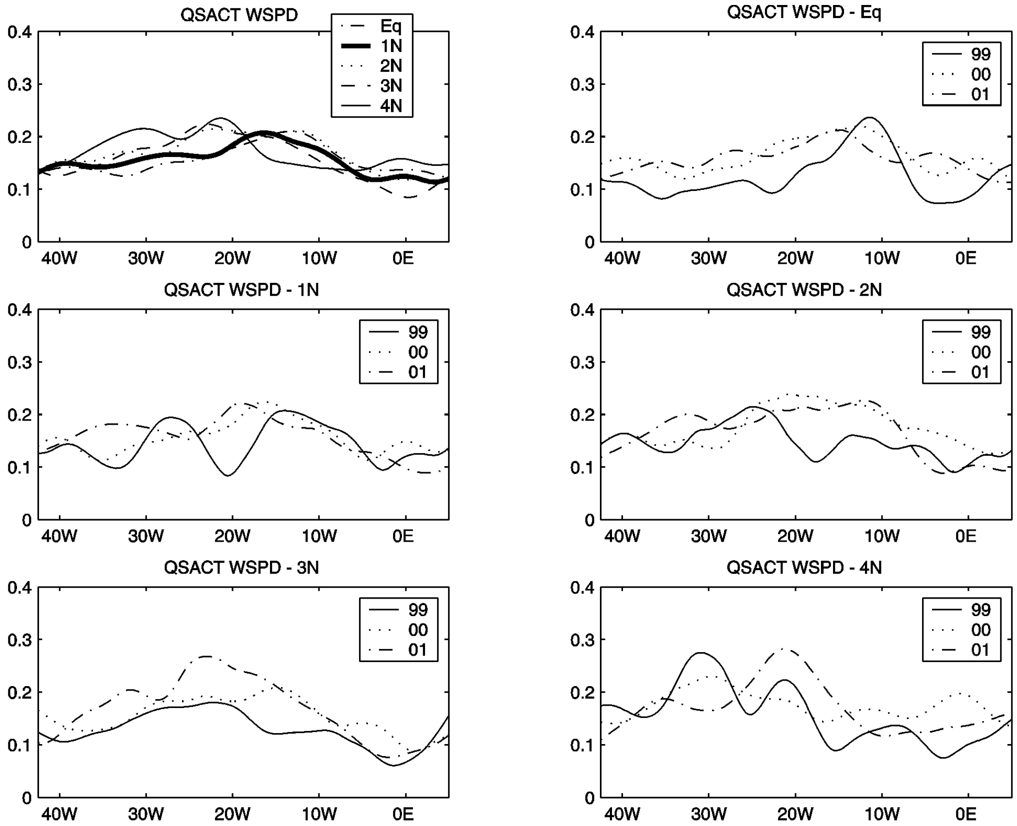

Figure 6.7 – Standard deviation of QuikSCAT wind speed data for several latitudes at the tropical Atlantic Ocean. Top left panel shows the standard deviation of the time series spanning from 1998 to 2001 for the latitudes of equator, 1°N, 2°N, 3°N and 4°N.The remaining panels are each zonally averaged for the same latitudes as above, and for the different years.

The zonal and meridional components of wind also show the influence of TIW as presented in Figures 6.8 and 6.9. Comparison between them shows a slight difference in the regions where the components are affected. The meridional wind shows a larger influence around the Equator and 1°N while the zonal wind seems to be a little more affected at 3°N and 4°N. Although care is needed with the results for 1999 due to its short time series, scrutiny of Figures 6.10 and 6.11 emphasizes the observations noted above, which are probably due to the larger contribution of the meridional component closer to the Equator.

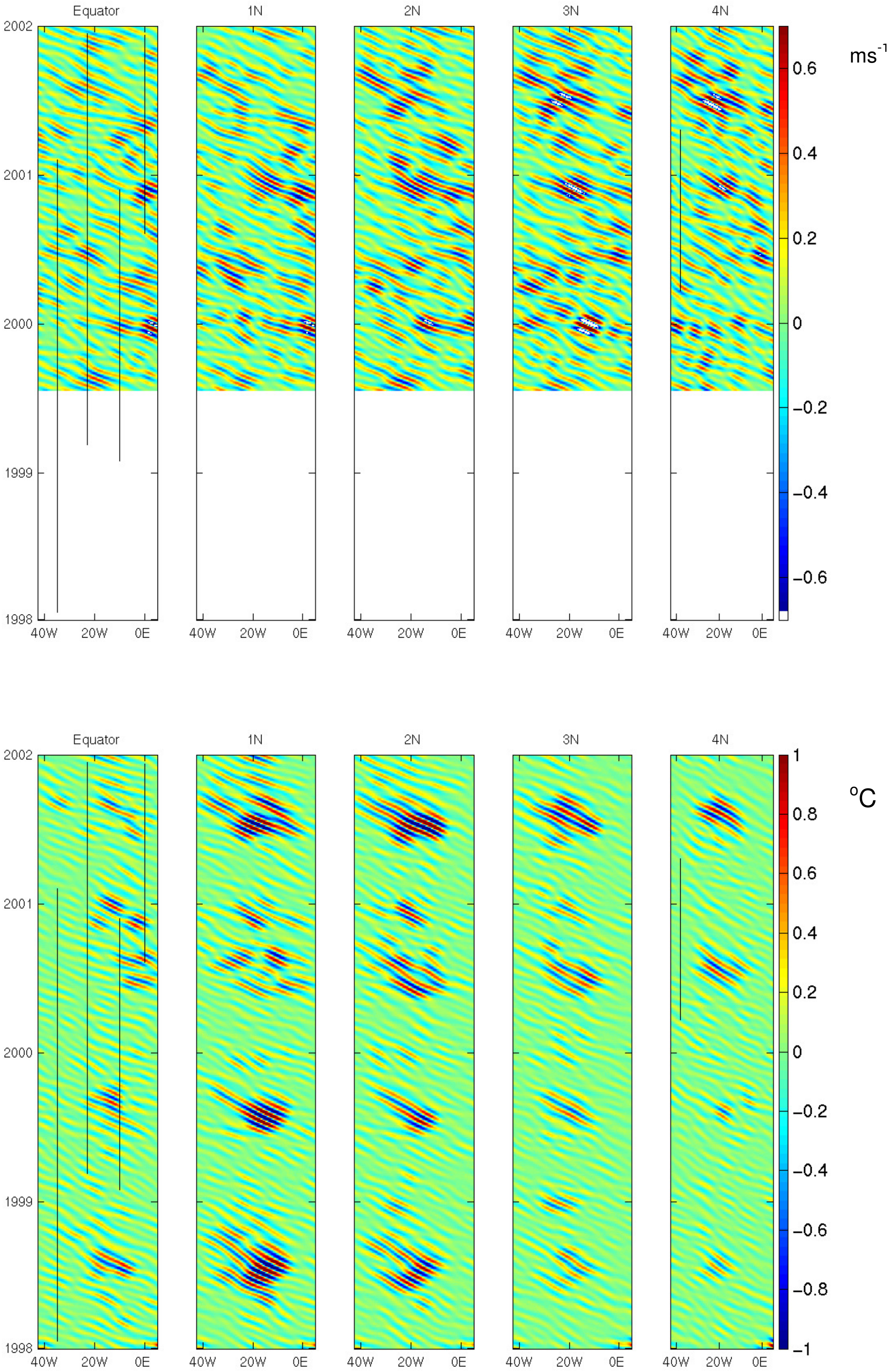

Figure 6.8 – Time-longitude plots of filtered data at the Equator, 1°N, 2°N, 3° N and 4°N for QuikScat zonal wind in ms^{-1} (top panels) and TMI SST in °C (bottom panels). Vertical black lines show the position and length of the SST data from the PIRATA buoys.

These results suggest that the coupling mechanism between SST and wind through the stability change in the atmospheric boundary layer, as illustrated by Hayes et al. (1989) and Wallace et al. (1989), is supported here. This hypothesis says that over warm waters, surface winds increase as a consequence of increased mixing and reduction of wind shear in the boundary layer. It will lead to the increase of the northward and eastward components of surface wind due to the turbulent mixing reaching down to the surface over warm water. The results are that the zonal component will be 180^{o} out of phase and the meridional component will be in phase with SST. These hypotheses will be further discussed in the next section.

6.4. Co-variability of fields with TIW signal

As shown in the previous section, TIW signals can be observed in atmospheric fields as well as in the SST. Two distinct hypothetical mechanisms of this coupled variability were proposed by Lindzen and Nigam (1987) and by Wallace et al. (1989), using data from the tropical Pacific. In this section, by using spacebased data from TMI and QuickSCAT, these two hypotheses are discussed and evaluated for the tropical Atlantic.

In order to carry out these analyses, anomaly fields of SST, integrated water vapour (VAP), rain and cloud liquid water (CLD) from TMI (1998 to 2001), and zonal (U) and meridional (V) wind from QuickSCAT (2000 and 2001) were computed by using the same 2-D finite impulse response (FIR) filter, described by Cipollini et al. (2001), and used in the previous sections. In order to map the spatial structure of the coupled TIW, a linear regression technique has been used, which searches for a linear relation between one of the filtered atmospheric fields F(x,y,t) and filtered SST at a reference station T(t):

$$F = aT \qquad (6.1)$$

A least squares fitting leads to the regression coefficient,

$$a(x,y) = \sum_{n=1}^{N} F(x,y,t_n) T(t_n) / \sum_{n=1}^{N} T^2(t_n) \qquad (6.2)$$

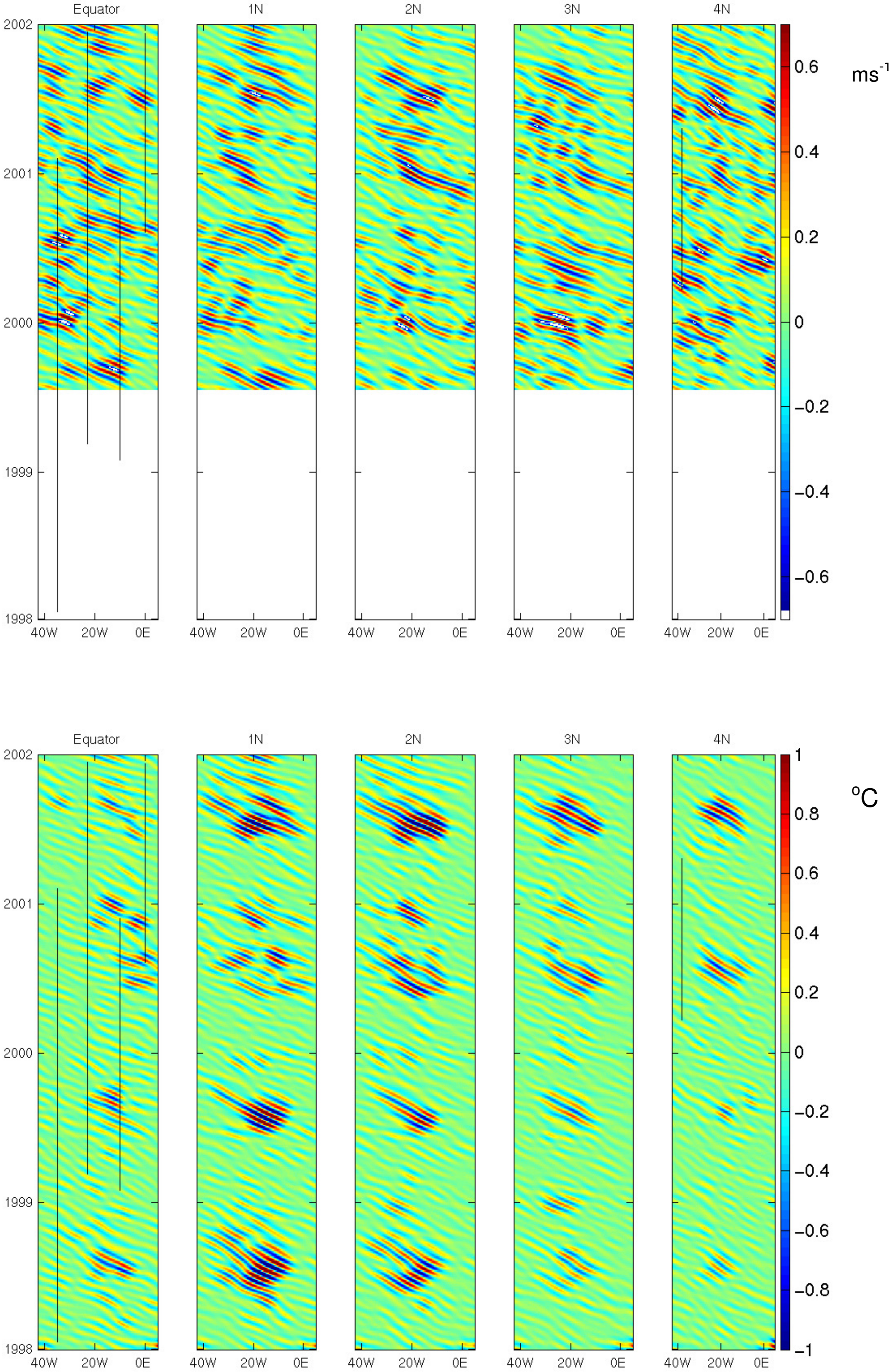

Figure 6.9 – Time-longitude plots of filtered data at the Equator, 1^{o}N, 2^{o}N, 3^{o} N and 4^{o}N for QuikScat meridional wind in ms^{-1} (top panels) and TMI SST in ^{o}C (bottom panels). Vertical black lines show the position and length of the SST data from the PIRATA buoys.

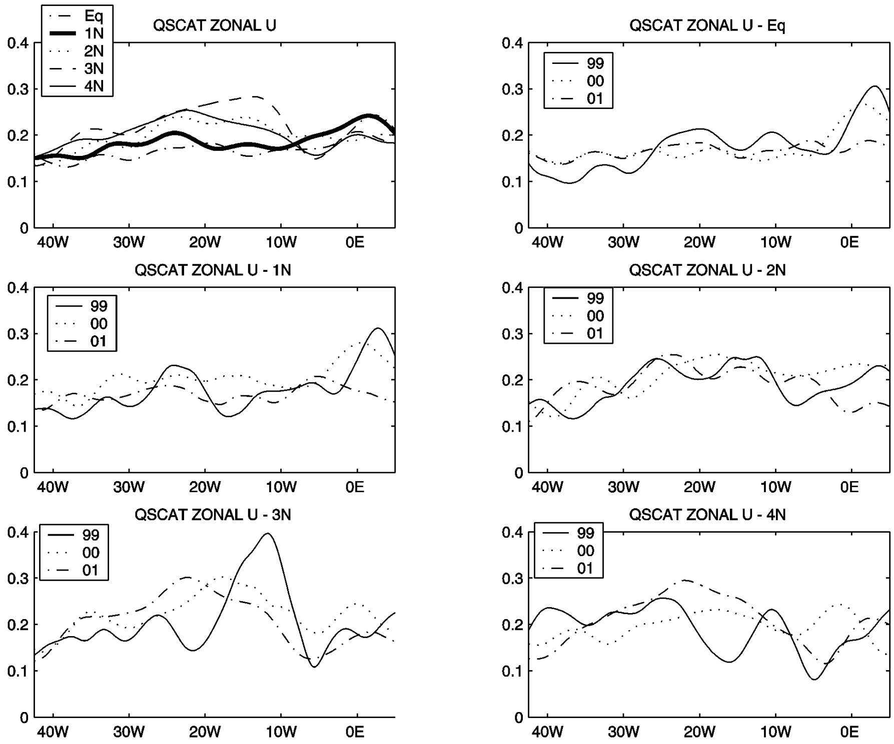

Figure 6.10 – Standard deviation of QuikSCAT zonal wind for several latitudes at the tropical Atlantic Ocean. Top left panel shows the standard deviation of the time series spanning from 1998 to 2001 for the latitudes of equator, 1°N, 2°N, 3°N and 4°N.The remaining panels are each zonally averaged for the same latitudes as above, and for the different years.

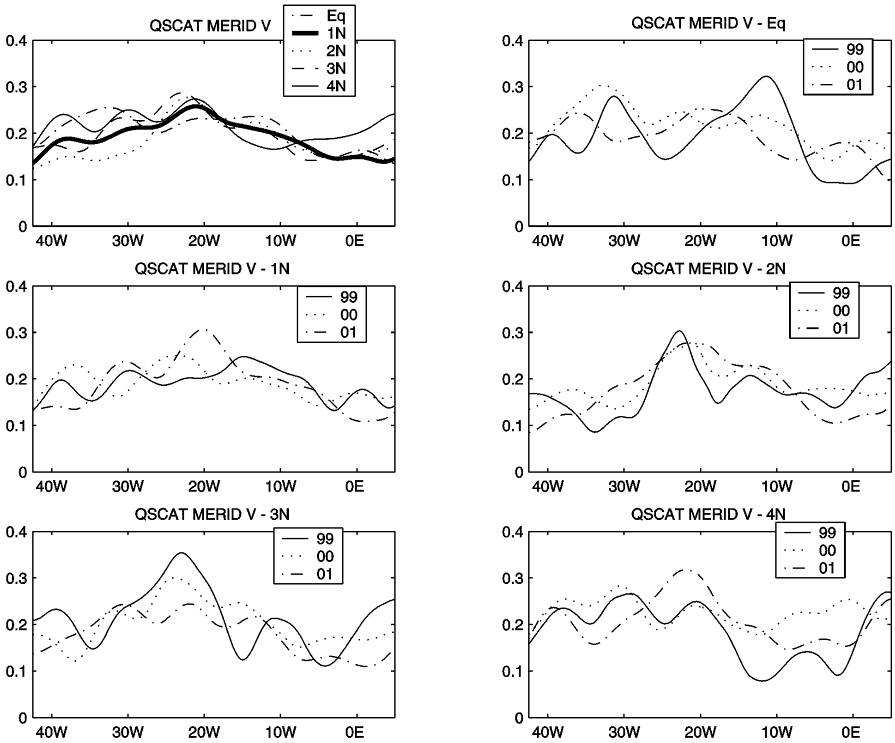

Figure 6.11 – Standard deviation of QuikSCAT meridional wind for several latitudes at the tropical Atlantic Ocean. Top left panel shows the standard deviation of the time series spanning from 1998 to 2001 for the latitudes of equator, 1°N, 2°N, 3°N and 4°N.The remaining panels are each zonally averaged for the same latitudes as above, and for the different years.

This regression technique is suitable for extracting regional characteristics, and has been successfully used by Hashizume et al. (2001). Because SST varies on much shorter timescales than other variables, the atmospheric fields will be regressed onto the SST time series at a chosen grid point, which is defined as the grid point with maximum SST variability. From the analysis in the previous sections, this point has been defined as being at 1°N and 15°W.

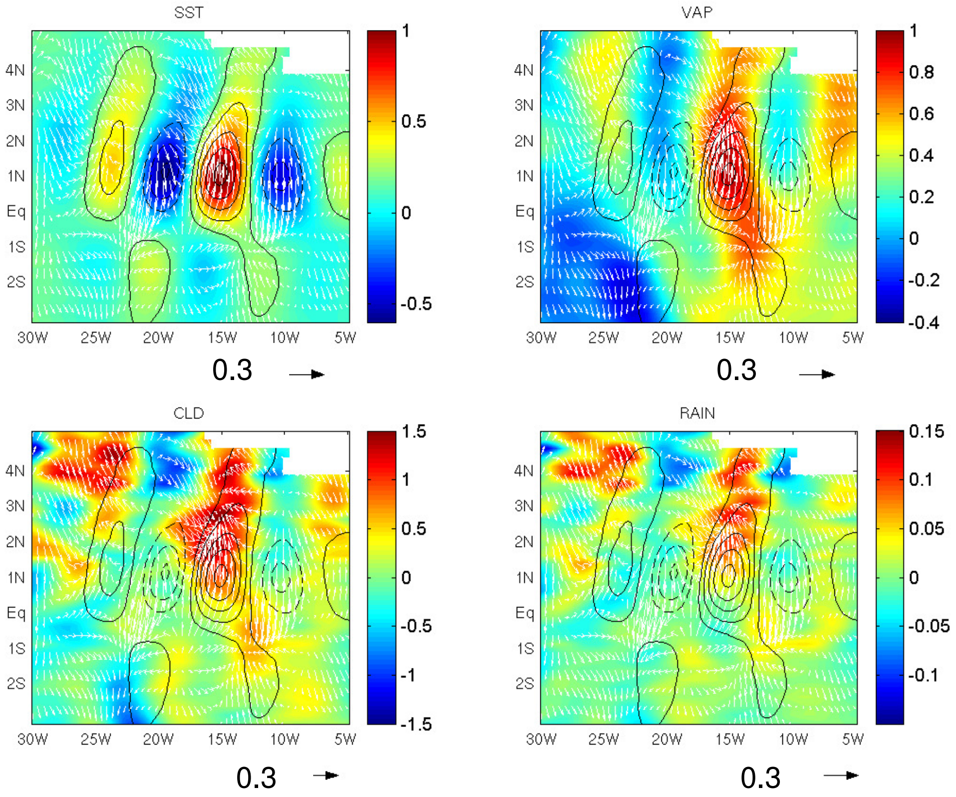

Figure 6.12 – Regression maps for SST, VAP (mm $^{o}C^{-1}$), CLD (10^{-2} mm $^{o}C^{-1}$) and rain (mm hr^{-1} $^{o}C^{-1}$). SST contours are plotted in all graphs. Vectors are for wind velocity. Black arrow shows wind velocity approximate to 0.3 m s^{-1} $^{o}C^{-1}$.

Figure 6.12 shows the regression maps for all the variables, for the entire period available. SST, VAP, CLD and RAIN data used were available from 1998 to 2001. Wind components were available for 2000 and 2001. As expected, the SST anomalies are confined between the equator and 2°N. Wind velocities are highly correlated with SST. In the tropical Atlantic, the meridional component dominates the wind field, so its reaction to the SST anomalies follows the acceleration southwards (northwards) over cold (warm) water.

VAP regression seems to be in phase with SST and meridional wind. These results are consistent with the hypothesis described by (Wallace et al., 1989), that buoyancy-induced mixing reduces wind shear in the boundary layer. The longitudinal variations presented in Figure 6.13 essentially reinforce those findings. From Figure 6.12, it is noticeable that wind moves across isotherms of SST, accelerating and decelerating, causing convergence and divergence. Wind convergence feeds moisture up into the atmosphere, and the increase of water vapour may be caused by both the surface warming and wind advection.

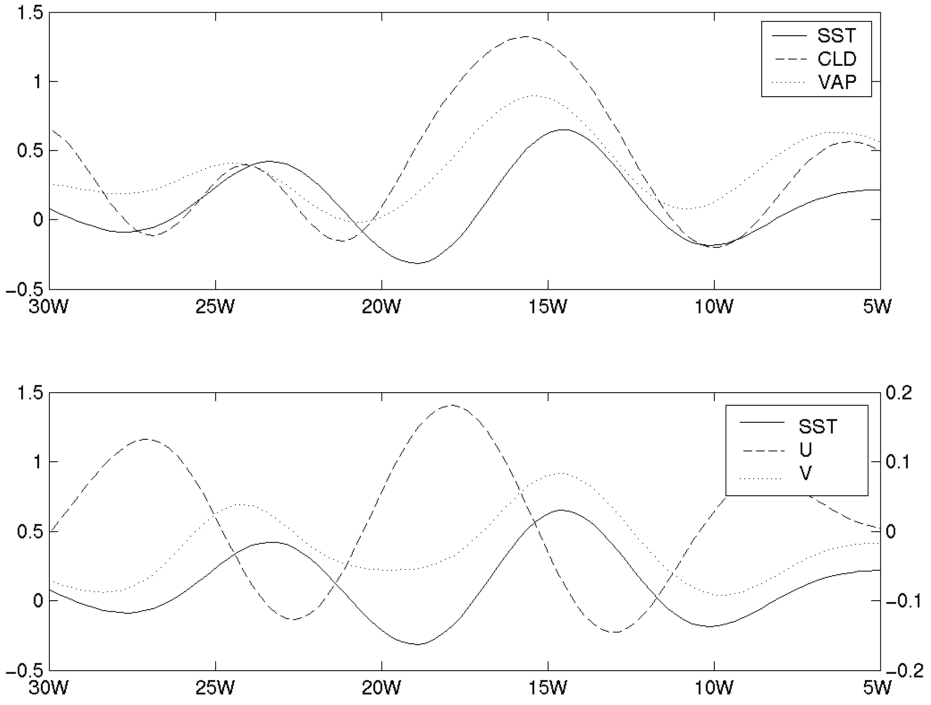

Figure 6.13 – Longitudinal variations at 1°N of the filtered anomalies of SST (°C), cloud liquid water (CLD) (10^{-2} mm), integrated water vapour (VAP) (mm), zonal (U) (ms^{-1}) and meridional (V) (ms^{-1}) wind.

In addition, CLD and RAIN regressions, which follow very similar spatial patterns, appear to be roughly in phase with wind divergence in the central tropical Atlantic. Further north, CLD anomalies are accompanied by precipitation changes in the ITCZ whose southern boundary is located at around 4°N. This more southern position of the Atlantic ITCZ, compared with its Pacific counterpart, makes it more liable to TIW variability. These results may be an indication that TIW variability has a high impact in the deep convection associated with the ITCZ. If so, one can expect the interannual variability of SST and wind associated with TIW will reflect on the CLD and RAIN signals.

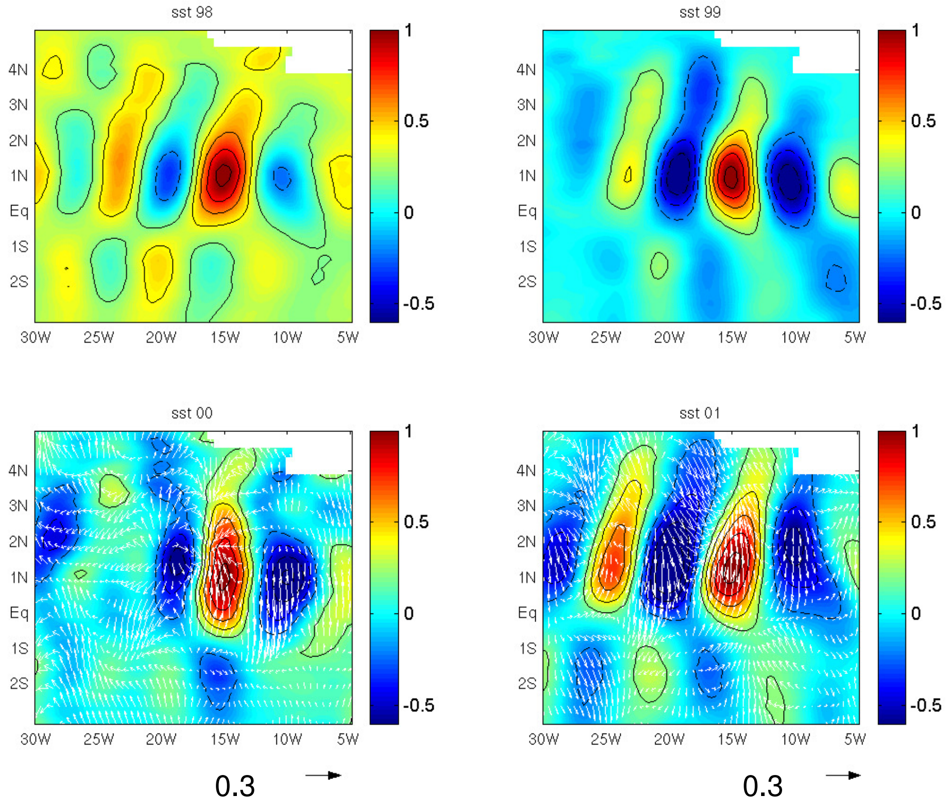

Figure 6.14 – Regression maps for SST (colour and contours). Vectors are for wind velocity. Black arrow shows wind velocity approximate to 0.3 m s^{-1} °C^{-1}.

The separate regression maps of SST for each of the years 1998 to 2001 are presented in Figure 6.14. Wind vectors appear only in the graphs for 2000 and 2001 because of wind data availability. TIW signals are present every year, with differences due to distinct oceanographic conditions. 1998 is a typical example of when the waves can be observed even during anomalous warm conditions. In contrast, in 2000, the equatorial cold tongue was well developed but failed to enhance the signals further west. The wind fields also did not respond in order to adjust to these anomalous conditions. The most active year appears to be 2001, when the influence of TIW can be observed further north, at around 4°N, and with strong regressions at 25°W. Wind velocity regressions are strong close to the equator, and remain so north of 4°N.

Figures 6.15, 6.16 and 6.17 exhibit regressions for VAP, CLD and RAIN, respectively. 1998 shows the typical pattern of an anomalously warm year, with high levels of VAP. Surprisingly, CLD and RAIN spatial distributions follow roughly the average pattern, with maxima at around 2°N and 4°N. 2000, which had a well developed cold tongue, does not show the expected imprint of TIW influence onto the atmospheric fields. Although the equatorial upwelling was strong, the whole tropical Atlantic basin was anomalously cold. This situation inhibited a strong gradient of temperature and, therefore, the development of the front instabilities. However, this does not indicate that TIW did not occur.

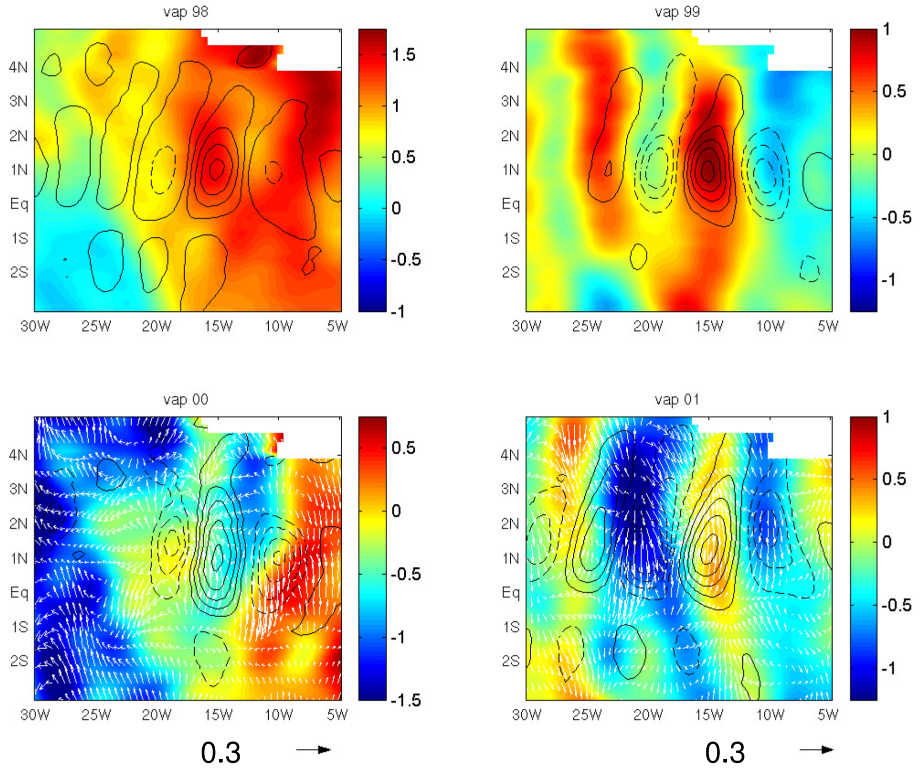

Figure 6.15 – Regression maps for VAP (mm °C^{-1}). Vectors are for wind velocity. Black arrow shows wind velocity approximate to 0.3 m s^{-1} °C^{-1}. SST contours from Figure 6.14 are present in all graphs.

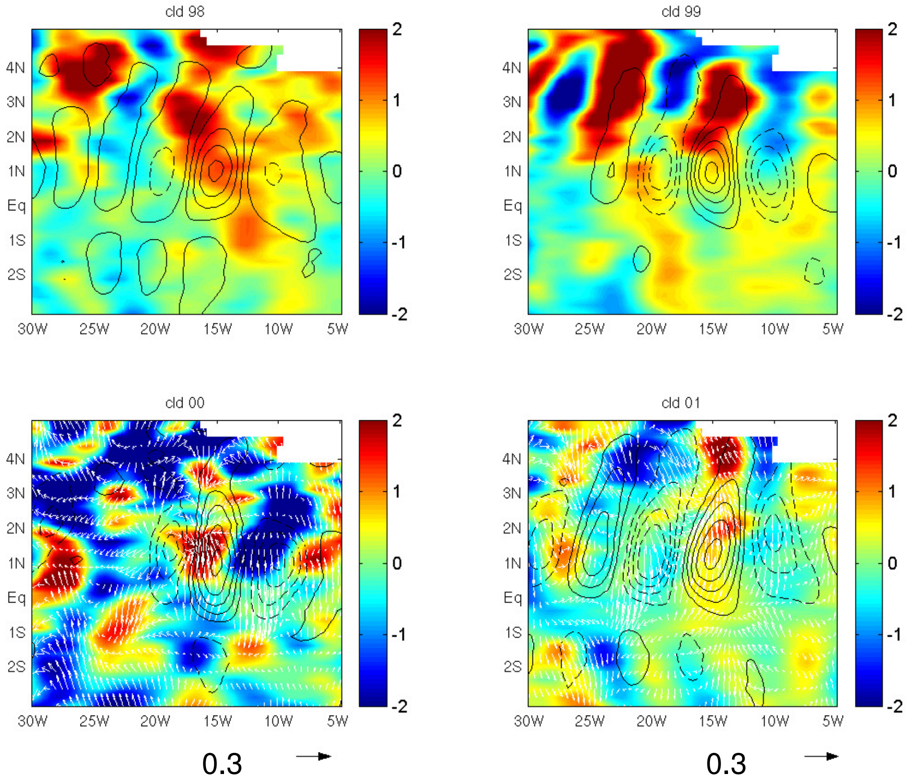

Figure 6.16 – Regression maps for CLD (10^{-2} mm $^{o}C^{-1}$). Vectors are for wind velocity. Black arrow shows wind velocity approximate to 0.3 m s^{-1} $^{o}C^{-1}$. SST contours from Figure 6.14 are present in all graphs.

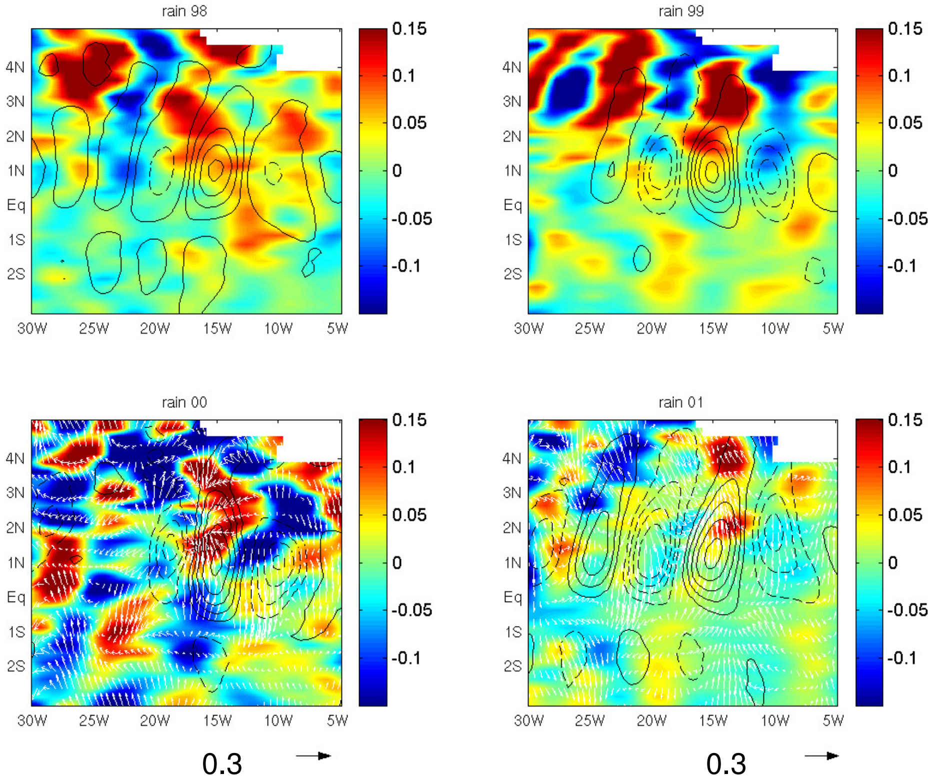

Figure 6.17 – Regression maps for RAIN (mm hr^{-1} $^{o}C^{-1}$). Vectors are for wind velocity. Black arrow shows wind velocity approximate to 0.3 m s^{-1} $^{o}C^{-1}$. SST contours from Figure 6.14 are present in all graphs.

1999 showed a clear signal of the instabilities, although they were short-lived (Figure 6.3) and, because of this, their influence in the western side of the basin is not well established. CLD and RAIN exhibit a more “local” influence, in particular the centre of deep convection at around 4°N. This centre seems to have been displaced from its mean longitudinal position at 25°W to around 20°W.

The most active year of TIW was 2001 (Figure 6.3) and its influence in the atmospheric fields is noticeable in Figures 6.15 to 6.17. VAP map regressions show clearly the influence of the wind divergence associated with the waves, although the magnitude of VAP is low, due to the strong upwelling and cold waters associated with it. As the instabilities' influence in this particular year reaches further north than any other year in this analysis, the observed displacement of CLD and RAIN is north of their usual position. This suggests that the more active (in time and space) the TIW are, the further their influence can be observed.

These results support the hypothesis that TIW variability has a high impact in the deep convection associated with ITCZ, in particular due to its more southern position. The interannual variability of SST and wind associated with TIW are clearly reflected in the atmospheric signals.

6.5. Summary

Tropical Instability Waves, although they have been observed for some time in the tropical Atlantic, have never had their characteristics analysed for the whole basin, as well as their variability from year to year. This chapter, by using observational satellite data, provides an important study of these instabilities.

The results here presented show that the TIW clearly vary their position and time of activity, depending on the degree of development of the equatorial cold tongue. The most active year analysed in this study was 2001, when the spectral characteristics could be observed as far north as 4°N. The imprints of the TIW are well marked in the wind fields, showing that clearly there are coupled mechanisms associated with the TIW. Moreover, this study clearly shows that the hypothesis of this coupling as originally suggested by Wallace et al. (1989) for the tropical Pacific, can also be applied to the tropical Atlantic basin. Although Hashizume et al. (2001) have suggested that Wallace's hypothesis could be applied to the tropical Atlantic, this had not been confirmed until now.

As the characteristics of the TIW have been observed to vary at different latitudes from year to year, it has been possible to test their influence on the ITCZ, which should be larger than its counterpart in the Pacific. As the TMI sensor provides simultaneous measurements of several variables that can be associated with the variability of the ITCZ, such as integrated water vapour, rain and cloud liquid water, it was possible to analyse this suggested influence. In conjunction with the Qscat wind data the results showed that these atmospheric fields are highly correlated with the SST fields at the timescale associated with the TIW, whose variability has a high impact in the deep convection associated with ITCZ, in particular due to its more southern position.

Chapter 7

Interactions between diurnal variability and TIW

7.1. Introduction

There has been considerable work showing cross-scale interactions at the lower frequency end of the ocean dynamics spectrum, such as the phase locking between the ENSO cycle and the annual cycle (Deser and Wallace, 1987; Harrison and Larkin, 1998), and between ENSO intensity and TIW activity, especially in the tropical Pacific, by use of modelling (Yu and Liu, 2003; Pezzi et al., 2004) or satellite measurements (Contreras, 2002). Only a few studies have investigated the cross-scale interactions with the high end of the spectrum, e.g. Cronin and Kessler (2002). In the tropical Atlantic, Wainer et al. (2003) made an initial evaluation of the scales of variability in the upper ocean thermal field, limiting the study by using only part of the PIRATA dataset. The question about how high frequency processes are modulated by, and in turn affect lower frequency seasonal and interannual variability is crucial for developing correct parameterizations of these processes that can affect and be affected by high frequency events, and has not been fully investigated. This interesting and important topic will be further discussed and analysed for the tropical Atlantic in the next chapter.

This chapter investigates the cross-scale interactions between the diurnal variability and TIW in the tropical Atlantic. In particular it relates the variability of SST and heat (latent and sensible) fluxes on the periods (20-40 days) associated with TIW activity and the diurnal variations of those properties, something that has not been fully investigated previously.

The motivation for this study has arisen from the results achieved by the previous wavelet analysis of the PIRATA buoy parameters, as shown in Chapter 5. In order to remind the reader, Figure 7.1 (a reproduction of Figure 5.10) shows in detail the results of the wavelet analysis for one of the buoys located on the equator (0°N 23°W). The upper panel shows the power spectrum of the analysis, with colorbar in °C^2 units. Black contour lines indicate the 95% confidence level. The horizontal dotted lines have been plotted to separate the bands of different periods, identified in the y-axis. The diurnal band is easily recognized for the band between 16 and 32 hours, and its signal is shown in the lower panel of Figure 7.1. In particular it relates the variability of SST and heat (latent and sensible) fluxes on the periods (20-40 days) associated with TIW activity and the diurnal variations of those properties, something that has not been fully investigated previously.

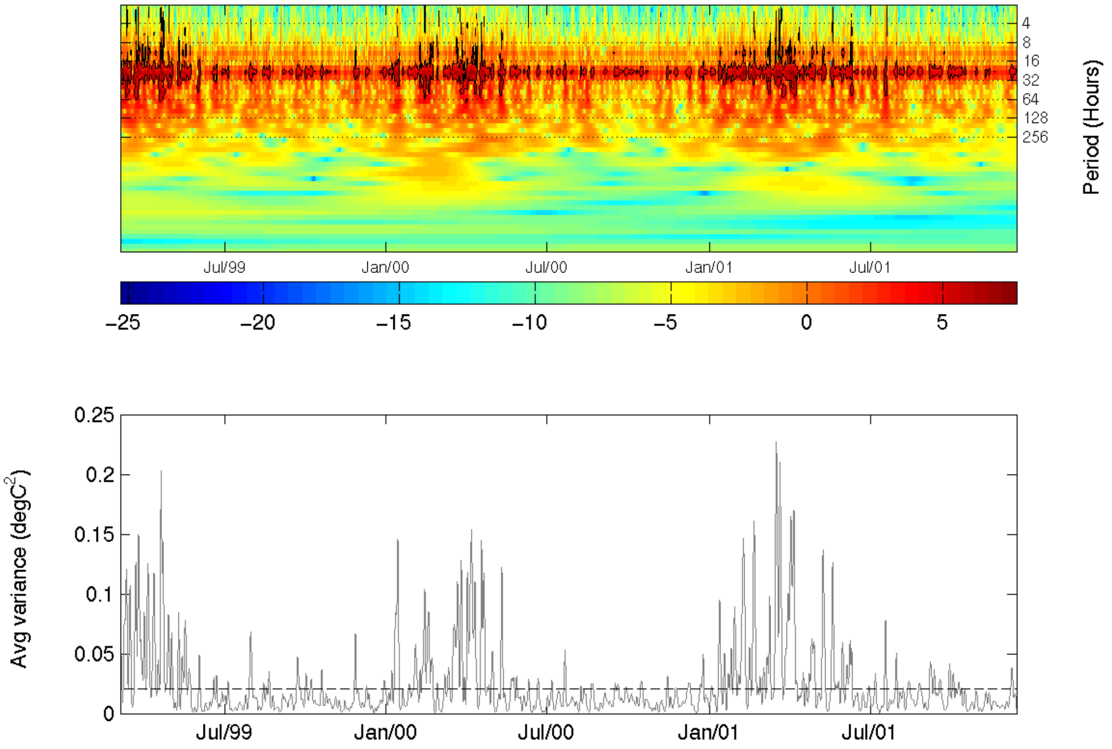

Figure 7.1 – Detail of SST wavelet power spectra for the buoy at 0°N 23°W (top panel). 16 – 32 hours band average time series (lower panel). Black contour lines in the upper panel and dashed line in the lower panel are the 95% confidence level. Units are (°C)^2.

7.2. Diurnal amplitude and TIW relationship

The annual and interannual cycles of SST and wind in the tropical Atlantic have already been well documented (Carton and Zhou, 1997; Dommenget and Latif, 2000). Referring to chapter 5, the diurnal cycle of those variables has been studied for the whole tropical Atlantic basin. From the results presented there, seasonal and interannual variations in wind mixing and surface heating can be expected to cause variations in the SST diurnal cycle. For instance, increased wind mixing will tend to both cool the SST and reduce the SST diurnal cycle, and solar warming will tend to both warm the SST and increase the SST diurnal cycle. Therefore, based on simple one-dimensional mixed layer physics, one might expect an increased SST diurnal cycle during warm phases of the low-frequency SST variability.

Nevertheless, more complicated issues, which are not purely one-dimensional, can control SST in the equatorial regions. The ocean thermal fields can respond to the passage of large-scale propagating waves, by interacting and changing the atmospheric layers above, which, in turn, will feedback the changes into the ocean. Also, on seasonal time scales, the equatorial trade winds vary in relation to the meridional location of the ITCZ.

As mentioned before, the SST diurnal cycle is a very important, and sometimes neglected, part of the variability in the tropical oceans. As other short-time scale processes present in this region can affect it, it is important to understand the possible relationship between different timescales. Chapter 6 showed how much the TIW signal can affect the atmosphere above it, which, in turn will feedback to the ocean. In order to quantify interactions between the diurnal signal and TIW variability in the tropical Atlantic, data from four buoys of the PIRATA array, located on the equator at longitudes of 0°E, 10°W, 23°W and 35°W, are examined.

Previous works (Torrence and Compo, 1998; Masina and Philander, 1999; Cromwell, 2001; Wainer et al., 2003) used a wavelet transform to study the variability of time series and the characteristics of nonstationary processes. Wavelet techniques decompose the signals into localized oscillations in a way that reveals information about the time variation of frequency modes. This was the approach used in the analysis made in chapter 5 of this thesis. As explained in chapter 3, wavelet analysis can also be considered as a series of bandpass filters and can be viewed as the decomposition of the signal into a set of independent, spatially oriented frequency channels. Once we have decomposed the signal into coefficients, we can isolate any frequency band by setting wavelet coefficients of the other frequencies towards zero, while preserving the frequency features of interest. Therefore, a filtering analysis, based on wavelet technique is performed on the time series of SST, latent and sensible heat. Details of the filtering analysis and interpretation of Figures 7.2 – 7.5 are explained below.

The top panels (plots ‘a’) show the band-average variance time series from the wavelet analysis, for the SST diurnal band (solid curve) and 20-40 day band (dashed curve). The diurnal band is the signal between the periods of 16 and 32 hours, as exemplified in Figure 7.1. Similarly, The 20-40 day band, which corresponds to the band period of the TIW as shown in Table 6.1, is the signal between the periods of 512 and 1024 hours.

The results for the top panels (plots ‘a’) in Figures 7.2 – 7.5 draw attention to the energy associated with both periods (diurnal and TIW) at the different locations on the equator, and show the time of the year of maximum variability for these signals. At the same time, it provides a useful and independent check of the results from the 2-D filtering analysis with a FIR filter, used to highlight the TIW activity in Chapter 6. As can be noticed, the energy associated with TIW variability in Figures 7.2 – 7.5 matches the variability in the filtered time-longitude plots shown in Figure 6.3.

As expected, TIW are more energetic in the eastern equatorial Atlantic (Figures 7.2a and 7.3a), with their energy vanishing towards the western side of the basin (Figures 7.4a and 7.5a). On the other hand, diurnal variability has the opposite behaviour, with the presence of the warm pool in the western equatorial Atlantic. It also shows that TIW were more active in 1999 and 2001, as previously reported in Chapter 6. The large peak observed in Figure 7.2a for 2000 may be associated with high activity of TIW only in the eastern side of the basin, without developing further west along the equator, as discussed in the previous chapter and shown in Figure 6.3.

For panels ‘b’ of Figures 7.2 – 7.5, the daily time series of diurnal amplitude was initially calculated from the original SST and skin-SST time series. On these new time series, we applied a bandpass filtering analysis, based on wavelet technique, as explained above. With this technique, it was possible to isolate the signal of the 20-40 day band of the diurnal amplitude of SST at 1-m and derived skin-SST. By analysing the 20-40 day band of the diurnal amplitude of SST, it is possible to infer how much the signal associated with the TIW (i.e., the 20-40 day band) is affecting the diurnal signal.

The typical 20-40 day variability in the equatorial Atlantic, as represented by the 95% confidence interval in panels ‘b’, ranges from around ±0.04°C to ±0.09°C (at 0°E and 10°W, respectively) for the diurnal amplitude of SST, and ±0.05°C to ±0.13°C (at 0°E and 10°W, respectively) for diurnal amplitude of skin-SST. This “natural modulation” differs from buoy to buoy as a result of the distinct variance of the signal analysed on each of the buoys. Since the size of the samples (i.e, the length of the time series) is large enough for this statistical analysis, the standard deviation is a good estimate of the variability of the sample. In this case, the ±1.96 standard deviation approximates to the 95% confidence limits, and can be used as an estimate of this “natural modulation”. The signals that fall beyond the confidence limits are understood to be “extra” variability at the 20-40 day timescale, therefore indicating a real modulation of the diurnal signal by the TIW.

Panels ‘c’ of Figures 7.2 – 7.4 are the 20-40 day signal of the original wind speed, and the way it was calculated is similar to the approach used on panels ‘a’. This means that the plots ‘c’ correspond to the wind speed signal between the periods of 512 and 1024 hours of the wavelet analysis. Panels ‘d’ of Figures 7.2 – 7.4 show the 20-40 day signals of the diurnal amplitude of latent and sensible heat flux, and it was calculated similarly as explained for panels ‘b’.

Variations at periods of 20-40 days are present in all the variables across the equatorial Atlantic, ranging up to ±0.4°C for diurnal amplitude of SST (panels ‘b’ of Figures 7.2 – 7.5), ±1.5 ms^{-1} for wind speed (panels ‘c’ of Figures 7.2 – 7.5), and ±15 Wm^{-2} for diurnal amplitude of latent heat flux and ±10 Wm^{-2} for diurnal amplitude of sensible heat flux (panels ‘d’ of Figures 7.2 – 7.5). These values give an indication that, at this timescale, the diurnal signal can be affected by up to a factor of 4 with the passage of instabilities associated with the TIW. This value is based on the statistical assumption of the “natural modulation” set by the 95% confidence limits explained above.

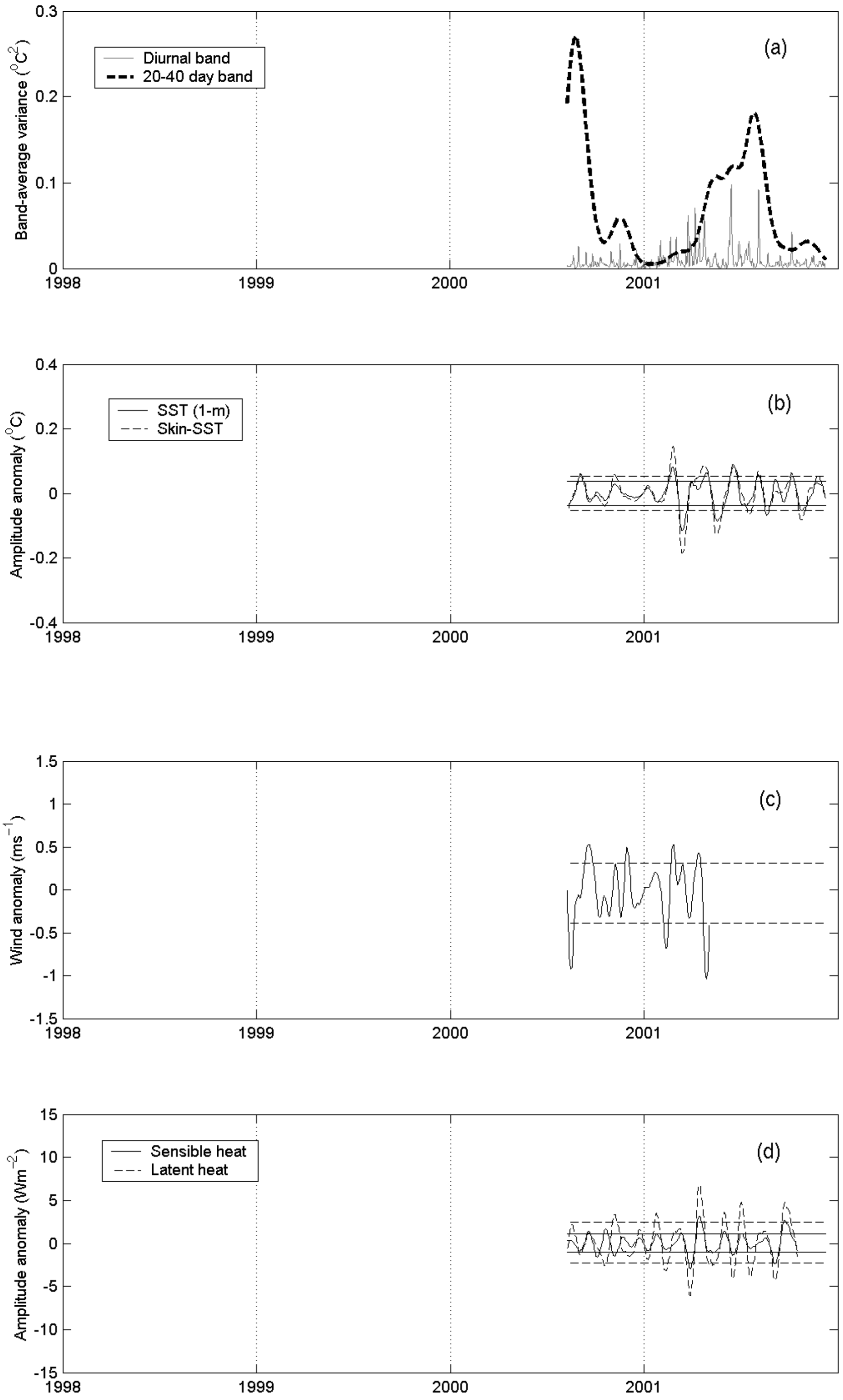

Figure 7.2 – Relationship between diurnal signal and 20-40 day period at 0^oN 0^oW. (a) Band-average variance of SST within the diurnal band (solid line) and 20-40 day band (dashed line). (b) Time series of the 20-40 day components for diurnal amplitude of SST (solid line) and diurnal amplitude of skin-SST (dashed line). (c) Same as (b) but for wind speed. (d) Same as (b) but for diurnal amplitude of sensible heat flux (solid line) and latent heat flux (dashed line). Horizontal lines in (b), (c) and (d) are the 95% confidence limits.

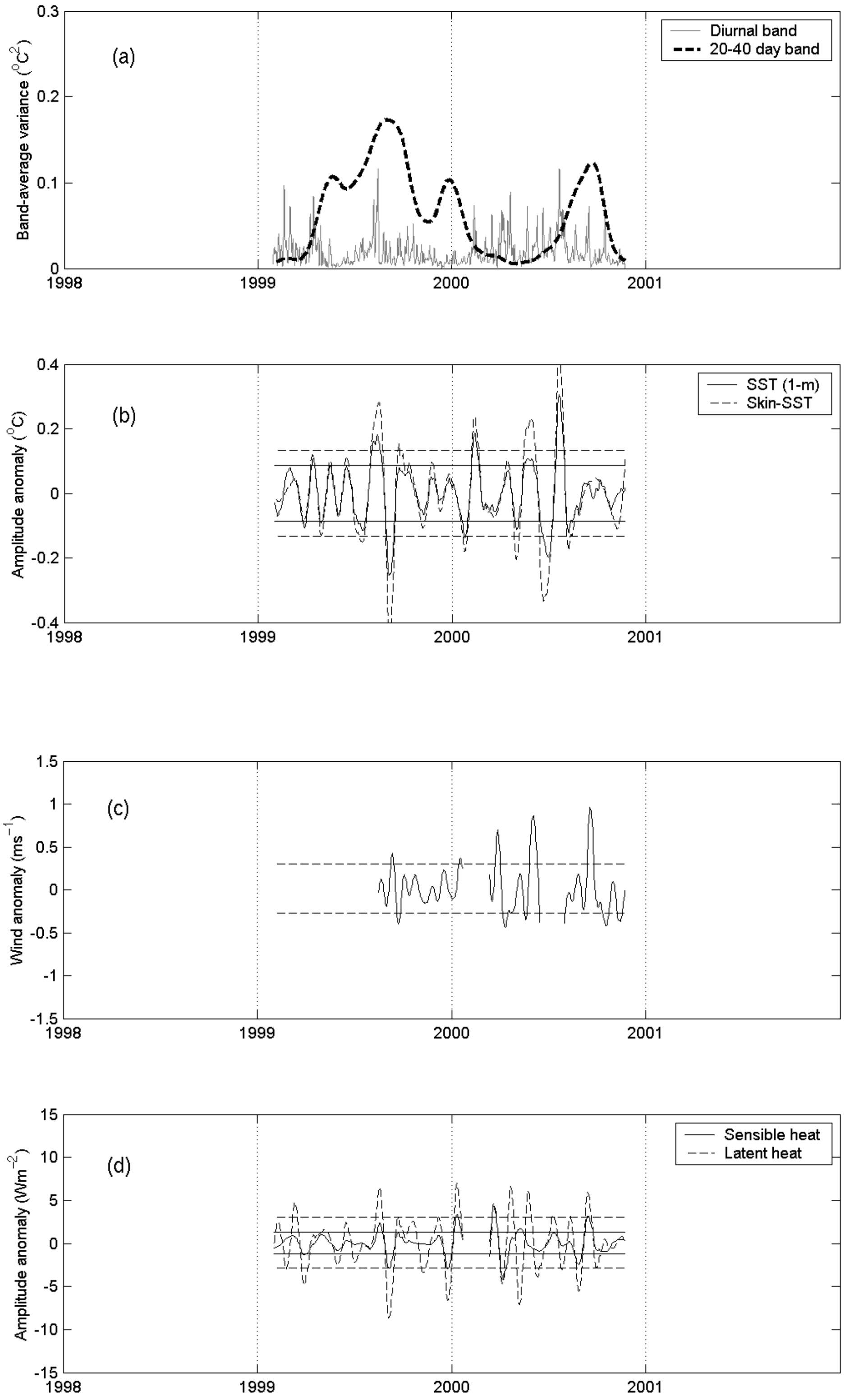

Figure 7.3 – Relationship between diurnal signal and 20-40 day period at 0°N 10°W. (a) Band-average variance of SST within the diurnal band (solid line) and 20-40 day band (dashed line). (b) Time series of the 20-40 day components for diurnal amplitude of SST (solid line) and diurnal amplitude of skin-SST (dashed line). (c) Same as (b) but for wind speed. (d) Same as (b) but for diurnal amplitude of sensible heat flux (solid line) and latent heat flux (dashed line). Horizontal lines in (b), (c) and (d) are the 95% confidence limits.

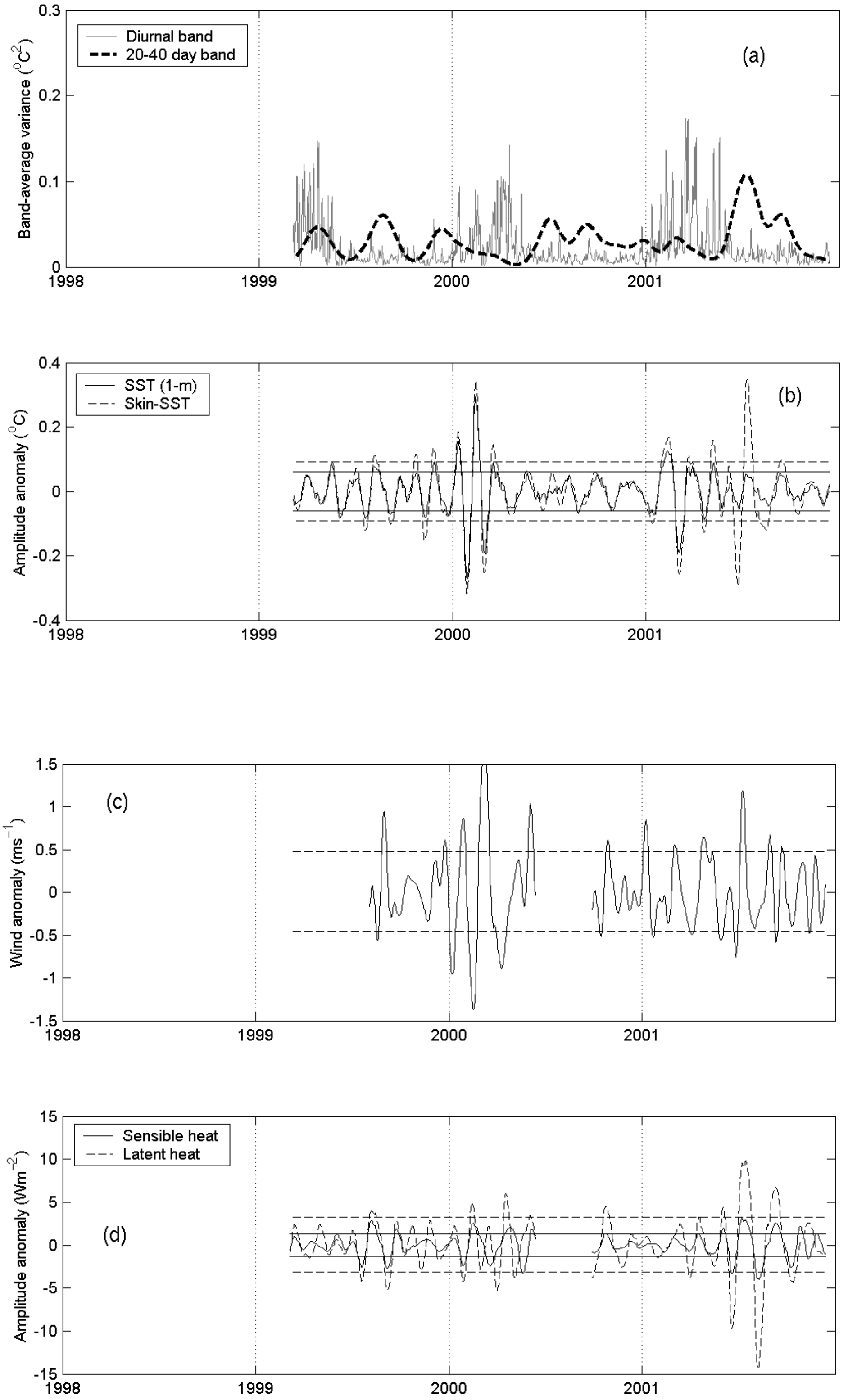

Figure 7.4 – Relationship between diurnal signal and 20-40 day period at 0^{o}N 23^{o}W. (a) Band-average variance of SST within the diurnal band (solid line) and 20-40 day band (dashed line). (b) Time series of the 20-40 day components for diurnal amplitude of SST (solid line) and diurnal amplitude of skin-SST (dashed line). (c) Same as (b) but for wind speed. (d) Same as (b) but for diurnal amplitude of sensible heat flux (solid line) and latent heat flux (dashed line). Horizontal lines in (b), (c) and (d) are the 95% confidence limits.

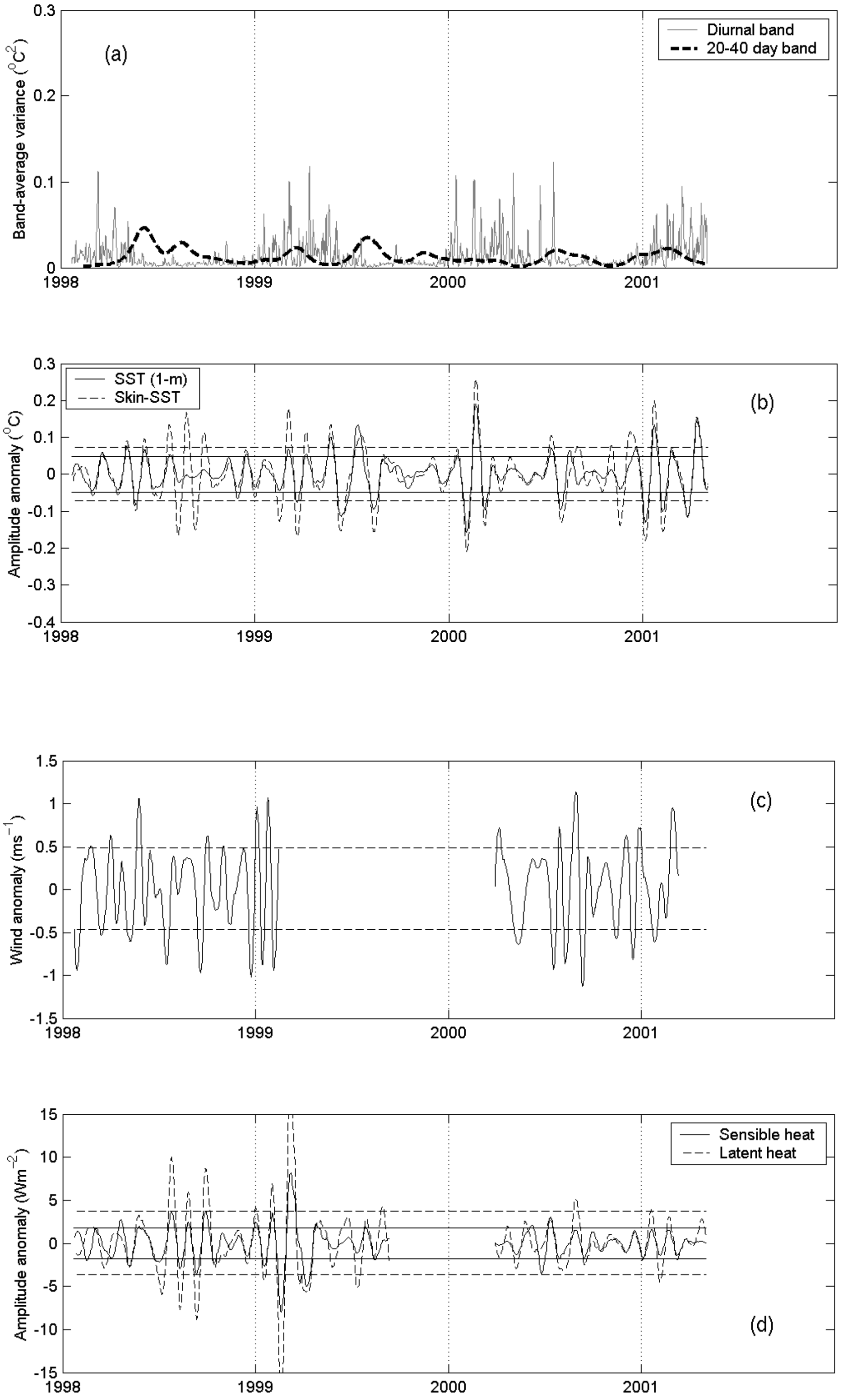

Figure 7.5 – Relationship between diurnal signal and 20-40 day period at 0°N 35°W. (a) Band-average variance of SST within the diurnal band (solid line) and 20-40 day band (dashed line). (b) Time series of the 20-40 day components for diurnal amplitude of SST (solid line) and diurnal amplitude of skin-SST (dashed line). (c) Same as (b) but for wind speed. (d) Same as (b) but for diurnal amplitude of sensible heat flux (solid line) and latent heat flux (dashed line). Horizontal lines in (b), (c) and (d) are the 95% confidence limits.

During periods of high TIW activity, as shown by the peaks of the dashed line in Figures 7.2a – 7.5a, variations of up to ±0.3°C larger than the confidence limits are noticeable in the SST diurnal amplitude time series, shown in Figures 7.2b – 7.5b. These large variations are more clearly seen in 1999 and 2000 for buoy at 0°N 10°W, 2000 and 2001 for buoy at 0°N 23°W, and every year for the buoy at 0°N 35°W. For the buoy located at 0°N 0°E, although it presents a large signal of TIW in 2001, it does not seem to modulate the diurnal signal at that location. A possible explanation for that would be that this location presents small diurnal signals, as the cold tongue, which brings cold water, dominates it.

As mentioned, the other buoys present larger diurnal signals on the 20-40 day timescale. It seems that the way the TIWs influence the diurnal signal also varies from buoy to buoy. On the equator, as the TIW are more energetic in the eastern side, the modulation of the diurnal signal seems to happen either when the waves are fully developed (e.g, Figure 7.3 (buoy at 0°N 10°W) in 1999) or at the beginning of the instabilities growth (e.g, Figure 7.3 (buoy at 0°N 10°W) in 2000). This suggests that the modulation of the diurnal cycle develops fast when the TIW are highly active. Another example is that this appears to happen also in 2001 for the buoy at 0°N 23°W (Figure 7.4).

However, high energy associated with TIW is not common for the buoys located on the western side. The general case seems to be that the modulation of the diurnal signal occurs as the energy of the instabilities decline. This happens for the following reason: on the equator, during a TIW "season", the signals of the instabilities are displaced towards the end of the season at the buoys on the western side, which in turn, will affect the diurnal signal at the beginning of that part of the year when its energy is largest. In other words, even low energy associated with TIW will have a large impact on the diurnal signal when it becomes more energetic. This seems to be the case for the beginning of 2000 (end of the 1999 TIW season) in Figure 7.4, and the beginning of 2000 and 2001 (end of the 1999 and 2000 TIW season, respectively) in Figure 7.5.

To some extent, these variations will also reflect in the diurnal amplitude variability of sensible and latent heat flux. By relating panels 'b' and 'd' of Figures 7.2 – 7.5, variations of around 0.2°C of skin-SST diurnal amplitude can be associated with changes of around 15 Wm^{-2} in latent heat flux diurnal amplitude. This is explained by the fact that TIW variability is a coupled process between the ocean and atmosphere, and anomalies of SST and wind fields are likely to be reflected in the variability of heat fluxes, as previously shown in chapter 6, and corroborated by Liu et al. (2000).

To assess the relationship on a 20-40 day timescale between the SST diurnal amplitude, the wind and the latent heat diurnal amplitude, cross-correlation analyses were carried out and the results are shown in Figure 7.6 – 7.7. In Figure 7.6 positive time lag means that diurnal amplitude of SST leads wind speed. In Figure 7.7 positive time lag means that diurnal amplitude of SST leads diurnal amplitude of latent heat flux. On this timescale, in the positions at 23°W and 35°W, SST diurnal amplitude and wind are out of phase (Figure 7.6), inferred from the negative coefficient at zero lag. As this region of the equatorial Atlantic is dominated by zonal winds, these results reinforce the findings from chapter 6 and presented in Figure 6.14, which shows the out of phase relationship between SST and zonal wind filtered time series.

This condition could explain the high positive and negative anomalies of the skin-SST on the 20-40 day timescale, as observed in Figures 7.4 and 7.5. With the passage of an instability wave, atmospheric conditions would change as suggested by Wallace et al. (1989), and verified in Chapter 6. Over warm water and consequent increase of wind, mixing would increase on the ocean surface, therefore reducing the diurnal amplitude of SST. The opposite is true over cold water: the reduction in wind speed would increase the stratification generated by the heating of the surface, therefore enhancing the diurnal amplitude of SST.

At 35°W, the cross-correlation analysis for the 20-40 day filtered time series (Figure 7.7) shows two distinct situations. The relationship between SST and latent heat flux tends to be in phase for zero lag, indicating that the development of the instabilities quickly affects the diurnal amplitude of the latent heat flux, where the increasing diurnal amplitude of SST will increase the diurnal amplitude of the latent heat flux, by increasing evaporation. As the waves pass by, the situation inverts. A negative correlation at a time lag of about –15 days, where high latent heat flux precedes low SST, indicates that latent heat flux has a direct cooling effect on the SST. This suggests that on this timescale, cooling by evaporation is important in regulating SST, or that TIW activity would lead to a cooling of SST. This is important, in particular because this buoy is located over the Atlantic warm pool.

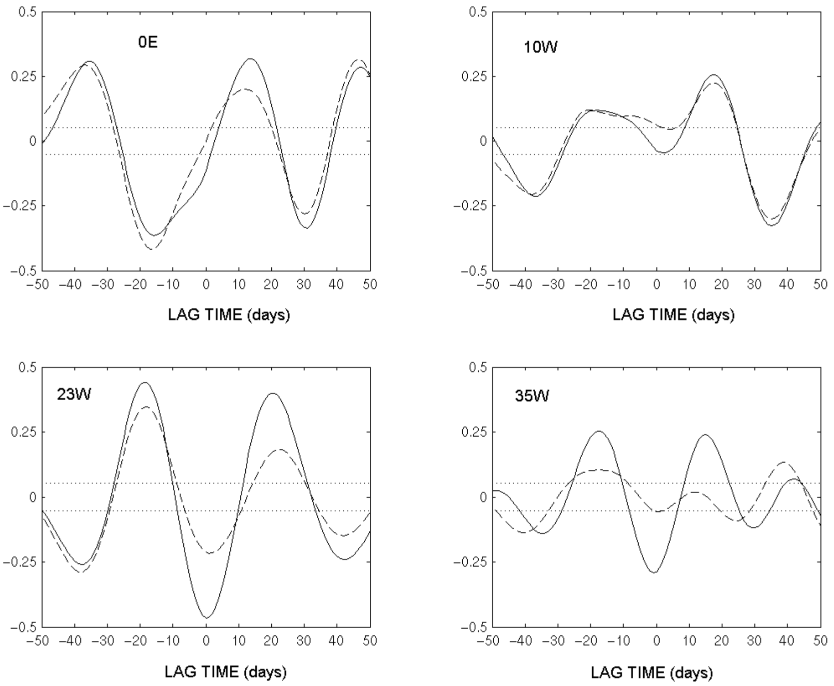

Figure 7.6 – Cross correlation between SST diurnal amplitude and wind speed (solid line) and skin-SST diurnal amplitude and wind speed (dashed line) on a 20-40 day timescale for the PIRATA buoys on the equator. Positive time lag means SST leads wind. Horizontal dotted lines are the 95% confidence limits.

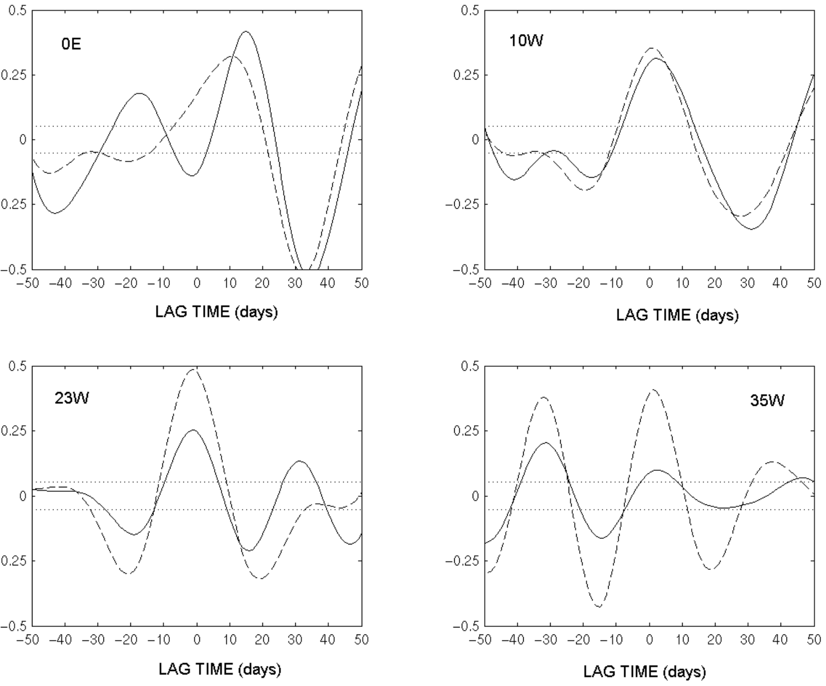

Figure 7.7 – Cross correlation between diurnal amplitude of SST and diurnal amplitude of latent heat flux (solid line) and diurnal amplitude of skin-SST and diurnal amplitude of latent heat flux (dashed line) on a 20-40 day timescale for the PIRATA buoys on the equator. Positive time lag means SST leads latent heat. Horizontal dotted lines are the 95% confidence limits.

The eastern Atlantic Ocean, the region of cold, upwelled water, shows a different interaction between TIW and diurnal amplitude. Figure 7.7 shows a positive cross-correlation coefficient between SST (and skin-SST) diurnal amplitude and latent heat flux diurnal amplitude on a 20-40 day timescale, with a maximum at a time lag around 15 days for the buoy at 0°N 0°E. This suggests that surface latent heat flux is responding to variations in SST, although the instability waves do not modulate the SST diurnal signal at this location, as mentioned previously. What takes place is that the TIWs affect the atmospheric structure above the sea surface, changing the wind fields, as suggested by Wallace et al. (1989). This will, in turn, affect further the diurnal amplitude of latent heat flux, as explained previously in this chapter.

For the analysis of the cross-correlation at the 0°N 10°W between SST and latent heat flux in Figure 7.7, the maximum positive time lag at around 3 days also indicates that surface latent heat flux is responding to variations in SST. However, at this location, it seems that a direct effect of the TIW on the diurnal amplitude of SST reproduces a similar effect on the diurnal amplitude of latent heat flux. This corroborates the analysis of Figure 7.3, which shows a fast response of the diurnal signal to the passage of these instabilities.

It is important to mention the high negative correlation between diurnal amplitudes of SST and latent heat flux, which can be seen at around 35 days for the 0°E buoy. As SST and wind are also out of phase at this time lag, this might indicate external forcings of different timescales interacting and modulating the variability in this region. As this is the buoy closest to the African coast, it could be that remotely forced Kelvin waves could modify, by themselves or by their reflection, the SST in the cold tongue, and those changes would affect air-sea humidity difference, thus affecting the latent heat flux.

7.3. Summary

This chapter has presented the interaction between the diurnal and TIW variability, the latter represented by filtered time series on a 20-40 day timescale. In order to filter the data, the wavelet technique was used, which adds and extend its use compared with the more common approach of showing the variability of time series by decomposing its signal. The study is based on the available dataset of PIRATA buoys located on the equator at longitudes of 0°E, 10°W, 23°W and 35°W, and is the first attempt to study a possible modulation of diurnal variability of SST and heat fluxes by TIW in the tropical Atlantic.

The results suggest that the passage of instability waves affect the diurnal amplitude of SST and skin-SST by up to 4 times. As the oceanic and atmospheric processes are coupled, the changes in the wind fields will feedback into the ocean by modifying its thermal structure and, consequently, the amplitude of the diurnal signal. Cross-correlation analysis shows that on a 20-40 day timescale, diurnal amplitude of SST, skin-SST and latent heat flux are modulated. The mechanisms that interact on the eastern and western side of the equatorial Atlantic tend to be distinct, especially due to the local oceanographic and meteorological conditions, and due to the level of TIW activity.

Few other studies have addressed the question about the modulation of high frequency phenomena by other processes of lower intraseasonal frequency. Previous works, e.g. (Stuart-Menteth, 2004) show the importance for Numerical Weather Prediction (NWP) models to take into account the diurnal cycle of SST. The results here extend these suggestions by showing how important it would be for NWP models to be able to resolve eddies, thus incorporating the influence of TIW in the diurnal variability.

Chapter 8

Discussion, conclusions and future work

8.1. General Discussion

The intention of the study reported in this thesis was to contribute towards a better understanding of the spatial and temporal variability of tropical instability waves, as well as their main spectral properties. In addition, it was to characterise the high-frequency variability in the tropical Atlantic Ocean, by means of integrating the high-resolution in situ dataset from the PIRATA array with high-quality satellite multi-sensor data. The combination of these datasets has sought to exploit their qualities of complementarity: the high temporal resolution of the buoys to characterise the diurnal cycle in the region, and the large repeated spatial coverage of the satellites, which was used to show the tropical instability waves.

As several environmental and instrumental factors can introduce errors in the retrieval of any variable measured by satellite, the validation of satellite data is essential, although this issue has not always been considered with the importance it deserves. In chapter 4, a comprehensive validation was made for the TMI (SST and wind) and QuickScat (wind) data. This careful step was necessary, in particular because of the fact that satellite-retrieved data were used to fill in gaps in the buoys wind time series. The satellite datasets have a very good agreement with the in situ data, with r^2 at the order of 0.81 and a bias around 0.26 ms^{-1}. Whereas an older version of the TMI processing produced SST fields with a warm bias, the results presented here from the latest version showed that this has been corrected. Satellite-based wind speed showed regional differences, highlighting that the algorithm used has problems in retrieving low winds, as the largest biases were observed for low wind speeds at the buoy located close to the ITCZ region, which is a region of convergence and low winds.

The importance of validation is clearly demonstrated by Gentemann et al. (2004). Their work was published during the writing of the present document, and confirms the results described in chapter 4, where the agreement between SST at 1-m and TMI SST are in the order of 0.90, with a small bias of around -0.12 ^{o}C. It is encouraging to note that both works show similar results, even though they were completely independent and used different approaches in the validation processes.

The diurnal variability, in particular of SST, has recently become the subject of several studies that show the importance of resolving the diurnal cycle, particularly for correct assimilation into model predictions. As an example, McCreary et al. (2001) compare results from a model in which the diurnal cycle can be turned on and off. This study demonstrated that, for the western tropical Pacific, the addition of the diurnal cycle produces a different and more accurate result.

As mentioned in chapter 5, the diurnal cycle in the tropical Atlantic has not been fully investigated, which could suggest a lack of interest by the research community. However, with the PIRATA array, there is the necessary high-resolution dataset available to explore the high-frequency variability for the whole basin. The present work makes the first contribution in characterising the mean diurnal cycle of several measured variables for the whole tropical Atlantic. The amplitude of the diurnal cycle of the derived skin-SST increases toward the Equator and varies from 0.35 to 0.70 ^{o}C, while that of observed SST at 1-m has a similar spatial pattern but smaller amplitudes (from 0.17 to 0.41 ^{o}C). It also presents the mean diurnal cycle of derived heat fluxes, which were calculated following Zeng's bulk flux algorithm (Zeng et al., 1998).

The results showed that the phase of the mean diurnal SST cycle is very similar for the whole tropical Atlantic basin, with maximum at around 15:00 hrs, with the mean diurnal skin SST cycle peaking one hour earlier. One interesting characteristic observed was that the mean diurnal cycle of wind speed is very variable, which indicates that it alone cannot control the phase of SST. However, the relationship of the wind speed change, defined as ∂(wind)/∂t, with SST is very similar for the buoys analysed, which would indicate that the way the wind speed changes, in particular the morning wind, would control the SST phase. The magnitude of the afternoon maximum of SST would then be tuned by insolation and local SST conditions.

Moreover, chapter 5 also developed a long-term analysis of the time series, by estimating the seasonal variation of the variables. The first half of the years present the strongest energy associated with the diurnal signals. However, it was also possible to notice significant diurnal signals at the equator during the second half of each year. This indicates a possible modulation of the diurnal signal by processes with different timescales. It was suggested that Tropical Instability Waves could be one of these processes, which then were analysed in a separate chapter.

In general, previous works have analysed systematic biases of fluxes in the tropics by addressing the impact of using averages (hourly, daily or monthly) of SST on the calculations of the diurnal cycle of heat fluxes. However, the biggest problem for calculating heat fluxes by using time series from moored arrays is the gaps in the wind speed time series. A study by Freitag et al. (2001) also reports the same problems for the majority of ATLAS buoys in the tropical Pacific. A valuable contribution of the work in this thesis has been the careful analysis addressing the impact of using daily average wind speed for the calculations of hourly heat fluxes. It has been shown that the errors introduced have similar magnitudes to those estimated due to measurement inaccuracies of the bulk variables by the *in situ* sensors. This indicates that wind speed data retrieved from satellites can be used to fill the gaps left in the buoys time series in order to calculate heat fluxes.

The study of TIW is mainly based on the availability of high-resolution satellite microwave data. Measurements of SST, wind, integrated water vapour, rain and cloud liquid water were used to analyse the co-variability of these fields on timescales associated with TIW. The exploitation of the interaction between these variables was only possible due to the capability of measurements of SST by microwave radiometry, which are unaffected by aerosols, and can be retrieved in the presence of clouds, simultaneously with the other fields. It made it possible to describe the long-term variability of TIW characteristics in the tropical Atlantic, which necessarily relies on the existence of long time series. Moreover, this study could clearly show that the hypothesis of ocean-atmosphere coupling as originally suggested by Wallace et al. (1989) for the tropical Pacific, is also applicable to the tropical Atlantic basin.

Although Hashizume et al. (2001) have suggested that Wallace's hypothesis could be applied to the tropical Atlantic, they could not confirm it as they analysed only one TIW season in 1999. The results presented here clearly show that Wallace's hypothesis can be applied to the Atlantic. They also support the suggestion that TIW variability has a high impact on the deep convection associated with ITCZ, in particular due to its more southern position in the Atlantic. This suggests that it is important for NWP models to take into account the interannual variability of SST and wind associated with TIW, as they are clearly reflected in the atmospheric signals.

The expansion of the heat fluxes time series, by filling the wind gaps with satellite-based data, has been shown to be very useful in understanding TIW coupling and their interaction with diurnal signals. The results suggest that the passage of instability waves might affect the diurnal amplitude of SST and skin-SST. Whereas Cronin and Kessler (2002), based on the measurements of only one moored buoy at the tropical Pacific, pointed out that the interannual variations of SST amplitude are associated with the ENSO signal, the analyses in this thesis have shown that variability associated with TIW in the tropical Atlantic also has an impact on the amplitude of the diurnal signal of SST. Stuart-Menteth et al. (2003) also show interannual variations of diurnal warming in large regions in the tropics and midlatitudes that are frequently susceptible to this process each year.

The present work, by using cross-correlation analysis, shows that the diurnal amplitude of SST, skin-SST and latent heat flux are modulated on a 20-40 day timescale. Foltz et al. (2003) described the importance that eddy heat advection, possibly associated with TIW, has for contributing to seasonal SST variability. The increase in SST would suggest increase in evaporation, which in turn, affected by changes in wind associated with TIW, might increase the diurnal amplitude of latent heat flux. As suggested in chapter 7, this increase would act as a negative feedback for diurnal amplitudes of SST. The mechanisms that interact on the eastern and western side of the equatorial Atlantic tend to be distinct, especially due to the local oceanographic and meteorological conditions, and due to the level of TIW activity.

Results presented here showed the importance of characterising processes of different time-scales. Moreover, the study suggests that there is a high degree of coupling and modulation between those processes, in particular between the diurnal signal and variability associated with TIW. Therefore, it contributes to a better understanding of those processes, indicating the importance of including both processes in NWP models, for better prediction of changes in climate patterns.

Finally, this study has clearly demonstrated the benefits of synergetic use of satellite and in situ data, as well as products of multiple sensors in addressing questions that could not be answered by a single dataset alone.

8.2. Conclusions

The main conclusions of this thesis are:

- The TMI-SST, TMI-winds and Quickscat datasets showed a very good agreement with the *in situ* data. Winds, permitting its use to fill the gaps in the buoys time series. This has been confirmed by the error analysis executed for the heat fluxes calculations, where relative humidity was identified as the major source of error for latent heat flux, and air temperature as the major source error for the sensible heat flux. The use of Zeng's bulk-to-skin algorithm seemed to be appropriate for the cool skin correction with results similar to previous studies.

- The diurnal cycle of the variables shows different patterns for distinct regions of the tropical Atlantic. The diurnal amplitude of skin-SST is larger over the central and eastern equatorial Atlantic, rather than over the western Atlantic warm pool. Zonal wind shows a marked semidiurnal fluctuation due to the semidiurnal variation of sea-level pressure in the tropics. The seasonal variation of the diurnal cycle is meridionally distributed with the strongest diurnal cycle signal found in the summer of the respective hemisphere. The buoys located on the equator follow the pattern for the southern hemisphere, with strong diurnal cycles in the beginning of the year. Moreover, they also showed significant diurnal signals in the second half of the year which are modulated by Tropical Instability Waves.

- Use of daily wind in order to calculate hourly surface heat fluxes appears to be in good agreement with hourly surface heat fluxes calculated with hourly wind speed. The errors introduced by using daily wind have similar magnitudes to those estimated for inaccurate measurements of the bulk variables by the *in situ* sensors.

- Analysis of satellite data reveals that the region of maximum variability associated with TIW occurs at 1°N and around 15°W. However, as TIW vary in exact location and phase velocity, it was possible to observe interannual differences, with 2001 representing the year when TIW were most active. Their signals are also visible in the wind fields, and the results support the coupling mechanism of SST and wind through the stability change in the atmospheric layer, as suggested by Wallace et al. (1989).

- The analysis of co-variability of fields retrieved from satellites supports the idea that variability linked with TIW has a high impact in the deep convection associated with ITCZ, in particular due to the more southern position of the convergence zone.

- The passage of instability waves affects the diurnal amplitude of SST and skin-SST on a 20-40 day timescale. Also, the diurnal amplitude of latent heat flux is modulated on this timescale, indicating the importance of models being able to resolve eddy advection and the diurnal cycle in order to perform more accurate predictions.

8.3. Future work

The study of TIW continues to be very interesting as there are outstanding questions still to be answered. The structures of TIW are essentially three-dimensional and seem to be mainly confined to the mixed-layer and the upper part of the thermocline. Nevertheless, the question remains to be addressed whether there are deeper features of variability associated with these instabilities. In the tropical Atlantic, the seasonal and interannual modulations of the mixed layer depth associated with the TIW have not been explored. TIW are mainly observed north of the equator, associated with the strong sea surface temperature (SST) front observed in this region. South of the equator, they are poorly documented but are probably not located at the same longitude as their northern counterparts due to the cold tongue variability in this region. However, is it only the local variability that maintains the difference between north and south of the equator? TIW, as the name suggests, result from complex mechanisms that involve tropical instabilities, either barotropic (or inertial) due to the shear of currents flowing in opposite directions, or baroclinic due to the large-scale SST front originated by the cold tongue. Nevertheless, there is no consensus about which mechanism has a major role in the generation and energetics of the TIW. Also, the impact that other equatorial propagating processes in the tropical Atlantic might have on the TIW variability is unknown.

It has been shown previously that the average heat convergence in the mixed layer associated with TIW is of the order of 60 W/m^2 (Jochum et al., 2004). Carton et al. (1996) demonstrated that wind-induced latent heat flux is a major contributing factor to the long-term variability of the SST in the tropical Atlantic. However, what are the spatial patterns of surface heat fluxes associated with TIW? And to what degree are the fluxes affected by these instabilities?

Regions of strong upwelling associated with the vortices originating in the TIW, should provide enhanced production as a result of increased nutrient flux to the euphotic zone (Strutton et al., 2001). The very intense upwelling at the trailing edge of the cool SST anomaly entrains subsurface nutrients into the euphotic zone and stimulates phytoplankton growth, in excess of the existing bloom conditions of the equatorial upwelling tongue (Morliere et al., 1994). Ocean colour data retrieved from satellites can be used to map the highly productive region of upwelling within few degrees of the equator in the eastern equatorial Atlantic. The calculation of surface currents associated with TIW should provide the means by which to evaluate horizontal phytoplankton budgets on seasonal to interannual time scales, which have not yet been assessed from observations.

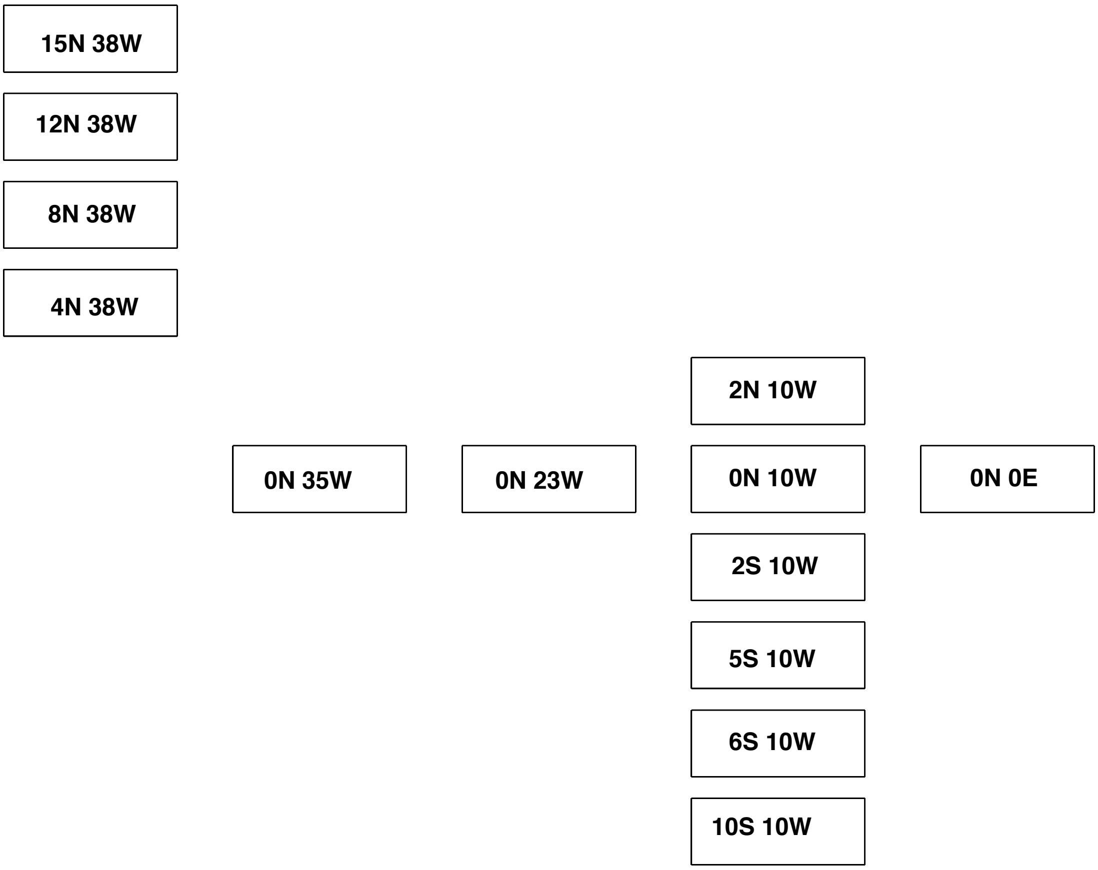

APPENDIX A – Schematic diagram with the positions of the PIRATA buoys

References

Albright, M.D., D.R. Mock, E.E. Recker, and R.J. Reed, A diagnostic study of the diurnal rainfall variation in the GATE B-scale area, *Journal of Atmospheric and Oceanic Sciences*, *38*, 1429 - 1445, 1981.

Allen, M.R., S.P. Lawrence, M.J. Murray, C.T. Mutlow, T.N. Stockdale, D.T. Llewellynjones, and D.L.T. Anderson, Control of Tropical Instability Waves in the Pacific, *Geophysical Research Letters*, *22* (19), 2581-2584, 1995.

Andreoli, R.V., and M.T. Kayano, Multi-scale variability of the sea surface temperature in the Tropical Atlantic, *Journal of Geophysical Research-Oceans*, *109* (C5), art. no.-C05009, 2004.

Bjerknes, J., Atmospheric teleconnections from the equatorial Pacific, *Monthly Weather Review*, *97*, 163-172, 1969.

Bond, N.A., and M.J. McPhaden, An Indirect Estimate of the Diurnal Cycle in Upper Ocean Turbulent Heat Fluxes at the Equator, 140-Degrees-W, *Journal of Geophysical Research-Oceans*, *100* (C9), 18369-18378, 1995.

Bourassa, M.A., D.M. Legler, J.J. O'Brien, and S.R. Smith, SeaWinds validation with research vessels, *Journal of Geophysical Research-Oceans*, *108* (C2), art. no.-3019, 2003.

Bourles, B., R.L. Molinari, E. Johns, W.D. Wilson, and K.D. Leaman, Upper layer currents in the western tropical North Atlantic (1989-1991), *Journal of Geophysical Research-Oceans*, *104* (C1), 1361-1375, 1999.

Brown, P.R., Climatic fluctuations over the oceans and in the Tropical Atlantic, pp. 109-123, Rome, 1961.

Bruce, J.G., and E. Firing, Temperature measurements in the upper 10 m with modified expamdable bathythermograph probes, *Journal of Geophysical Research-Oceans*, *79*, 4110-4111, 1974.

Brunke, M.A., C.W. Fairall, X.B. Zeng, L. Eymard, and J.A. Curry, Which bulk aerodynamic algorithms are least problematic in computing ocean surface turbulent fluxes?, *Journal of Climate*, *16* (4), 619-635, 2003.

Brutsaert, W.A., *Evaporration into the atmosphere*, 299 pp., Reidel, Dordrecht, 1982.

Buck, A.L., New Equations for Computing Vapor Pressure and Enhancement Factor, *Journal of Applied Meteorology*, *20* (12), 1527–1532, 1981.

Carton, J.A., X.H. Cao, B.S. Giese, and A.M. daSilva, Decadal and interannual SST variability in the tropical Atlantic Ocean, *Journal of Physical Oceanography*, *26* (7), 1165-1175, 1996.

Carton, J.A., and B.H. Huang, Warm Events in the Tropical Atlantic, *Journal of Physical Oceanography*, *24* (5), 888-903, 1994.

Carton, J.A., and Z.X. Zhou, Annual cycle of sea surface temperature in the tropical Atlantic ocean, *Journal of Geophysical Research-Oceans*, *102* (C13), 27813-27824, 1997.

Casey, K.S., and P. Cornillon, A comparison of satellite and in situ-based sea surface temperature climatologies, *Journal of Climate*, *12* (6), 1848-1863, 1999.

Castro, S.L., G.A. Wick, and W.J. Emery, Further refinements to models for the bulk-skin sea surface temperature difference, *Journal of Geophysical Research-Oceans*, *108* (C12), art. no.-3377, 2003.

Chang, P., L. Ji, and H. Li, A decadal climate variation in the tropical Atlantic Ocean from thermodynamic air-sea interactions, *Nature*, *385* (6616), 516-518, 1997.

Chang, P., R. Saravanan, L. Ji, and G.C. Hegerl, The effect of local sea surface temperatures on atmospheric circulation over the tropical Atlantic sector, *Journal of Climate*, *13* (13), 2195-2216, 2000.

Chelton, D.B., S.K. Esbensen, G. Schlax, N. Thum, M.H. Freilich, F.J. Wentz, C.L. Gentemann, M.J. McPhaden, and P.S. Schopf, Observations of coupling between surface wind stress and sea surface temperature in the eastern tropical Pacific, *Journal of Climate*, *14* (7), 1479-1498, 2001.

Chelton, D.B., and M.G. Schlax, Global observations of oceanic Rossby waves, *Science*, *272* (5259), 234-238, 1996.

Chelton, D.B., F.J. Wentz, C.L. Gentemann, R.A. de Szoeke, and M.G. Schlax, Satellite microwave SST observations of transequatorial tropical instability waves, *Geophysical Research Letters*, *27* (9), 1239-1242, 2000.

Chou, S.H., C.L. Shie, R.M. Atlas, and J. Ardizzone, Air-sea fluxes retrieved from special sensor microwave imager data, *Journal of Geophysical Research-Oceans*, *102* (C6), 12705-12726, 1997.

Cipollini, P., D. Cromwell, P.G. Challenor, and S. Raffaglio, Rossby waves detected in global ocean colour data, *Geophysical Research Letters*, *28* (2), 323-326, 2001.

Clayson, C.A., and J.A. Curry, Determination of surface turbulent fluxes for the Tropical Ocean-Global Atmosphere Coupled Ocean-Atmosphere Response Experiment: Comparison of satellite retrievals and in situ measurements, *Journal of Geophysical Research-Oceans*, *101* (C12), 28515-28528, 1996.

Contreras, R.F., Long-term observations of tropical instability waves, *Journal of Physical Oceanography*, *132*, 2715-2722, 2002.

Cornillon, P., and L. Stramma, The Distribution of Diurnal Sea-Surface Warming Events in the Western Sargasso Sea, *Journal of Geophysical Research-Oceans*, *90* (NC6), 1811-&, 1985.

Cox, M.D., Generation and propagation of 30-day waves in a numerical model of the Pacific, *Journal of Physical Oceanography*, *10*, 1168-1186, 1980.

Craeye, C., Study of microwave scattering from rain and wind roughened seas, Ph.D. thesis, Universite Catholique de Louvain, Louvain, 1998.

Craeye, C., P.W. Sobieski, and L.F. Bliven, Scattering by artificial wind and rain roughened water surfaces at oblique incidences, *International Journal of Remote Sensing*, *18* (10), 2241-2246, 1997.

Cromwell, D., Sea surface height observations of the 34 degrees N 'waveguide' in the North Atlantic, *Geophysical Research Letters*, *28* (19), 3705-3708, 2001.

Cronin, M.F., and W.S. Kessler, Seasonal and interannual modulation of mixed layer variability at 0 degrees, 110 degrees W, *Deep-Sea Research Part I-Oceanographic Research Papers*, *49* (1), 1-17, 2002.

Cronin, M.F., and M.J. McPhaden, The upper ocean heat balance in the western equatorial Pacific warm pool during September-December 1992, *Journal of Geophysical Research-Oceans*, *102* (C4), 8533-8553, 1997.

Curry, J.A., C.A. Clayson, W.B. Rossow, R. Reeder, Y.C. Zhang, P.J. Webster, G. Liu, and R.S. Sheu, High-resolution satellite-derived dataset of the surface fluxes of heat, freshwater, and momentum for the TOGA COARE IOP, *Bulletin of the American Meteorological Society*, *80* (10), 2059-2080, 1999.

Curtis, S., and S. Hastenrath, Forcing of Anomalous Sea-Surface Temperature Evolution in the Tropical Atlantic During Pacific Warm Events, *Journal of Geophysical Research-Oceans*, *100* (C8), 15835-15847, 1995.

Dai, A.G., and C. Deser, Diurnal and semidiurnal variations in global surface wind and divergence fields, *Journal of Geophysical Research-Atmospheres*, *104* (D24), 31109-31125, 1999.

Daubechies, I., S. Mallat, and A.S. Willsky, Special Issue on Wavelet Transforms and Multiresolution Signal Analysis - Introduction, *Ieee Transactions on Information Theory*, *38* (2), 529-531, 1992.

Deans, S.R., *The Radon transform and some of its applications*, John Willer, 1983.

Deser, C., Daily Surface Wind Variations over the Equatorial Pacific-Ocean, *Journal of Geophysical Research-Atmospheres*, *99* (D11), 23071-23078, 1994.

Deser, C., J.J. Bates, and S. Wahl, The Influence of Sea-Surface Temperature-Gradients on Stratiform Cloudiness Along the Equatorial Front in the Pacific-Ocean, *Journal of Climate*, *6* (6), 1172-1180, 1993.

Deser, C., and C.A. Smith, Diurnal and semidiurnal variations of the surface wind field over the tropical Pacific Ocean, *Journal of Climate*, *11* (7), 1730-1748, 1998.

Deser, C., and J.M. Wallace, El-Nino Events and Their Relation to the Southern Oscillation - 1925-1986, *Journal of Geophysical Research-Oceans*, *92* (C13), 14189-14196, 1987.

Dickinson, S., K.A. Kelly, M.J. Caruso, and M.J. McPhaden, Comparisons between the TAO buoy and NASA scatterometer wind vectors, *Journal of Atmospheric and Oceanic Technology*, *18* (5), 799-806, 2001.

Dommenget, D., and M. Latif, Interannual to decadal variability in the tropical Atlantic, *Journal of Climate*, *13* (4), 777-792, 2000.

Donelan, M.A., and W.J. Pierson, Radar Scattering and Equilibrium Ranges in Wind-Generated Waves with Application to Scatterometry, *Journal of Geophysical Research-Oceans*, *92* (C5), 4971-5029, 1987.

Donlon, C.J., The GODAE High Resolution Sea Surface Temperature - Pilot Project Development and Integration Plan, GHRSST-PP Project Office - UK MetOffice, Exeter, 2004.

Donlon, C.J., P.J. Minnett, C. Gentemann, T.J. Nightingale, I.J. Barton, B. Ward, and M.J. Murray, Toward improved validation of satellite sea surface skin temperature measurements for climate research, *Journal of Climate*, *15* (4), 353-369, 2002.

Donlon, C.J., T.J. Nightingale, T. Sheasby, J. Turner, I.S. Robinson, and W.J. Emery, Implications of the oceanic thermal skin temperature deviation at high wind speed, *Geophysical Research Letters*, *26* (16), 2505-2508, 1999.

Donlon, C.J., L. Nykjaer, and C. Gentemann, Using sea surface temperature measurements from microwave and infrared satellite measurements, *International Journal of Remote Sensing*, *25* (7-8), 1331-1336, 2004.

Donlon, C.J., and I.S. Robinson, Observations of the oceanic thermal skin in the Atlantic Ocean, *Journal of Geophysical Research-Oceans*, *102* (C8), 18585-18606, 1997.

Donlon, C.J., and I.S. Robinson, Radiometric validation of ERS-1 along-track scanning radiometer average sea surface temperature in the Atlantic Ocean, *Journal of Atmospheric and Oceanic Technology*, *15* (3), 647-660, 1998.

du Penhoat, Y., and A.M. Treguier, The seasonal linear response of the Tropical Atlantic Ocean, *Journal of Physical Oceanography*, *15*, 316-329, 1985.

Duing, W., P. Hisard, E.J. Katz, J. Knauss, J. Meincke, L. Miller, K. Moroshkin, S.G.H. Philander, A. Rybnikov, K. Voigt, and R.H. Weisberg, Meanders and long waves in the equatorial Atlantic, *Nature*, *257*, 280-284, 1975.

Ebuchi, N., H.C. Graber, and M.J. Caruso, Evaluation of wind vectors observed by QuikSCAT/SeaWinds using ocean buoy data, *Journal of Atmospheric and Oceanic Technology*, *19* (12), 2049-2062, 2002.

Enfield, D.B., and D.A. Mayer, Tropical Atlantic sea surface temperature variability and its relation to El Nino Southern Oscillation, *Journal of Geophysical Research-Oceans*, *102* (C1), 929-945, 1997.

Esbensen, S.K., and M.J. McPhaden, Enhancement of tropical ocean evaporation and sensible heat flux by atmospheric mesoscale systems, *Journal of Climate*, *9* (10), 2307-2325, 1996.

Evans, D.L., and S.S. Signorini, Vertical Structure of the Brazil Current, *Nature*, *315* (6014), 48-50, 1985.

Fairall, C.W., E.F. Bradley, J.S. Godfrey, G.A. Wick, J.B. Edson, and G.S. Young, Cool-skin and warm-layer effects on sea surface temperature, *Journal of Geophysical Research-Oceans*, *101* (C1), 1295-1308, 1996a.

Fairall, C.W., E.F. Bradley, D.P. Rogers, J.B. Edson, and G.S. Young, Bulk parameterization of air-sea fluxes for Tropical Ocean Global Atmosphere Coupled Ocean Atmosphere Response Experiment, *Journal of Geophysical Research-Oceans*, *101* (C2), 3747-3764, 1996b.

Feely, R.A., R. Wanninkhof, C.E. Cosca, P.P. Murphy, M.F. Lamb, and M.D. Steckley, Co2 Distributions in the Equatorial Pacific During the 1991- 1992 Enso Event, *Deep-Sea Research Part Ii-Topical Studies in Oceanography*, *42* (2-3), 365-386, 1995.

Flament, P., J. Firing, M. Sawyer, and C. Trefois, Amplitude and Horizontal Structure of a Large Diurnal Sea- Surface Warming Event During the Coastal Ocean Dynamics Experiment, *Journal of Physical Oceanography*, *24* (1), 124-139, 1994.

Flament, P.J., S.C. Kennan, R.A. Knox, P.P. Niiler, and R.L. Bernstein, The three-dimensional structure of an upper ocean vortex in the tropical Pacific Ocean, *Nature*, *383* (6601), 610-613, 1996.

Foltz, G.R., J.A. Carton, and E.P. Chassignet, Tropical instability vortices in the Atlantic Ocean, *Journal of Geophysical Research-Oceans*, *109* (C3), art. no.-C03029, 2004.

Foltz, G.R., S.A. Grodsky, J.A. Carton, and M.J. McPhaden, Seasonal mixed layer heat budget of the tropical Atlantic Ocean, *Journal of Geophysical Research-Oceans*, *108* (C5), art. no.-3146, 2003.

Foufoula-Georgiou, E., and P. Kumar, *Wavelets in Geophysics*, 373 pp., Academic Press, San Diego, 1994.

Freilich, M.H., Validation of vector magnitude datasets: effects of random component errors, *Journal of Atmospheric and Oceanic Technology*, *14* (3), 695-703, 1997.

Freitag, H.P., M. O'Haleck, G.C. Thomas, and M.J. McPhaden, Calibration procedures and instrumental accuracies for ATLAS wind measurements., pp. 20 pp, NOAA/Pacific Marine Environmental Laboratory, Seattle, 2001.

Garraffo, Z.D., W.E. Johns, E.P. Chassignet, and G.J. Goni, North Brazil Current rings and transport of southern waters in a high resolution numerical simulation of the North Atlantic, in *Interhemispheric Water Exchnage in the Atlantic Ocean*, edited by P. Malanotte-Rizzoli, and G.J. Goni, pp. 375-409, 2003.

Garzoli, S.L., and E.J. Katz, The Forced Annual Reversal of the Atlantic North Equatorial Countercurrent, *Journal of Physical Oceanography*, *13* (11), 2082-2090, 1983.

Geernaert, G.L., Bulk parameterizations for the wind stress and heat fluxes, in *Surfaces Waves and Fluxes*, edited by G.L. Geernaert, and W.J. Plant, pp. 91-172, Kluwer Academic Publishers, Dordrecht, 1990.

Gentemann, C.L., F.J. Wentz, C.A. Mears, and D.K. Smith, In situ validation of Tropical Rainfall Measuring Mission microwave sea surface temperatures, *Journal of Geophysical Research-Oceans*, *109* (C4), art. no.-C04021, 2004.

Goni, G.J., and W.E. Johns, A census of North Brazil Current rings observed from TOPEX/POSEIDON altimetry: 1992-1998, *Geophysical Research Letters*, *28* (1), 1-4, 2001.

Goyet, C., and E.T. Peltzer, Variation of CO2 partial pressure in surface seawater in the equatorial Pacific Ocean, *Deep-Sea Research Part I-Oceanographic Research Papers*, *44* (9-10), 1611-1625, 1997.

Gray, W.M., and R.W. Jacobson Jr., Diurnal variation of deep cumulus convection, *Monthly Weather Review*, *105*, 1171-1188, 1977.

Grossmann, A., and J. Morlet, Decomposition of Hardy Functions into Square Integrable Wavelets of Constant Shape, *Siam Journal on Mathematical Analysis*, *15* (4), 723-736, 1984.

Gulev, S.K., Climatologically significant effects of space-time averaging in the north Atlantic sea-air heat flux fields, *Journal of Climate*, *10* (11), 2743-2763, 1997.

Halpern, D., Comparison of Moored Wind Measurements from a Spar and Toroidal Buoy in the Eastern Equatorial Pacific During February March 1981, *Journal of Geophysical Research-Oceans*, *92* (C8), 8303-8306, 1987.

Halpern, D., R.A. Knox, and D.S. Luther, Observations of 20-Day Period Meridional Current Oscillations in the Upper Ocean Along the Pacific Equator, *Journal of Physical Oceanography*, *18* (11), 1514-1534, 1988.

Halpern, D., and R.K. Reed, Heat budget of the upper ocean under light winds, *Journal of Physical Oceanography*, *6*, 972-975, 1976.

Hamilton, K., The geographical distribution of the solar semidiurnal surface pressure oscillation, *Journal of Geophysical Research*, *85*, 1945-1949, 1980.

Hamilton, K., Latent-Heat Release as a Possible Forcing Mechanism for Atmospheric Tides, *Monthly Weather Review*, *109* (1), 3-17, 1981.

Hansen, D.V., and C.A. Paul, Genesis and Effects of Long Waves in the Equatorial Pacific, *Journal of Geophysical Research-Oceans*, *89* (NC6), 431-440, 1984.

Harrison, D.E., and N.K. Larkin, El Nino-Southern Oscillation sea surface temperature and wind anomalies, 1946-1993, *Reviews of Geophysics*, *36* (3), 353-399, 1998.

Hashizume, H., S.P. Xie, M. Fujiwara, M. Shiotani, T. Watanabe, Y. Tanimoto, W.T. Liu, and K. Takeuchi, Direct observations of atmospheric boundary layer response to SST variations associated with tropical instability waves over the eastern equatorial Pacific, *Journal of Climate*, *15* (23), 3379-3393, 2002.

Hashizume, H., S.P. Xie, W.T. Liu, and K. Takeuchi, Local and remote atmospheric response to tropical instability waves: A global view from space, *Journal of Geophysical Research-Atmospheres*, *106* (D10), 10173-10185, 2001.

Hastenrath, S., Daily wind, pressure and temperature variation up to 30 km over the tropical western Pacific, *Quarterly Journal of the Royal Meteorological Society*, *98*, 49-59, 1972.

Hastenrath, S., Interannual Variability and Annual Cycle - Mechanisms of Circulation and Climate in the Tropical Atlantic Sector, *Monthly Weather Review*, *112* (6), 1097-1107, 1984.

Hastenrath, S., and L. Heller, Dynamics of climatic hazards in northeast Brazil, *Quarterly Journal of the Royal Meteorological Society*, *103*, 77-92, 1977.

Hastenrath, S., and P.J. Lamb, Heat budget atlas of the tropical Atlantic and eastern Pacific oceans, pp. 103, University of Wisconsin Press, 1978.

Haurwitz, B., and A.D. Cowley, The diurnal and semidiurnal barometric pressure oscillations: global distribution and annual variations, *Pure and Applied Geophysics*, *102*, 193-222, 1973.

Hayes, S.P., M.J. McPhaden, and J.M. Wallace, The Influence of Sea-Surface Temperature on Surface Wind in the Eastern Equatorial Pacific - Weekly to Monthly Variability, *Journal of Climate*, *2* (12), 1500-1506, 1989.

Hellerman, S., and M. Rosenstein, Normal Monthly Wind Stress over the World Ocean with Error- Estimates, *Journal of Physical Oceanography*, *13* (7), 1093-1104, 1983.

Hendon, H.H., and K. Woodberry, The Diurnal Cycle of Tropical Convection, *Journal of Geophysical Research-Atmospheres*, *98* (D9), 16623-16637, 1993.

Hill, K.L., I.S. Robinson, and P. Cipollini, Propagation characteristics of extratropical planetary waves observed in the ATSR global sea surface temperature record, *Journal of Geophysical Research-Oceans*, *105* (C9), 21927-21945, 2000.

Hisard, P., and J. Merle, Onset of summer surface cooling in the Gulf of Guinea during GATE, *Deep-Sea Research (Suppl II)*, *26*, 325-341, 1980.

Holtslag, A.A.M., E.I.F. Debruijn, and H.L. Pan, A High-Resolution Air-Mass Transformation Model for Short-Range Weather Forecasting, *Monthly Weather Review*, *118* (8), 1561-1575, 1990.

Horel, J.D., V.E. Kousky, and M.T. Kagano, Atmospheric Conditions in the Atlantic Sector During 1983 and 1984, *Nature*, *322* (6076), 248-251, 1986.

Houghton, R.W., Influence of Local and Remote Wind Forcing in the Gulf of Guinea, *Journal of Geophysical Research-Oceans*, *94* (C4), 4816-4828, 1989.

Houghton, R.W., and Y.M. Tourre, Characteristics of Low-Frequency Sea-Surface Temperature- Fluctuations in the Tropical Atlantic, *Journal of Climate*, *5* (7), 765-771, 1992.

Huang, B.H., and E.K. Schneider, The Response of an Ocean General-Circulation Model to Surface Wind Stress Produced by an Atmospheric General-Circulation Model, *Monthly Weather Review*, *123* (10), 3059-3085, 1995.

Imaoka, K., and R.W. Spencer, Diurnal variation of precipitation over the tropical oceans observed by TRMM/TMI combined with SSM/I, *Journal of Climate*, *13* (23), 4149-4158, 2000.

Imberger, J., The Diurnal Mixed Layer, *Limnology and Oceanography*, *30* (4), 737-770, 1985.

Jacobs, C.A., Mean diurnal and shorter period variations in the air-sea fluxes and related parameters during GATE, *Deep-Sea Research - Part A (Suppl I)*, *26*, 65-97, 1978.

Jochum, M., P. Malanotte-Rizzoli, and A.J. Busalacchi, Tropical instability waves in the Atlantic Ocean, *Ocean Modelling*, *7*, 145-163, 2004.

Katz, E.J., Equatorial Kelvin Waves in the Atlantic, *Journal of Geophysical Research-Oceans*, *92* (C2), 1894-1898, 1987a.

Katz, E.J., Seasonal Response of the Sea-Surface to the Wind in the Equatorial Atlantic, *Journal of Geophysical Research-Oceans*, *92* (C2), 1885-1893, 1987b.

Kelly, K.A., S. Dickinson, M.J. McPhaden, and G.C. Johnson, Ocean currents evident in satellite wind data, *Geophysical Research Letters*, *28* (12), 2469-2472, 2001.

Kennan, S.C., and P.J. Flament, Observations of a tropical instability vortex, *Journal of Physical Oceanography*, *30* (9), 2277-2301, 2000.

Kessler, W.S., M.J. McPhaden, and K.M. Weickmann, Forcing of Intraseasonal Kelvin Waves in the Equatorial Pacific, *Journal of Geophysical Research-Oceans*, *100* (C6), 10613-10631, 1995.

Kondo, J., Y. Sasano, and T. Ishii, On wind-driven current and temperature profiles with diurnal period in the oceanic planetary boundary layer, *Journal of Physical Oceanography*, *9*, 362-372, 1979.

Kummerow, C., W. Barnes, T. Kozu, J. Shiue, and J. Simpson, The Tropical Rainfall Measuring Mission (TRMM) sensor package, *Journal of Atmospheric and Oceanic Technology*, *15* (3), 809-817, 1998.

Legeckis, R., Long waves in the eastern equatorial Pacific Ocean: a view from a geostationary satellite, *Science*, *197*, 1179-1181, 1977.

Lindzen, R.S., and S. Nigam, On the Role of Sea-Surface Temperature-Gradients in Forcing Low-Level Winds and Convergence in the Tropics, *Journal of the Atmospheric Sciences*, *44* (17), 2418-2436, 1987.

Liu, W.T., X.S. Xie, P.S. Polito, S.P. Xie, and H. Hashizume, Atmospheric manifestation of tropical instability wave observed by QuikSCAT and tropical rain measuring mission, *Geophysical Research Letters*, *27* (16), 2545-2548, 2000.

Lukas, R., The diurnal cycle of sea surface temperature in the western equatorial Pacific, *TOGA Notes*, *2*, 1-5, 1991.

Lynn, R.J., and J. Svejkovsky, Remotely Sensed Sea-Surface Temperature Variability Off California During a Santa-Ana Clearing, *Journal of Geophysical Research-Oceans*, *89* (NC5), 8151-8162, 1984.

Masina, S., and S.G.H. Philander, An analysis of tropical instability waves in a numerical model of the Pacific Ocean - 1. Spatial variability of the waves, *Journal of Geophysical Research-Oceans*, *104* (C12), 29613-29635, 1999.

Masina, S., S.G.H. Philander, and A.B.G. Bush, An analysis of tropical instability waves in a numerical model of the Pacific Ocean - 2. Generation and energetics of the waves, *Journal of Geophysical Research-Oceans*, *104* (C12), 29637-29661, 1999.

McCreary, J.P., K.E. Kohler, R.R. Hood, S. Smith, J. Kindle, A.S. Fischer, and R.A. Weller, Influences of diurnal and intraseasonal forcing on mixed-layer and biological variability in the central Arabian Sea, *Journal of Geophysical Research-Oceans*, *106* (C4), 7139-7155, 2001.

McPhaden, M.J., A.J. Busalacchi, R. Cheney, J.R. Donguy, K.S. Gage, D. Halpern, M. Ji, P. Julian, G. Meyers, G.T. Mitchum, P.P. Niiler, J. Picaut, R.W. Reynolds, N. Smith, and K. Takeuchi, The tropical ocean global atmosphere observing system: A decade of progress, *Journal of Geophysical Research-Oceans*, *103* (C7), 14169-14240, 1998.

Mehta, V.M., Variability of the tropical ocean surface temperatures at decadal-multidecadal timescales. Part I: The Atlantic Ocean, *Journal of Climate*, *11* (9), 2351-2375, 1998.

Mehta, V.M., and T. Delworth, Decadal Variability of the Tropical Atlantic-Ocean Surface- Temperature in Shipboard Measurements and in a Global Ocean-Atmosphere Model, *Journal of Climate*, *8* (2), 172-190, 1995.

Menkes, C.E., S.C. Kennan, P. Flament, Y. Dandonneau, S. Masson, B. Biessy, E. Marchal, G. Eldin, J. Grelet, Y. Montel, A. Morliere, A. Lebourges-Dhaussy, C. Moulin, G. Champalbert, and A. Herbland, A whirling ecosystem in the equatorial Atlantic, *Geophysical Research Letters*, *29* (11), art. no.-1553, 2002.

Merle, J., and S. Arnault, Seasonal Variability of the Surface Dynamic Topography in the Tropical Atlantic-Ocean, *Journal of Marine Research*, *43* (2), 267-288, 1985.

Meyer, Y., and H. Xu, Wavelet analysis and chirps, *Applied and Computational Harmonic Analysis*, *4* (4), 366-379, 1997.

Miller, L., D.R. Watts, and M. Wimbush, Oscillations of Dynamic Topography in the Eastern Equatorial Pacific, *Journal of Physical Oceanography*, *15* (12), 1759-1770, 1985.

Molinari, R.L., Observations of Eastward Currents in the Tropical South- Atlantic Ocean - 1978-1980, *Journal of Geophysical Research-Oceans and Atmospheres*, *87* (NC12), 9707-9714, 1982.

Moore, R.K., Y.S. Yu, A.K. Fung, D. Kaneko, G. Dome, and R. Werp, Preliminary study of rain effects on radar scattering from water surfaces, *IEEE Journal of Oceanic Engineering*, *OE-4*, 31-32, 1979.

Morliere, A., A. Lebouteiller, and J. Citeau, Tropical Instability Waves in the Atlantic-Ocean - a Contributor to Biological Processes, *Oceanologica Acta*, *17* (6), 585-596, 1994.

Moura, A.D., and J. Shukla, On the Dynamics of Droughts in Northeast Brazil - Observations, Theory and Numerical Experiments with a General-Circulation Model, *Journal of the Atmospheric Sciences*, *38* (12), 2653-2675, 1981.

Neelin, J.D., D.S. Battisti, A.C. Hirst, F.F. Jin, Y. Wakata, T. Yamagata, and S.E. Zebiak, ENSO theory, *Journal of Geophysical Research-Oceans*, *103* (C7), 14261-14290, 1998.

Nirala, M.L., and A.P. Cracknell, Microwave measurement of rain and sea surface temperature by the TRMM Microwave Imager (TMI), *International Journal of Remote Sensing*, *23* (13), 2673-2691, 2002.

Nitta, T., and S.K. Esbensen, Diurnal variations in the Western Atlantic Trades during BOMEX, *Journal of Meteorological Society of Japan*, *52* (2), 254 - 257, 1974.

Nobre, P., and J. Shukla, Variations of sea surface temperature, wind stress, and rainfall over the tropical Atlantic and South America, *Journal of Climate*, *9* (10), 2464-2479, 1996.

Pezzi, L.P., Equatorial Pacific Dynamics: Lateral Mixing and Tropical Instability Waves, Ph.D. thesis, University of Southampton, Southampton, 2003.

Pezzi, L.P., and I.F.A. Cavalcanti, The relative importance of ENSO and tropical Atlantic sea surface temperature anomalies for seasonal precipitation over South America: a numerical study, *Climate Dynamics*, *17* (2-3), 205-212, 2001.

Pezzi, L.P., J. Vialard, K.J. Richards, C. Menkes, and D.L.T. Anderson, Infuence of ocean-atmosphere coupling on the properties of Tropical Instability Waves, *Geophysical Research Letters*, *31* (L16306), 2004.

Philander, S.G.H., Instabilities of zonal equatorial currents, 2, *Journal of Geophysical Research-Oceans*, *83*, 3679-3682, 1978.

Philander, S.G.H., and Y. Chao, On the Contrast between the Seasonal Cycles of the Equatorial Atlantic and Pacific Oceans, *Journal of Physical Oceanography*, *21* (9), 1399-1406, 1991.

Philander, S.G.H., W.J. Hurlin, and R.C. Pacanowski, Properties of Long Equatorial Waves in Models of the Seasonal Cycle in the Tropical Atlantic and Pacific Oceans, *Journal of Geophysical Research-Oceans*, *91* (C12), 14207-14211, 1986.

Philander, S.G.H., and R.C. Pacanowski, The Mass and Heat-Budget in a Model of the Tropical Atlantic- Ocean, *Journal of Geophysical Research-Oceans*, *91* (C12), 14212-14220, 1986a.

Philander, S.G.H., and R.C. Pacanowski, A Model of the Seasonal Cycle in the Tropical Atlantic-Ocean, *Journal of Geophysical Research-Oceans*, *91* (C12), 14192-14206, 1986b.

Picaut, J., Propagation of the Seasonal Upwelling in the Eastern Equatorial Atlantic, *Journal of Physical Oceanography*, *13* (1), 18-37, 1983.

Picaut, J., J. Servain, P. Lecomte, M. Seva, R. Lukas, and G. Rougier, Climatic atlas of the tropical Atlantic wind stress and sea surface temperature 1964-1979, Universite de Bretagne Occidentale, 1985.

Polito, P.S., and P. Cornillon, Long baroclinic Rossby waves detected by TOPEX/POSEIDON, *Journal of Geophysical Research-Oceans*, *102* (C2), 3215-3235, 1997.

Price, J.F., R.A. Weller, and R. Pinkel, Diurnal Cycling - Observations and Models of the Upper Ocean Response to Diurnal Heating, Cooling, and Wind Mixing, *Journal of Geophysical Research-Oceans*, *91* (C7), 8411-8427, 1986.

Qiao, L., and R.H. Weisberg, Tropical Instability Wave Kinematics - Observations from the Tropical Instability Wave Experiment, *Journal of Geophysical Research-Oceans*, *100* (C5), 8677-8693, 1995.

Ravier-Hay, P., and J.S. Godfrey, A model of diurnal changes in sea surface temperature for the western equatorial Pacific Ocean, *TOGA Notes*, *11*, 5-8, 1993.

Reynolds, R.W., and T.M. Smith, Improved Global Sea-Surface Temperature Analyses Using Optimum Interpolation, *Journal of Climate*, *7* (6), 929-948, 1994.

Robinson, I.S., N.C. Wells, and H. Charnock, The Sea-Surface Thermal-Boundary Layer and Its Relevance to the Measurement of Sea-Surface Temperature by Airborne and Spaceborne Radiometers, *International Journal of Remote Sensing*, *5* (1), 19-45, 1984.

Rossow, W.B., and Y.C. Zhang, Calculation of Surface and Top of Atmosphere Radiative Fluxes from Physical Quantities Based on Isccp Data Sets .2. Validation and First Results, *Journal of Geophysical Research-Atmospheres*, *100* (D1), 1167-1197, 1995.

Ruiz-Barradas, A., J.A. Carton, and S. Nigam, Structure of interannual-to-decadal climate variability in the tropical Atlantic sector, *Journal of Climate*, *13* (18), 3285-3297, 2000.

Saravanan, R., and P. Chang, Interaction between tropical Atlantic variability and El Nino- Southern Oscillation, *Journal of Climate*, *13* (13), 2177-2194, 2000.

Schluessel, P., W.J. Emery, H. Grassi, and T. Mammen, On the Bulk-Skin Temperature Difference and Its Impact on Satellite Remote-Sensing of Sea-Surface Temperature, *Journal of Geophysical Research-Oceans*, *95* (C8), 13341-13356, 1990.

Schmitz, W.J., and P.L. Richardson, On the Sources of the Florida Current, *Deep-Sea Research Part a-Oceanographic Research Papers*, *38*, S379-S409, 1991.

Schott, F.A., J. Fischer, and L. Stramma, Transports and pathways of the upper-layer circulation in the western tropical Atlantic, *Journal of Physical Oceanography*, *28* (10), 1904-1928, 1998.

Schulz, J., J. Meywerk, S. Ewald, and P. Schlussel, Evaluation of satellite-derived latent heat fluxes, *Journal of Climate*, *10* (11), 2782-2795, 1997.

Servain, J., Simple Climatic Indexes for the Tropical Atlantic-Ocean and Some Applications, *Journal of Geophysical Research-Oceans*, *96* (C8), 15137-15146, 1991.

Servain, J., A.J. Busalacchi, M.J. McPhaden, A.D. Moura, G. Reverdin, M. Vianna, and S.E. Zebiak, A Pilot Research Moored Array in the Tropical Atlantic (PIRATA), *Bulletin of the American Meteorological Society*, *79* (10), 2019-2031, 1998.

Servain, J., and R. Lukas, Climatic atlas of the tropical Atlantic wind stress and sea surface temperature 1985-1989, Institut Francais de Recherche pour l'Explotation de la mer, Plouzane, France, 1990.

Servain, J., I. Wainer, H.L. Ayina, and H. Roquet, The relationship between the simulated climatic variability modes of the tropical Atlantic, *International Journal of Climatology*, *20* (9), 939-953, 2000.

Servain, J., I. Wainer, J.P. McCreary, and A. Dessier, Relationship between the equatorial and meridional modes of climatic variability in the tropical Atlantic, *Geophysical Research Letters*, *26* (4), 485-488, 1999.

Slingo, J., and P. Delecluse, Scale interactions and the tropical atmosphere-ocean system, in *TOGA coupled ocean-atmosphere response experiment (COARE)*, pp. 59-69, WMO, Geneva, 1999.

Smith, S.D., Coefficients for Sea-Surface Wind Stress, Heat-Flux, and Wind Profiles as a Function of Wind-Speed and Temperature, *Journal of Geophysical Research-Oceans*, *93* (C12), 15467-15472, 1988.

Sobieski, P.W., and L.F. Bliven, Scatterometry of a Drop Impact on a Salt-Water Surface, *International Journal of Remote Sensing*, *16* (14), 2721-2726, 1995.

Sobieski, P.W., C. Craeye, and L.F. Bliven, Scatterometric signatures of multivariate drop impacts on fresh and salt water surfaces, *International Journal of Remote Sensing*, *20* (11), 2149-2166, 1999.

Soden, B.J., The diurnal cycle of convection, clouds, and water vapor in the tropical upper troposphere, *Geophysical Research Letters*, *27* (15), 2173-2176, 2000.

Soloviev, A., and R. Lukas, Observation of large diurnal warming events in the near-surface layer of the western equatorial Pacific warm pool, *Deep-Sea Research Part I-Oceanographic Research Papers*, *44* (6), 1055-1076, 1997.

Sorooshian, S., X. Gao, K. Hsu, R.A. Maddox, Y. Hong, H.V. Gupta, and B. Imam, Diurnal variability of tropical rainfall retrieved from combined GOES and TRMM satellite information, *Journal of Climate*, *15* (9), 983-1001, 2002.

Stammer, D., F. Wentz, and C. Gentemann, Validation of microwave sea surface temperature measurements for climate purposes, *Journal of Climate*, *16* (1), 73-87, 2003.

Steger, J.M., and J.A. Carton, Long Waves and Eddies in the Tropical Atlantic-Ocean - 1984- 1990, *Journal of Geophysical Research-Oceans*, *96* (C8), 15161-15171, 1991.

Stockdale, T.N., D.L.T. Anderson, M.K. Davey, P. Delecluse, A. Katternberg, Y. Kikamura, M. Latif, and T. Yamagata, Intercomparison of tropical oceans GCMs, World Climate Research Programme, WMO, Geneve, 1993.

Stramma, L., Geostrophic Transport of the South Equatorial Current in the Atlantic, *Journal of Marine Research*, *49* (2), 281-294, 1991.

Stramma, L., P. Cornillon, R.A. Weller, J.F. Price, and M.G. Briscoe, Large Diurnal Sea-Surface Temperature Variability - Satellite and Insitu Measurements, *Journal of Physical Oceanography*, *16* (5), 827-837, 1986.

Stramma, L., and F. Schott, The mean flow field of the tropical Atlantic Ocean, *Deep-Sea Research Part Ii-Topical Studies in Oceanography*, *46* (1-2), 279-303, 1999.

Stramma, L., and G. Siedler, Seasonal-Changes in the North-Atlantic Sub-Tropical Gyre, *Journal of Geophysical Research-Oceans*, *93* (C7), 8111-8118, 1988.

Strutton, P.G., J.P. Ryan, and F.P. Chavez, Enhanced chlorophyll associated with tropical instability waves in the equatorial Pacific, *Geophysical Research Letters*, *28* (10), 2005-2008, 2001.

Stuart-Menteth, A., A global study of diurnal warming, PhD thesis, University of Southampton, Southampton, 2004.

Stuart-Menteth, A.C., I.S. Robinson, and P.G. Challenor, A global study of diurnal warming using satellite-derived sea surface temperature, *Journal of Geophysical Research-Oceans*, *108* (C5), art. no.-3155, 2003.

Stull, R.B., *An Introduction to Boundary Layer Meteorology*, Kluwer Academic Publishers, Dordrecht, 1988.

Swenson, M.S., and D.V. Hansen, Tropical Pacific ocean mixed layer heat budget: The Pacific cold tongue, *Journal of Physical Oceanography*, *29* (1), 69-81, 1999.

Takahashi, T., S.C. Sutherland, C. Sweeney, A. Poisson, N. Metzl, B. Tilbrook, N. Bates, R. Wanninkhof, R.A. Feely, C. Sabine, J. Olafsson, and Y. Nojiri, Global sea-air CO2 flux based on climatological surface ocean pCO(2), and seasonal biological and temperature effects, *Deep-Sea Research Part Ii-Topical Studies in Oceanography*, *49* (9-10), 1601-1622, 2002.

Taylor, P.K. Intercomparison and validation of ocean-atmosphere energy flux fields, Final Report of the Joint WCRP/SCOR Working Group on Air-Sea Fluxes, 2000.

Thum, N., S.K. Esbensen, D.B. Chelton, and M.J. McPhaden, Air-sea heat exchange along the northern sea surface temperature front in the eastern tropical Pacific, *Journal of Climate*, *15* (23), 3361-3378, 2002.

Torrence, C., and G.P. Compo, A practical guide to wavelet analysis, *Bulletin of the American Meteorological Society*, *79* (1), 61-78, 1998.

Tsuchiya, M., L.D. Talley, and M.S. McCartney, An Eastern Atlantic Section from Iceland Southward across the Equator, *Deep-Sea Research Part a-Oceanographic Research Papers*, *39* (11-12A), 1885-1917, 1992.

Verstraete, J.M., The Seasonal Upwellings in the Gulf of Guinea, *Progress in Oceanography*, *29* (1), 1-60, 1992.

Wacongne, S., and B. Piton, The near-Surface Circulation in the Northeastern Corner of the South-Atlantic Ocean, *Deep-Sea Research Part a-Oceanographic Research Papers*, *39* (7-8A), 1273-1298, 1992.

Wainer, I., G. Clauzet, J. Servain, and J. Soares, Time scales of upper ocean temperature variability inferred from the PIRATA data (1997-2000), *Geophysical Research Letters*, *30* (5), art. no.-8004, 2003.

Wainer, I., and J. Soares, North northeast Brazil rainfall and its decadal-scale relationship to wind stress and sea surface temperature, *Geophysical Research Letters*, *24* (3), 277-280, 1997.

Wallace, J.M., T.P. Mitchell, and C. Deser, The Influence of Sea-Surface Temperature on Surface Wind in the Eastern Equatorial Pacific - Seasonal and Interannual Variability, *Journal of Climate*, *2* (12), 1492-1499, 1989.

Wang, W.M., and M.J. McPhaden, The surface-layer heat balance in the equatorial Pacific Ocean. Part I: Mean seasonal cycle, *Journal of Physical Oceanography*, *29* (8), 1812-1831, 1999.

Webster, P.J., C.A. Clayson, and J.A. Curry, Clouds, radiation, and the diurnal cycle of sea surface temperature in the Tropical Western Pacific, *Journal of Climate*, *9* (8), 1712-1730, 1996.

Webster, P.J., and R. Lukas, Toga Coare - the Coupled Ocean Atmosphere Response Experiment, *Bulletin of the American Meteorological Society*, *73* (9), 1377-1416, 1992.

Weisberg, R.H., Instability Waves Observed on the Equator in the Atlantic-Ocean During 1983, *Geophysical Research Letters*, *11* (8), 753-756, 1984.

Weisberg, R.H., and T.Y. Tang, On the Response of the Equatorial Thermocline in the Atlantic- Ocean to the Seasonally Varying Trade Winds, *Journal of Geophysical Research-Oceans*, *90* (NC4), 7117-7128, 1985.

Weisberg, R.H., and T.Y. Tang, Further-Studies on the Response of the Equatorial Thermocline in the Atlantic-Ocean to the Seasonally Varying Trade Winds, *Journal of Geophysical Research-Oceans*, *92* (C4), 3709-3727, 1987.

Weisberg, R.H., and T.Y. Tang, A Linear-Analysis of Equatorial Atlantic-Ocean Thermocline Variability, *Journal of Physical Oceanography*, *20* (12), 1813-1825, 1990.

Weisberg, R.H., and T.J. Weingartner, Instability Waves in the Equatorial Atlantic-Ocean, *Journal of Physical Oceanography*, *18* (11), 1641-1657, 1988.

Weissman, D.E., M.A. Bourassa, and J. Tongue, Effects of rain rate and wind magnitude on SeaWinds scatterometer wind speed errors, *Journal of Atmospheric and Oceanic Technology*, *19* (5), 738-746, 2002.

Weller, R.A., and S.P. Anderson, Surface meteorology and air-sea fluxes in the western equatorial Pacific warm pool during the TOGA coupled ocean-atmosphere response experiment, *Journal of Climate*, *9* (8), 1959-1990, 1996.

Wentz, F.J., and M. Schabel, Precise climate monitoring using complementary satellite data sets, *Nature*, *403* (6768), 414-416, 2000.

Wick, G.A., W.J. Emery, L.H. Kantha, and P. Schlussel, The behavior of the bulk-skin sea surface temperature difference under varying wind speed and heat flux, *Journal of Physical Oceanography*, *26* (10), 1969-1988, 1996.

Williams, C.R., S.K. Avery, J.R. McAfee, and K.S. Gage, Comparison of Observed Diurnal and Semidiurnal Tropospheric Winds at Christmas-Island with Tidal Theory, *Geophysical Research Letters*, *19* (14), 1471-1474, 1992.

Wilson, W.D., E. Johns, and R.L. Molinari, Upper Layer Circulation in the Western Tropical North-Atlantic Ocean During August-1989, *Journal of Geophysical Research-Oceans*, *99* (C11), 22513-22523, 1994.

WMO, International list of selected, supplementary and auxiliary ships, pp. 427, World Meteorological Organization, 1998.

WOCE, The Atlantic Circulation and Climate Experiment, pp. 43-46, US WOCE Implementation Report, 1997.

Xie, S.P., M. Ishiwatari, H. Hashizume, and K. Takeuchi, Coupled ocean-atmospheric waves on the equatorial front, *Geophysical Research Letters*, *25* (20), 3863-3866, 1998.

Yan, Z.W., P.D. Jones, A. Moberg, H. Bergstrom, T.D. Davies, and C. Yang, Recent trends in weather and seasonal cycles: An analysis of daily data from Europe and China, *Journal of Geophysical Research-Atmospheres*, *106* (D6), 5123-5138, 2001.

Yokoyama, R., S. Tanba, and T. Souma, Sea-Surface Effects on the Sea-Surface Temperature Estimation by Remote-Sensing, *International Journal of Remote Sensing*, *16* (2), 227-238, 1995.

Yu, J.-Y., and W.T. Liu, A linear relationship between ENSO intensity and tropical instability wave activity in the eastern Pacific Ocean, *Geophysical Research Letters*, *30* (14), art. no.-1735, 2003.

Yu, X., and M.J. McPhaden, Seasonal variability in the equatorial Pacific, *Journal of Physical Oceanography*, *29* (5), 925-947, 1999.

Zebiak, S.E., Air-Sea Interaction in the Equatorial Atlantic Region, *Journal of Climate*, *6* (8), 1567-1568, 1993.

Zeng, X.B., and R.E. Dickinson, Impact of diurnally-varying skin temperature on surface fluxes over the tropical Pacific, *Geophysical Research Letters*, *25* (9), 1411-1414, 1998.

Zeng, X.B., M. Zhao, and R.E. Dickinson, Intercomparison of bulk aerodynamic algorithms for the computation of sea surface fluxes using TOGA COARE and TAO data, *Journal of Climate*, *11* (10), 2628-2644, 1998.

Zeng, X.B., M. Zhao, R.E. Dickinson, and Y.P. He, A multiyear, hourly sea surface skin temperature data set derived from the TOGA TAO bulk temperature and wind speed over the tropical Pacific, *Journal of Geophysical Research-Oceans*, *104* (C1), 1525-1536, 1999.

Zhang, C.D., Intraseasonal variability of the upper-ocean thermal structure observed at 0 degrees and 165 degrees E, *Journal of Climate*, *10* (12), 3077-3092, 1997.

Zhou, Z.X., and J.A. Carton, Latent heat flux and interannual variability of the coupled atmosphere-ocean system, *Journal of the Atmospheric Sciences*, *55* (4), 494-501, 1998.